# Atmospheric Pressure Plasma Coupled with Aerosol for Biomedical Applications

Ivana Sremački

Doctoral dissertation submitted to obtain the academic degree of
Doctor of Engineering Physics

**Supervisors**

Prof. Christophe Leys, PhD - Anton Nikiforov, PhD

Department of Applied Physics
Faculty of Engineering and Architecture, Ghent University

March 2022

**GHENT UNIVERSITY**

**Atmospheric Pressure Plasma Coupled with Aerosol for Biomedical Applications**

Ivana Sremački

Doctoral dissertation submitted to obtain the academic degree of
Doctor of Engineering Physics

**Supervisors**
Prof. Christophe Leys, PhD ‑ Anton Nikiforov, PhD

Department of Applied Physics
Faculty of Engineering and Architecture, Ghent University

March 2022

## Members of the Examination Board

### Chair

Prof. Filip De Turck, PhD, Ghent University

### Other members entitled to vote

Prof. Uroš Cvelbar, PhD, University of Ljubljana, Slovenia

Prof. An Ghysels, PhD, Ghent University

Prof. Ahmad Reza Mehdipour, PhD, Ghent University

Prof. Rino Morent, PhD, Ghent University

Prof. Nevena Puač, PhD, University of Belgrade, Serbia

### Supervisors

Prof. Christophe Leys, PhD, Ghent University

Anton Nikiforov, PhD, Ghent University

## Acknowledgments

This research was carried out in the Research Unit Plasma Technology, Department of Applied Physics of Ghent University. Throughout the last four-year, I have received a great deal of support from my promoters, colleagues, friends, and family. Thus, the following words are to you all.

In the first place, I offer my sincerest gratitude to my promoters, Prof. Christophe Leys and Dr. Anton Nikiforov, who accepted me as their Ph.D. student. Christophe, I greatly appreciate your support and the opportunity you gave me to perform this research. Furthermore, I appreciate the independence you gave me and the chance to improve my teaching skills.
Anton, thank you for your patience and guidance during these four years. Your immense expertise inspired me. Again, thank you for sharing your knowledge with me and contributing to this research; I'm in debt to you forever.

I want to extend my gratitude to the examination members for their critical comments on this thesis and their willingness to be part of the committee. Special thanks I owe to Prof. Uroš Cvelbar, who was closely involved in this research and enabled my stay at Jožef Stefan Institute. Uroše, veliko hvala na svemu, zadovoljstvo je bilo raditi sa vama. Further, my gratitude goes to the RUPT members, my colleagues, and professors Rino Morent and Nathalie De Geyter. Special thanks go to Tim and Joris for their technical support.

Hereby, I must appreciate my colleagues with whom I shared the office and who made me feel at home, Yulia, Mahtab, Silvia, Savita, Mehrnoush, Tim, and Mikhail. Yulia, thank you for all your numerous advice and support during these four years; our friendship means great to me. Mahtab, thank you for the knowledge and experience you unselfishly shared with me. The encouragement you gave me was important to me; I owe you many. Mikhail, I must not forget to appreciate our long conversations and discussions; your brutal honesty always made my day. My friends, your presence made my life in Ghent beautiful; I am honored knowing you all.

Finally, I want to show appreciation to you, my love. Thank you for your continuous help, consideration and understanding. Heaven knows I made your life difficult in the last months, yet you did everything to make me smile. Thank you for being part of my life. In joy and sorrow, my home is in your arms.

Miljana, Kristina, Karmen, hvala vam što ste mi ostale blizu iako ste daleko.

I naposletku, poneka reč i za vas prijatelji i porodico, neiscrpna podrško moja. Hvala vam što ste me ispraćali, dočekivali, sa mnom se smejali i sa mnom plakali. Nevena, mama, tata hvala vam što ste moji. Sve što jesam, dugujem vama.

Ivana Sremački
Ghent, 2022

# TABLE OF CONTENTS

## LIST OF ACRONYMS

**A**

Ar Argon

AC Alternating Current

APPJ Atmospheric Pressure Plasma Jet

AS Absorption Spectroscopy

atm Atmosphere

**C**

CAP Cold Atmospheric Plasma

CAT Catalase

CCD Charge Coupled Device

CCP Capacitively Coupled Plasma

COL Collagen

CE (mark) Marking according to Europian Commission

**D**

DBD Dielectric Barrier Discharge

DC Direct Current

DFU Diabetic Foot Ulcer

DMPO 5,5-Dimethyl-1-Pyrroline-N-Oxide

DMSO Dimethyl Sulfoxide

DNA Deoxyribonucleic Acid

DSB Double Strand Break

**E**

ECM Extra-Cellular Matrix

EGF Epidermal Growth Factor

EPR Electron Paramagnetic Resonance

**F**

FAK Focal Adhesion Kinase

FDA Food and Drug Administration

FGF-2 Fibroblast Growth Factor 2

FE-DBD Floating Electrode Dielectric Barrier Discharge

FTIC Fluorescein Isothiocyanate

FTIR Fourier Transform Infra-Red

**G**

GF Growth Factor

GHz Giga Hertz
GPX Glutathione Peroxidase

**H**
HA Hyaluronic Acid
He Helium
HPLC High-Pressure Liquid Chromatography

**I**
IC Ion Chromatography
ICCD Intensified Charge-Coupled Device
ICNIRP International Commission on Non-Ionizing Radiation Protection

**K**
kbp Kilobase Pair
kHz Kilohertz
Ki-67 Proliferation index

**L**
LIF Laser-Induced Fluorescence
L929 NCTC clone 929 [L cell, L-929, derivative of Strain L] connective mouse tissue

**N**
$N_2$ Nitrogen
Nd: YAG Neodymium-doped yttrium aluminum garnet
NF Nuclear factor
Nrf2 Nuclear Related Factor 2

**M**
MS Mass Spectrometry
MTT (3-[4,5-dimethylthiazol-2-yl]-2,5-diphenyltetrazolium bromide)
MW Microwave

**O**
O Atomic Oxygen
OES Optical Emission Spectroscopy

**P**
PAL Plasma Activated Liquid
PAW Plasma Activated Water

PCR Polymerase Chain Reaction

ppm Part Per Million

PXN Paxillin

**R**

RF Radio Frequency

RMS Root Mean Square

RNA Ribonucleic Acid

RNS Reactive Nitrogen Species

RONS Reactive Oxygen and Nitrogen Species

ROS Reactive Oxygen Species

**S**

SCCM Standard Cubic Centimeter per Minute

SLM Standard Liter per Minute

SMA Smooth Muscle Actin

SNDC Syndecan

SOD Superoxide Dismutase

SSB Single-Strand Break

**T**

TALIF Two-photon Absorption Laser-Induced Fluorescence

TGF  Transforming Growth Factor

TEMPD 2,2,6,6-tetramethyl-4-piperidone

TEMPO 2,2,6,6-tetramethyl-1-piperidinyloxyl

TEMPONE-H 1-Hydroxy-2,2,6,6-tetramethyl-4-oxo-piperidine

TLN Talin

TDD Transdermal Drug Delivery

**U**

UV Ultra violet

**V**

VUV Vacuum Ultra Violet

VU Venous Ulcer

VCL Vinculin

## LIST OF PUBLICATIONS

1. Ivana Sremački, Mikhail Gromov, Christophe Leys, Rino Morent, Rony Snyders, Anton Nikiforov
"*An atmospheric pressure non-self-sustained glow discharge in between metal/metal and metal/liquid electrodes*"
Plasma Processes and Polymers, vol. 17, no. 6, 2020.

2. Ivana Sremački, Andrea Jurov, Martina Modic, Uros Cvelbar, Lei Wang, Christophe Leys, Anton Nikiforov
"*On diagnostics of an annular-shape radio-frequency plasma jet operating in argon at atmospheric conditions*"
Plasma Sources Science & Technology, vol. 29, no. 3, 2020.

3. Ivana Sremački, Giuliana Bruno, Helena Jablonowski, Christophe Leys, Anton Nikiforov and Kristian Wende
"*Influence of aerosol injection on the liquid chemistry induced by an RF argon plasma jet*"
Plasma Sources Science & Technology, vol. 30, no. 9, 2021.

4. Ivana Sremački, Špela Kos, Maša Bošnjak, Andrea Jurov, Gregor Serša, Martina Modic, Christophe Leys, Uroš Cvelbar and Anton Nikiforov
„*Plasma Damage Control: From Biomolecules to Cells and Skin*"
ACS Applied Materials & Interfaces, 2021.

5. Ivana Sremački, Mahtab Asadian, Nathalie De Geyter, Christophe Leys, Liesbet Geris, Anton Nikiforov
"*Potentials of the plasma-aerosol system for wound healing advanced by drug introduction: in vitro study*"
In preparation.

6. Andrea Jurov, Špela Kos, Nataša Hojnik, Ivana Sremački, Anton Nikiforov, Christophe Leys, Gregor Serša and Uroš Cvelbar
"*Analysing mouse skin cell behavior under a non-thermal kHz plasma jet*"
Applied Sciences-Basel, vol. 11, no. 3, 2021.

7. Andrea Jurov, Špela Kos, Tanja Blaguš, Ivana Sremački, Gregor Filipič, Nataša Hojnik, Anton Nikiforov, Christophe Leys, Maja Čemezar, Gregor Serša and Uroš Cvelbar
"*Atmospheric pressure plasma jet-mouse skin interaction: mitigation of damages by liquid interface and gas flow control*"
Accepted for publication, AVS Biointerphases.

## CONFERENCE PROCEEDINGS PAPERS

1. Ivana Sremački, Lei Wang, Andrea Jurov, Martina Modic, Uroš Cvelbar, Christophe Leys, Anton Nikiforov
 "Radio-Frequency Plasma in Combination with Aerosol Injection for Biomedical Applications"
24th International Symposium on Plasma Chemistry, ISPC 24, Proceedings. International Plasma Chemistry Society (IPCS), 2019.

2. Ivana Sremački, Špela Kos, Christophe Leys, Gregor Serša, Uroš Cvelbar, Anton Nikiforov
"Annular shape RF jet in contact with aerosol: UV emission control for safe biomedical application."
The 47th IEE International Conference On Plasma Science, ICOPS 2020 Singapore, Singapore.

## CONTRIBUTION TO NATIONAL AND INTERNATIONAL CONFERENCES

1. Ivana Sremački, Martina Modić, Uroš Cvelbar, Christophe Leys, Anton Nikiforov
*„Dynamics and temperature measurement of RF plasma"*
Conference On Cold Plasma Sources and Applications, COPSA 2018, Ypres, Belgium.

2. Ivana Sremački, Andrea Jurov, Martina Modić, Uroš Cvelbar, Christophe Leys, Anton Nikiforov
„Gas temperature characterization of annular shape RF APPJ for biomedical application"
13th Frontiers in Low-Temperature Plasma Diagnostics, FLTPD 2019, Bad Honnef, Germany.

3. Ivana Sremački, Andrea Jurov, Martina Modić, Uroš Cvelbar, Christophe Leys, Anton Nikiforov
„Plasma temperature diagnostic methods of large size RF APPJ for biomedical application"
24th International Symposium on Plasma Chemistry, ICPS 2019, Naples, Italy.

4.Ivana Sremački, Špela Kos, Gregor Serša, Uroš Cvelbar, Christophe Leys, Anton Nikiforov
"Annular shape RF jet in contact with aerosol: UV emission control for safe biomedical application"
The 47th IEE International Conference On Plasma Science, ICOPS 2020 Singapore, Singapore.

5. Ivana Sremački, Špela Kos, Gregor Serša, Martina Modic, Uroš Cvelbar, Christophe Leys, Anton Nikiforov
"Plasma-aerosol system: controlled RONS and UV flux for the safe wound healing and topical drug delivery"
8th International Plasma Science & Entrepreneurship Workshop 2021, Prague, Czech Republic.

## SUMMARY IN ENGLISH

Cold plasmas are described by their non-equilibrium character and a huge difference in electron and ion temperature. The gas in plasma can remain close to room temperature while electrons can be heated above 10 000 K≈1 eV. The fast electrons drive plasma chemistry and generate species such as charged particles, neutrals, radicals, metastables, radiation, etc. Due to their high chemical reactivity and low gas temperature, cold plasmas are fast-developing alternatives for various biomedical and industrial purposes. In the last two decades, plasmas have been used to selectively inhibit or promote the growth of prokaryotic and eukaryotic cells. Furthermore, biological responses initiated by cold plasma have been shown to be of use in wound care, specifically for healing chronic wounds.

Chronic wounds fail to go through the normal healing process. Abnormal wounds often develop in patients suffering from vascular diseases, diabetes, patients with decreased mobility, and patients with complicated infections. Considering the growing number of diabetic patients, the problem of chronic wounds spread globally. Nowadays, different techniques are employed to enhance the healing of chronic wounds after infection is sanitized. The advanced healing methods include oxygenation of wounds, production of NO species in the wound bed by electric RF field, cellular, growth factor, and collagen therapy. Often, for the best performances, these methods must be combined. Accordingly, a good alternative would perform solely throughout all healing phases.

Many plasma devices are developed for application in wound healing; however, only a few are medically certified but still not commercially used in clinics. This is because of strict requirements when designing the plasma sources for application on humans. Firstly, plasma has to be electromagnetically compatible with the human skin. Furthermore, plasma has to be generated under atmospheric conditions cold and stable. In addition, it should produce crucial chemical species to enhance wound healing. Regarding existing studies, the highest expectations have been recognized in radio-frequency atmospheric pressure plasma jets (RF APPJ). Radio-frequency (RF) plasma is one of the promising candidates due to the advantages of relatively low cost and electrical safety. Moreover, plasma jets in argon Ar are interesting due to their low cost compared to helium He. However, generating a diffuse Ar plasma jet under atmospheric conditions is challenging when increasing the size above a millimeter scale.

This thesis focuses on current problems reported in plasma medicine. Herein, a new geometry of plasma reactor coupled with aerosol for biomedical application is investigated. The relatively large-sized ($d_{out}$=14 mm) RF plasma jet reactor is designed in annular geometry, allowing the introduction of aerosols (d≈22

μm) in plasma effluent. Throughout this thesis, the physical, chemical, and finally biological aspects of this reactor are presented.

In the first instance, the safe, stable, and low gas temperature operation of the plasma reactor is examined. Plasma diagnostics tools are employed to electrically and optically characterize the operation of the plasma jet in the diffuse, α-mode. Moreover, gas temperature in plasma jet is evaluated by three different techniques to label this device as cold and potent for further biomedical use. It is shown that sheaths stabilize plasma formed in this geometry. Plasma sheaths allow diffuse and uniform discharge operation on dissipated power densities below 30 W/cm$^3$. Gas temperature in plasma depends on the gas flow and dissipated power in plasma. Coupling three different techniques, it is shown that Rayleigh laser scattering is a good temperature indicator in this type of plasma jets. Accordingly, the plasma jet is evaluated as safe for biomedical use above flow 2 standard liter per minute and below dissipated power of 10 W, resulting in 60° C jet temperature.

Further, plasma-induced liquid chemistry is investigated. In the chemical study of the jet, water aerosols are introduced, and their influence on plasma chemistry is examined. This study applies advanced liquid chemical diagnostics to detect and measure reactive oxygen and nitrogen species (RONS). RONS have a central role in biomedicine. At moderate concentrations, RONS initiate cellular responses (e.g., in defense against infectious agents), have functions in many cellular signaling pathways, and induce mitogenic responses. Liquid-chemistry diagnostics of the Ar APPJ revealed strong dominance of oxygen (ROS) and UV radiation-driven chemistry. The dominant species generated in this plasma jet are short-living atomic oxygen O, singlet oxygen $^1O_2$. UV radiation has an essential role in the photolysis of water and the production of OH and $H_2O_2$. Aerosol introduction in plasma jet is shown to change plasma chemistry and translate it in the aerosol region. Due to interaction with the droplets, aerosol partially scavenges radicals (e.g., O) and absorbs UV radiation.

Following the highlights of the previous study, the biological impact of plasma on biomolecules, cells, and tissues is investigated. Special focus is given to the role of UV radiation from plasma in biomedical treatments. It is seen that Ar plasma emits intense UVC photons λ=126, 130 nm from Ar excimer $Ar_2^*$ and atomic oxygen OI, respectively. This radiation is detected in the direction of Ar gas flow far as 14 mm, and accordingly must be considered in biomedical treatments. In this study, the strong influence of plasma UV radiation on the stability of the biomolecule plasmid DNA is revealed. Furthermore, although cells in a liquid environment are shown not to be affected by plasma UV radiation, a strong cytotoxic impact on cells in a dry environment is revealed. The introduction of aerosol changes the interface of plasma-biological target interaction. As a result, the aerosol is shown to increase the stability of plasmid DNA with respect to plasma treatment. Moreover, when

treating cells in a limited-liquid environment, aerosols are shown to improve cell viability by 10 %. Finally, the aerosol injection in plasma effluent is shown to be a good choice in first skin treatment trials. The presence of micro-droplets between plasma and biological targets limits RONS' flux and UV radiation towards the skin. To this end, aerosol droplets in plasma treatment reduce skin heating and potential tissue damage.

At last, aspects of plasma-assisted wound healing are studied *in vitro*. A step further is taken to study plasma-assisted drug delivery *in vitro*. With this aim, an extensive study is performed to investigate the viability and proliferation of connective tissue fibroblast cells after being treated with Ar and Ar/$N_2$ plasma. It is shown that cells proliferation improves during 7 days when shortly (t<60 s) treated with low power plasma ($P_{diss}$=7 W). No significant distinction in cell-proliferation is noticed between Ar and Ar/$N_2$ plasma treatment. However, the expression of genes essential in wound healing was different. Better proliferation is confirmed by better adhesion of cells, improved cell signaling, and communication with ECM. Although a crucial ROS role in this process is claimed, RNS (RONS) should not be neglected. It is shown that long-living downstream products of NO, $NO_2^-$ and $NO_3^-$ play an important role in cell adhesion, migration, signaling, and communication with ECM. Ultimately, plasma-assisted cell permeabilization is studied in this thesis. Plasma species such as O, OH, and $H_2O_2$ cause lipid peroxidation of the cell membrane. In controlled conditions, transient nanopores on the cell membrane can be created, and through them, a drug can be introduced (e.g., gene transfection). Accordingly, we studied the localized introduction of the drug carrier molecule-dextran. Once more, the aerosol introduction is shown to soften and change the spatial delivery of plasma species. This result is helpful in studying safe and localized drug delivery by cold atmospheric plasma.

The results presented in this thesis contribute to the fundamental and practical understanding of large-size RF argon jets in contact with aerosol. Aerosol injection in plasma effluent can be used in plasma medicine for safe and controlled delivery of plasma species and controlled interaction with biological objects.

## NEDERLANDSTALIGE SAMENVATTING

Koude plasma's worden gekenmerkt door hun thermisch niet-evenwichtskarakter wat zich vertaalt in een groot verschil tussen de elektronentemperatuur en de ionentemperatuur. Terwijl het plasmagas dicht bij kamertemperatuur blijft, worden de elektronen verhit tot temperaturen hoger dan 10000 K of energieën hoger dan 1 eV. Deze snelle elektronen drijven de plasmachemie aan en produceren geladen deeltjes, radicalen, metastabiele deeltjes, straling, enz. Dankzij de hoge chemische reactiviteit en de lage gastemperatuur, worden koude plasma's in sterk toenemende mate gebruikt voor diverse biomedische en industriële toepassingen. In de twee voorbije decennia, werden plasma's gebruikt om selectief de groei van prokaryotische en eukaryotische cellen te verhinderen of te stimuleren. Ook is gebleken dat de biologische respons die wordt geïnitieerd door een koud plasma nuttig kan zijn in de context van wondzorg, meer bepaald bij de behandeling van chronische wonden.

Bij chronische wonden is het normale genezingsproces verstoord. Abnormale wonden ontwikkelen zich vaak bij patiënten die lijden aan vaatziekten of diabetes, bij patiënten met verminderde mobiliteit of patiënten met complexe ontstekingen. Gelet op het groeiende aantal diabetespatiënten, breidt het probleem van chronische wonden zich wereldwijd uit. Vandaag de dag worden verschillende technieken gebruikt om de genezing van chronische wonden, na ontsmetting van de ontsteking, te bevorderen. De geavanceerde genezingsmethodes omvatten zuurstofvoorziening, de productie van NO in de wonde met een RF elektrisch veld, cellulaire, groeifactor- en gentherapie. Vaak wordt voor het beste resultaat een combinatie van deze methodes toegepast. Een methode die gedurende de verschillende fasen in het genezingsproces onafhankelijk van andere methodes werkzaam is, zou daarom een goed alternatief zijn.

Er worden verschillende types van plasmabronnen ontwikkeld voor wondzorg. Enkele daarvan zijn medisch gecertifieerd maar worden nog niet commercieel gebruikt in ziekenhuizen. Dit komt door de strenge regelgeving voor plasmabronnen die toegepast worden op mensen. Het plasma moet enerzijds elektromagnetisch compatibel zijn met de menselijke huid. Anderzijds moet het plasma, dat wordt opgewekt bij atmosfeerdruk, koud en stabiel zijn. Bovendien moet het die chemische deeltjes genereren die cruciaal zijn om de wondgenezing te bevorderen. In de literatuur wordt het grote potentieel erkend van radiofrequente atmosferische plasmastralen (RF APPJ). Voordelen van de RF AAPJ zijn de relatief lage kost en de elektrische veiligheid. In het bijzonder zijn plasmastralen in argon interessant omwille van de lage kost in vergelijking met helium. Echter, het opwekken van een diffuse argonplasmastraal bij atmosfeerdruk met afmetingen groter dan enkele mm, vormt nog steeds een uitdaging.

Deze scriptie richt zich op actuele problemen die zich aandienen binnen de plasmageneeskunde. Er wordt een nieuwe geometrie onderzocht voor een plasmareactor, gekoppeld aan aerosolinjectie, die inzetbaar is voor biomedische toepassingen. De bestudeerde RF-plasmastraalreactor heeft een relatief grote buitendiameter ($d_{out}$ = 14 mm) en een ringvormige geometrie, waardoor aerosolen ($d \cong 22$ $\mu$m) kunnen toegevoegd worden aan het uitstromende plasma. In dit werk wordt het fysisch, chemisch en uiteindelijk biologisch potentieel van deze reactor onderzocht.

In eerste instantie wordt de veilige en stabiele werking bij lage temperatuur van de plasmareactor onderzocht. Plasmadiagnostieken worden ingezet om de plasmastraal, werkend in de diffuse $\alpha$-mode, elektrisch en optisch te karakteriseren. De gastemperatuur in de plasmastraal wordt met drie verschillende technieken bepaald, teneinde de plasmabron als koud en biomedisch toepasbaar te kunnen bestempelen. Er wordt aangetoond dat in de onderzochte geometrie het plasma wordt gestabiliseerd door de ruimteladingslaag waardoor een diffuse en homogene werking mogelijk is tot een gedissipeerde vermogendichtheid van 30 W/cm$^3$. De gastemperatuur is verder afhankelijk van het gasdebiet en het gedissipeerde vermogen. Door drie verschillende technieken te koppelen, wordt aangetoond dat Rayleigh laserverstrooiing een goede temperatuurindicator is in laminaire plasma's. De plasmabron wordt als veilig voor biomedische toepassingen beschouwd voor gasdebieten hoger dan 2 slm en gedissipeerde vermogens lager dan 10 W. Dit stemt overeen met een gastemperatuur in de plasmastraal van 60° C.

Vervolgens wordt de plasma-geïnduceerde chemie in de vloeistoffase onderzocht. Wateraerosolen worden toegevoegd aan de plasmastraal en hun invloed op de plasmachemie wordt bestudeerd. In deze studie worden geavanceerde analytische technieken ingezet om de reactieve zuurstof- en stikstofdeeltjes te kwantificeren (RONS). RONS spelen een centrale rol in biomedische processen. In gematigde concentraties initiëren RONS cellulaire respons (e.g. in de verdediging tegen besmettelijke agentia), vervullen ze een rol in verschillende mechanismen van celseining en induceren ze mitogene respons. De chemische analyse van de APPJ in argon toont de sterke dominantie van door zuurstof (ROS) en door UV-straling aangedreven reactiemechanismen aan. De belangrijkste deeltjes die gegenereerd worden in de plasmastraal zijn het kortlevende atomaire zuurstof en singlet dizuurstof. UV-straling vervult een essentiële rol in de fotolyse van water en in de productie van OH en H$_2$O$_2$. De toevoeging van aerosolen aan de plasmastraal verandert de plasmachemie en verplaatst die naar de aerosolzone. De aerosolen reageren met radicalen (bijv. O) en absorberen UV-straling.

Rekening houdend met de voornaamste resultaten van de voorgaande studie werd de biologische impact van plasma op biomoleculen, cellen en weefstel

onderzocht. Speciale aandacht werd besteed aan de rol van de in het plasma gevormde UV-straling bij biomedische behandelingen. Argonplasma zendt intense UVC-fotonen uit bij golflengtes van 126 nm en 130 nm, afkomstig van respectievelijk het excimeer $Ar_2^*$ en de atomaire zuurstoftoestand OI. Deze straling wordt gedetecteerd tot 14 mm ver in de uitstroomzone en moet derhalve in overweging genomen worden bij biomedische behandelingen. Het onderzoek toont de sterke invloed aan van de in het plasma gevormde UV-straling op de stabiliteit van de biomolecule plasmid DNA. Daarnaast blijkt uit de studie dat, waar cellen in een vloeistofomgeving niet worden aangetast door de UV-straling van het plasma, er wel een sterk cytotoxisch effect is van de straling op cellen in een droge omgeving. De toevoeging van aerosolen verandert de interface tussen plasma en biologische target, waardoor de stabiliteit van plasmid DNA onder plasmabehandeling toeneemt. Wanneer cellen behandeld worden in een beperkte vloeistofomgeving, stijgt de levensvatbaarheid van de cellen met 10 %. Aerosolinjectie in het uitstromende plasma bleek ook een gunstig effect te hebben bij de eerste huidbehandelingsexperimenten. Door de aanwezigheid van microdruppels tussen plasma en biologische target wordt de flux van RONS en UV-straling naar de huid beperkt. Hierdoor vermindert de opwarming van de huid en het risico op weefselbeschadiging.

Tenslotte worden in vitro enkele aspecten van plasma-geassisteerde wondgenezing bestudeerd. Er wordt een volgende stap gezet in de studie van het potentieel van plasma-geassisteerde toediening van geneesmiddelen. Hiertoe wordt een uitgebreid onderzoek gevoerd naar de levensvatbaarheid en proliferatie van fibroblastcellen in *verbindingsweefsel* na behandeling in een Ar- of $Ar/N_2$-plasma. Er wordt aangetoond dat de celproliferatie verbetert na een korte ($t < 60$ s) behandeling in een laagvermogenplasma ($P_{diss} = 7$ W), en dit gedurende minstens zeven dagen. Er werd geen significant verschil in celproliferatie vastgesteld tussen Ar- en $Ar/N_2$-plasma. Er was wel een verschil in de expressie van voor wondgenezing essentiële genen. De verbeterde proliferatie wordt bevestigd door de betere hechting van cellen en een verbeterde celseining en communicatie met de ECM. Hoewel in dit proces vaak de cruciale rol van ROS wordt benadrukt, mag ook de bijdrage van RNS (RONS) niet verwaarloosd worden. Er wordt aangetoond dat langlevende NO-, $NO_2$- en $NO_3$-deeltjes in de uitstroomzone een belangrijke rol spelen in celadhesie, celmigratie, celseining en communicatie met de ECM.

In het laatste deel van de thesis wordt plasma-geassisteerde celpermeabilisatie bestudeerd. Plasmadeeltjes zoals O, OH en $H_2O_2$ veroorzaken de oxidatie van lipiden in het celmembraan. Onder gecontroleerde omstandigheden kunnen nanoporiën in het celmembraan aangebracht worden waarlangs een geneesmiddel kan binnengebracht worden (bijv. gentransfectie). In dit verband werd de locale introductie van de dragermolecule dextran onderzocht. Opnieuw bleek dat

de toevoeging van aerosolen de ruimtelijke verdeling van de plasmadeeltjes verandert. Dit is een nuttig resultaat in de zoektocht naar een veilige en gelocaliseerde toediening van geneesmiddelen door koud atmosferisch plasma.

De resultaten die in deze scriptie worden getoond, dragen bij tot een fundamenteel en praktisch inzicht met betrekking tot RF argonplasmastralen met grote afmetingen, die in contact staan met aërosolen. Aërosolinjectie in het plasma-effluent kan in de plasmageneeskunde gebruikt worden voor de veilige en gecontroleerde aanvoer van plasma-deeltjes en voor de gecontroleerde interactie met biologische voorwerpen.

# CHAPTER 1: INTRODUCTION

## 1.1 SCOPE OF THE THESIS

Plasma or partially ionized gas is a physically and chemically active medium that displays a lot of potential in industry and biomedicine. Various applications of plasmas dictate the working conditions of these. Therefore, plasmas are generated under low or high pressure; in DC, AC, RF, MW electric fields, pure noble and molecular gases, and their mixtures. Over the past few decades, there has been a rising interest in developing atmospheric non-equilibrium/cold plasmas and their use for heat-sensitive substrates treatment, e.g., skin. Due to the rich and diverse production of chemically reactive species, cold plasmas can oxidize, activate, and modify substrates, synthesize gases and polymerize. Nowadays, different cold plasma reactors have been designed and employed in the biomedical field to inactivate microbes from medical surfaces and tissues and promote the proliferation of healthy cells. As a result of selective cell inactivation and growth promotion, cold atmospheric plasmas (CAPs) found their utilization in the field of chronic wound healing.

The healing process of chronic wounds exceeds the normal healing period of 4 weeks and can take as long as one year. Factors contributing to chronic wound development are pressure, trauma, lower extremity wounds, increased bacterial load, excessive proteases, or inappropriate treatment. Most commonly, chronic wounds appear in patients suffering from vascular diseases (venous ulcer), diabetes (diabetic foot ulcer), or due to the limited mobility of patients (pressure ulcers). Long handling and slow healing of chronic wounds make a great challenge for healthcare programs around the globe. Considering the fact that one-third of half a billion diabetic patients (2020) are likely to develop a foot ulcer, which can result in morbidity and disability, the development of proper healing therapy is a hot topic.

Wound healing undergoes four time-overlapping stages. Initially, after the open injury, wound creation, hemostasis occurs. In this first stage, blood tends to clot and suppress further blood loss. Hemostasis is followed by inflammation, in which injured tissue fights against foreign bodies and microbes. After cleaning the wound debris, the proliferation phase proliferates cells, resulting in tissue granulation and wound closure. Finally, a remodeling phase occurs when the wound has closed, followed by collagen reorganization and tissue straightening. Typically topical antimicrobial dressings are used to treat chronic wounds in the first stage of development (4 weeks). However, upon abnormal or unsuccessful healing advanced wound care technologies are mandatory. Advanced therapies include oxygenation of wounds as in hyperbaric (topical) therapy, electrical stimulation, growth factor therapy (fibroblast growth factor, epidermal growth factor), cellular matrix tissues, cell therapies, and others. For best performances, conventional and existing wound care technologies must be used combined. Accordingly, new technologies developed

to enhance chronic wound healing solely are welcome. One of the promising technologies in the wide range of biomedical and medical sciences is cold plasma.

In the last decades, the healing prospects of cold atmospheric plasmas have been put to the test; however, these devices are still not medically certified due to safety reasons. Accordingly, some issues such as high gas temperature and electromagnetic compatibility must be solved before safe human use. Furthermore, plasma devices are developed worldwide in different electrode geometries, in contact with liquids, in atomic and molecular gases producing a diapason of reactive species. Still, the interaction between plasmas and the biological target is not yet fully understood. More importantly, the interaction between plasma and biological targets is often not fully controlled, utilizing controlled delivery of plasma species and radiation. As a result, the patient's health is put at risk. In that manner, handled interaction between plasma and biological targets remained one of the biggest technical challenges for commercializing plasma devices for clinical use.

In this thesis, a newly designed atmospheric pressure plasma jet coupled with an aerosol system was designed for wound healing and topical drug delivery. At first, the safety aspects of this device were brought to the focus and examined. Then, advanced plasma temperature diagnostics were carried out to qualify our device as potent for biomedical use. In the next step, chemistry initiated in the argon plasma jet was investigated. Special attention was given to the possibility of plasma-chemistry control through injected aerosols into plasma effluent. In this manner, an extensive liquid chemistry diagnostic was carried out to detect central reactive oxygen and nitrogen species. Finally, biological effects and the effective control of the plasma-aerosol system were examined on wide-scale biomaterials, biomolecules, cells, and tissues. As a result, the focus was given to the energetic VUV/UV radiation and its biological effect. *In vitro* studies were performed to understand and manipulate plasma-cell interaction. Cell proliferation after plasma treatment was studied with special attention. In this thesis, a new feature of plasma-assisted drug delivery was presented, with the final goal of crossing existing research borders and boosting plasma wound healing with simultaneous transdermal drug delivery.

**Chapter 2** gives a comprehensive explanation of plasma, aspects of its utilization in the medical field, and an overview of the existing literature in plasma science focusing on wound healing. **Chapter 3** gives an overview of experimental techniques employed in this thesis. In this thesis, physical (**Chapter 4**), chemical (**Chapter 5**), and biological (**Chapter 6,7**) approaches have been employed to characterize and optimize atmospheric pressure plasmas for safe human use. The plasma reactor has been designed in the Research Unit Plasma Technology (RUPT) group of Ghent University, in the unique annular shape geometry which supports aerosol introduction into plasma effluent. The plasma jet is driven by radio-frequency (RF) voltage, and it is generated with pure argon gas or with molecular mixtures, e.g., nitrogen, under atmospheric conditions.

In the first instance, the RF plasma jet has been subjected to extensive physical plasma diagnostics, described in **Chapter 4**. Biomedical applicability of the plasma reactor was demonstrated through the stability of diffuse mode plasma, and studied employing electrical characterization and fast imaging. For energy balance purposes, voltage and current have been measured with an RF I-V probe, and dissipated discharge power has been calculated. It has been shown that a large plasma jet ($d_{in}$=12 mm, $d_{out}$=14 mm ) is capacitive coupled plasma (CCP) that operates in a diffuse, α-mode regime and can be sustained at power density lower than 30 W/cm$^3$. Stabilization of the discharge in diffuse mode is enhanced by sheath formation. Based on the energy balance between leading processes in plasma diffusion and recombination, electron temperature and concentration in this discharge are estimated to be $T_e$≈1 eV and $N_e$≈3.2·10$^{12}$ cm$^{-3}$, respectively.

The gas temperature of a plasma designed for biomedical purposes, e.g., contact with human skin, is of great importance. Therefore, gas temperature in the plasma jet has been measured by three techniques. Firstly, optical emission spectroscopy (OES) as a passive temperature diagnostic method has been utilized to measure the temperature in the plasma. Gas temperature in non-equilibrium plasma is obtained based on the rotational temperature of molecules in plasma. For this purpose rotational temperature of OH (A-X) radicals and $N_2$ (C-B) have been determined. Disadvantages of the OES method to measure temperature in plasma (space-averaged, excited rotational states measured) are overcome by probing the plasma jet by laser. In this manner, the gas temperature obtained by the OES technique has been validated by laser-scattering-based techniques, namely Rayleigh and Raman scattering. Gas temperature in the plasma jet based on three different physical approaches has been estimated to be below 340 K (±15 K). It has been shown that the rotational temperature of OH radicals in argon plasma is in good agreement with the gas temperature measured based on Rayleigh scattering and

temperature of ambient air molecules $N_2/O_2$ in ground state measured by Raman scattering.

On the other hand, the rotational temperature of excited $N_2$ molecules is not a good representation of temperature in Ar plasma due to highly effective energy transfer between Ar and $N_2$ species resulting in temperature overestimation. The low gas temperature of the plasma jet and its stability were promising for further optimization and studying chemistry initiated in the annular-shape plasma jet. The study presented in **Chapter 4** is published under the title "*On diagnostics of an annular-shape radio-frequency plasma jet operating in argon at atmospheric conditions*" in the international journal *Plasma Sources, Science & Technology.*

Once the plasma is defined as safe and cold, the biomedical application is determined by its productivity of chemically active species, namely reactive oxygen and nitrogen species (RONS). Moreover, biomedical application of plasmas necessarily involves plasma interaction with liquid and delivery of produced RONS to the liquid environment of treated targets. With this aim, **Chapter 5** presents detailed gas and liquid chemistry diagnostics performed to detect and measure short- and long-living species generated in the annular shape atmospheric plasma jet coupled with aerosol. In this chapter, special attention has been given to the influence of aerosol on RONS production and their deposition to the liquid environment. Firstly, gas-phase chemistry diagnostics based on OES and Fourier Transform Infra-Red (FTIR) spectrometry have been engaged to detect produced species. Produced long-living species were measured in treated liquid using colorimetric assays ($H_2O_2$) and ion chromatography ($NO_2^-$, $NO_3^-$).

Two different techniques are combined to detect and measure short-living species and radicals produced in plasma-treated liquid. Initially, short-living RONS deposited to the liquid environment are measured utilizing Electron Paramagnetic resonance (EPR) with spin trap and spin probe. A recently developed cysteine oxidation model has been used to evaluate EPR results. Cysteine derivatives created in treated liquid upon plasma impact were qualitatively and quantitatively analyzed by high-pressure liquid chromatography and mass spectrometry (HPLC-MS). The chemical activity of argon annular shape jets generated in ambient air can be entirely ascribed to reactive oxygen species (ROS) and ultra-violet (UV) radiation. Introduction of aerosol micro-droplets (d≈20 µm, flow rate≈100 µl/min) in plasma effluent changes plasma chemistry in both gas and liquid phases. Plasma coupled with the aerosol showed overall lower oxidation efficiency. This behavior is ascribed to the interaction of RONS in plasma effluent with aerosols and their consequent quenching (e.g., O quenching). It was revealed that photochemistry plays a significant role in RONS production because the plasma is a strong source of UV radiation (argon excimers $A_2^*$, atomic oxygen OI, etc.).

Accordingly, aerosols effectively partially absorb energetic UV photons and change plasma-liquid chemistry. General conclusions arising from the chemical analysis offered macroscopic soothing effects of the aerosol-assisted jet. Accordingly, biological safety and a controlled treatment of biomolecules, cells, and tissues are put on to test. The study described in **Chapter 5** has been published in the journal *Plasma Sources, Science & Technology*, entitled *"Influence of aerosol injection on the liquid chemistry induced by an RF argon plasma jet"*.

In **Chapter 6,** the first biological assessments of RF APPJ are put on trial, including both plasma jet's potentials and risks. The focus has been given to the often neglected VUV/UV radiation from APPJ and its biological impact. In the first instance, VUV/UV emission above 115 nm from argon RF APPJ has been detected along the radial and axial axis. The emission from plasma was scanned radially and axially to localize the main UV emitters and estimate the direction and propagation length of this energetic radiation. Argon excimers $Ar_2^*$ and oxygen OI are the strongest emitters originating from the inter-electrode region. However, due to the interaction of plasma with ambient air, the emission of $N_2$ has also been detected.

Moreover, UV radiation from plasma has been detected only in the gas flow direction but as far as 14 mm from the plasma nozzle. Next, the interaction of the plasma jet with a target has been visualized using oxidation/photo-bleaching of the fluorescent compound dichlorofluorescein (DCF). The purpose of the DCF tests was to separate the effects of different parts of the UV light spectrum from the integral plasma effect where both RONS and VUV/UV photons from plasma are affecting the decomposition of a fluorescent target. These experiments have demonstrated the influence of the aerosol on the oxidation and photo-bleaching of the DCF. It has been shown that UV radiation from plasma strongly contributes to the effect of photo-bleaching on the degradation of DCF, demonstrating different localization of emitters in agreement with spatial resolved VUV/UV spectroscopy. The aerosol introduction leads to the droplets' partial quenching/absorption effect, resulting in the decreased oxidation power of plasma and modifying the interface between the plasma and a target. The manipulation and limitation of the plasma RONS and UV flux towards the target utilizing aerosol injection can control the interaction and possibly damage a treated biomaterial.

Accordingly, the effect of UV radiation from plasma and the controlling power of aerosol has been tested on biomolecules, cells, and tissues. Modeled biomolecules in this study were chosen to be plasmid DNA. This molecule is very sensitive to radiation and reactive particles; consequently, it is considered a good model of cell DNA damage before the cell-reparation process starts. The stability and the fragmentation upon damage of plasmid DNA have been tested after treatment with plasma, plasma-aerosol, and UV radiation from plasma. Although dissolved in phosphate-buffered saline PBS, plasmid DNA suffered severe damage upon exposure

to the UV emission from Ar APPJ. As expected, introducing aerosol into plasma effluent has shown a lower degree of damage, especially a lower degree of unrepairable damage type double-strand break (DSB). Plasma effect on the fibroblast cells has been tested when cells were in a cell-medium and limited liquid environment (dry). The slight cell-proliferative impact of the plasma jet during the short treatments (t<60 s) and cytotoxic effect of plasma jet during long treatments (t>60 s) has been demonstrated, while the effect of filtered plasma UV light on fibroblast cells was negligible. Once fibroblasts were treated in a dry environment, the cytotoxic effect of UV radiation from plasma was shown to be instant and strong (≈70-80%). However, the addition of aerosols into plasma effluent resulted in 10 % higher cell survival and milder treatment. Finally, the plasma-aerosol system evaluated as safest has been tested on the mice's skin regarding its damage. In conclusion, the addition of aerosol into plasma shows an excellent opportunity to control plasma biological effects by controlling RONS and photochemistry. Biological prospects and risks of APPJ described in **Chapter 6** are published in the journal *ACS Applied Materials & Interfaces*, entitled *"Plasma Damage Control: From Biomolecules to Cells and Skin"*.

The attempts to expand the view on the APPJ coupled with aerosol and demonstrate its boosted wound healing-*in vitro*, are presented in **Chapter 7**. This research has performed a detailed *in vitro* study on cell proliferation and differentiation upon plasma treatment combined with localized drug delivery. In the first instance, the proliferation of connective tissue-fibroblast cells has been studied after plasma and plasma-aerosol treatment. Cell proliferation and viability have been analyzed by employing colorimetric and staining assays. In addition, the expression of genes indicating cell proliferation has been measured in the plasma-treated cells. Short (<60 s) Ar and Ar/$N_2$ plasma treatments on a 10 mm distance have been shown to enhance the proliferation of fibroblast cells by 10-40 % during the seven days of the monitoring period.

Further study has been conducted to study cell mechanisms crucial in a wound healing model *in vitro*. Accordingly, gene expressions of integrin focal adhesions (vinculin, talin, paxillin, focal adhesion kinase) and syndecans have been measured to study the impact of plasma generated ROS and RNS (RONS) on the induced cell migration, adhesion, and communication with extracellular matrix ECM. These pathways are essential in a wound-healing model. Upon injury, fibroblasts tend to migrate towards injured tissue, adhere and start to proliferate and differentiate while closing the wound. Accordingly, proliferative index KI-67 and differentiation marker α-smooth muscle actin (α-SMA) have been measured in plasma-treated fibroblasts. Collagen secretion is essential in the final remodeling stage of healthy wound healing. Therefore, the expressions of the most critical ECM protein collagens (I, IV) have been measured. Undoubtedly, all of the genes

concerning focal adhesions (cell signaling, migration, adhesion), proliferation, and differentiation are upregulated in plasma treatment of 35 s.

The principal difference can be seen between expressions of genes treated with Ar and $Ar/N_2$ plasma. Namely, $Ar/N_2$ plasma treatment has the most potent effect on wound healing genes upregulation. The proliferative effect of $Ar/N_2$ plasma on the cells is ascribed to the long-living $NO_2^-/NO_3^-$ ions. During the treatment of the cells with ROS dominating pure Ar plasma, the maximal expression of upregulating genes happens in the first hours after the treatment, indicating the importance of short-living ROS. On the other hand, the genes indicative for wound healing (except α-SMA) are upregulated after 48h when treated with $Ar/N_2$ plasma. Once more, this demonstrates the importance of RNS - NO, and its long-living downstream products $NO_2^-$, $NO_3^-$ in pathways of wound healing.

In Chapter 7, a novel aspect of plasma in wound healing has been introduced and discussed. This APPJ assisted with aerosol offers controllable localized transcellular drug delivery. This study examines the importance of OH and $H_2O_2$ molecules for cell permeabilization and drug delivery. Moreover, different patterns of drug delivery have been recognized in plasma and plasma-aerosol cell treatment. To this end, spatial manipulation of drug delivery molecules reveals the capability of plasma-aerosol employment as a localized drug delivery agent.

# CHAPTER 2: LITERATURE REVIEW ON COLD ATMOSPHERIC PLASMAS AND THEIR APPLICATION IN WOUND HEALING

This chapter briefly discusses the physics and chemistry of cold atmospheric plasmas. The attention has been driven on the non-equilibrium, cold plasmas generated under atmospheric conditions. Following the objects of this research, the biomedical prospects and applications of cold plasmas are presented. Specifically, this chapter focuses on the employment of cold plasmas in wound care.

### 2.1.1. PHYSICS OF PLASMAS

Plasma is partially ionized gas (1-10% of the atoms are ionized) or fully ionized gas that exhibits electromagnetic properties[1]. Depending on the gas type and its ionization energy, energies ranging from 15.8 to 24.6 eV/atom have to be brought to the argon and helium, respectively, to ionize the gas and generate plasma. Examples of partially ionized plasmas appearing in nature are lightning and the polar light in the ionosphere, while fully ionized plasma appears in the form of stellar cores, and interstellar matter, Figure 2.1.



Figure 2.1. Examples of atmospheric plasmas: Lightening (left) and Polar Light *Aurora Borealis* (right).

In laboratory conditions, plasmas can be generated by heating the gas above the ionization threshold or applying a strong electrical field– gas discharge plasma. Primarily plasma was identified as a radiant matter by William Crooks (1879); however, Irving Langmuir (1920) introduced the term itself. In 1928 Langmuir established the concept of electrical breakdown of gases and their ionization. The ionized gas, a cocktail of electrons, ions, and neutrals, has been recognized as a state of the matter- plasma. His findings on gas discharges defined the beginning of research and application interest for this phenomenon[2], and ever since, plasmas have been generated worldwide for fundamental or practical reasons. Today, we

know that plasma can be generated in almost any gas when a sufficiently high electrical field is applied. To ignite the plasma, voltage higher than breakdown voltage $V_b$ of the specific gas should be applied. Breakdown voltage is defined by pressure p, and the distance d between the electrodes and their mathematical relation is known in the literature as Paschen law[3-4] (Eq. 2.1):

$$V_b = \frac{B(p \cdot d)}{lnln\,[A(p \cdot d)] - ln[ln(1 + \frac{1}{\gamma_{SE}})]}$$ 

Eq. 2.1

A and B are experimental constants, and $\gamma_{SE}$ is the secondary electron emission coefficient. For example, for the plain electrodes in the same experimental conditions, $p \cdot d$=5 cm·Torr breakdown voltage $V_B$ for molecular gases, air, and $N_2$ is about three times higher than for monoatomic gases Ar and He. Breakdown voltage in the function of the product $p \cdot d$ for typically used gases is given in Figure 2.2 (a).
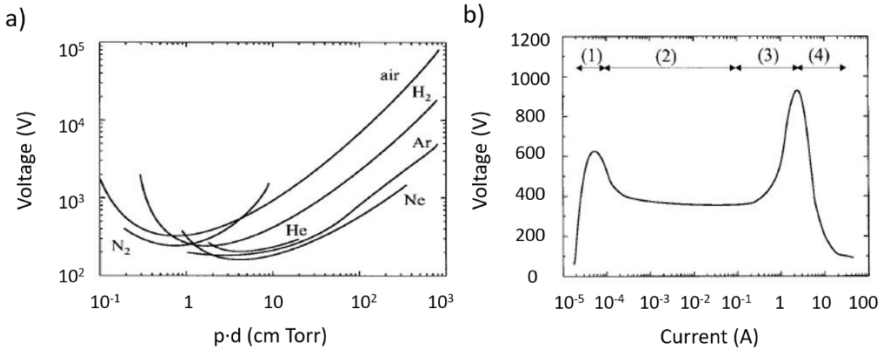


Figure 2.2. a) Breakdown potential for various gases as a function of gas pressure and the distance between the electrodes $(p \cdot d)^4$. b) Current-voltage characteristics of low-pressure DC plasma: 1) Townsend discharge, 2) normal glow, 3) abnormal glow, and 4) arcing[5].

$V_b$ rapidly increases with pressure for Ar on atmospheric pressure between electrodes 5 mm apart; the breakdown voltage exceeds 2.5 kV. Nevertheless, the generation of plasma in atmospheric conditions in monoatomic gases (He, Ar) is more energy-efficient than molecular gases ($H_2$, $N_2$, air). The operation of the plasma is characterized by its I-V (current-voltage) characteristic. In the post breakdown phase, different discharge behaviors can be classified based on the voltage and current dependence, shown in Figure 2.2. (b). Before spark ignition, dark or Townsend discharge appears (1), this type of discharge is characterized by a rapid current increase and small voltage increase. Above spark breakdown (600 V, Figure 2.2. (b)), the voltage changes little with increasing current; this regime is known as normal glow (2). Further increase of plasma current results in plasma voltage

11

increase and appearance of abnormal discharge (3). Finally, the plasma becomes highly conductive on very high plasma currents ≈10 A, and the voltage rapidly decreases with the current (4)[4]. This regime is known as arcing, shown in Figure 2.2 (b). Similar I-V behavior, normal, abnormal glow, and arcing of atmospheric pressure plasmas have been demonstrated in He plasma[5]. Depending on a gas property and operating parameters, plasma can experience diffuse and filamentary character[5]. In diffuse discharges, plasma is uniform, spread over a larger surface, and characterized with low current (normal and abnormal glow). These discharges are favorable in low-temperature application fields for material modification and biomedical application. Diffuse plasma can often be met in low-pressure RF resistive dielectric barrier discharges (RBD), DBDs in He/$N_2$, and APPJs operating in He, Ar under low working power[6-7]. Opposite to diffuse discharges, filaments can appear in plasma volume resulting in nonhomogeneous plasma. These discharges are usually hotter plasmas, characterized by spatial non-uniformity, often used to treat bulk liquids and synthesize gases and materials. Filamentary discharges are generated when high metastable and charge concentrations appear locally, leading to local instabilities[8]. Often, filaments are a result of the low driving frequency. A typical example of filamentary discharge is a gliding arc used for gas synthesis, e.g., $CO_2$ and $N_2$ conversion[9]. Filamentary discharges are also coronas and DBDs.

The applied electrical field controls the motion of free accelerated charges and their collisions with the neutrals leading to ionization. Charged particles interact through long-distance electromagnetic force, macroscopically behaving as a charged fluid. Electric fields of charged particles are modified, and plasma particles can move to shield each other[6]. With few exceptions, the plasma fluid model successfully explains and understands the behavior of commonly studied industrial and laboratory plasmas. Plasmas are often described as quasi-neutral charged fluid consisting of the same concentration of ions $n_i$ and electrons $n_e$ ($n_i=n_e$), determined by Maxwell equation[1]. In plasma science, plasma temperature is often referred to as the kinetic energy of plasma constituents ($E_K=3/2k_BT$). Accordingly, the temperature of electrons and ions describes their velocity distribution (Eq. 2.2):

$$f(v) = \left(\frac{m}{2\pi k_B T}\right)^{3/2} e^{-\frac{mv^2}{2k_B T}}$$

Eq. 2.2

where f(v) is Maxwell-Boltzmann probability distribution of particle velocity, m and T are mass and temperature of the particle, while $k_B$ is Boltzmann constant. Once the electrical field is applied between electrodes, it will act in a different direction on the negative electrons, and positive ions and charges will be separated. As a result of charge separation, an internal electric field of opposite direction is established, and charged particles appear to oscillate with the plasma frequency (Eq. 2.3):

$$w = \left(\frac{ne^2}{\varepsilon_0 m}\right)^{1/2}$$

Eq. 2.3

The concentration of plasma constituents is marked with n, while constants e and $\varepsilon_0$ are used to describe the elementary charge and dielectric constant of vacuum. Considering the huge difference between an electron and ion masses ($m_i \sim 10^3 \cdot m_e$), plasma frequency $\omega_P$ is determined by electron oscillating frequency $\omega_e$ in plasma $\omega_P \approx \omega_e$. Although plasma is macroscopically considered quasi-neutral, plasma oscillations resulting in space charge perturbation happen in a limited area, close to the electrodes (sheaths) or inserted probes. This perturbed area can be described with the use of the Debye radii or Debye length $\lambda_D$ (Eq. 2.4):

$$\lambda_D = \left(\frac{\varepsilon_0 k_B T}{e^2 n}\right)^{1/2}$$

Eq. 2.4

Accordingly, only on a scale larger than Debye length L>> $\lambda_D$, the quasi-neutral character of ionized gas is preserved, and the system is called plasma.

Due to the charged particles' presence in neutral gas and their movement following the applied electrical field, plasma has high chemical reactivity. Plasmas in which both types of charged particles, electrons and ions, have the same kinetic energy or temperature are thermal (hot) or equilibrium plasmas. Accordingly, thermal or equilibrium plasma is characterized by one plasma temperature $T_e = T_i = T_G$, and plasma reactivity is determined by electron concentration $n_e$ and ion concentration $n_i$. However, a significant difference in the masses of charged particles in ionized gas allows selective acceleration of the electrons while the ions remain cold $T_e > T_i = T$. These non-equilibrium plasmas are particularly interesting due to their electron-driven chemical reactivity while the plasma temperature is low $T_i = T_G$. The high reactivity of hot and cold plasmas, driven by ions and electrons, assured their application in different scientific disciplines. Hot plasmas are widely used in areas where the high gas temperature in plasma is not a drawback but favorable, as in arc welding and hydrocarbons destruction, waste decomposition, nanolithography, and material modification[10]. Nevertheless, this thesis is focused on cold plasmas and their biomedical application when temperature plays a role of great importance.

## 2.1.2. COLD PLASMAS AND THEIR APPLICATION

The decrease of the gas temperature in plasmas expanded the application range of this chemically active medium. Cold plasmas are non-equilibrium plasmas characterized by the high temperature of the electrons ($10^4$ -$10^5$ K) while heavy particles ions and neutrals preserve low temperature (300-1000 K)[11]. The

classification of cold plasmas cannot be made simply since all the working conditions such as driving voltage and frequency, working power, type of the feeding gas, and working pressure determine plasma chemistry and the consequent application[12]. Cold plasma can be generated in the reactors supplied with direct current DC[13], alternating current AC (kHz)[14], radio-frequency RF (MHz) [15], pulsed voltage ($\Delta t \approx ns$)[16] or guided by microwaves (MW) [17]. These plasmas can be ignited in noble and molecular gases in a wide working pressure range (mTorr- 100 atm). Selective energy delivery to the electrons is determined by plasma (electron) frequency $f_P \sim (n(10^{12}cm^{-3})^{1/2}$(GHz) and accordingly accomplished by the right combination of driving voltage frequency, working power, and gas pressure. The engineering of cold plasmas engineering lies in the mass difference between plasma constituents and their different response to the applied electrical field. Less inert electrons can follow oscillating electrical field if the alternating frequency is lower than plasma frequency ($f < f_P \sim f_e$) and accordingly increase their translational energy. However heavier ions are unable to synchronize with the fast oscillating fields ($f_i \ll f_e$) and their translational energy will not be increased in accordance with electrical field. As stated, cold plasma reactor design and operating conditions determine plasma parameters and the consequent application. Low-pressure (mTorr-Torr) DC driven and low frequency voltage driven reactors are mainly focused on the chemical processes driven by ions and heavy particles. Low pressure plasmas are favorable in material processing and microelectronic industry due to the longer ion mean free paths and accordingly enhanced directional ions deposition and etching[10]. Energetic ion flux can be used for the purposes of ion incorporation, etching, sputtering, cleaning, deposition and surface modification, and activation[10]. However, the limitations of vacuum equipment, complex and expensive systems, and the need for the treatment under ambient conditions moved the borders of plasma engineering. Those are replaced by high-frequency discharges operating in ambient air [18-19]. For two decades, atmospheric pressure plasmas have been generated in the room conditions (T≈300 K, p=1 atm), opening an entirely new chapter of their biomedical application. Today cold biomedical plasmas are widely used for surface activation[20] for improved cell adhesion[21], bacterial[22], viral[23] and fungal[24] inactivation, antibacterial coating[25], dental implants[26], and surgery[27], wound healing[28-29] and cancer treatment[30].

### 2.1.3. ATMOSPHERIC PRESSURE NON-THERMAL PLASMAS

Classification of atmospheric pressure plasmas can be made based on: 1) discharge geometry, electrode arrangement, and field configuration; 2) type of plasma (e.g., arc/torch, non-thermal, cold plasmas); 3) the excitation frequency (e.g., DC, AC-driven, RF, MW)[31]. Typical discharges used for biomedical purposes are corona discharge, dielectric barrier discharges (DBD), and plasma jet (APPJ), shown in Figure 2.3 (a-c). Depending on chosen electrode arrangement, field geometry and

14

driving frequency discharges are generated in a wide range of gas and electron temperatures, as shown in Figure 2.3. (d).

### 2.1.3.1. CORONA DISCHARGE

Corona discharge is a type of filamentary plasma generated by applying high DC or AC voltage on the pin electrode resulting in a high localized electrical field and low current density (below the arcing onset)[32]. A typical pin to plate configuration is presented in Figure 2.3 (a). Due to the low radius of the powered electrode (μm-mm), the electrical field around the electrode is very high, forming a lightning crown "Corona" of positively or negatively charged ions (positive or negative corona). Furthermore, due to the high electric field in the electrode region and secondary emission of electrons upon ions impact, secondary energetic electrons (10 eV) followed by lower energy electrons (1 eV) are forming streamers. These energetic electrons in inelastic collisions with plasma gas are the source of the creation of reactive species (see Figure 2.3 (d)). The appearance of the streamers, a low production rate of species, and the small size of coronas are the main drawbacks of this discharge; however, their simple geometry, physical robustness, and operation under atmospheric conditions assured their industrial application[10].

### 2.1.3.2. DIELECTRIC BARRIER DISCHARGE

Dielectric barrier discharge (DBD) is generated in the gas between two plane AC (kHz-MHz) powered electrodes (d≈0.1-10 mm) from which at least one is covered by a dielectric material, see Figure 2.3 (b). Dielectric material limits the charged particles' flow, discharge current, and transition to the arcing, assuring continuous and uniform self-pulsing discharge operation[31].In DBD configuration, gas breakdown occurs in many randomized filamentary micro discharges or streamers. DBDs showed the best performances and uniform diffuse operation when operating in the helium gas. He atoms have high energy metastable states (20 eV), and those can extend micro discharge points on a dielectric plate by ionizing molecules with lower ionization energy, such as $N_2$ ($E_i$=15 eV). This effect is known as Penning ionization and appears in the mixtures of He with air or $N_2$[33]. Diffuse and uniform operation in other gases than He, restricts the application of DBDs; however, DBDs reactors are extensively used for plasma processing. DBDs are used as ozone generators[34] and henceforth in surface treatment, gas purification, air activation for biomedical purposes, decontamination of biological surfaces, and tissues treatment[35]. A typical volume DBD (VDBD) is given in Figure 2.3 (b). Surface DBD (SDBD) configuration[36] is often used for industrial purposes, e.g., the flow control in the field of plasma actuators. The particular configuration of DBD extensively used for biomedical application is floating electrode dielectric barrier discharge FE-DBD[35]. FE-DBD uses

the treated object as another electrode, and this special plasma generated in atmospheric air shows excellent potential for sterilization, wound healing, cancer treatments, etc. Resistive barrier discharge (RBD) is a type of DBD where one of the electrodes is covered by resistive material; in this design, a large stable plasma can be generated on the low frequency of AC voltage[37]. The main disadvantages of DBD configuration are their filamentary character resulting in non-homogenous treatment and limitations regarding the choice of working gas. DBDs are characterized by low temperature (50-400°C) and thus found application in heat-sensitive treatments (see Figure 2.3 (d)).

### 2.1.3.3. PLASMA JET

*Plasma jets* are generated with the gas flow between the concentric electrodes under ambient conditions in the temperature range 25-200°C[38]. More commonly, these devices are called Atmospheric Pressure Plasma Jets APPJs; corresponding electrode configuration and schematics of the plasma jet are shown in Figure 2.3 (c). Plasma jets have a DBD configuration if one of the electrodes is covered with dielectric. DBD jets are typically ignited by high DC, pulsed DC, or AC voltage (U≈10's kV). Due to the higher electrical efficiency, DBD jets are replaced by bare electrode jets, where plasma is generated between metal electrodes powered by RF voltage (100's V). Similar to DBDs, jets can be generated between powered and floating electrodes (e.g., skin). In this thesis, a plasma jet between metal electrodes is investigated.

Usually, plasma jets are generated in the flow of noble gases He, Ar, or mixtures with molecular gases $N_2$, $O_2$. Due to the gas flow, the plasma jet is formed in ambient air and can be directed to the treated target[4]. Depending on the gas type, the gas flow rate between the electrodes and the gap size jet can have a velocity higher than 10 m/s. Based on the directions of feeding gas flow and electrical fields, linear and cross jets can be created[39]. Linear jets are characterized by an electrical field parallel with feeding gas flow, while at cross-field jets, the directions of these two are perpendicular. Linear jets are described by higher downstream activity, commonly used for material treatments (e.g., etching). In this thesis, a cross-field jet has been investigated. In cross-field jets, an electrical field confines ions and electrons in the region between electrodes. At the same time, species created in plasma, e.g., radicals, metastables, etc., and radiation from plasma leave active plasma volume with the flux in the gas flow direction. The interaction with ambient air occurs in this active radiative region called plasma effluent or afterglow. Plasma effluent is formed with the gas exiting the nozzle, which plays a vital role in plasma chemistry due to the direct contact with ambient air and the generation of reactive oxygen and nitrogen species RONS. Except for the temperature of plasma effluent, the production of RONS is crucial for plasma application, especially in biomedicine.

Their uniform and direct operation in ambient air and low temperature ensured the implementation of these devices for heat-sensitive polymer modification[40], plasma polymerization[41], coating[42], thin-film deposition[43], cells[44] and tissue treatments (see Figure 2.3. (d)).
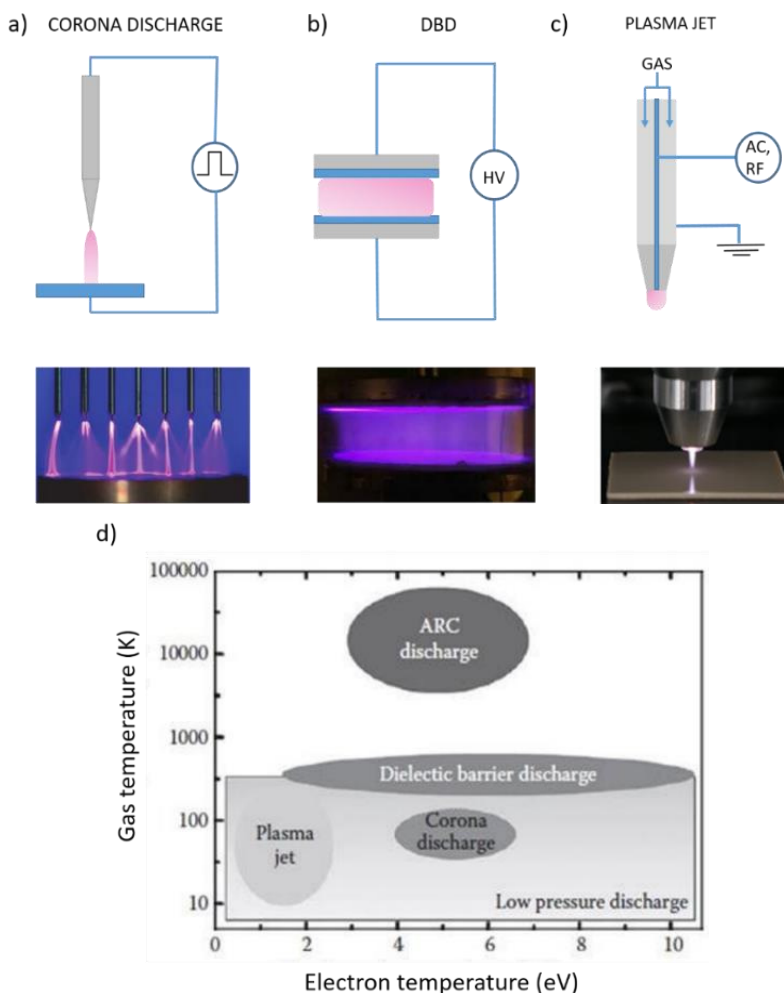


Figure 2.3. Schemes of typical reactor configuration where atmospheric pressure plasma is generated: a) Corona discharge. Below is the image of multi-pin corona configuration [45]; b) Dielectric barrier discharge DBD and a corresponding image of the discharge[46]; c) Plasma jet and image of the jet for biofilm removal[47]; d) Comparison of gas and electron temperatures in different plasmas[48].

APPJs show great potential for clinical commercialization and utilization in wound healing. This thesis discusses a novel design of the annular shape APPJ coupled with aerosol and its prospects for safe wound healing and drug delivery.

## 2.1.4. CHEMISTRY OF PLASMAS: PRODUCTION OF SPECIES IN ATMOSPHERIC PLASMAS

The main advantage of atmospheric pressure plasmas is their chemical efficiency while the gas temperature in plasma remains low. Plasma chemistry in non-equilibrium plasmas is mainly driven by electrons which gain energy higher than 10 eV; enough to trigger chemical reactions in inelastic collisions with neutrals via excitation, dissociation, ionization in the bulk gas. Reaction kinetics and the range produced species are thus macroscopically determined by careful reactor design, driving voltage and frequency, plasma gas composition, and the environment (ambient air or shielding gases). Generation and transport of plasma species occur in several stages, as presented in Figure 2.4 for a typical atmospheric pressure plasma for biomedical application. Initially, primary species (electrons, ions, metastables, excited species and radiation) are formed in plasma in the nanosecond-microsecond time range. In the non-radiative plasma afterglow, relatively long-living secondary species are produced in the range µs-ms processes due to the interaction with the ambient atmosphere (RONS). Consequently, with the gas flow, long-living species are transported and deposited into liquid surrounding initiating tertiary or liquid chemistry[49] on the time scale ms-min. Finally, biochemistry during a period ranging from seconds to days is started once species from liquid reach and react with biomolecules or penetrate cells and tissues.
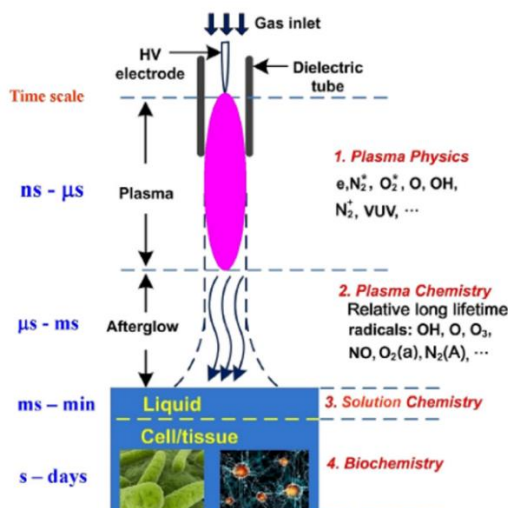


Figure 2.4. Temporal and spatial resolved interaction of typical atmospheric pressure plasma with biological objects and generation of species[50].

### 2.1.4.1. CHEMISTRY OF ARGON PLASMA IN AMBIENT AIR

The most common plasmas used for direct biomedical application (interaction with cells and skin) are plasma jets. Most plasma jets operate in the inert and cost-effective gas argon in ambient air or other shielding gases. Accordingly, argon jet chemistry is studied experimentally and by utilizing kinetic modeling. A 0-D kinetic model is made for argon plasma jet (P=6.5 W, $T_G$=600 K, $V_{gas}$≈30 ms$^{-1}$, Te=1-2.6 eV, Ne=$10^{19}$m$^{-3}$)[51] operating in humid air and considers 84 species[52]. Moreover, the effect of dissipated power (2-20 W) in plasma, gas temperature effect (300-800 K), plasma feeding gas velocity, and humidity effect is also discussed in the model. Reaction chemistry can be caused by electron impact resulting mainly in particle excitation (or momentum transfer or ionization) and heavy particle reaction with the chemical change as the main result. In atmospheric pressure plasmas, due to the high pressure, only lower electronic levels can be excited (~eV); however, high collisional frequency and electron energy loss play an important role in vibrational (≈4000 K) and rotational states (≈0.01 eV) excitation.

A short overview of the chemistry of the critical biomedical species created in argon plasma operating in ambient air and some of the corresponding competing reactions are summarized in the set of equations in Table 2.1. In argon APPJs, argon species chemistry is dominated by molecular argon $Ar_2^*$ presence due to three-body collision (Table 2.1, Eq.1) and long-living argon metastable Ar (4s[3p$_2$]) (Table 2.1, Eq.2). Besides those under electron impact ions $Ar_2^+$ and $Ar^+$ are created (Table 2.1, Eq.3-Eq.4)[52]. With the argon jet leaving the nozzle and spreading in ambient air, collisions with air molecules are important, and the density of Ar species and electrons drops quickly. Moreover, in collisions with air molecules, Ar species lose their energy in charge and energy transfer reactions. Considering the high excitation and ionization energy 10.6-15.7 eV of Ar, the energy lost in collisions is not gained back[52].

Chemistry initiated by atmospheric pressure plasmas operating in argon is not limited to Ar species production. Plasma in contact with ambient air is a rich source of RONS (Table 2.1. Nitrogen, NO$_x$, Oxygen species chemistry). RONS compounds predisposed to react rapidly with cellular molecules. Consequently, the RONS chemistry of a plasma defines its biomedical application. Ambient air chemistry and the generation of RONS have strong spatial dependency down the Ar flow (deposited power, $T_e$, $T_g$) and mixing rate. In the plasma and the close effluent, chemistry is mainly driven by electron impact dissociation, for example, atomic O and N, upon dissociation of $O_2$ (5.15 eV) and $N_2$ (9.8 eV). While in the far effluent where both $n_e$ and $T_e$ drop, the effect of UV radiation becomes significant and inelastic collisions heavy species (e.g., O is created in a reaction between excited $O_2$ and ozone $O_3$).

Table 2.1. Chemistry in argon plasma

| Eq. | Species | Reaction |
|---|---|---|
| Argon species chemistry | | |
| 1 | $Ar_2{}^*$ | $Ar(4s[3p_2]) + Ar + M \rightarrow Ar_2^* + M$ |
| 2 | $Ar(4s[3p_2])$ | $e^- + Ar \rightarrow Ar(4s(3p_2)) + e^-$ |
| 3 | $Ar_2{}^+$ | $Ar^+ + Ar + M \rightarrow Ar_2^+ + M$ |
| 4 | $Ar^+$ | $e^- + Ar(4s[3p_2]) \rightarrow Ar^+ + e^- + e^-$ |
| Nitrogen species chemistry | | |
| 5a | N | $Ar(4s(3p_2)) + N_2 \rightarrow Ar + N + N$ |
| 5b | | $Ar_2^* + NO \rightarrow Ar + Ar + N + O$ |
| 6 | $N_2(A)$ | $e^- + N_2 \rightarrow N_2(A) + e^-$ |
| 7 | $N_2(C)$ | $Ar^* + N_2 \rightarrow N_2(C) + Ar$ |
| $NO_x$ species chemistry | | |
| 8 | NO | $O + N_2(A) \rightarrow NO + N$ |
| 9 | $NO_2$ | $O + NO + M \rightarrow NO_2 + M$ |
| 10 | $N_2O$ | $O_2 + N_2(A) \rightarrow N_2O + O$ |
| 11 | $NO_3$ | $O + NO_2 + M \rightarrow NO_3 + M$ |
| 12 | $N_2O_3$ | $NO + NO_2 \rightarrow N_2O_3$ |
| 13 | $N_2O_5$ | $NO_2 + NO_3 + Ar \rightarrow N_2O_5 + Ar$ |
| 14 | $ONOO^-$ | $NO + O_2^- \rightarrow ONOO^-$ |
| 15a | $NO_2{}^-$ | $O^- + NO + M \rightarrow NO_2^- + M$ |
| 15b | | $O_2^- + NO_2 \rightarrow NO_2^- + O_2$ |
| 16a | $NO_3{}^-$ | $O + NO_2^- \rightarrow NO_3^- + e$ |
| 16b | | $O_3^- + NO \rightarrow NO_3^- + O$ |
| Oxygen species chemistry | | |
| 17a | O | $e^- + O_2 \rightarrow O + O + e^-$ |
| 17b | | $^1O_2 + O_3 \rightarrow O_2 + O_2 + O$ |
| 18 | $^1O_2$ | $O(^1D) + O_3 \rightarrow {}^1O_2$ |
| 19a | $O_2{}^-$ | $O^- + O_2 \rightarrow O_2^- + O$ |
| 19b | | $O + O_3^- \rightarrow O_2^- + O_2$ |
| 20 | $O_3$ | $O + O_2 + M \rightarrow O_3 + M$ |
| Water species chemistry | | |
| 21 | $HO_2$ | $H + O_2 \rightarrow HO_2$ |
| 22a | OH | $e^- + H_2O^+ \rightarrow OH + H$ |
| 22b | | $HO_2 + O \rightarrow OH + O_2$ |
| 23 | $H_2O_2$ | $OH + OH + M \rightarrow H_2O_2 + M$ |

In argon plasmas, interaction with nitrogen is of particular importance due to highly effective energy transfer from Ar metastable atoms in Ar ($3p_2$) and Ar ($3p_0$) states to the nitrogen ground state $N_2$ (X). The result of this nearly resonant process is vibrational excitation of nitrogen to the $N_2$(C) state[53] (Table 2.1, Eq 7). Moreover, dissociation of $N_2$ and production of atomic nitrogen occurs during chemical quenching of argon or in competing reactions between $Ar_2^*$ and $^•NO$ (Table 2.1, Eq 5a,b). RONS typically produced in argon plasmas generated in atmospheric conditions are $NO_x$ radicals, e.g., $^•NO$, $^•NO_2$, $N_2O$, $N_2O_3$, $N_2O_5$ (Table 2.1, Eq 8-13). Ions $ONOO^-$, $NO_2^-$, $NO_3^-$ are stable downstream products of nitric oxide $^•NO$ (Table 2.1, Eq 14-16).

Upon plasma interaction oxygen from ambient air, abundantly produced ROS are atomic oxygen O, singlet oxygen $O_2^1$, ozone $O_3$, superoxide $O_2^-$ (Table 2.1, Eq 17-20). Besides interaction with ambient air, plasma interaction with water is principal and reactive compounds such as hydroxyl radical $^•OH$, hydroperoxyl $HO_2^•$, and hydrogen peroxide $H_2O_2$ are created (Table 2.1, Eq 21-23). Water is inevitably present in ambient air in vapor or appears as a feeding gas impurity. Therefore, it plays an essential role in the biological environment as a liquid layer surrounds all biomaterials (biomolecules, cells, tissues). Species created mainly in the gas phase, e.g., $^•NO$, $^•OH$, $O^•$, $O_3$, $H_2O_2$ on the gas-liquid interface, interact with each other or with aqueous solutions resulting in secondary species production $^•OH$, $^•NO_2$ (from HOONO), $HNO_2$, and $HNO_3$ in reaction $NO/NO_2$[54].

Reactive oxygen species ROS, atomic oxygen O, superoxide $O_2^{•-}$, singlet oxygen $^1O_2$, ozone $O_3$, hydroxyl radical $^•OH$, hydrogen peroxide $H_2O_2$, etc., are famous for their oxidative properties. Besides driving plasma chemistry, ROS have a role in surface activation or modification. In addition, ROS induce oxidative stress in cells and tissues and therefore have wide application in bacterial inactivation and sterilization. Reactive nitrogen species NO is well known in cell biology to be a signaling molecule by signal transduction mediators or triggering molecules[55]. To further tailor the production of reactive species and radiation, plasma can be surrounded by other shielding gas[56] except for ambient air or even in contact with liquid[57]. For example, for purposes of nitrogen fixation into ammonia $NH_3$, inert gas $N_2$ together with water $H_2O$ is introduced into plasma reactor[58]. In addition, water is also needed to convert greenhouse gases such as $CO_2$ into fuels[59]. Moreover, water can be added in atmospheric plasmas in the form of bubbles, aerosols, etc., to boost water-derived chemistry, production of $^•OH$, $H_2O_2$, and limit oxygen species, e.g., $O_3$[60].

## 2.1.4.2. RADIATIVE CHEMISTRY OF ARGON PLASMA IN AMBIENT AIR

Energetic radiation from plasma, namely vacuum ultraviolet VUV and UV have an essential role in plasma chemistry, e.g., in photolytic and photoionization

processes [61-62]. Argon plasmas are strong radiation sources, especially in the UV C range due to argon excimer emission $Ar_2^*$ ($\lambda_{MAX}$=126 nm, $E_{hv}$≈9.8 eV ). In atmospheric conditions, emission from atomic oxygen ($\lambda$=130 nm, $E_{hv}$≈9.5 eV) and nitrogen ($\lambda$=119, $E_{hv}$≈10.4 eV) can also be detected in most of the Ar plasmas. These photons have energy high enough to dissociate water molecules and produce OH radicals ($E_{diss}$≈5 eV). Bond dissociation energies for some of the biologically relevant molecules are summarized in Table 2.2[63]. Corresponding wavelengths needed to dissociate the bond are accordingly given.

Table 2.2. Photochemistry in Ar plasma in ambient air

| Eq. | Reaction | $\lambda$(nm) | Energy(eV) |
|---|---|---|---|
| 24 | $H_2O_2 \overset{hv}{\to} HO_2 + H$ | 319.5 | 3.88 |
| 25 | $OH \overset{hv}{\to} O + H$ | 279.2 | 4.44 |
| 26 | $H_2 \overset{hv}{\to} 2H$ | 274.3 | 4.52 |
| 27 | $O_2 \overset{hv}{\to} 2O$ | 240.3 | 5.16 |
| 28 | $H_2O \overset{hv}{\to} OH + H$ | 239.8 | 5.17 |
| 29 | $NO \overset{hv}{\to} N + O$ | 189.3 | 6.55 |
| 30 | $N_2 \overset{hv}{\to} 2N$ | 126.5 | 9.8 |

Considering that atmospheric pressure plasma jets are optically thin plasmas – transparent for their radiation, radiation chemistry initiated by the VUV photons plays a role in the plasma afterglow and ambient air. However, the contribution of VUV/UV radiation to plasma chemistry and biology is debatable among researchers as UV radiation (especially in the UV C range) is partially absorbed in ambient air or biological liquids. Nevertheless, UV emission from plasma has been detected from many plasma sources, acting in synergy with RONS to damage biomolecules and bacteria[64-65].

As presented, plasmas are sources of various chemical species and radiation. For decades different targets are exposed to the plasma species in plasma treatments, and accordingly, their chemical and physical properties are affected. Due to the simultaneous generation of RONS species, radicals, metastables, radiation, heat, and even shock waves, plasmas have a promising future in biomedical and medical sciences. With the revelation of plasmas operating at atmospheric pressure, their direct application on heat-sensitive objects such as skin gained value. Today, dozens of laboratories around the globe are taming plasmas for direct application on skin and plasma-wound healing, but only a few are successfully treating them.

### 2.1.5. ON CHEMISTRY OF THE EXISTING ATMOSPHERIC PLASMAS USED IN BIOMEDICINE

The most examined plasma devices engaged in biomedicine are Floating Electrode – Dielectric Barrier Discharge FE-DBD (Drexel University), COST Reference microplasma jet (Ruhr University Bochum), and kINPen plasma jet (Greifswald University). Accordingly, a summary of their chemistry is provided in the following text.

#### 2.1.5.1. FE-DBD IN AMBIENT AIR

FE-DBD is generated in ambient air. Discharge is generated between an AC high voltage insulated electrode and treating surface (e.g., tissue) playing the floating, counter electrode. The schematic and the image of the floating electrode DBD is shown in Figure 2.5. Accordingly, in treatment with FE-DBD, plasma tissue is in direct contact with the plasma. In the direct treatments, both positive and negative ions are believed to play a major role in biological processes[66]. The effect of these charged species is chemical and not related to effects such as shear stress, ion bombardment, and heating due to ion flux. In the presence of oxygen, both positive and negative ions catalyze the peroxidation process inside and outside biological organisms. As a result, oxygen in plasma is necessary and created RONS play a crucial intermediate biological role. The biological act of FE-DBD is explained through cell membrane lipid and polysaccharides' peroxidation, catalyzed by charged particles. Peroxidation and thus biological effect depends on the surrounding of the biological target, and it is promoted in the presence of moisture.

RONS play a crucial intermediate role in the plasma chemistry of air DBDs. Generation of RONS in FE-DBD ($T_{rot}$=300-350, $T_{vib}$=3000-4000, $P_{density}$=0.1-1 W/cm$^2$is in the range 0.3-0.5 per eV[67]. For a plasma dose of 3.9 J/cm$^2$, 7.32-12.2·$10^{16}$cm$^{-3}$ ROS are created in the gas phase. Typical concentrations of RONS generated in the air FE-DBD are presented in Table 2.3[68].

Table 2.3. RONS generated in FE-DBD[68]

| Plasma generated species | Density (cm$^{-3}$) |
|---|---|
| Superoxide $O_2^{\bullet-}$ | $10^{10}$-$10^{12}$ |
| Hydroxyl radical $^{\bullet}OH$ | $10^{15}$-$10^{17}$ |
| Hydrogen peroxide $H_2O_2$ | $10^{14}$-$10^{16}$ |
| Singlet oxygen $^1O_2$ | $10^{14}$-$10^{16}$ |
| Ozone $O_3$ | $10^{15}$-$10^{17}$ |
| Nitric Oxide $^{\bullet}NO$ | $10^{13}$-$10^{14}$ |
| Electrons $e^-$ | $10^9$-$10^{11}$ |
| Positive ions $M^+$ | $10^{10}$-$10^{12}$ |

Direct treatment by this plasma in small doses <1 J/cm$^2$ results in bacterial decontamination without damaging healthy cells. Intermediate doses of 2-6 J/cm$^2$ result in reparable DNA damage and stimulation of growth factor release. Higher dosages 7-10 J/cm$^2$ respectively cause apoptosis and necrosis of cells.

Impact of UV radiation and photo-driven chemistry in FE-DBD is shown to be insignificant. Authors report emissions above 220 nm from NO and OH species; however, more energetic radiation in the UVC range is likely to be absorbed in the air before reaching the target. In plasma medicine, indirect treatments by FE-DBDs/DBDs are also employed. For example, plasma-activated liquid/water (PAL/PAW) is rich in long-living species $H_2O_2$, $NO_2^-$, $NO_3^-$ and is often used to sterilize materials and tissues.

DBDs can treat bigger surfaces (determined by electrode size), so precise treatments are not favorable with these devices. One of the disadvantages of DBDs used in medicine is their complete dependence on ambient conditions. As no synthetic gas flow is applied, changes in ambient air, e.g., humidity, can cause changes in plasma chemistry and repetition of treatment. Moreover, as a floating electrode in biomedical treatments with FE-DBD is living tissue, treatment distance plays a crucial role and should be rigorously fixed for good treatment repetition. Few drawbacks regarding RONS production stability in terms of plasmas with controlled gas flow and lower dependency of treatment distance are overcome with plasma jets.

a)                                                              b)
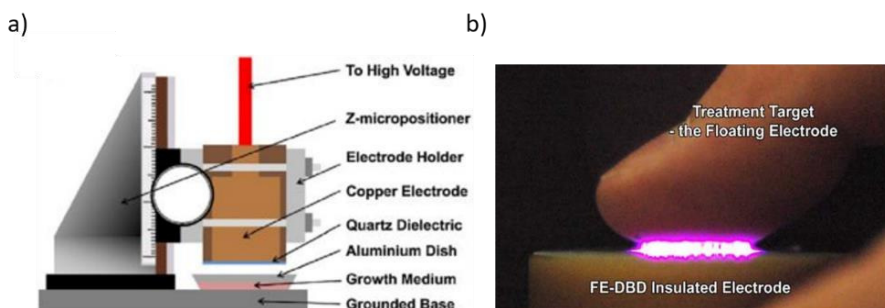


Figure 2.5. a) Construction of FE-DBD;  b) Image of FE-DBD in contact with living tissue having a role of the floating electrode[69].

### 2.1.5.2. COST JET IN HELIUM

COST μ-jet is designed as a reference source for studying cold atmospheric pressure plasmas for biomedical applications. COST jet is a diffuse capacitively coupled RF 13.56 MHz discharge generated between two coplanar electrodes (d=1 mm) in He flow (1.4 SLM) with small admixing of $N_2$ or $O_2$ (0.5 %)[70]. Power of 0.25 W dissipated in this discharge results in 37°C temperature of plasma effluent at the

distance of 3 mm from the electrodes. The chemistry of this μ-jet has been studied employing two-photon absorption laser-induced fluorescence (TALIF), UV, and cavity ring-down laser absorption spectroscopy, mass spectrometry, and the results provide benchmarking for modeling of liquid chemistry[13]. The corresponding schematics and the image is given in Figure 2.6.

Adding $O_2$ or $N_2$ into the He feeding gas manipulates plasma chemistry created in the plasma jet. Namely, adding oxygen results in the favorable generation of atomic oxygen O, singlet oxygen $^1O_2$, and ozone $O_3$. Further, fine-tuning in the $O/O_3$ ratio is accomplished in shorter or longer treatment distances. On the contrary, the addition of $N_2$ boosts the production of N and $NO_x$, while water admixture changes the production of $H_2O_2$, $^\bullet OH$, $OOH^\bullet$. Charged species (ions and electrons) are preserved between electrodes in the active plasma volume; with the gas flow, only He metatables, RONS, and UV radiation are present in the effluent. Table 2.4 overviews COST jet chemistry in effluent and treated liquid[71-72].

Table 2.4. COST jet chemistry in effluent and treated liquid[71-72]

| Admixture in He | Species in the gas | Density ($cm^{-3}$) |
|---|---|---|
| 0.6 vol. % $O_2$ | O | $3 \cdot 10^{15}$ |
| 0.6 vol. % $O_2$ | $O_3$ | $1 \cdot 10^{15}$ |
| 0.1 vol. % $N_2$ (0.25% max N) | N | $6 \cdot 10^{13}$ |
| Admixture in He | Species in liquid | Concentration (μM) |
| 20 % $H_2O$ | $H_2O_2$ | 2000 |
| 20 % $H_2O$ | $^\bullet OH$ | 150 |
| Pure He | $NO_2^- + NO_3^-$ | 30 |

Liquid diagnostics of RONS (EPR, UV-VIS) combined with computational modeling (3D fluid dynamics and 0D chemical kinetics model) reveal that major amounts of RONS species ($H_2O_2$) and radicals ($^\bullet OH$, and H) are created in plasma. In contrast, minor concentrations are created in effluent and then deposited into treated liquid[13]. Dissimilarity in RONS species origin implies a fundamental difference in micro COST jet and other parallel jets where RONS are primarily created in the effluent region. UV emission from the He COST jet is dominated by the excimer emission of $He_2^*$ ($\lambda_{max}=86.5$ nm), but it depends on the metastable density and decreases with molecular gas admixture, mainly $O_2$.
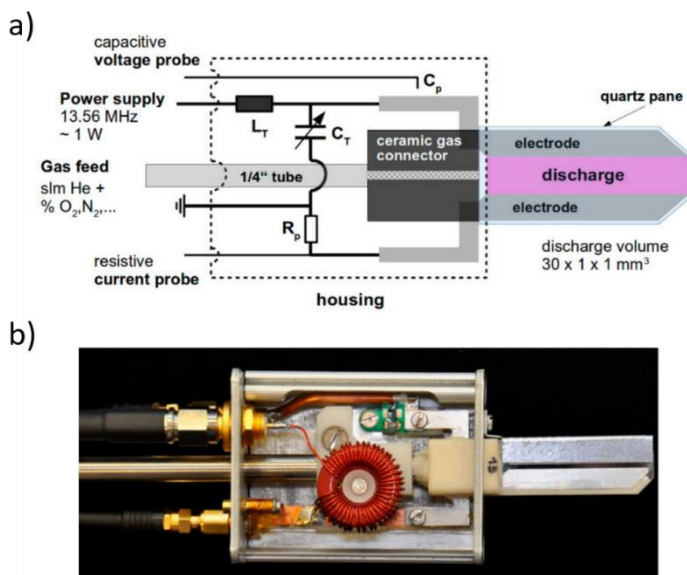
Figure 2.6. a) Schematics of COST jet construction; b) COST jet image[73].

### 2.1.5.3. KINPEN JET IN ARGON

kINPen produces a millimeter RF 1 MHz plasma jet in argon. It is probably the most examined APPJ for biomedical application. For controlled ambient conditions and enhanced production of NOx species, Ar jet is applied in combination with an $N_2$ gas curtain. Dissipated power in discharge is below 3.5 W, and in the Ar flow of about 3-5 SLM, the gas temperature in the effluent is kept in the range 35-38°C.

Initially, atomic oxygen O has been studied as the most abundant and reactive ROS through two-photon absorption laser-induced fluorescence TALIF[74]. Detailed gas chemistry of jet with $N_2$ and $O_2$ shielding gases is determined by combining an experimental approach and numerical modeling (electron impact model)[56] shown in Figure 2.4. In this unified approach, the absolute density of the metastable Ar (4s, $3p_2$) has been measured using laser atom absorption spectroscopy (LAAS). The density of long-living RONS $O_3$, $NO_2$, $N_2O_5$, $HNO_3$, $H_2O_2$ was measured in the effluent by FTIR in different gas mixtures of current gas ($N_2/O_2$, 5 SLM in total). Through turbulent jet guided streamers are propagating with the speed in the range km/s. The propagation of streamers in plasmas is characterized by very fast and localized (100 μm) chemistry initiated by electrons ($T_e \approx 3.9$ eV, $n_e \approx 10^{12}$ cm$^{-3}$) in the streamer's head, followed by slow neutral reactions in the plasma plume[56]. Experiments combined with modeling show that RONS chemistry in the kINPen plasma plume is initiated by Ar metastables created by electron impact in the

26

streamer's head. RONS chemistry in plasma plume is independent of the molecular composition of the shielding gas (excitation in streamer faster than quenching). However, on the 2 mm distance, Ar* density seems to be lower in $N_2$ than $O_2$ curtains due to higher electronegativity of $O_2$ and thus streamer propagation assistance. The most present argon species in kINPen are determined by LAAS to be Ar (4s, 3p$_2$) and excimers $Ar_2^*$, followed by Ar (4s, 3p$_0$) and dominant ions $Ar_2^+$. Maximal yields of detected RONS in the downstream flow of kINPen as a function of shielding gas admixture are summarized in Table 2.5[56, 74-75].

Table 2.5. RONS produced in downstream gas flow of kINPen

| Shielding gas $n_{o2}/n_{o2}+n_{N2}$ (0-1) | Species in gas | Density (cm$^{-3}$) |
|---|---|---|
| 0 | O | $3.5 \cdot 10^{15}$ |
| 0.4 | $^1O_2$ | $6 \cdot 10^{14}$ |
| 1 | $O_3$ | $4 \cdot 10^{14}$ |
| 0.4 | $NO_2$ | $5 \cdot 10^{12}$ |
| 0.1 | $N_2O$ | $8 \cdot 10^{11}$ |
| 0.5 | $N_2O_5$ | $4 \cdot 10^{12}$ |
| 0.2 | $HNO_3+HNO_2$ | $4 \cdot 10^{12}$ |
| 0 | $H_2O_2$ | $2 \cdot 10^{12}$ |
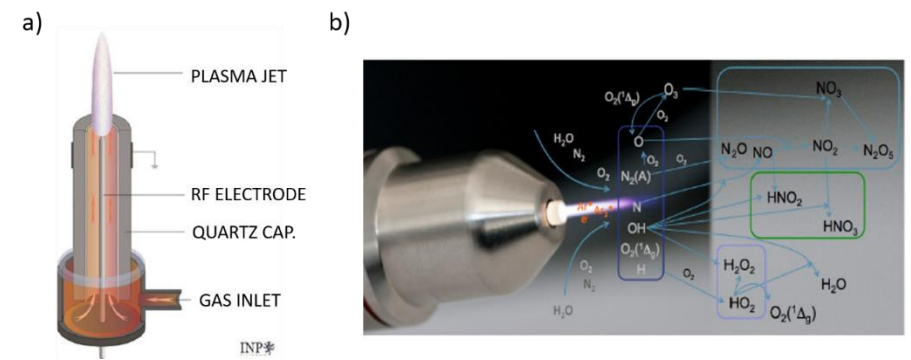


Figure 2.7. a) Schematics of kINPen geometry; b) kINPen initiated gas chemistry[76].

Short and long-living RONS produced or deposited to the treated liquid are measured using EPR spectroscopy, UV-absorption, HPLC, colorimetry, and ion chromatography. Liquid chemistry is of greater importance for biomedical plasmas as biomedical treatments occur almost inevitably in the presence of liquid being water, PBS, cell medium, blood, etc. Tertiary chemistry initiated in liquid can be driven by RONS created in the gas phase and UV light, e.g., hydrolysis. The most

relevant RONS measured in the treated liquid produced by kINPen are revised in Table 2.6[75-76].

Table 2.6. Maximal yields of RONS detected in liquid post kINPen treatment

| Shielding gas $n_{o2}/n_{o2}+n_{N2}$ (0-1) | Short-living RONS in liquid | EPR adduct production rate (µM/s) |
|---|---|---|
| 1 | $O+ {}^1O_2+O_3$ | $7 \cdot 10^{-3}$ |
| 0 | $O_2^{\bullet-}$ | $2 \cdot 10^{-2}$ |
| 0 | $^\bullet OH$ | $8 \cdot 10^{-3}$ |
| 0.7 | $^\bullet NO$ | $1.7 \cdot 10^{-2}$ |
| Shielding gas $n_{o2}/n_{o2}+n_{N2}$ (0-1) | Long-living RONS in liquid | Concentration (µM) |
| 0 | $H_2O_2$ | 0.4 |
| 0.7 | $NO_2^-$ | 0.16 |
| 0.7 | $NO_3^-$ | 0.5 |

All of the mentioned species contribute to the integral biological effects of plasmas, causing different direct and indirect impacts on bio objects under treatment. The most prominent biological effects of ROS and RNS/RONS: oxidative stress and nitrosylation are discussed in the following sections.

### 2.1.6. BIOLOGICAL EFFECTS OF RONS

The effect of reactive oxygen species ROS on any cell type can be described through oxidation-reduction reaction, critical for cell homeostasis and signaling, including energy metabolism, gene expression, immune response, cell cycle, growth, and apoptosis[77]. Mitochondria is the main endogenous source of ROS, especially $H_2O_2$, a by-product of natural cell activity, and is participating in cellular signaling pathways involved in cell proliferation and differentiation. Superoxide $O_2^{\bullet-}$ is produced in several sites in mitochondria and released inside the mitochondrial matrix. By using superoxide dismutase is converted to $H_2O_2$, further converted to $^\bullet OH$. Peroxisomes, organelles involved in the cell metabolic processes also generate a wide range of ROS and RNS, such as $H_2O_2$, $O_2^{\bullet-}$, $^\bullet OH$, $^\bullet NO'$ and $ONOO^{-}$[78]. Besides, $^\bullet NO$ can be produced from L-arginine in a reaction catalyzed by nitric oxide synthase, while very reactive peroxynitrite is generated in the reaction of $O_2^{\bullet-}$ with $^\bullet NO$[78].

Transduction of cellular signals appears by modifying targeted molecules in cells; this can be ascribed to oxidation processes (ROS) and nitrosylation (RNS). ROS may directly interact with specific receptors and cause membrane oxidation, leading to downregulation of intracellular ROS and a signal transduction from the membrane to the nucleus. Otherwise, ROS can interact through redox-activation of protein kinases/phosphates and cooperate with intracellular $Ca^{2+}$ in signaling pathways

which regulate the cell proliferation/arrest or death balance. Cellular signaling pathways are expressed through redox regulation, and cellular signaling pathways regulate the cellular redox state[68]. Activated by extracellular stimuli, the cells produce ROS, which further stimulates other cellular signaling pathways, whereas ROS behave as second messengers. Moreover, some cell-death signals induce ROS production in the cells or induce activation of programmed death enzyme caspases, while oxidation of caspases results in their inactivation[68]. Accordingly, the communication between the cellular signaling system and redox state is evident, thus controlling the cell's life and death[77].

### 2.1.6.1. OXIDATIVE STRESS

Intracellular increase of the ROS level harms cell metabolic activity, structure, function and results in oxidative stress[78]. Enzymes, lipids (lipid membranes), and DNA are the most sensitive to oxidative stress[79], as shown in Figure 2.8. Many cells respond to low doses of oxidative stress ROS by proliferating and adapting. Cell adaptation to external oxidative stress is realized through upregulation of the defense system. The defense system may completely protect the cells against the damage or overprotect them and make them resistant to future exposure. Higher levels of oxidative stress can lead to cell injury, namely damage of DNA, lipids, proteins, carbohydrates. After the cellular damage due to oxidative stress, cells can recover by repairing or replacing damaged molecules. They can survive with persistent injury, or damage of DNA may trigger death by apoptosis or necrosis[80].
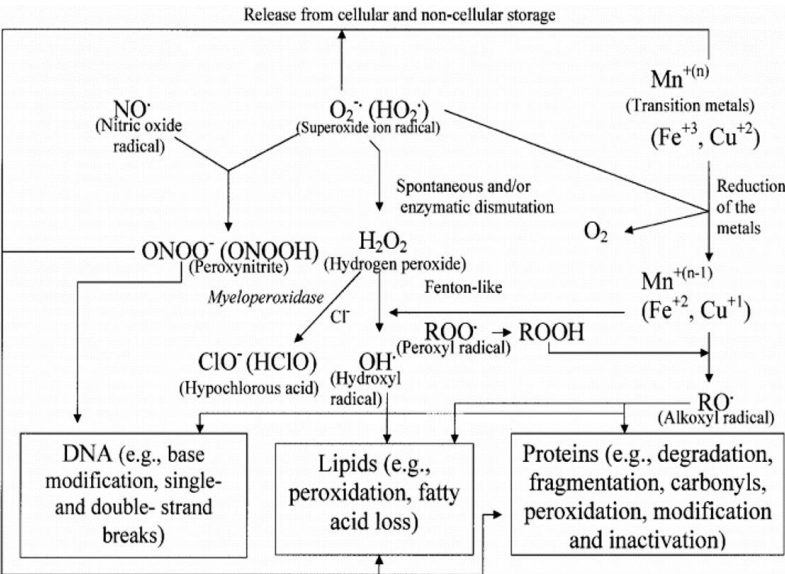


Figure 2.8. Oxidative damage of cells (DNA, lipids, proteins) induced by RONS[79].

29

The effect of RONS on mammalian cells can be modeled by an oxidizing agent $H_2O_2$[81]. Exposure of mammalian cells to the low concentration of $H_2O_2$ (3-15 μM or 0.1-0.5 μmol/$10^7$cells) has been shown to cause a significant mitogenic response and stimulate proliferation for 25-45%. Applying a higher dosage of $H_2O_2$ (120-150 μM or 2-5 μmol/$10^7$ cells) results in temporary growth arrest, which protects the cell from excess use of energy and DNA damage. 4-6 h hours later, cells will express genes for oxidative protection and damage repair; after 18 h, cells express adaptation and the maximal protection against oxidants. After 36 h, gradual de-adaptation occurs, leading to the original sensitivity. Exposure to the high concentration of $H_2O_2$ (250-400 μM or 9-14 μmol/$10^7$ cells) fibroblasts is incapable of adapting and entering a permanent-growth arrest, the state often confused with apoptosis. Further increase of the oxidant concentration (0.5-1 mM or 15-30 μmol/$10^7$ cells) results in the nuclear condensation, degradation of mitochondrial mRNA/rRNA and mitochondrial and nuclear DNA degradation followed by apoptosis and (5-10 mM or 150-300 μmol/$10^7$ cells) nucleic acid denaturation and necrosis.

### 2.1.6.2. NYTROSILATION

The post-translational modifications mediated by reactive nitrogen species are active cell signaling pathways. These modifications of all main classes of proteins happen, among the other, through the processes of nitrosylation. Thiol nitrosylation (S-nitrosylation) plays a vital role in the inflammatory process appearing in wound healing. Furthermore, it plays a crucial role in protecting proteins by scavenging RONS $^•NO_2$ and $N_2O_3$, thus producing the side-products such as $O_2^{•-}$, $O^•$, $O_3$[82]. Created S-nitrosothiols are considered $^•NO$ donors, and as such precursors for $^•NO$-producing enzymes, in this manner, their anticancer effect has been proved *in vitro* and *in vivo*[78]. Some drugs containing thiol groups, such as *6-Mercaptopurine,* are used to treat cancer and autoimmune diseases, while *Captopril* is used to treat hypertension. Plasmas' ability to produce various spectra of reactive oxygen and nitrogen species offers a great opportunity to interact with living cells and tissues with multiple outcomes. Controlled production of RONS upon plasma interaction with cells or living tissues can cause oxidative stress and various cellular responses. For example, the unique properties of plasma to simultaneously inactivate prokaryotic cells while promoting the growth of eukaryotic cells is a good starting point for employing CAPS in wound healing.

### 2.1.7. PLASMAS IN CONTACT WITH LIQUIDS

Ability to change plasma chemistry via enhancement of particular species production (OH, $H_2O_2$) launched new technologies in plasma reactor designs[83]. On the other hand, plasma-liquid interaction is inevitable for CAP applications such as

plasma-assisted polymerization, environmental remediation - water purification, material synthesis, cell treatments, etc. Accordingly, it is crucial to study fundamentals and apply physical and chemical processes on the plasma-liquid interface or liquid bulk. To this end, plasmas in contact with liquid are developed in various designs, as shown in Figure 2.9.
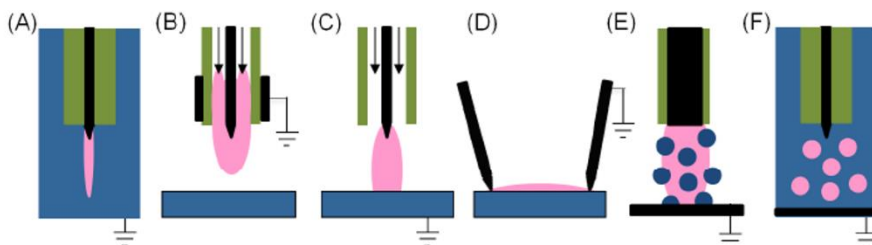


Figure 2.9. a) Direct discharges in liquid; b) Plasma jet in indirect contact with liquid; c) Plasma jet in direct contact with liquid; d) Surface discharge; e) Gas-phase plasma with dispersed phase-aerosols; f) Discharge in bubbles[60].

Discharges generated in liquids (Figure 2.9. (a)) are dynamic and transient, often streamers and corona discharges. Typically, discharges in liquid are created by a rapid breakdown process induced by a strong electric field. Discharge current in liquid discharges is achieved by slow ions and displacement current rather than mobile electrons (such as in the gas phase). A bulk liquid discharge generation is explained through the pre-formation of bubbles once the voltage is applied, followed by micro-gap discharges[84]. Due to the transient vapor phase of dissolved gas in liquid bulk (nitrogen, oxygen), plasma-created species can significantly differ from those created in the plasma gas phase. According to the simple model of a microsecond, pulsed plasma generated in liquid bulk, two regions can be distinguished. Generated filament dissociates and ionizes surrounding water, surrounded by the region where recombination occurs, and long-living species are generated[85].

Gas-phase plasmas can be in contact with water, or one of the electrodes can be in the form of liquid (Figure 2.9 (b-d)). Usually, this type of plasmas operates under atmospheric conditions. Liquid electrodes similar to the resistive electrodes stabilize the discharge preventing the localization and contraction in the electrode area. Discharge stabilization probably occurs due to the distributed resistivity of the liquid electrode[60]. Accordingly, diffuse glow discharges can be generated with water electrodes even with the DC excitation under ambient conditions[86]. The liquid electrode has been used as an anode and cathode. With the liquid cathode configuration, a large fraction of plasma power is dissipated in water, and the temperature near the cathode is much larger than in the positive column[87]. Reactive chemistry modeling has shown that plasma interaction with liquid results in the

boosted production of radicals $\bullet$NO, O$\bullet$ and $\bullet$OH. More recently, APPJs are brought in contact with liquids where no direct interaction is realized. For example, cross-field jets can generate guided streamers producing ions and electrons far from the nozzle, e.g., on the liquid interface or even liquid bulk. Moreover, the photolysis of liquid by UV radiation emitted from plasma jets is essential in producing biomedically active species such as OH and $H_2O_2$[60].

Multiphase plasmas are in contact with aerosols and bubbles/foams, presented in Figure 2.9. (e, f). Micro-size bubbles are common phenomena in liquids, and these can be sources of instabilities in plasma generated in the bulk liquid. Accordingly, plasma-bubbles interaction is extensively investigated[88]. Typically, feed gas capillary tube injects gas into the liquid, which also serves as an electrode biased with high voltage. A plasma is formed inside the bubble with sufficiently high voltage before breaking off the capillary. The discharge tends to be developed as a streamer propagating along the plasma-liquid interface. Gas temperatures and electron densities significantly vary and strongly depend on the composition of the gas in the bubble, conductivity of the liquid, discharge power, excitation voltage, and size of the bubbles[89].

This thesis has studied a plasma jet in contact with aerosol droplets. Aerosol is a suspension of fine micrometer particles or liquid droplets in a carrier gas. Aerosols are widely used to support surface treatments, material synthesis, and deposition. Aerosol spraying in the electrical field (electrospray) is a well-established phenomenon in science, e.g., electrospinning and electrospray ionization mass spectrometry. Electrical discharges with water electrospray are used in plasma sciences for efficient mass transfer of plasma active species ($H_2O_2$) into the water due to the large plasma/liquid interface area. The screening effect of aerosol has been recognized in plasma species transportation from the gas phase to the liquid. Namely, $H_2O_2$ generated in molecules of aerosol droplets can be safely transferred to the target as they are protected from other harsh plasma species (ROS, UV radiation)[90]. The plasma jet discussed in this thesis is not in direct contact with aerosols; however, plasma chemistry is greatly influenced when droplets are introduced. Once aerosols are injected into plasma effluent, safe and controlled operation of APPJ is granted, which is of crucial importance for plasma assistance in wound healing and topical drug delivery.

The following sections discuss the physiology of wounds and wound care technologies. The advantages and disadvantages of currently employed wound care technologies have been summarized and requirements for developing future technologies have been underlined. To this end, the benefits of cold plasma application in wound healing are reasoned and supported by published studies.

## 2.2. WOUNDS – A GLOBAL PROBLEM

A wound is a skin injury. *Open wounds* appear when skin is cut, punctured, or torn, while *closed wounds* are developed when underlying tissue is damaged. Wounds can be categorized as acute, e.g., abrasions, scalds, burns, post-operative incisions, or chronic. The normal wound healing process takes up to 4 weeks; however, wounds that fail to pass through the normal healing process (>4 weeks) are known to be chronic. Chronic wounds can be classified as vascular inflammation (venous and arterial), diabetic, and pressure ulcers[91]. With the increase in the number of adult diabetic patients (537 million worldwide, 2021) and patients suffering from venous diseases, these are major healthcare issues in the 21st century. More importantly, with the increase of obesity and developing autoimmune diseases in the aging population, predictions of the International Diabetes Federation are that this number will grow to 643 million by 2030 and 783 million by 2045[92]. Studies show that up to one-third of diabetic patients worldwide will develop diabetic foot ulcers (DFU). Half of those will develop infections, and 17% will result in amputation[93-94]. On average, chronic leg or foot ulcers are cured in 70% of patients; however, the healing process takes 12-13 months. The long healing process explains high therapy costs. In Europe, average healing costs are estimated in the range of 6000-10 000 euros per year and 2-4% of the health budget of a high-income country[95]. Suffering from chronic wounds is often associated with chronic pain, change in self-image, limited physical activity followed by depression, and lower life quality. The seriousness of the problem comes to the focus with the high therapy costs and lack of wound care expertise and specialist knowledge limit access of many patients to the clinics.

The following chapters briefly introduce skin anatomy and wound physiology. The comprehension of wound formation is expected to give the right approach in wound assessment, handling, and healing. Existing technologies employed in chronic wound management are summarized, and requirements of future technology development are provided.

### 2.2.1. SKIN ANATOMY, PHYSIOLOGY, AND SKIN DAMAGE

As the largest organ in a mammal's body, the skin accounts for approximately 15% of body weight. The skin has a protective function against physical (UV radiation), chemical (radicals), and biological (microbes) attacks. In addition, it prevents water loss from the body and regulates body temperature. The skin consists of three layers: *epidermis* – the most outer layer, *dermis* – the middle layer, and the inner layer - *hypodermis* or subcutaneous tissue, shown in Figure 2.10.
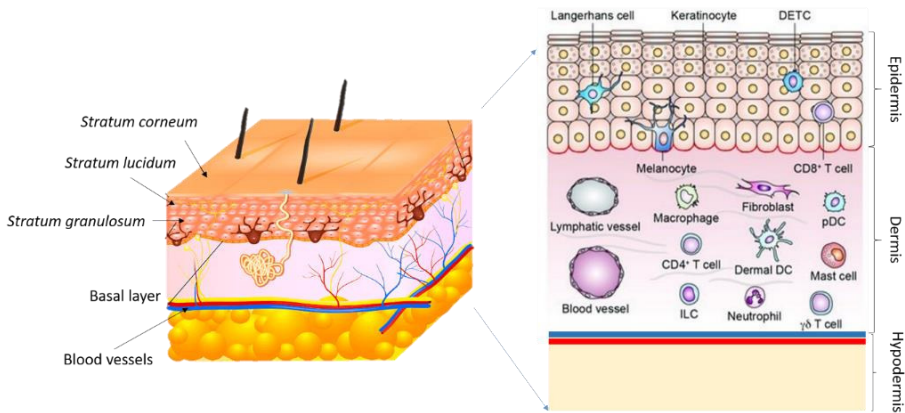
Figure 2.10. Structure of human skin and cell types in epidermis and dermis[96]. DETC is the abbreviation for dendritic epidermal T cell, DC- dendritic cell, pDC – plasmacytoid dendritic cell, and ILC - innate lymphoid cell.

*The epidermis* mainly consists of keratinocytes (80 %), cells synthesizing protective insoluble structural protein keratin. Other cells can be found in lower sublayers of the epidermis, e.g., basal cells (column-shaped keratinocytes) and dendritic cells: melanocytes, Merkel, and Langerhans cells. Melanocytes are the cells in the basal layer of the epidermis responsible for producing melanin pigment and its transfer to keratinocytes. Skin pigmentation is related to the melanin-genesis and the dispersion of the pigment in the keratinocytes. Merkel cells are oval-shaped mechanoreceptors cells. The highest concentration of these cells is in the localizations with the highest sensitivity, such as fingertips. Langerhans cells are macrophages[97] localized in the suprabasal layer of the epidermis found in the oral cavity, lymphoid organs, and normal organs. The epidermis is the dynamic tissue, continually undergoing renewal due to the proliferation cycles of the basal cells in the bottom basal sublayer and their migration towards the external layer. The interface between the epidermis and dermis is a porous membrane that allows the exchange of liquids and cells, mostly populated with basal keratinocytes.

*The dermis* is a system of fibrous, filamentous, and connective tissue that hosts blood vessels and nerves[98]. Although the dermis is populated with fibroblasts, macrophages, and mast cells, blood cells such as plasma cells and leukocytes, e.g., neutrophils, monocytes, and lymphocytes (T cells), enter the dermis layer to respond to a specific event such as blood vessels injury. The principal component of the dermis is collagen (70 % of the dry skin weight[99]), and it is a significant stress-resistant, elastic material found in the skin. Fibroblasts synthesize extracellular matrix and collagen, the structural framework in connective tissue.

Consequently, fibroblasts have a major role in healing damaged tissue and scarring. An essential role in the inflammation process also have mast cells. These are localized mainly around blood vessels. These cells activate upon injury or contact with an allergen, resulting in the selective release of mediators (histamine, lipid mediators, cytokines, ROS) or compounds that induce inflammation in the extracellular environment.

Structures such as hair follicles, sebaceous, and sweat glands are localized in the dermis (see Figure 2.10). Hypodermis or subcutaneous tissue is the most inner layer of the skin, and it serves as fat storage. It mainly consists of connective tissue, fat, and large blood vessels.

In case of injury, skin tends to repair or regenerate, passing through four-time overlapping biochemical phases[100]:

   i.  the hemostasis (immediately after the injury) – damaged blood vessels constrict to reduce blood loss;

   ii. the inflammatory phase (6-8 h post-injury) – leukocyte and phagocyte are secreted to fight microbes;

   iii. the proliferative phase (2-3 days post-injury) – angiogenesis, tissue granulation, and wound contraction;

   iv. remodeling or maturation phase (up to 4 weeks) – connective tissue remodeling and scarring.

Key players in the skin reparation process are macrophages, fibroblasts, and keratinocytes[100]. However, external factors or a patient's profile can extend and complicate the healing process.

## 2.2.2. PHYSIOLOGY OF A CHRONIC WOUND

Why are chronic wounds chronic? Typically, the healing process of an injury undergoes four overlapping phases, hemostasis (blood clotting), inflammation, proliferation, and remodeling phases[101] as presented in Figure 2.11. Nevertheless, for different reasons in some patients, e.g., patient's immobility, decreased blood circulation, bacterial resistance to antibiotics, etc., the process of wound healing fails to proceed through all the stages in the correct timeline.
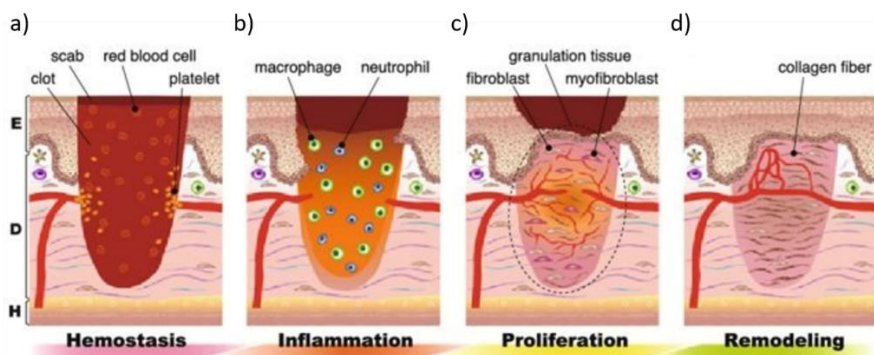
Figure 2.11. Wound healing phases: a) Hemostasis or blood clotting; b) Inflammation; c) Proliferation and d) Remodeling phase. E – Epidermis, D - Dermis, and H - Hypodermis[102].

Immediately after the injury, blood tends to clot in the homeostasis phase, preventing its loss providing the provisional matrix for cell migration. Platelets gather around damage cite, secrete cytokines, growth factors and attract fibroblast and immune cells to start the healing process[95]. The inflammation phase begins to clear all the pathogens or foreign bodies and localize the damage[103]. Localization of the wound site is achieved by differentiation of monocytes to macrophages, cells responsible for detecting and destroying bacteria and thus regulating the inflammatory phase. Other than macrophages, neutrophils are also abundantly present in this stage of healing; their role mirrors ROS release, preventing bacterial contamination and cleaning cellular wound debris. At the end of the inflammation phase, immune cells undergo apoptosis. Macrophages release growth factors and cytokines, and the proliferation phase begins. The proliferation phase is characterized by tissue granulation, angiogenesis, and epithelization. At the very least, the remodeling phase occurs when the wound has closed. During this phase, the provisional matrix is reorganized into collagen bundles.

Wound abnormality reflects in long-lasting inflammation, persistent infection, formation of drug-resistant microbial biofilms, and dermal/epidermal cells disability to repair[104]. The main aspects of molecular and cell deficiencies leading to a chronic wound formation are summarized and marked in red in Figure 2.12, and corresponding overcoming factors are marked in green. The choice of appropriate therapy depends on a patient's profile, type, size, and etiology of the wound and must be accordingly tailored. Advanced techniques discussed in the following text are developed to treat complicated wounds, mainly diabetic foot ulcer (DFU) and venous ulcers (VU).

| Molecular/cellular deficiencies | Corresponding overcoming factors |
|---|---|
| High level ROS | Antioxidants |
| Defective stem cells | Delivery of the healthy stem cells |
| Lack of microvasculature | Angiogenesis factors |
| Impaired cells function | Inflammation and ROS decrease |
| Senescent cells | Recruitment of active cells |
| Lack of GF and ECM secretion | GF and ECM |
| GF and ECM degradation | Inhibition of proteases to protect GF,ECM |
| Protease | Inhibition of protease |
| Low grade infection | Antibacterial peptides |
| Inflammatory cytokines | Anti-inflammatory cytokines |

Figure 2.12. Scheme of chronic wound development: Molecular and cellular deficiencies (red) and factors required to overcome them[95].

### 2.2.3. WOUND CARE AND DRESSINGS

As a first step, conventional wound care considers removing non-viable tissue material or wound debridement. Then, the wound bed is covered (protected) so that the epithelization is enhanced[103]. Removing the non-viable tissue is necessary to prevent or stop further infection due to necrotic debris. In complicated cases, the wound debridement is handled surgically. Less effective towards deep wounds is autolytic debridement with a plaster. This technique is non-invasive, selective, easy, does not need anesthetizing of a patient, and is painless. The autolytic debridement plaster is a sort of occlusive dressing (air and watertight). This prevents bacterial contamination and can further improve the re-epithelization and healing process. Except for occlusive, low-adherent dressings are commonly applied. Accordingly, these restrict microbial contamination but partially allow air and water vapor through, e.g., gauze. Appropriate dressing can be chosen depending on whether a wound is exudative (releases liquid). For example, a dry injury is treated with promoting moisture hydrogels while highly absorbing dressings such as alginates and foams are applied in case of high or moderate exudative wounds. Collagen dressings are attractive in expediting an environment, attracting the cells, and screening from ROS. Recent technologies are concentrated on incorporating antibacterial coating on the dressing, often based on silver nanoparticles[105], iodine, or conventional antibiotics. However, some general drawbacks of the latter two, such as iodine

37

toxicity if applied in large amounts on big surfaces and antibacterial resistance, limit the applications of the later two type dressings[103].

### 2.2.4. NEGATIVE PRESSURE THERAPY

In case of traumatic (burns), acute and chronic wounds, and stabilization of surgical sections, negative pressure wound therapy has shown to be very effective in the first stage of wound handling. Negative pressure wound therapy (NPWT) or vacuum-assisted closure (VAC) uses a suction pump (~50-120 mmHg) and tubing for wound drainage and physical removal of the infection. After wound drainage, tissue granulation is promoted and the wound contracts, prepared for closure or primary healing. This technique is mainly combined with others for successful wound healing, e.g., wound dressings or bioengineered therapies. NPWT uses suction canisters, catheters/drains, tubing, gauze, and adhesive drapes regarding medical material utilization and waste. Although their use was officially approved in 1995, the high cost of NPWT devices limits their accessibility in many institutions (5k-10k euro). The price is the main drawback of NPWT. The approximate cost of the treatment is 100 euro/day, while the healing period can take 9.55 days/patient (2-40 days)[106] depending on a wound type and a patient profile.

### 2.2.5. HYPERBARIC OXYGEN THERAPY

A critical physiological step in wound healing is oxygen content in the wound bed[103]. Oxygenation of wounded tissue is needed from a few points of view: wound-cytokines interaction, to supply proliferation of healthy cells and respiratory burst, decrease necrotic debris and microbes. The estimated tissue oxygenation pressure for a wound to heal is about 20 mmHg while, in long-lasting wounds, the oxygen level is about 5 mmHg[107]. Accordingly, one commonly used technology to treat chronic wounds is treatment with *hyperbaric oxygen*[108]. In pressurized oxygen chambers (p>1 atm), wounded tissue is exposed to pure oxygen. Appropriately wound oxygenation is promoted, followed by cell proliferation and angiogenesis. Over the last two decades, hyperbaric oxygenation showed positive healing of complicated diabetic ulcers. Nevertheless, this technology also has drawbacks. Besides the high cost (5k-10k euro for 80 sessions) of this technology and long exposure of the patients (≈1 year), side effects can appear after exposure to pressurized oxygen[109]. Negative aspects experienced by patients are oxygen toxicity, lung collapsing, change in vision and blood pressure, accordingly pressurized oxygen therapy is not applicable for any patient.

### 2.2.6. BIOPHYSICAL TECHNOLOGIES

Biophysical technologies, e.g., radio-frequency electromagnetic field stimulation[110] and low-frequency ultra sound[111], positively affect a wound in the inflammatory stage. A pulsed radio-frequency electromagnetic field applied to the wound bed results in high nitric oxide production. Exposure of a wound bed to the increased NO concentration resulted in the upregulation of genes essential in the inflammatory phase and growth factors. Enhanced release of growth factors in wounded tissue resulted in increased cellular mobilization, angiogenesis, and thus wound repair[110]. Low-frequency ultrasound therapy has been engaged in wound debridement, removal of infected material, or necrosis from the wound bed. Moreover, extracorporeal shock wave therapy uses high-pressure pulses in wounded tissue and has been employed to treat surface cutaneous wounds[112]. This treatment promotes cytokine and growth factor production leading to improved anti-inflammatory response and tissue regeneration. Nevertheless, none of these techniques employed individually showed satisfying results in terms of healing rate, and primarily those have to be combined with bioengineered therapies[95].

### 2.2.7. BIOENGINEERED THERAPIES

Bioengineered therapies employed to treat chronic wounds are tissue substitute-based treatment, cellular or acellular-ECM, platelet-rich plasma, and human growth factor therapies.

### 2.2.5.1. CELLULAR THERAPY

Cellular therapy is a living skin replacement therapy[113] (Organogenesis CA, since 1998). A cellular product is based on a bilayer collagen matrix with neonatal or human fibroblasts and keratinocytes embedded in the matrix (Apligraf, Dermagraft). Besides introducing collagen matrix to the deficient extracellular matrix (ECM) of the wound, healthy living cells are introduced, ready to proliferate, and synthesize growth factors, cytokines, and ECM products[114]. Other than fibroblast-based cell therapies, more advanced techniques are directed towards using stem cells that restore tissue to the pre-injured state. Of particular interest, multipotent adult stem cells have great proliferative potential. They can differentiate into different cell types (including bone) and produce cytokines and growth factors affecting cell migration, proliferation, and metabolic activity of the host tissue[115]. In the randomized wound healing study, cellular therapies have shown to be approximately 30% more effective than conventional methods[116]. However, this bioengineered therapy must be combined with debridement, infection control, and revascularization procedures.

### 2.2.5.2. ACELLULAR THERAPY: ECM AND GF - BASED

Acellular therapies consider the insertion of collagen-based scaffolds into which cells can migrate to initiate angiogenesis, tissue granulation, and regeneration. Extracellular matrix (ECM) plays an active part in tissue regeneration through interaction with growth factors and host cells[117]. Commercialized ECM-based therapies are based on non-human products/dressings (porcine, bovine, and ovine) containing structural collagen, fibronectin, and hyaluronan. These components are essential in replacing ECM of damaged tissues (Hyalomatrix, Anica Therapeutics, MA and Integra Lifesciences, NJ). Moreover, human allografts showed to be also a very effective acellular method for diabetic and venous ulcer treatments. Namely, the allografts are harvested from a donor, decellularized, and dehydrated. In this procedure, the natural dermis structure of collagen and ECM are preserved. These dermal matrixes serve as scaffolds for cellular migration and angiogenesis. Together with conventional wound care, acellular technologies are effective tools for treating deep and acute wounds[117].

As physiological deficiency of chronic wound manifests in the decreased levels of epidermal growth factor (EGF), fibroblast growth factor (FGF), transforming growth factor (TGF)[103] healing can be accomplished through increasing the levels of these proteins. Platelet-derived growth factor (PDGF) is the first and only recombinant growth factor approved by the Food and Drug Administration (FDA), and it is topically applied to the wound in the form of gel[118]. The best performances of the PDGF have been noted to be in a randomized controlled trial in 20 weeks of non-healing diabetic ulcers. They have shown that the application of 100 µg/g of PDGF-BB Becaplermin (Regranex) increases the healing of diabetic ulcers by 32% compared to the control group[119]. However, topical application of PDGF for venous ulcer (VU) treatment has shown no efficiency; this might be due to limited penetration of growth factors into the wound and failure in reaching targeted cells[120]. Other than limited topical effect, disadvantages of PDGF (Becaplermin) application are the high cost and the lengthy application period, approximately 1.2k /2.5k euro for a 10/20 week treatment of 2 cm$^2$ ulcer. As in the case of cellular tailored therapies, wound debridement and disinfection must be performed before ECM of GF therapy is applied.

### 2.2.8. FUTURE DEVELOPMENT

The abovementioned issues in currently employed wound care technologies motivate the further development of advanced healing methods. Nanotechnology-based therapies are targeted therapies - acting on molecular/cellular level and successfully engaged in all phases of wound healing[121]. In hemostasis polymeric drug nanoparticles, zinc oxide nanoparticles are used.

Synthesized polymeric (drug, NO), gold and zinc oxide nanoparticles, polymeric nanofibers (plasmid DNA), nano-scaffolds (stem cells), and liposomes (GF and drugs) are used in the proliferative phase. Besides polymeric nanoparticles (NO), liposomes (GF, drugs), and carbon-based nanotubes (fullerene, graphene), gold, silver, and copper nanoparticles are specifically helpful in the inflammation phase. Finally, in the remodeling phase of wound healing, the most successful nanotechnologies employ polymeric nano-scaffolds and iron oxide nanoparticles, releasing signaling molecule NO, promoting re-epithelization and communication between cells. Targeted application based on the localized treatment of cells/tissues is the most efficient approach to wound healing. In localized applications, materials are used in small amounts, limiting the general costs, waste, and development of resistance to a drug (antibacterial resistance).

The requirements for healthy healing of a wound and deficiencies of existing techniques set precise demands on the future developing methods. One promising and rapidly growing technology is non-thermal or cold plasma-assisted wound healing. The existence of this form of matter in the atomic and molecular state suggests an entirely new approach in medicine.

## 2.3. PLASMA MEDICINE: FOCUS ON WOUND HEALING

A decade-long study of industrial non-thermal plasmas and their use in material sciences finally resulted in the development of a glow discharge reactor suitable for biological use[122]. This finding resulted in indirect biomedical purposes – sterilizing medical instruments and surfaces. Plasmas' physical and chemical activity shows excellent prospective for their multiple purposes. Functional aspects of plasma, e.g., electrical field, shock waves, electrons, ions, metastables, radicals, and UV radiation, can be used simultaneously or separately to tailor the desired application. Accordingly, plasma therapy could be tailored and controlled on the cellular or molecular level.

Focusing on the requirements for an effective wound healing device, significant perspective aspects of cold plasmas can be recognized. Namely, it has been shown *in vivo* trials that plasma is capable of:
   i. hemostasis – cessation of bleeding, blood coagulation,
   ii. sterilization – bacterial decontamination on the damaged tissue,
   iii. ablation – damaged tissue removal,
   iv. scarring – cell proliferation and wound closure.

Accordingly, one may ask why this powerful plasma phenomenon is still not globally used in conventional wound healing therapies. Although some plasma healing effects were confirmed *in vitro* and *in vivo*, many questions are still to be answered before atmospheric pressure plasma reactors are commercialized for

clinical purposes. In addition, medically certified plasma devices must fulfill requirements essential for human safety :

   i.   Electromagnetic compatibility (EMC)– Electrical equipment and plasma reactors must be designed to not cause electrical disturbances in the operation room or deliver electrical shocks to the treated objects. Plasma power or plasma voltage and electrical current are assumed to be responsible for the electric shock potentially caused in biomaterials. Accordingly, limiting the delivered power to a few wats can mitigate the damage of a biological sample[123].

   ii.   Operation under atmospheric conditions – Considering Paschen's law, it is apparent that plasma can be generated more easily in gas chambers at lower and moderate pressures. However, this case is not usable for clinical application. Therefore, it is essential for plasma to operate under atmospheric conditions for practical application on patients. In most cases, plasma is generated in noble gas flowing between electrodes, forming a jet in the ambient air.

   iii.   Stability and reproducibility –  To plan a clinical therapy, plasma parameters must be constant in ambient conditions. Moreover, plasma-produced species must be reproducibly produced during therapeutical treatments.

   iv.   A temperature lower than (T≈42°C) – Exposure of the cells to a temperature high as 46-60°C for 10-15 min results in irreversible cell damage, while 60-100°C has a fatal effect on cells[124]. Accordingly, the temperature required for the safe plasma treatment on animals and humans should not exceed the optimal 42°C.

   In this section, the most crucial aspect of plasmas in wound healing have been overviewed:

   i.   Blood coagulation – As the discussed first step in wound care is hemostasis and prevention of blood loss, both thermal and non-thermal aspects of plasma are used in clinical trials to test plasma effect on blood coagulation.

   ii.   Contaminated or necrotic tissue removal – Debridement improves healing of an injury, as follows features of plasma on contaminated or necrotic tissue removal are presented.

   iii.   Sterilization – Abnormal and prolonged wound healing is often caused by pathogens populating the wound bed. Therefore, one of the main issues in conventional wound healing is the decontamination of antibiotic-resistant bacteria. This section demonstrates the sterilization aspect of non-thermal plasma, focusing on clinically most essential bacteria.

   iv.   Proliferation – Final stage of proper wound healing is the proliferation of connective tissue cells and the remodeling of a matrix. Non-thermal plasmas generated under ambient conditions show a capability to stimulate cell proliferation and differentiation.

   The results of the most important aspects of plasmas in wound healing are presented in the next chapters: plasma-assisted hemostasis, plasma removal of

debris (necrotic tissue), plasma sterilization, and finally, plasma-assisted proliferation and tissue epithelization. Special attention has been given to the stimulated growth of cells upon interaction with plasma, wherein the biological role of RONS is discussed on the molecular level. Finally, other medical applications of cold plasmas are briefly presented.

### 2.3.1. PLASMA-ASSISTED BLOOD COAGULATION

Once the skin is injured and blood vessels are damaged, the most important step is to stop the bleeding and blood loss. Conventional methods to stop the bleeding are based on applying pressure, thermal devices, or hemostatic agents. The first clinical application of plasma relied on the hot argon plasma beam (V≈6.5 kV, P=40-155 W, f=750 kHz, Ar flow = 2-7 SLM)[125]. In the first instance, penetration depth (0.1-2.4 cm) and width (0.1-1 cm) on the tissue have been tested, and the hot argon beam was labeled as safe for clinical use during the treatment time t=1-10s. The first plasma-driven no-touching method was applied in gastroenterology in 1997 and compared with laser therapy. Argon beam coagulation has shown to be a more effective, good low-cost alternative with minimal tissue damage. Non-thermal aspects of plasma involved in blood coagulation were studied in more detail one decade later. Blood coagulation has been demonstrated in a safe tissue treatment by floating electrode dielectric barrier discharge FE-DBD with operating conditions f=200-1000 Hz, Vp-p=20 kV (Drexel University)[69]. This study pays attention to the chemical processes induced by plasma in blood during their direct contact. Accordingly, blood samples from healthy or hemophilic donors and *ex vivo* tissues were treated. Blood underwent faster clotting after only 30 s treatment with non-thermal plasma shown with the standard coagulation tests. Enhanced blood clotting by plasma was explained through the concentration increase of the main mediator $Ca^{2+}$, the central mediator of the coagulation cascade. Namely, $Ca^{2+}$ ion concentration in the blood increases through a redox mechanism provided by hydrogen ions generated in air plasma. The leading role of ROS, mainly atomic oxygen O, on plasma-enhanced blood clotting has been confirmed with the portable air plasma torch designed for large area treatment[126]. The authors concluded that blood clotting could be attributed to oxidants' stimulation of erythrocyte-platelets and leukocytes interaction (probably O and less likely NO). Coagulation effect of no-touching He plasma jet (f=20 kHz, Vp-p=8-20 kV, 2 SLM) was compared with conventional thermal coagulator[127] after abdominal incision on the liver of healthy mice. This report evaluated the inflammation phase that appears after the hemostasis. Concretely, during the non-thermal plasma coagulation, necrotic cells disappeared in 5 days, and during the thermal plasma coagulation, these remained up to 15 days after hemostasis. Results of the study not only promote more effective coagulation by non-thermal He plasma jet in respect with conventional method, but

43

favor application of plasmas in other phases of wound healing. This would mean that use of plasma for surgical cuts handling would omit use of other products in following stages of wound healing e.g. antibiotics in the inflammation phase.

### 2.3.2. PLASMA TISSUE REMOVAL

In chronic wound development, separation of necrotic from healthy tissue or total removal of necrotic tissue is crucial for further healing. Conventional methods employ laser ablation, focused ultrasound ablation, radio-frequency waves, or cryoablation to separate tissues. However, controlled ablation can also be achieved with plasma. The first plasma-driven ablation technology was patented in 1998 (Coblator, Plasma wand, Smith &Nephew). RF glow discharge of size 100-200 µm and generated in the air is an excellent choice for precise tissue removal. Plasma-mediated ablation of tissue is caused by molecular disintegration, while the damage of the surrounding tissue is kept minimal[128]. It has been reported that RF plasma hydrogen ions, hydroxyl radicals, and other ions in a saline solution may disrupt molecular bonds within targeted tissue[100]. Plasma ablation is clinically used in tonsillectomy[129]; see Figure 2.13(b).
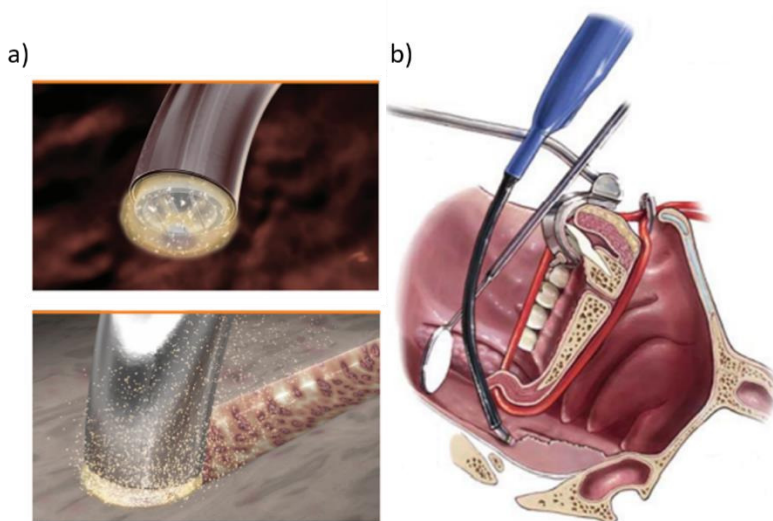


Figure 2.13. a) Plasma coblator (Smith & Nephew) plasma glow discharge in air and ablation on soft tissue; b) Tonsillectomy with plasma mediated coblation[129].

Moreover, a helium plasma needle has demonstrated noninvasive detachment of eukaryotic cells. Namely, in a short, (1 s) treatment with the RF helium plasma needle T≈300 K (TU Eindhoven) treated epithelial cells have shown to detach from cell adhesive surface without being damaged[130]. Cell non-invasive detachment was associated with adhesions molecules damage (cadherin and

integrin). Interaction with plasma and successive detachment of cells has been attributed to the oxidation of cell adherence molecules by RONS ($O^•$, $O_2^-$, $O_3$, $^•OH$, $^•NO$, $H_2O_2$ ) produced in plasma in contact with ambient air. Plasma detachment of cells without damaging them has application in cell manipulation, removal of cells and tissues, and cell rearrangement and tissue engineering.

### 2.3.3. PLASMA STERILIZATION

Sterilization considers any process used to remove, kill, or deactivate any form of microbes, e.g., bacteria, viruses, fungi, spores, etc. Bacterial contamination and the lack of contamination control are often why 15-20 % of chronic wounds do not respond to conventional treatments. Accordingly, decontamination is considered crucial for proper wound care[100]. Traditional methods to sterilize medical surfaces, food, and living tissues employ heat (dry - flaming, glass beads, moist-steam autoclave); chemicals (gas- ethylene oxide, ozone, nitrogen dioxide, liquid-hydrogen peroxide, peracetic acid, formaldehyde), radiation (non-ionizing UV Hg lamp, ionizing γ-radiation $^{60}$Co, $^{137}$Cs); sterile mechanical filtration (d<0.22 μm). Some conventional sterilizing agents have disadvantages such as low penetration (chemical liquids), toxicity (ozone, hydrogen peroxide, peracetic acid), or can have a carcinogenic effect (ethylene oxide). Therefore in the following text, advantages of plasma as an alternative effective, green, non-toxic sterilization agent have been displayed.

The unique property of plasma to simultaneously produce electrons, ions, excited atoms and molecules, and radiation (UV) qualified these phenomena as a sterilization agent. For more than fifty years, plasma sterilization technology has been investigated in medicine, the food industry, and even agriculture. The driving idea is to overcome existing techniques' drawbacks and develop an eco-friendly, non-toxic, universal mechanism to destroy all, including drug-resistant bacteria and spores, on heat-sensitive biomaterials. The first patent was issued in 1968 to Arthur D. Little Company for pulsed, high pressure, and high-temperature plasma sterilization. In the following years, various low-pressure and low-temperature plasmas were developed in precursor, halogen, and flow-through gases[131]. One of the first detailed studies involving sterilization mechanism and comparison with conventional sterilizers was on the efficiency of low-temperature $H_2O_2$ vaporized plasma (Johnson & Johnson Inc, CA)[131]. The room temperature plasma was generated in a vacuum chamber (0.3 mTorr) in vaporized hydrogen peroxide when an RF electric field was applied. Sterilization of objects (d<6 mm, l<31 cm) would be achieved after 15 min. The main advantages have been noted to be low plasma temperature, short sterilization cycle, no waste, and user-friendly handling due to the vacuum-closed environment and no physical contact of the operator with the $H_2O_2$. However, the main drawbacks were expensive vacuum equipment, handling

of the objects, and physical limitations, e.g., restriction of the treated object dimensions by the reactor's size.

Consequently, design drawbacks moved future plasma sterilization outside vacuum chambers, and attempts have been made to design safe plasma reactors to sterilize tissues. The antimicrobial character has been demonstrated in atmospheric glows[132], resistive barrier discharges (RBD)[133], DBD[134], coronas[135], and plasma jets[136]. In these studies, the bactericidal effect of plasma was confirmed on several clinically essential microbes, e.g., *E. Coli* - gram-negative model bacteria, *B. Subtilis* - gram-positive model bacteria, bacterial spores, bacteriophages. In the studies focused on applying plasma in wound healing, inactivation of invasive bacteria isolated from wounds was put on trial[137-138]. One of the leading causes of the abnormal healing process and chronic wound creation is multidrug-resistant *Methicillin-resistant Staphylococcus Aureus* (MRSA) and *Pseudomonas aeruginosa*. Complete inactivation of these bacteria has been demonstrated *in vitro* with 50 Hz air DBD[137]. Additionally, argon APPJ has been an effective tool for inactivating acute wounds bacteria *S. aureus*, *P. aeruginosa,* and typical wound colonizers *E. faecium* and *C. albicans*[138].

Plasma bactericidal effect is the result of the simultaneous act of the physical and chemical agents[139]:

a) Heat – in case of thermal or high-temperature non-equilibrium plasma, heat plays an important role similar to conventional dry (170°C, 1 h) or moist heating methods (autoclave 120°C).

b) Shock waves – shock waves can be generated in pulsed thermal plasmas and cause the high pressure-based bacteria membrane rupture[140].

c) UV radiation – doses of several $mW·s/cm^2$ are known to cause lethal damage to cells, usually UV effect mirrors in DNA strand break, pyrimidine cross-linking, and formation of thymine dimers. The destruction of nucleic acids and disruption of DNA results in reproduction failure and microbe death.

d) Charged particles – charged particles are important inactivation agents, only in the direct plasma treatments when plasma is in physical contact with liquid or bacteria. In indirect, treatment with afterglow amount of ions and electrons is negligible. Charged particles significantly affect the destruction of irregular shape, gram-negative bacteria due to the electrostatic force caused by charge accumulation on the bacteria membrane and its rupture[87]. Except for causing membrane rupture, a flux of energetic ions can cause etching of the biomaterial and consequent bacteria removal after their inactivation; this is common in DBD devices[141].

e) Reactive species – air plasma and plasmas generated in the air environment are rich sources of RONS. First, ozone is toxic for cells and thus interferes with the cell respiration system. Second, OH radicals are likely to cause peroxidation of the cell bilayer lipid membrane, and finally, atomic oxygen O is a strong oxidizer,

powerful to oxidize essential proteins. This effect is of incredible importance for destroying resistant gram-positive bacteria and their spores[142]. Nitrogen reactive species $^\bullet NO$ and $^\bullet NO_2$ are also reported to have a germicidal effect[139]. Microbial effects of plasma species are presented in the diagram in Figure 2.14 (a).
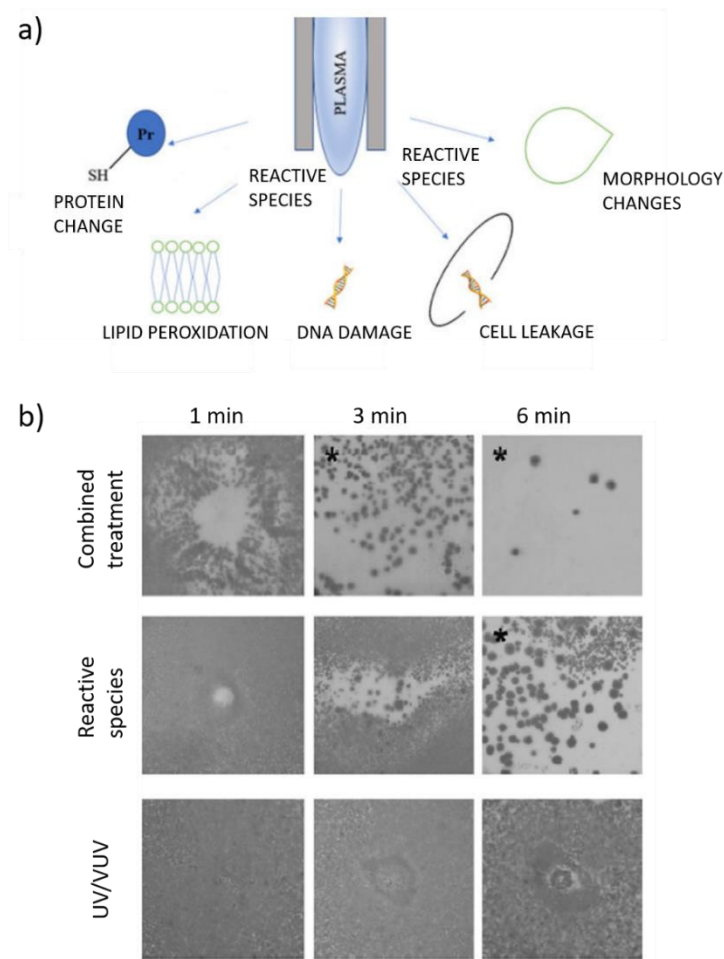


Figure 2.14. a) Plasma microbes inactivation principle[143]; b) *E. Coli* treated with He plasma cross jet[64].

In direct treatments, when plasma is in direct contact with a sample, charged particles play a major bactericidal role; this was confirmed in air FE-DBD[66], where a treated tissue behaves as another electrode. Indirect antibacterial aspects of plasma are mainly ascribed to UV radiation and RONS. Role of UV radiation in bacterial inactivation is shown to play a significant role in $N_2/O_2$ [144] and Ar[145] plasmas MW discharges (2.45 GHz). However, in most published studies on plasma

decontamination, RONS' role is crucial. RONS are the main bactericidal agents in APPJs where the feeding gas is mixed with $O_2$, e.g., DC-driven Ar/$O_2$ plasma[146], RF-driven Ar, or He/$O_2$ plasma[136], $N_2$/$O_2$ high voltage DBD[147], air fed high voltage DBD[148], MW discharges[149], and corona[150]. In addition, the synergetic effect of UV radiation and RONS is shown to be crucial for cold plasma bacterial inactivation[65], see Figure 2.14 (b). Recent studies report enhanced effectiveness of plasma decontamination when water or water vapor is added to the feeding gas or sprayed directly onto dry microbial sample[151].

The typical treatment time needed to inactivate bacteria with non-thermal plasma depends on bacterial species, plasma properties, and the type of the contaminated surface. In a realistic biomedical scenario, commonly used models are plasma jets operating in noble gases in ambient air while characterized by low temperature. Ar APPJ has better properties in deactivating endospores *Bacillus atrophaeus* than APPJ in He[136]. Moreover, its impact can be enhanced when oxygen is added. The treatment time required to inactivate 90 % of microbes is known as D-value and represents an essential parameter for describing plasma decontamination processes. Bacterial reduction during treatment time can be characterized by one or multiple D-values (slopes $D_1$, $D_2$, $D_3$). The effect of oxygen addition on E. Coli survival, when treated with Ar APPJ, is shown in Figure 2.15.
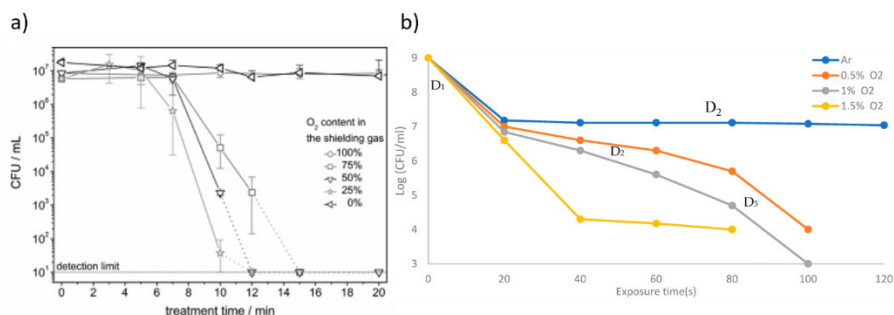


Figure 2.15. The survival rate of E. Coli upon direct exposure to Ar APPJ: a) with different $O_2$ content in shielding gases[152], b) with the addition of $O_2$ to feeding gas Ar[153].

*Ex vivo* sterilization of human skin samples with DBD is one step technology of skin graft preparation without antibiotics. In this way, antibacterial and multidrug resistance can be defeated[154]. Plasma sterilization aspects have also been confirmed *in vivo* on the rat model wound 4 h after the bacterial contamination (*S. aureus*)[155]. However, the inactivation of wound bacteria ($10^3$ CFU in the 60 s) was reported to be one order of magnitude less efficient than the inactivation of bacterial load deposited on an agar plate. The authors suggested that decreased efficiency might

be related to the small wound region treated directly (75 % of a 2 cm wound). Other explanation for the decreased efficiency refers to protective role of the wound liquids. More recently, the antibacterial properties of another device employed in clinical studies, kINPen (INP Greifswald), have been tested *in vivo*[156]. Unfortunately, no remarkable disinfection has been achieved with the device alone. Therefore, plasma treatment of a contaminated wound should be combined with conventional antiseptics.

Moreover, plasma is effective in inactivating biofilm-forming bacteria. Biofilms can be found on medical devices (prosthesis), solid-liquid interfaces, etc., between implants and body fluids (blood). Their most important property is their resistive character to the immune system of a host and antibacterial treatment[157]. Therefore, infections due to the biofilm formation on biomedical devices (e.g., implants) are complicated to treat. Bacterial inactivation is mainly driven by RONS species, while biofilm removal can be described through the etching process with ions (closed low-pressure plasma systems). Nevertheless, inactivation of *C. Albicans* biofilm is possible with APPJ in Ar but only when $O_2$ was added to the gas mixture[158], see Figure 2.16. On the other hand, broad spectra of clinically important bacteria e.g., *S. aureus*, *P. aeruginosa*, can be removed in a 4-minute treatment ($5 \cdot 10^6$ CFU) from a polymeric sample with atmospheric pressure cold plasma discharge[159].



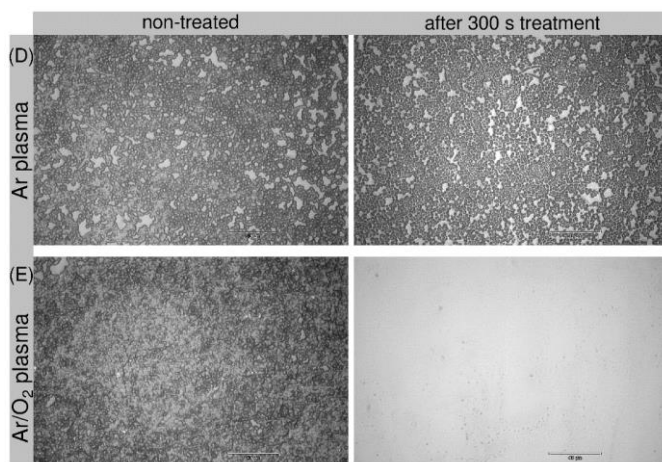Figure 2.16. *C. Albicans* biofilm inactivation with Ar plasma (up) and Ar/$O_2$ plasma (bottom)[158].

Non-thermal atmospheric pressure plasmas have proven throughout the last decade to be an environmental-friendly and effective new age sterilization technology causing minimal damage to the living tissue and without generating toxic byproducts. The ability to damage a wide range of microbes while healthy tissue

remains intact during the treatment is one of the steps that plasma has accomplished to be further examined and used in wound healing[152].

## 2.3.4. PLASMA ASSISTED CELL PROLIFERATION AND TISSUE EPITHELIZATION

Only cells essential for wound healing are discussed here, focusing on the connective tissue cells – fibroblasts and their proliferation. A two-decade-long study on plasma-cell interaction shows that the plasma dosage deposited on the cell determines the outcome. Long exposure (~minutes) to a non-thermal plasma has cytotoxic, bactericidal effects. On the contrary, short plasma exposure (~seconds) modifies cell functions: proliferation, attachment, and migration. The following text discusses the modulation of cell functions on the molecular level upon oxidative stress caused by RONS or ionization upon radiation.

### 2.3.4.1. CELL PROLIFERATION AND TISSUE EPITHELIZATION: *IN VITRO* & *IN VIVO*

A low level of oxidative stress stimulates cell proliferation in cell culture. Oxidative stress in cells can be induced upon controlled plasma treatment, low dosage of ROS, and radiation. The promoted proliferation of mammal cells upon atmospheric pressure plasma nursing is studied worldwide in jets[160-161], torches[29], and DBDs[162], see Figure 2.14(a). Numerous studies have shown that cold plasma induces secretion of growth factors (GF)[162], transforming growth factor-β1 (TGF-β1)[163], increment of intracellular ROS[68], and the number of cells in S-phase (DNA replication phase)[160]. Promoted production of intracellular ROS and a low dosage of UV radiation and radicals activate nuclear factors-κB (NF- κB) signaling pathway[160]. Nuclear factors- κB regulate genes involved in immune and inflammatory responses[164]. Eventually, their activation plays an essential role in the inflammatory phase of wound healing.

Moreover, studies have shown that cold plasma reduces inflammation by activating peptides crucial for protection against pathogens and recruitment of immune cells into the wound bed[165]. RONS activate cytokines and growth factors relevant to wound healing in fibroblast and keratinocytes[29]. In the combined, *in vitro/in vivo* study role of ROS has been demonstrated in triggering upregulation of genes in charge of cell adhesion (focal adhesion kinase, paxillin), migration, and spreading (integrin 5β1, syndecan 4) of the treated cells, and formation of new cell-matrix contact (vinculin, talin)[161]. Furthermore, ROS are shown to promote differentiation of fibroblasts into myofibroblasts, an indicator of plasma-assisted wound closure and scarring. The remodeling phase in wound healing has been explained through ROS-driven upregulation of collagen and the new ECM

synthesis[161]. Improved cell proliferation after treatment with FE-DBD is presented in Figure 2.17.
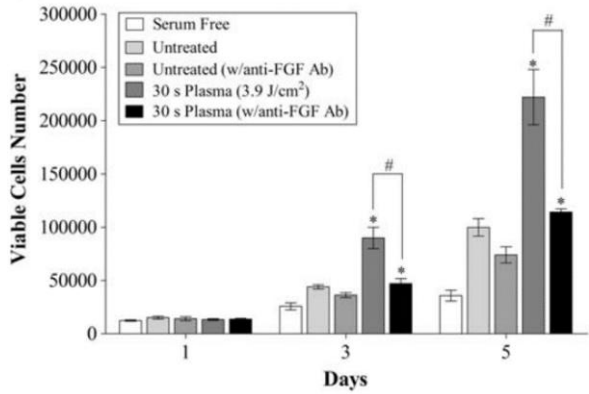


Figure 2.17. Cell proliferation induced by FE-DBD treatment [162].

Preclinical studies performed on an animal wound model have been demonstrated in many studies; the main findings are given in Table 2.7[166]. Wound healing is a complex process passing through overlapping stages hemostasis, inflammation, proliferation, and remodeling. In the inflammatory phase, acute and chronic sub-phases can be differentiated, where the acute phase is characterized by neutrophil infiltration and chronic is characterized by mononuclear infiltration (lymphocytes, macrophages). Infiltrated neutrophils, lymphocytes, and macrophages play a role in immune response and help fight the infection. In the proliferative phase, re-epithelization, angiogenesis, and collagen synthesis happen. Finally, the remodeling phase mirrors collagen maturation, ECM creation, and wound contraction. Common phenomena induced by cold plasma important in wound healing are reported: decreased inflammation, increased angiogenesis, vascularization, epithelization, wound closure, and granulation. The first animal studies have been performed with air arc, employed as NO generator far away from plasma where the gas temperature is about 20-40°C. The NO generator - Plason[167] has been clinically certified and used successfully to improve the healing of stubborn wounds by improving angiogenesis, granulation, and suppressing inflammation. Helium jets have been shown to accelerate wound healing epithelization and decrease inflammation. However, adding the molecular ($O_2$, $N_2$) or even argon gas has improved its performance. The first wound healing aspects of argon plasma *in vivo* have been demonstrated in 2013 on the SteriPlas device[29], which was later medically certified and since employed in clinical treatments of chronic wound healing. SteriPlas exhibited the first potentials of cold argon plasma, expressing its capabilities to accelerate wound closure, infiltration of macrophages and neutrophils in the wound bed, secretion of collagen and FGF-2, and angiogenesis. Since the first

*in vivo* confirmations on healing prospects of argon plasma, different modifications, e.g., feeding/shielding gas, electrode geometry, driving frequency, treatment times, and distances, have been examined.

Table 2.7. The principal findings on the plasma wound healing employment *in vivo*

| Plasma | The main findings |
|---|---|
| Air (NO-generator) | Improves angiogenesis, granulation, suppressing of inflammation (*S. aureus*)[167] |
| He | Accelerated wound closure and re-epithelization (long treatments harmful), accelerated healing in diabetic rats[168], increased angiogenesis and microcirculation[169] Accelerated wound healing, less scar formation, TGF-β/pSmad2/3/α-SMA positive cells, and collagen deposition[170] |
| He/O$_2$/N$_2$ | Improves epithelization, neovascularization decreases microbial flora of a wound bed[171] |
| He/Ar | Accelerated wound healing and granulation tissue formation, He/Ar has better performance than He plasma[172] |
| Ar | Accelerated wound healing and re-epithelization, myofibroblasts in humid wounds[173] Increased angiogenesis and FGF-2 expression[29] Less fibrosis and more acute inflamation[174], Accelerated wound healing in healthy and diabetic rats (Type I, II), fewer neutrophils and T-cells in the later stage of wound healing in diabetic rats, and increase of antioxidants in treated area [175], Long exposure and heating of tissue (>50°C) was highly detrimental for wound healing – longer treatment distances suggested[176] Accelerated angiogenesis, increased collagen fibers, keratin production, Nrf2 response, and p53 activation, macrophage infiltration, inflammation and granulation[177] Changes in matrix remodeling and focal adhesion complex, elevated microcirculation, Increased tissue oxygenation, and tissue hemoglobin index[161] |
| Ar/Air | Accelerated healing in comparison with Ar only, improved immune response (IL-6 mRNA expression)[178] |
| Ar/N$_2$ | Improved healing performances, wound contraction, epithelization, angiogenesis, the concentration of RONS (RNS) in a wound bed [179] |

Healing performances of argon plasma are shown to improve by adding small percentages (0,1-1%) of molecular gases air and nitrogen. The addition of $N_2$ into argon feeding gas improved healing performances, angiogenesis, blood flow, epithelization, wound contraction, and concentration of RONS in the treated tissue[179]. Probably the most studied Ar plasma jet is kINPen. During the last several years, the kINPen plasma jet in Ar has accelerated wound healing and angiogenesis, wound closure, re-epithelization, less fibrosis, and acute inflammation[174], see Figure 2.18.
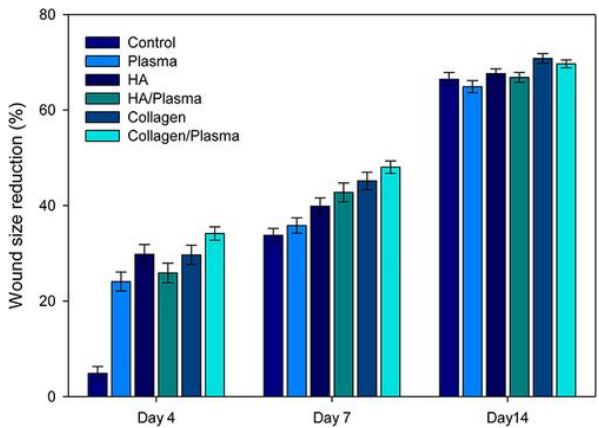


Figure 2.18. Mean percentage wound size reduction on days 4, 7, and 17 in rodents after the treatment with Ar plasma jet (Plasma), hyaluronic acid (HA), HA/plasma, Collagen, and Collagen/Plasma[174].

Positive results of *in vivo* studies on wound healing enhancement by cold plasmas encouraged a few groups to test their devices on patients. In the next chapter, three medically certified devices are presented and the results of their clinical use.

### 2.3.4.2. WOUND HEALING: CLINICAL STUDIES

Although positive aspects of plasma in wound healing have been broadly discussed and demonstrated *in vitro* and *in vivo*, only a few cold plasma devices are medically certified for clinical application. Among them are the Plason[167] (Onkocet, Russian/Czech Republic /Slovakia, 2009)[76], SteriPlas/MicroPlaSterβ®[29](Adtec Plasma Technology Japan/ UK, 2019), and kINPen®MED[180](INP/neoplas med GmbH, Germany, 2013), shown in the Figure 2.19. In addition, the essential commercial properties of these three medical devices are overviewed in Table 2.8.
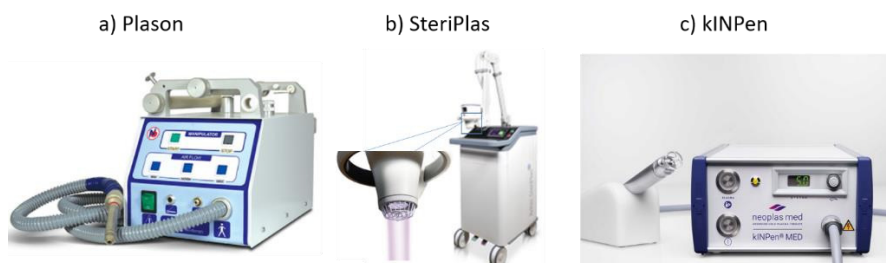
Figure 2.19. Medically certified cold plasma devices employed in wound healing: a) Plason, b) SteriPlas, c) kINPen.

Table 2.8. Commercial overview of three medically CE devices Plason, MicroPlaSter/SteriPlas, and kINPen

| Device | Plasma | Gas | f, P | T | RONS | Clinical trials |
|---|---|---|---|---|---|---|
| Plason | Arc D≈1-4 mm | Air | DC P<500 V·A | 20-40°C (2000-4000°C) | NO | Disinfection, vascularization, treatments of trophic ulcers, diabetic foot, non-healing wounds |
| SteriPlas/ MicroPla Sterβ® | Torch d≈5 cm | Ar | 2.45 GHz P~110 W | ≈30°C | ROS, UV | Treatment of venous and arterial diseases, actinic keratosis, herpes zoster, diabetic foot, chronic burns, deep infection, skin graft donor sites |
| kINPen® MED | Jet d≈1 mm | Ar (+N$_2$) | 1 MHz, P$_{diss}$<3, 5 W | 35-38°C | ROS | Treatment of infections, stubborn wounds, diabetic foot |

Above mentioned certified devices have been engaged to promote the healing of chronic wounds in patients for more than a decade. Accordingly, the most important findings[166] have been summarized in Table 2.9.

Table 2.9. Plasma promotion of chronic wound healing, clinical studies on CE plasma devices[166]

| Plasma | Therapy | Patients | The main findings |
|--------|---------|----------|-------------------|
| Plason | t=5-12 s; every or every other day; no direct plasma | 68 | Improved tissue hemodynamics and healing responses[181] |
| SteriPlas | t=5 min, daily days-weeks | 36 | Well tolerated, bacterial load significantly reduced[28] |
| | t=3-7 min, daily days-weeks | 70 | Well tolerated, no significant wound size reduction but significant wound width decrease[182] |
| kINPen | 60 s/cm$^2$ | 35 | Well tolerated; significantly reduced wound exudation and microbial load, the best performance when combined with antiseptics[183] |
| | 60 s/cm$^2$ 3X week over 2 weeks | 16 (DFU) | Well tolerated; significantly reduced bacterial load and complete removal of *P. aeruginosa*[184] |
| | 30 s/cm$^2$ per day for 5 days, followed by 3 treatments every second day | 45 (DFU) | Well tolerated; improved wound healing speed, wound reduction independent on the infection[185] |

kINPen is the most examined plasma device concerning its physics, chemistry[76], and direct clinical application in wound healing[180]. Moreover, in the world's first randomized trial, kINPen has proven the successful application of cold plasma kINPen MED for diabetic ulcers[185]. In this study, 65 diabetic ulcers have been treated on 45 patients, with cold plasma or placebo patient-blinded manner. Patients were treated with the manufacturer's recommended plasma treatment 30 s/cm$^2$, 8 times in 14 days (5 consecutive days, 3 treatments every other day). Plasma has shown to be relevant for reducing wound size, granulation, and time of wound closure rather than microbial sterilization. However, the limitations have been recognized in the failure to decontaminate bacterial load in a wound bed. The importance of this problem has been emphasized and highlighted as a point of improvement. The results of a first randomized trial and attempt to clinically treat diabetic foot ulcers with cold plasma have been presented in Figure 2.20.

**Table 2. Primary Study End Points**

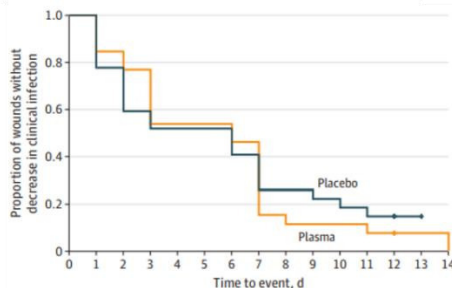| Parameter | CAP Start of therapy | CAP End of therapy | Placebo Start of therapy | Placebo End of therapy | P value |
|---|---|---|---|---|---|
| Wound area, median (95% CI), % | 100 | 30.5 (12.3-53.5) | 100 | 55.2 (25.2-72.0) | .03 |
| Clinical infection mean score, No.[a] | | | | | .91 |
| 0 | 5 | 26 | 4 | 25 | |
| 1 | 16 | 3 | 20 | 4 | NA |
| 2 | 10 | 1 | 7 | 1 | |
| Mean (SD) | 1.16 (0.54) | 0.17 (0.29) | 1.10 (0.41) | 0.13 (0.23) | |
| Quantitative microbial infection score, mean (SD)[b] | 4.10 (4.57) | 1.94 (2.22) | 3.16 (4.66) | 1.58 (2.25) | .59 |
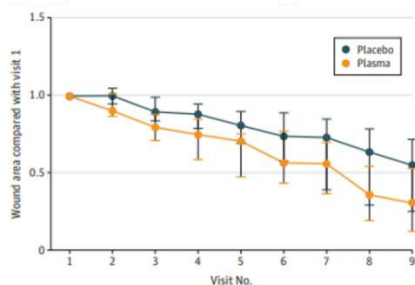
Figure 2.20. Overview of the results published in the world's first randomized trial: Treatment of DFU by kINPen[185].

Conclusions arising from *in vivo* applications of plasmas ensured medical use of plasmas in other fields as well, among which is plasma for cancer treatment. The following few sections briefly present other clinical benefits of cold plasmas.

### 2.3.5. OTHER APPLICATION OF CAPS IN MEDICINE

Clinical application of non-thermal plasma relies on RONS production. RONS express oxidative stress on/in cells and affect essential proteins, DNA, cell life cycle, etc. Accordingly, plasma found its application in other medical fields besides wound management. Plasmas are studied and successfully applied in cancer therapy, **regenerative medicine (skin diseases and esthetic dermatology), dentistry, and ophthalmology.**

### 2.3.5.1. CANCER TREATMENT – PLASMA ONCOLOGY

The ability of cold plasma to cause apoptosis and detachment of treated cells found application in cancer treatment. *In vitro* studies on cancerous cells (lung[186], pancreas[187], breast[188], melanoma[35], etc.) have shown that plasma can selectively affect cell motility, interfere with the cell cycle[189], and induce apoptosis/necrosis in these cells. Plasma selectivity towards cancerous and healthy cells is strongly correlated with interaction mechanisms. The interaction between plasma and cells is determined by RONS production and causes oxidative stress. It has been reported that the membrane of cancerous cells contains less cholesterol, which makes them more sensitive to lipid peroxidation and consequent creation of

pores on the membrane and penetration of RONS[190]. Upon interaction with produced RONS, integrin activation can be expressed in cells (a protein that regulates cell migration). This process is crucial for tumor growth and metastasis[191]. The high flux of RONS can damage essential proteins and DNA or cause the immediate or programmed death of cancerous cells depending on the delivered plasma dose. It has been reported that short treatments and low plasma doses (RONS) induce apoptosis in cancerous cells (programmed death) through direct interaction with cells. In contrast, overexposure induces immediate necrosis without damaging healthy tissue[35].

Anticancer plasma properties are confirmed *in vivo* on different types of cancers glioma[192], melanoma, human bladder tumors[30], colon cancer[193], pancreas cancer[187]. Plasma-treated tumors resulted in the tumor (ablation) removal followed by complete healing without new growth, while only treatment without removal resulted in slower further growth[30]. Moreover, chemotherapy together with plasma is also applied for tumor treatment[194-195]. Some research groups study the effect of plasma-activated liquid PAL (e.g., medium, PBS) on tumors. In this treatment, PAL is injected into the tumor, and only long-living RONS ($H_2O_2$ and $NO_2^-$) are considered to have anti-cancer effect[196]. Nevertheless, a recent study showed a better survival rate among mice and an increased immune system directly treated with plasma (*invivoPen*) than with plasma-activated medium PAM[197].

### 2.3.5.2. PLASMA DERMATOLOGY AND REGENERATIVE MEDICINE

Plasma expresses anti-itch, anti-microbial, anti-inflammatory, tissue-stimulating, blood flow enhancing, and apoptotic effect[198]. Accordingly, plasma offers a great chance to treat skin disorders and dermatological issues. PlasmaDerm[199] is an FE-DBD device commercialized for dermal utilization. As a patient's skin acts as one of the electrodes, treatment with PlasmaDerm is considered direct. Besides successful decontaminating and treating chronic wounds, a positive effect of this plasma has been confirmed on a wide range of dermal issues. Some of those are caused by bacteria, viruses, fungi, and rare diseases such as epidermolysis bullosa[200]. Plasma can successfully treat atopic eczema, relieve itch and pain, sterilize skin bacteria, fungi and viruses. Due to stimulated tissue revitalization and regeneration, plasma is used to heal scars[201], actinic keratosis[202], and skin tumors[35]. Plasma enhanced skin regeneration is also used for esthetic purposes, e.g., scar removal, removal of hyperpigmentation, and skin resurfacing and rejuvenation[203]. In the long clinical studies of the plasma resurfacing program, patients were subjected to 3.5 J plasma treatment for skin resurfacing. The resurfacing program uses plasma energy to create a thermal effect on the skin. Plasma has been shown to not vaporize or damage skin, as conventional $CO_2$ lasers, but rather leave an intact layer of dried epidermis acting as a natural protective and

biological dressing that enhances rapid skin recovery. The effect of plasma in the first instance can be assigned to the thermal denaturation of dermal collagen (>60°C). Further, fibroblasts are activated to stimulate wound healing and reduce of solar elastosis. Typically, conventional methods to promote skin regeneration and rejuvenation use lasers or aggressive chemical peelings, both of these can be painful, causing a burning sensation and have long recovery period. In comparison with these, plasma is a painless and inexpensive way to handle skin issues, either dermatological or esthetical.

### 2.3.5.3. PLASMA DENTISTRY

Plasmas found their application in dentistry, cariology, periodontology, endodontics, oral prosthetics, and oral oncology[204]. Due to their biological activities, cold plasmas are used for microbial (bacteria, viruses, fungi) deactivation and root canal disinfection before and during the standard dental procedure. *In vitro* studies, *P.gingivalis* and *T.forsythia* biofilms proved the effectiveness of plasma jets against common dental conditions, gingivitis, and periodontitis. During standard dental procedures, a root canal is exposed and often colonized by *F.feacelis* biofilm without affecting canal dentin. $Ar/O_2$ plasma has been shown to successfully fight 3 weeks grown biofilm during 12 min[205], while a He jet in combination with 3% $H_2O_2$ also showed better results than He jet only. However, few studies with Ar CAP, microwave-induced torch, and He jet showed anti-biofilm properties against *C.albicans*, a condition known as oral candidiasis. Moreover, reduction in inflammation and fungal tissue invasion has also been demonstrated in murine experimental models[206].

Oral cancers stand as one of the most common cancers, with 177.000 deaths and 354.000 new yearly cases worldwide. The possible solution to this widely spread problem is combining radiotherapy and smart drug delivery. The potential of cold plasmas lies in their selective cytotoxic effect on malignant cells. One of the most successful studies has shown that $N_2$ plasma selectively damages the DNA of oral cancer cells (SCC-25), leaving non-cancerous cells intact[207]. Esthetical application of plasma mirrors in their rich $H_2O_2$ production can be used for painless teeth bleaching and carious cleaning. Moreover, properties of plasmas to influence material physical and chemical characteristics can be used for the modification of the dental surface, enhancement of adhesion and polymerization, and surface coating[208].

### 2.3.5.4. PLASMA OPHTHALMOLOGY

Infections of soft tissue such as an eye are challenging to treat; however, as a non-invasive phenomenon, plasma shows its applicability in ophthalmology. In

clinical studies, *S. aureus, S. epidermidis, E. Coli, P. aeruginosa,* and *C. Albicans* are effectively inactivated with plasma without affecting corneal epithelial cell viability[209]. The clinical study showed the possible utilization of Ar APPJ to eliminate the most common pathogens from the patient's eye. It can be used as a supplement or an alternative therapy for therapy-resistant corneal infections. Moreover, CAP was used to treat complicated eyelid wounds with air plasma[210]. Only two plasma treatments of 5 s in 5 days are shown to have a positive effect and reduce inflammation and initialize tissue granulation. After the sixth treatment, the patient was discharged from the hospital.

Cold atmospheric plasmas are employed in various medical applications - from various cancer treatments to sterilization of soft tissues. Although the healing effects of plasmas are already clinically tested and examined, the existing literature lacks information about the potential risks of plasmas on human health. Therefore, early and long-term risks post plasma treatments are briefly discussed in the next chapter.

## 2.4. RISKS OF COLD PLASMA UTILIZATION ON HUMAN HEALTH

Despite well-known healing aspects of cold plasmas, potential short and long-term risks on human health still raise some questions. Unfortunately, these are not familiar due to the lack of clinical data.

Plasma is a cocktail of charged particles, radicals, metastables, RONS, UV, and thermal radiation submerged in the electrical field. This chemically reactive environment, like every other, brings risks when used in uncontrolled circumstances. Uncontrolled and non-localized exposure of living tissue to cold plasma can cause heating upon high species and radiation flux and consequent instant damage of the tissue (uncontrolled fluxes of OH radicals, $H_2O_2$ can cause cell leakage and necrosis)[211]. The relation between the development of skin cancer and exposure to UV light is well-known. The maximal UV dose defined by ICNIRP for intact human skin is 30 $J/m^2$. Therefore, when tissue is subjected to an Ar plasma, the effect of UV radiation should not be neglected, and possible side effects must be accordingly evaluated. Long-term risks, namely the genotoxic effect of plasma, have been tested *in vitro* on the isolated DNA (plasmid DNA)[212], cellular DNA (γ-H2AX DSB damage marker)[213] as well as *ex vivo* (γ-H2AX). E*x vivo* studies on humans (FlatPlaSter 2.0, UV dose 25 $nW/cm^2$)[214] and porcine skin (FE-DBD, Plasma dose 0.17 $W/m^2$)[215] demonstrated safety threshold and plasma-dosage dependent DNA damage above this threshold, 120 s for FlatPlaSter and 3-5 min for FE-DBD. These studies emphasize accurate plasma UV diagnostics and well-controlled treatment to keep the plasma dosage below the recommended mutagenic threshold. In addition, the same study investigates the toxicity of byproducts $O_3$, $^\bullet NO$, and $^\bullet NO_2$[214]. Namely, upon inhalation

of these gases above the safety limit defined by the National Institute for Occupational Safety & Health NIOSH, respiratory problems may appear. Respiratory problems are typically associated with coughing, shortness of breath, burning sensation of throat and chest, inflammation, and damage to the airways and lungs. For example, the maximum safe value for a continuous inhaling of ozone during 8 h must be kept below 0.1 ppm. For continuous inhalation of gases NO and $NO_2$ during 8 h, safe concentrations are 25 ppm and 5 ppm. Production of ozone in the large Ar plasma torch FlatPlaSter was measured in the area between the electrode and treated object. Given the dilution of ozone in ambient air and short exposure (t~min) of the patient, it has been calculated that the generation of ozone would have to be 2.5 times higher to reach the safety limits. Moreover, NO and $NO_2$ concentrations are measured in the open air and evaluated to be below the safety limit (<1ppm, 3 ppm)[214].

Recently, a long-term post-interventional clinical study evaluated possible plasma risks 5 years after the plasma wound treatments (1 $J/m^2$)[216]. In this research, no malignant changes have been observed nor change in the tissue microcirculation or cell morphology of the treated skin in respect to untreated skin.

The excellent healing aspects of cold plasmas are demonstrated worldwide; however, their utilization must be handled with care. For example, suppose the flux of reactive species and UV radiation towards the target is not controlled. In that case, instant damages like burns, edema, and long-term damages as DNA breaks and mutations can appear. Knowledge about potential risks and damages is of fundamental importance when plasma is in contact with biomolecules, cells, and tissues. For example, the harshness of plasma treatment must not be neglected if plasma is desired to be applied simultaneously with cell therapy (wound healing) or localized topical introduction, gene therapy, etc. The final section of Chapter 2 summarizes fundaments of localized drug delivery through the skin. Besides existing delivery techniques, the potentials of plasmas are discussed in the following text.

## 2.5. TOPICAL AND TRANSDERMAL DRUG DELIVERY

Topical and transdermal drug deliveries offer a non-invasive alternative to the conventional drug delivery methods, oral administration, and injection. Topical and transdermal delivery differ in the depth of drug penetration, as shown in Figure 2.21 (a). The flux of a passively diffusing drug is a function of its concentration. Topical delivery considers the dermal application of creams and ointments and the localized penetration of molecules into the dermis (d≈50-1500 μm). At the same time, a transdermal patch realizes transdermal delivery, and a drug is delivered directly to blood vessels (d≈2 mm). The main advantages of the transdermal application are introducing molecules into circulation without their gastrointestinal

and liver degradation, controlled and sustained delivery, and user-friendly application. However, the stratum corneum acts as a barrier through which only small (M<400 Da), potent and lipophilic molecules can diffuse. This fact sincerely limits transdermal delivery therapeutical application. The diffusion through the epidermis can occur following the transcellular route (delivery through horny cells), follicular route (delivery through hair follicle), and intracellular route (delivery through intracellular space). Diffusion routes are presented in Figure 2.21 (b). However, if not boosted, passive diffusion of these molecules across the skin is very slow, and hours are needed to reach steady-state drug flux[217]. Hence, achieving effective therapeutical drug delivery is difficult without additional enhancement. Delivery facilitation is obtained by drug or skin modulation using liposomes, chemicals, and electrical, mechanical, and ultrasonic approaches, shown in Figure 2.21 (b)[218]. Depending on the targeted therapy, chemical enhancers and liposomes boost the delivery of small lipophilic molecules (higher dosage of small molecules delivered). On the other hand, electrical, mechanical, and ultrasound enhancers enable and boost the delivery of larger molecules (larger dosage of larger molecules delivery). The corresponding techniques improve diffusion kinetics by inducing temporal changes in the skin's chemical and physical environment or applying a driving force that stimulates drug transportation across the stratum corneum[219].
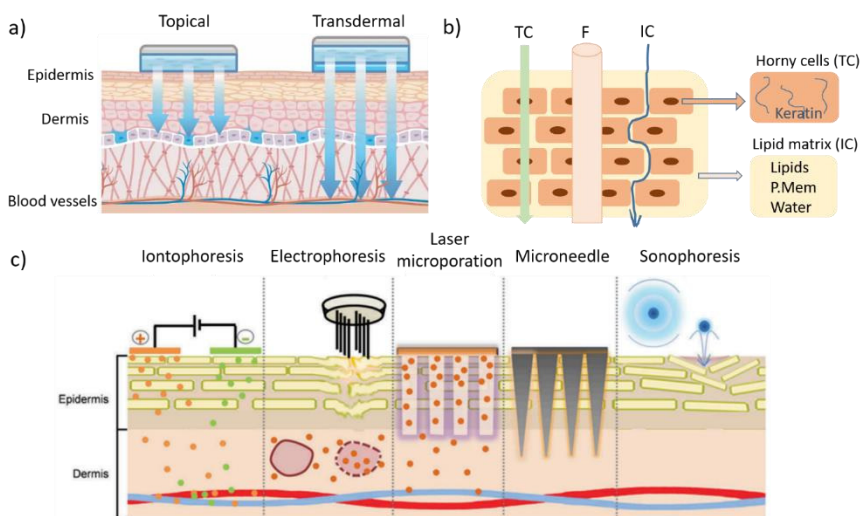


Figure 2.21 a) Visualization of topical and transdermal delivery of drugs through epidermis and dermis to blood vessels, b) Drug diffusion through epidermis: TC-transcellular route, F-follicular route, IC- Intracellular route, c) Advanced techniques for dermal drug delivery[218].

### 2.5.1. CHEMICAL ENHANCERS AND LIPOSOMES

Chemical enhancers alter the chemical and physical properties of the skin to promote drug delivery through the skin. Mechanisms of the activities are organized through disruption of stratum corneum lipid, interaction with intracellular protein, and/or improved partition of drug or solvent into stratum corneum. Ideally, chemical enhancers should not be toxic, irritating, or allergenic. Furthermore, these should have no pharmacological activity, allowing therapeutic agents penetration while preventing loss of endogenous material from the body, with the instant and temporal act. For example, "universal solvent" dimethyl sulphoxides DMSO is one of the first penetration enhancers. However, it creates a problem as only a high concentration is pharmaceutically effective upon which denaturation of proteins, stinging, and burning sensation appear[220]. Generally, chemical enhancers are rarely used due to a lack of drug delivery control and stability, reproducibility, pain, and skin irritation.

Liposomes are drug carrier systems, modulating drug diffusion properties leaving skin intact. In this type of drug delivery, the drug of choice is encapsulated in lipid vesicles (d≈100 nm) prepared from phospholipids which further enhance drug delivery through the stratum corneum. Liposomes may enhance topical drug delivery using: penetration enhancement through the lipid layer, organic solvation of poorly soluble drugs, a local depot for the sustained release of active compounds, e.g., antibiotics, corticosteroids, retinoic acid; limiting membrane ad controlled transdermal release. Moreover, liposomes are shown in different scenarios to enhance and reduce drug delivery flux (lower molecular concentration gradient). Ameliorating effect of liposomes plays a significant role when targeted delivery should be retained only in the epidermis and dermis and avoid blood circulation[221]. Although painless, simple, and cheap improvement of topical drug delivery, both chemicals enhancers and liposomes have relatively low molecular mass limitation M<600 Da, with a penetration depth of about 20 µm. Accordingly, enhancers based on physical manipulation of intracellular space have been developed to enable the delivery of larger molecules in the range kDa-MDa.

### 2.5.2. ELECTRICAL ENHANCERS

Electrical enhancers deliver low-intensity current or electrical voltage to promote drug penetration through the skin. Iontophoresis and electroporation are technologies used to deliver drugs employing an electrical field.

During iontophoresis, a voltage gradient is applied across the skin, and the low-intensity current ($0.5 mA/cm^2$) acts as an ionic drug driving force. In contrast, skin structural changes are a secondary effect. Iontophoresis affects both drug and skin, namely the effect of electro repulsion and migration on the applied drug

followed by electro-permeabilization of skin. In this process, a drug must be ionic or dissolved with ions in solution. Electrodes material and shape should be designed to induce minimal pH change in treated skin; mostly, this is a silver-silver chloride Ag/AgCl system. The silver at the anode oxidizes and reacts with $Cl^-$ to form insoluble ArCl, while AgCl at the cathode releases $Cl^-$ staying with $Ag^+$.

In vivo studies showed 30 μg/cm²·h flux delivery of a chemotherapeutic fluorouracil 5-FU (130 Da) when the drug has been driven by a current of 0.5 mA/cm² for 3 hours across the mice's skins[222]. Interestingly, the drug continued being transported even after cessation of current, implying that drug storage was formed. The efficiency of iontophoresis depends on a few parameters: pH of the solution, concentration and ion competition, molecular size, stability of a drug in ionic solution (insulin). Accordingly, iontophoresis is not applicable in any drug delivery therapy. However, it is often combined with electroporation for the best performances. First, electro-permeabilization of skin is performed, followed by iontophoresis current driving the drug.

Electroporation occurs when a short-high voltage pulse (100-1500 V, 1-100 ms) is applied to disrupt the lipid bilayer and create transient aqueous pathways (cell membrane reorganization)[217]. Besides drug delivery through the skin, electrophoresis is in electro-chemotherapy for the last 20 years[223] and electro-gene transfer (DNA vaccines[224], RNA transfection[225]). Electro-chemotherapy is of great interest for the oncology society and treatment of cutaneous and subcutaneous tumors as the metabolic passage of strong chemotherapeutics is known to cause harsh side effects on patients. The principal mechanism in electro-chemotherapy is the electroporation of tumor cells delivering the drug directly to the intracellular target. In this way, the uptake of a drug inside a tumor is 2-4 times higher (bleomycin and cisplatin)[223]. The efficiency of chemotherapeutics delivery to the tumor utilizing electroporation mirrors in two separate processes. In the first instance, cell membrane permeabilization happens, and the drug is delivered. Secondly, electroporation causes a reduction of blood flow to the tumor up to 80%, which results in drug entrapment in the tumor for a few hours, enhancing its effectiveness. In tumors, blood flow returns to normal after 24 hours, while restoration of normal tissue happens in a few hours. Among listed techniques, electroporation is the most promising as the flux delivery enhancement increases four orders of magnitude for the wide ranges of molecular masses 10 Da-1 MDa with particles neutral, charged, and heavily charged (+,-). Electroporation is very often used as pretreatment of other techniques such as iontophoresis or ultrasound to amplify drug delivery[219]. Although promising alternative drug delivery therapy, electrophoresis shows drawbacks such as depth of penetration, muscle contractions in patients treated repeatedly but also limitations regarding a patient's condition, e.g., patients with cardiac pacemakers and with anticoagulant therapy[223].

### 2.5.3. MECHANICAL ENHANCERS

Microporation or microdermabrasion is performed microneedles of length l=200-1500 µm, and width w= 50-250 µm. In this therapy, micropores are mechanically created in the stratum corneum, and macromolecules' drug delivery is enhanced accordingly. Micro-needling can be an individual process used just to enhance the production of collagen (regenerative medicine and rejuvenation) or coupled with drug injection through the needle. Upon large pores creation in the skin, drug rate diffusion is enhanced without chemical modulation of a drug. Microneedling is a relatively simple, user-friendly therapy with already commercialized devices. The main drawback of this large pore creation is more accessible bacterial decontamination (d=0.5-2 µm); accordingly, this process should be handled with care.

Microporation via laser is another mechanical technique to promote transdermal drug delivery. Er: YAG (2940 nm) and $CO_2$ (10.60 µm) are in the center of attention in drug permeation through skin[226]. In regenerative and rejuvenation medicine, effect of lasers is described by in light absorption in biological tissues. Upon light absorption, tissue is heated, and elimination of epidermal or dermal layers can occur. The mechanisms of drug delivery via lasers are ablation, photo-mechanical and photo-thermal. Laser ablation is explained by selective damage of chromophores in the skin; this ablation decreases the barrier function and promotes drug penetration. The mechanical effect caused by applied light is polarization and consequent enlargement of intracellular space during the passage of laser pulse. Finally, laser energy delivery to the skin can heat tissue and disrupt the lipid layer locally, promoting drug penetration through the skin. In different clinical studies, drugs such as Methyl ALA, 5-FU, and oligopeptides and vitamins are successfully delivered to patients via 300-500 µm size pore-creation after applying laser pulses ranging from 2.5-70 mJ[226]. The main drawbacks of laser-assisted drug delivery are complex and expensive handling, post-skin irritation, burning sensation, and a long recovery period.

### 2.5.4. ULTRASONIC, ULTRASOUND ENHANCERS

Sonophoresis disrupts the stratum corneum by thermal effect, microbubble cavitation, induction of convective transport, and mechanical effects caused by ultrasound[218]. By the passage of ultrasound through a medium (0.1-2W/cm$^2$), energy is partially absorbed, and tissue temperature increases. Moreover, cavitation (creation of cavities) is related to the process of mechanical expansion and contraction upon passage of ultrasound in a liquid medium. Created cavities can be stable and inertial. Stable cavities oscillate around equilibrium radius while inertial cavities correspond to violent growth and collapse of the bubbles followed by shock

waves propagation in the bulk of the liquid or micro-jet distortion if the surface is larger. Shock waves generated by inertial cavitation can cause structural changes in skin and skin-poration of 1-2 μm when low frequency 25 kHz ultrasound is applied for 5 min. Sonophoresis is applied in a wide frequency range and duty cycles (20 kHz-1 MHz, CW-50% DC) to introduce molecules in a wide range of molecular weights as high as 66 kDa[227]. However, the best performances are obtained when used in combination with electrophoresis. The main drawback of sonophoresis is robust setup and re-optimization for each desired body part. In addition, it has to be noted that this therapy has limitations regarding the patients' clinical history. Specifically, it is not recommended in situations concerning heart problems and pacemakers, implants (metal, silicone), pregnancy, thrombophlebitis, impaired sensation, and eye region.

## 2.5.5. PLASMA PROSPECTIVES FOR TOPICAL & TRANSDERMAL DRUG DELIVERY

Transdermal drug delivery (TDD) promotion can be realized through chemical and mechanical enhancers. Both these groups change chemical or physical properties of the drug or skin so that: 1) higher dosage (of pharmaceutical importance) of smaller molecules or 2) larger molecules can be delivered to the targeted skin layer or blood vessels. To this end, plasma shows potential as a unified chemical and physical modulator of drugs or epidermis and dermis. Namely, RONS and radiation can induce chemical changes of both drug and skin. Appropriately, great aspects of cold atmospheric plasma for wound healing assisted by drug introduction are more than imaginable. Furthermore, plasma can be combined with other TDD enhancers as pre/post-treatment to techniques such as electroporation. Nonetheless, plasma-assisted TDD is a new and purely examined aspect in plasma medicine.

Plasma's ability to oxidize biomolecules can play an essential role in the transcellular and intercellular transport of drugs and macromolecules. In other words, species and heat from plasma can disrupt the lipid matrix between cells or cell membrane to transport drugs through the skin.

A novel approach to gene transfection utilizing plasma was introduced almost two decades ago as an alternative to the best performing viral vectors-driven and electroporation gene transfection [228-229]. Transfection of 4.7 kbp plasmid DNA (d≈10-13 nm[230]) was successfully performed on different mammalian cells HeLa and epithelial cells HT-1080, MCF7, SH-SY5Y. Short treatment (1-3 s) by air AC plasma (40 kHz, 90 SLM airflow) was shown to create transient pores on the cell membrane, closing after the plasma treatment. As a result, plasmid DNA was introduced into cells with an efficiency of approximately 20 % and cell mortality of approximately 2% (depends on the cell line and duration of treatment). Moreover, transfection

efficiency was increased with the plasmid DNA concentration in the cell medium and treatment duration[228]. Accordingly, the mechanisms of plasma-cell permeabilization were correlated to electroporation and generation of the localized electrical field. In the study, plasma technology was reported as safer than viral vector-driven gene therapy and with a better transfection efficiency/cell death ratio than electroporation. Moreover, a simple procedure of plasma-based gene transfection, no need for cell detachment, and usage of special reagents encourage further investigation of plasmas as drug delivery agents.

Further, cell permeabilization by He RF APPJ was studied with the drug carrier dextran to study pore size creation[231]. Dextrans are high-molecular-weight polymers available in a wide range of molecular weights 3-500.000 kDa and have a crucial role in drug delivery research as they do not penetrate cells freely[232]. In this study, 6.5 nm pore creation utilizing plasma was confirmed. Furthermore, the cell-permeabilization by plasma was evaluated by plasmid DNA (4 kbp) transfection. Opposite to the plasma gene transfection study[228], the effect of a plasma jet on cell permeabilization was explained by the acting of ROS from plasma. In fact, $^{\bullet}$OH, and $H_2O_2$ were reported to cause lipid membrane peroxidation and the consequent introduction of a drug.

Recently, an *ex vivo* model was developed to study the effect of Ar APPJ (kINPen) on human epidermal lipids: ceramides, free fatty acids, and cholesterol[233]. The oxidation of these lipids after the plasma exposure was minimal. Authors doubt that this might be due to the quenching of RONS by water presence. In addition, low detection of the lipid oxidation products can also be assigned to the limited database of lipid oxidative modifications. Accordingly, further examination of the cold plasma effect on lipid oxidation is required.

Plasma shows extraordinary features of interest in medical sciences. Chapter 2 reviews the positive aspects of CAPs employment in wound healing, considering existing literature. Specifically, plasma stimulates blood coagulation, decontaminates a wound bed, and enhances tissue epithelization. In addition, CAPs offer an excellent possibility to be employed in localized drug delivery. However, this highlight stays on the level of cellular studies and is yet to be evaluated.

## 2.6. CONCLUSIONS

The main aim of Chapter 2 was to give a comprehensive literature review on the medical aspects of CAPs, problems of current wound care technologies, and the evolution of plasma medicine with a focus on wound healing. Simultaneous sterilizing and proliferative effects of CAPs play a critical role in healing stubborn and chronic wounds. During the last two decades, many attempts have been made to advertise medical utilization of atmospheric pressure plasmas. However, some

fundamental and technical issues are still recognized, opposing to higher rate medical commercialization of these devices.

Current problems concern design for the safe operation of plasma jets: EM compatibility, stability under atmospheric conditions, low temperature. Atmospheric pressure plasma jets in Ar gas are probably the best candidates. Ar is economically favorable over other noble gases; however, filamentary instabilities appear in some designs, resulting in non-uniform treatment and higher local temperature. In addition, large-sized chronic wounds require long treatments with existing micro-and millimeter jets; accordingly, upscaling of diffuse jets is challenging but of high importance.

Other unanswered questions are controlled production of RONS in plasmas and absolute treatment control. The flexibility of plasma parameters is tuned by gas composition and flow, deposited power, treatment distance, and treatment time. However, these are not answers for finely-tuned and safe treatment. Moreover, the lack of literature about long-lasting biological side effects is one of the drawbacks of plasma commercialization. Learning how these risks can be diminished is an essential step towards clinical application. The final question concerns the future development of plasma jets and their improved healing effects.

In this thesis, a stable, cold Ar large size ($d_{eff} \approx 15$ mm) APPJ reactor coupled with aerosol has been designed to answer these questions. In the first instance, fundamental research on large jet plasma electrical stability and gas temperature has been performed and presented in Chapter 4. Secondly, a study on plasma-induced chemistry and its manipulation with aerosol droplets is carried out and presented in Chapter 5. Next, the biological potentials and risks of APPJ have been tested on a scale, from biomolecules to cells and tissues. In the risk assessment study, a special focus has been given to the often neglected UV radiation emitted from Ar plasma. Accordingly, risk manipulation and damage control aspects are presented in Chapter 6. Finally, the plasma proliferative effect is studied *in vitro* on fibroblast cells, accordingly presented in last Chapter 7. Moreover, Chapter 7 of this thesis demonstrates the possibility of localized delivery of modeled drugs (*in vitro*) by plasma-aerosol.

# CHAPTER 3: EXPERIMENTAL METHODOLOGY

## 3.1. INTRODUCTION

In this thesis, a newly constructed annular-shape RF 13.56 MHz atmospheric pressure plasma jet in Ar coupled with aerosol has been put on the first tests. The APPJ presented in this thesis is designed for biomedical application in wound healing and topical drug introduction. Evaluation tests consider physical plasma diagnostics, RONS generation in a liquid environment, and finally, biological effects caused by RF jet. The stability of the RF plasma jet and the gas temperature in effluent were studied using electrical and optical plasma diagnostics. In addition, a simple computational model has been built to visualize the interaction of Ar hot gas in the effluent with aerosol droplets. Later, an extensive set of liquid chemistry diagnostics was performed to measure short and long-living RONS generated and deposited into the treated liquid. Finally, biological tests have been implemented to evaluate RF Ar jet coupled with aerosol as potent for medical use and define the safety limits. Biological tests included stability of the extracellular DNA, cell viability and proliferation, mice skin damage, and cell permeabilization after plasma treatment. In the following chapter, the employed techniques in this research are briefly explained.

## 3.2. PLASMA DIAGNOSTICS

The first step in the characterization and optimization of plasma sources is their electrical and optical characterization. The plasma current and voltage are measured with an RF I-V probe. Then, fast ICCD imaging is employed to investigate the dynamics of the plasma jet. Electrical characterization gives insight into plasma operational mode, electron density, electrical field, deposited power, etc. Radiation from plasma provides information about physical and chemical processes in plasma. Accordingly, the analysis of plasma radiation gives an insight into chemical composition, the temperature of electrons and gas in plasma, the concentration of excited and ground species, etc. Hereby, non-invasive optical emission spectroscopy (OES) has been employed to measure the temperature of excited species. Moreover, gas temperature in plasma has been validated by laser scattering techniques, Rayleigh, and Raman scattering spectroscopy. Finally, a simplified computational model is used to visualize Ar heated gas interaction with aerosol.

### 3.2.1. ELECTRICAL CHARACTERIZATION OF APPJ

In this thesis, applied voltage and electrical current between electrodes have been measured with an RF current-voltage (I-V) probe. RF I-V probe has been installed between the matching network and the reactor, and the I-V waveforms are monitored on a broadband oscilloscope.

### 3.2.1.2. ICCD FAST IMAGING

ICCD imaging techniques witness the evolution of the physical mechanisms of a discharge. Namely, fast imaging with the time resolution of Δt≈1 ns offers an excellent opportunity to follow physical phenomena in AC and RF discharges. An ICCD camera consists of an image intensifier coupled with a CCD camera. The intensifier works as a photon-multiplication tube (by a photoelectric effect), see Figure 3.1. First, the incident photo-electron is amplified between electrodes then this intensified photo-electron beam is transmitted onto the phosphorous screen and again converted to photons. Finally, these photons are projected onto CCD by using coupling lenses.
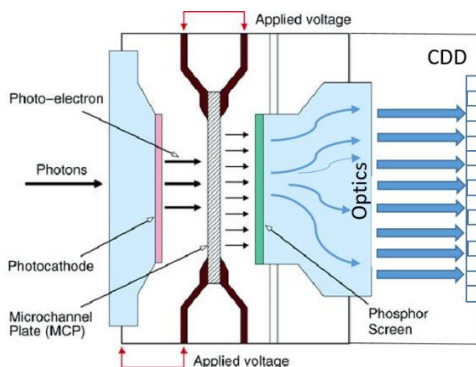


Figure 3.1. ICCD imaging principle and ICCD Hamamatsu camera[234].

The intensifier chamber of the ICCD camera enables the detection of very low signals and amplifies them above the thermal noise level. Moreover, high time resolution, short gate width, high frame rate, and high spatial resolution offer great opportunities to detect transient phenomena in plasmas. ICCD cameras are used to capture the propagation of streamers, plasma bullets, formation and dynamics of plasma sheaths. Optical filters can be mounted in front of an ICCD camera to separate the radiation of species. In addition, an ICCD camera can be coupled with a monochromator, wherein detected light can be spectrally resolved, and the excitation of species in plasma *in situ* can be monitored.

### 3.2.2. OPTICAL CHARACTERIZATION OF APPJ

Plasma is a radiative active medium where the excitation of atomic or molecular feeding gas continuously occurs. Optical characterization of an APPJ considers the collection of plasma radiation, its resolution, and analysis. This thesis employs passive and active optical spectroscopic techniques to characterize RF APPJ in Ar. The passive optical approach assumes light collection from plasma, while active spectroscopy means sampling a plasma jet with a laser.

### 3.2.2.1. OPTICAL EMISSION SPECTROSCOPY (OES)

Optical emission spectroscopy OES is a non-invasive (passive), simple, fast, and low-cost technique employed to estimate the chemical composition of plasma, mechanisms of excitation and provide benchmarking for computational modeling. Based on the plasma radiative models, parameters such as the electron temperature $T_e$, vibrational $T_{vib}$, and rotational temperature $T_{rot}$ of exciting species can be determined. Moreover, concentrations of the plasma species and the electrical field in plasma can be calculated.

Atoms or molecules in plasma are excited due to the inelastic collisions with other atoms, molecules, and electrons. Once excited, the energy balance of an atom/molecule is disturbed, and a particle strives to release the gained energy through collisions or radiation. A lifetime of a specific excited state is directly proportional to the transition probability in a certain system, which is measured as the radiation intensity. Plasma emissivity of the specific transition $\varepsilon_{ji}$ is thus directly proportional to the atoms in excited state $n_j$:

$$\varepsilon_{ji} = n_j \frac{hc}{\lambda_{ji}} A_{ji} \qquad\qquad \text{Eq. 3.1}$$

where h is Planck's constant, c is the speed of light, $\lambda_{ji}$ wavelength of the emitted photon, and $A_{ji}$ Einstein coefficient or probability of the transition j-i. Accordingly, measuring relative and absolute intensities of atomic lines or molecular bands provides information about the density, temperatures of species, and the electrical field in the plasma. In the plasmas generated under atmospheric conditions, OES is mainly employed to estimate gas temperature $T_g$ in plasma based on the rotational temperature $T_{rot}$ of molecules such as $N_2$ or OH. The estimation uses the Boltzmann interpretation of temperature[235] and gives a good approximation for the gas temperature in non-equilibrium plasmas. UV-VIS radiation from plasma is resolved by its wavelengths (frequencies) with a spectrometer. The spectral power of a spectrometer is determined by its resolution. Spectrometers of resolution better than 0.05 nm can resolve the vibrational and rotational bands of molecules. A schematic diagram of Ar atoms energy levels and transitions and a scheme of a typical spectrometer are presented in Figure 3.2.
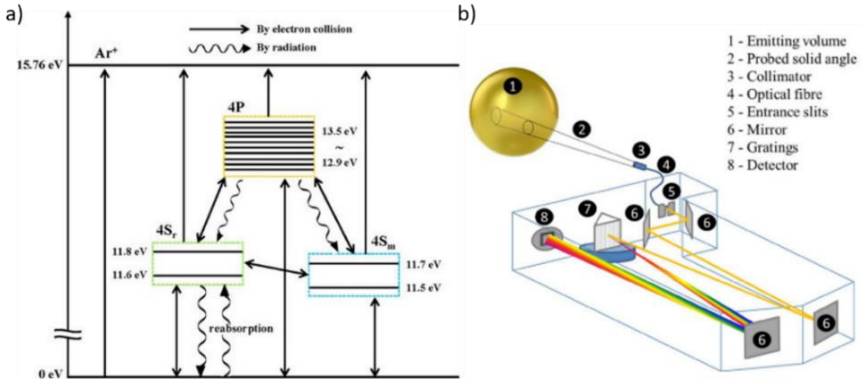
3.2. a) A schematic diagram of energy levels and transitions of Ar atom[236], b) A scheme of a typical spectrometer used in OES[237].

### 3.2.2.2. LASER SCATTERING

Lasers can study the spatial and temporal behavior of discharges in ambient air. A laser beam passing through plasma is scattered on the plasma constituents elastically and inelastically. In this thesis, elastic-Rayleigh and inelastic-Raman scattering is realized. By utilizing laser beam scattering in a plasma jet, the gas temperature in the plasma jet is measured.

Rayleigh scattering spectroscopy is based on the elastic scattering of laser light on heavy particles. The intensity of scattered light depends on the intensity of incident light, type, and density of scatters[238]. The intensity of the scattering signal directly depends on the density of heavy particles-scatterers; therefore, Rayleigh scattering is widely employed for the gas temperature estimation. Two signals in the same condition must be recorded for the temperature measurements. Reference signal $I_0$ corresponds to the intensity of laser scattered in working gas without plasma on the referent temperature $T_0$. The signal from plasma $I_P$ corresponds to the intensity of the laser scattered in plasma with the temperature $T_P$. Accordingly, plasma temperature is calculated as shown in Eq.3.2.

$$T_P = \frac{I_0}{I_P} T_0$$ 

Eq.3.2

A recorded scattered signal is an effective Rayleigh signal originating from different heavy particles present in plasma. In atmospheric pressure plasmas in Ar, species cannot be differentiated as these have similar cross-sections for Rayleigh scattering. Rayleigh scattering can also be used to study the plasma effect on the gas dynamics of plasma actuators.

Raman scattering spectroscopy is a spectroscopic method based on the inelastic scattering of laser light on molecules. Spectra consists of two symmetrical wings called Stokes, and Anti-Stokes components, with lines equally shifted relative to the central incident wavelength. The main problem of rotational Raman spectroscopy is its low intensity and coverage of spectrum with about $10^4$ times higher Rayleigh peak, so good filtration of the elastically scattered light should be done to avoid saturation of the detector and observe the rotational Raman spectra. Since energy levels are characteristics of a specific molecule, spectra are species-dependent, so disadvantages of Rayleigh scattering spectroscopy can be overcome. Rotational Raman spectroscopy enables the calculation of the rotational temperature of ground states of Raman active molecules such as $O_2$ and $N_2$. Simple schematics of laser scattering in plasma, namely, Rayleigh and Raman's scattering, are presented in Figure 3.3.
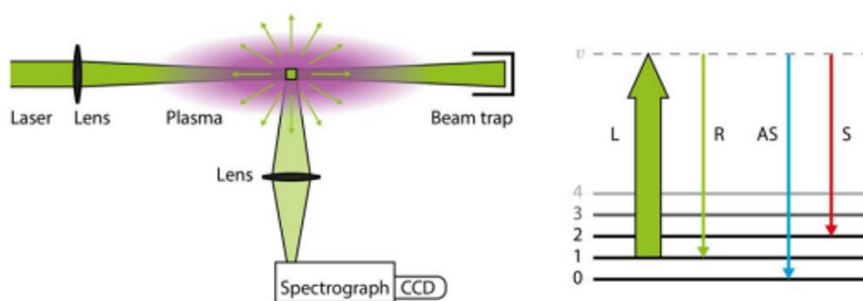


Figure 3.3. Laser scattering in plasma and corresponding transitions due to Rayleigh (R) and Raman scattering (AS, S)[239].

Besides Rayleigh and Raman scattering, Thomson scattering is often employed in plasma diagnostics to study electron concentration; however, this method was not applicable in this thesis.

### 3.2.3. COMPUTATIONAL MODELING OF APPJ GAS DYNAMICS AND INTERACTION WITH WATER AEROSOL DROPLETS

Computational modeling can improve applications of low-temperature plasmas. The aim of simulations is to compare experimental results with a theoretical base and observe phenomena that cannot be easily noticed during the experiments. COMSOL Multiphysics simulation interactive environment offers an excellent opportunity to solve different scientific and engineering problems. With this powerful modeling package, various multi-physics libraries can be linked in order to model physical phenomena as real as possible. For example, gas flow dynamics in plasma can often be approximated with hot gas flow dynamics. In this simplified model, no plasma chemistry is assumed. However, gas mixing due to the interaction

with ambient air, and the interaction with liquid/solid target, can be visualized and numerically calculated. In this thesis, computational fluid dynamics (CFD), transport of chemical species, and particle tracing are coupled and employed to explain the behavior of the Ar plasma jet in ambient air[7, 240]. Modeled region of interest, the edge of the nozzle and substrate in the air box, is constructed in the 2D axial symmetry with a fine element size of the physics-controlled mesh, as shown in Figure 3.4.
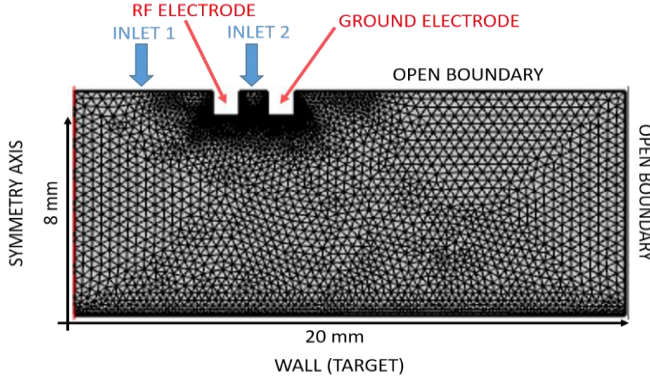


Figure 3.4. The 2D axial symmetry model: The edge of the plasma reactor's nozzle and the area below 8 mm long and 20 mm wide. INLET1 corresponds to the inner (RF electrode) through which aerosol droplets and 1 SLM Ar are introduced; INLET2 corresponds to the plasma feeding Ar gas (3 SLM). Ambient air is defined on open boundaries.

Calculated Reynolds number for reactor geometry and 3 SLM Ar flow indicates the laminar character of the flow. For velocity field calculation, the computational model uses Navier-Stokes equations for the conservation of momentum (Eq.3.3) and the continuity equation for the conservation of mass (Eq.3.4).

$$\rho(\vec{u} \cdot \nabla)\vec{u} = \nabla \cdot \left[ -p\vec{I} \cdot \mu \nabla \vec{u} \right] + \vec{F} \qquad \text{Eq.3.3}$$

$$\rho \nabla \cdot (\vec{u}) = 0 \qquad \text{Eq.3.4}$$

Where $\rho$ is density (SI unit: kg/m³), u is velocity vector (SI unit: m/s), p is pressure (SI unit: Pa), I is an identity matrix, $\mu$ dynamic viscosity (SI unit: Pa·s), F is volume force vector (SI unit: N/m³) and $\nabla$ is a vector differential operator. Fully developed flow has been defined on the two inlets (INLET 1 and INLET 2), defined as follows:

$$\vec{u} \cdot t = 0 \qquad \text{Eq.3.5}$$

$$\left[-p\vec{I} \cdot \mu \nabla \vec{u})\right]\vec{n} = -p_{grad}\vec{n} \qquad\qquad \text{Eq.3.6}$$

where n is the normal boundary pointing out of the domain. The boundary condition, WALL, was defined to describe gas interaction with a solid target (u=0). While OPEN BOUNDARIES are defined to describe boundaries in contact with open-air:

$$\left[-p\vec{I} \cdot \mu \nabla \vec{u})\right]\vec{n} = -f_0\vec{n} \qquad\qquad \text{Eq.3.7}$$

$f_0$ is normal stress, equal to zero in this particular model.

Transport of concentrated species has been included in the model to estimate mass fractions of plasma feeding gas argon in ambient air. The diffusion and convection were considered to be a driving transport mechanism in this model, and the mixture-averaged model was used to estimate the mass fraction of air in Ar:

$$\nabla \cdot \vec{J_i} + \rho(\vec{u} \cdot \nabla)\omega_i = R_i \qquad\qquad \text{Eq.3.8}$$

$$\vec{J_i} = -\left(\rho D_i^m \nabla \omega_i + \rho \omega_i D_i^m \frac{\nabla M_n}{M_n} + D_i^T \frac{\nabla T}{T}\right) \qquad\qquad \text{Eq.3.9}$$

where $j_i$ (SI unit: kg/m$^3$) is a relative mass flux vector component, $\omega_i$ is a mass fraction, $R_i$ is the species expression (SI unit: mol/m$^3$·s ), and $D_i^T$ is the thermal diffusion coefficient (SI unit: kg/m·s). Mixture-averaged diffusion coefficients $D_i^m$ can be derived as shown in Eq.3.10, while the mean molar mass $M_n$ is calculated according to Eq.3.11.

$$D_i^m = \frac{1-\omega_i}{\sum_{k \neq i}\frac{x_k}{D_{ik}}} \qquad\qquad \text{Eq.3.10}$$

$$M_n = \frac{1}{\left(\sum_i \frac{\omega_i}{M_i}\right)} \qquad\qquad \text{Eq.3.11}$$

$D_{ik}$ is an element of the Maxwell-Stefan diffusivity matrix. For argon air mixture, this is $D_{12}=D_{21}=1.48 \cdot 10^{-5}$ m$^2$/s and $M_n$ mean molar masses 0.029 for air and 0.039 kg/mol for argon. Initially, the mass fraction of argon in the region of interest is set to 0, while in the inflow region, air mass fraction was assumed to be zero.

Time-resolved Particle tracing for fluid flow Multiphysics has been coupled with a stationary fluid dynamics model to estimate non-charged particle spatial distribution and its eventual interaction with feeding argon gas. This library is used for modeling microscopic particles in the fluid flow (previously determined velocity

field u), considering that the volume of particles is much smaller than the fluid volume. Time-resolved particle moving is considered to be Newtonian, described with the force vector $F_t$:

$$\frac{d(m_p \vec{v})}{dt} = \overrightarrow{F_T}$$
Eq.3.12

where $m_p$ and $v$ are a particle's mass and velocity vector.

The size-dependent force considers the size of aerosol particles– Stokes drag force $F_D$:

$$\overrightarrow{F_D} = \frac{1}{\tau_P} m_p (\vec{u} - \vec{v})$$
Eq.3.13

$\tau_p$ is determined by particle density $\rho_p$, diameter $d_p$, and particle's dynamic viscosity $\mu$:

$$\tau_P = \frac{\rho_p d_p^2}{18\mu}$$
Eq.3.14

## 3.2. CHEMICAL DIAGNOSTICS

Production of RONS in CAPs is crucial for their utilization in plasma medicine. Plasmas generated under ambient conditions inevitably interact with the surrounding air and create RONS in the effluent. However, upon the interaction of plasmas with biomaterials, RONS are deposited to the liquid that surrounds biomolecules, cells, and tissues. Accordingly, chemical diagnostics of biomedical CAP almost always consider the analysis of treated liquid. The biggest challenge of RONS diagnostics is measuring short-living species (t≈µs). At the same point, these species are crucial for plasma chemistry as being the most reactive.

### 3.2.1. GAS CHEMISTRY DIAGNOSTICS

Gas-phase RONS can be identified and quantified using spectroscopic techniques, namely, OES, absorption spectroscopy AS, and laser-induced fluorescence LIF. Other techniques employed to qualify and quantify RONS in the gas phase are molecular beam mass spectrometry, Schlieren imaging, and electrical probe diagnostics[76]. This thesis focuses on RONS produced and deposited in liquid, gas-phase chemistry has been estimated employing AS Fourier-Transform Infrared FTIR spectroscopy.

### 3.2.1.1. FTIR SPECTROSCOPY

FTIR spectroscopy is a technique used to measure the infrared IR spectrum of functional groups incorporated in a solid, liquid, and gas sample. Principles of IR spectroscopy are based on the absorption of the resonant frequency that corresponds to the vibrational frequency of a functional group, molecule. Particularly, the modulating IR beam (in the wide range of wavelengths) passes through the sample of interest. When the frequency of IR light matches the vibrational frequency of a functional group, absorption of the initial beam occurs. Analysis of the transmitted light reveals the type and the concentration of absorbers. In Figure 3.5. schematics of the FTIR system are presented. In the FTIR system, incident light is split by beam splitter into two perpendicular beams, one passing through the sample and the reference beam, as shown in Figure 3.5. The superposition of these two beams results in an interference pattern. As a result, Fourier transform resolves interferogram, and IR spectra of functional groups can be recognized.
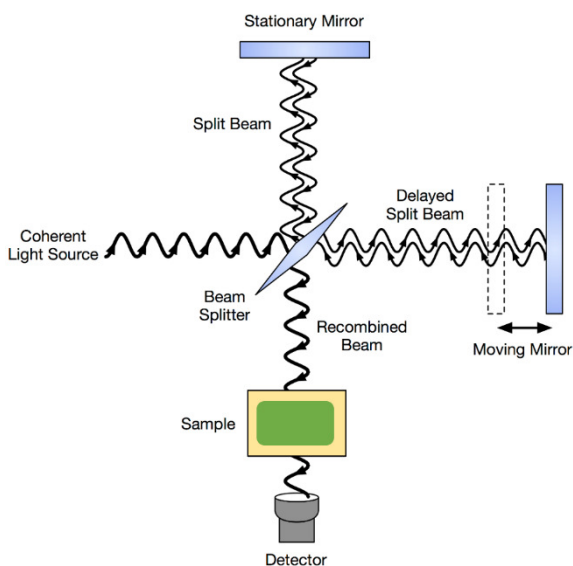
Figure 3.5. Schematics of FTIR system.

### 3.2.2. LIQUID CHEMISTRY DIAGNOSTICS

Since biological samples are inevitably surrounded by liquid (water, phosphate-buffered saline PBS, physiological solution, blood), the detection of RONS generated or deposited in liquid is necessary. Due to the short-living time of some of the RONS, researchers choose to combine a few different diagnostic methods to assure accurate measurement. In this thesis, both long-living and short-living RONS

generated and deposited into the liquid are measured. Therefore, colorimetry, ion chromatography IC, high-pressure liquid chromatography-mass spectrometry HPLC-MS, and electron paramagnetic resonance EPR are combined.

### 3.2.2.1. COLORIMETRY

The colorimetric analysis determines the presence and concentration of a chemical compound in a solution based on the color change in the presence of a specific reagent. For absolute concentration measurements spectrophotometer is used to analyze the fluorescence or absorbance of the colored sample. Many assays are developed in biology, biochemistry, and chemistry to detect and measure the concentration of alive cells, metabolic activity of cells, enzymes, antibodies, hormones, and different chemical compounds. In plasma science, colorimetry is often employed to measure long-living species such as $H_2O_2$ and $NO_2^-/NO_3^-$. For example, the Griess assay is used to measure nitrate and nitrite concentrations. At the same time, titanyl sulfate and resorufin-producing dye assay are used to detect hydrogen peroxide. Limitations of colorimetric assays can be related to a narrow range of sensitivity, a narrow range of pH, and some agents are light sensitive (dichlorofluorescein used in biology). Colorimetry principles are shown in Figure 3.6.
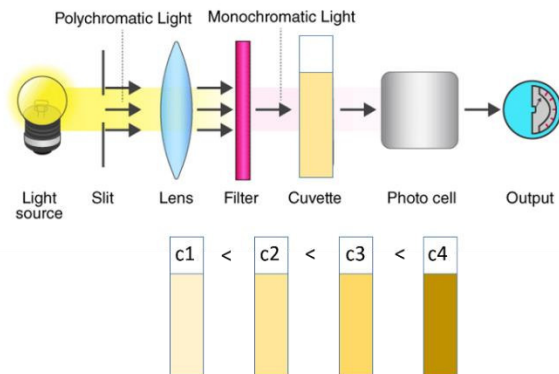


Figure 3.6. Experimental principles of concentration measurement by colorimetry.

### 3.2.2.2. ION CHROMATOGRAPHY

Ion chromatography is used in liquid chemistry to separate ions and polar molecules based on their interaction with the resin (stationary phase) and the eluent (mobile phase). The stationary and mobile phases differ between the anion column, which attracts anion, and the cation column, which attracts cations. Upon electrostatic interaction between an analyte and a resin, ions will move through a column of the ion chromatograph with different speeds due to their different sizes

and charges. Therefore, separation of ions is promoted by the passing of mobile phase eluent through the column, where ions with lower affinity for the resin will move faster through the column and be removed first. On the exit of the column, ions are measured by an electrical conductivity detector, producing a chromatogram – a function of conductivity versus time. In Figure 3.7., a scheme of the ion separation by ion chromatography is presented. The proper column, resin, and elute must be chosen depending on the targeted ions. Ion chromatography is used to measure ions such as nitrate, nitrite, sulfate, chloride in plasma science.
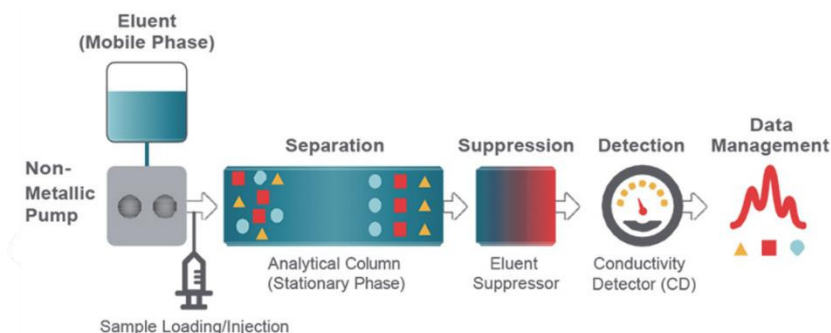


Figure 3.7. Principles of ion chromatography[241].

### 3.2.2.3. MASS SPECTROMETRY (MS)

Mass spectrometry MS is an analytical technique used to measure ions separated based on their mass/charge ratio. This system consists of an ion source or ionizer, mass analyzer, and detector. First, an ionizer ionizes the sample into ions. The ionization technique depends on the phase of the sample (liquid, gas) and the ionization efficiency of the species. Created ions are then transported to the mass analyzer in a magnetic and/or electrical field. Finally, ions are separated by their mass/charge ratio in quadrupole magnetic field regarding their motion in perpendicular, electric and magnetic fields, given by Lorentz law (Eq.3.15):

$$\frac{m}{q} \cdot a = E + v \, X \, B \qquad\qquad\qquad \text{Eq.3.15}$$

Where m and q are respectively mass and charge of the ion, a is acceleration and v velocity of the ion in the electric E and magnetic B field. The separation of ions can be based on the time of flight (TOF-MS). This mass-spectrometer uses an electrical field to accelerate ions and measures the time needed to reach the detector. Quadrupole mass-spectrometers use an oscillating electrical field to selectively control (stabilize, destabilize) the path of ions in the RF field. In this way, only ions with a specific m/q ration can pass through the oscillating field. A similar

principle is used with ion traps MS, where certain ions m/q are trapped in the quadrupole field.

Mass spectrometry is often combined with other techniques, e.g., gas or liquid chromatography coupled with mass spectrometry LC-MS. In this system, ions are separated before being introduced into the ion source. The most common electrospray ionization source is used in LC-MS. The principle of mass separation in a mass spectrometer is presented in Figure 3.8.
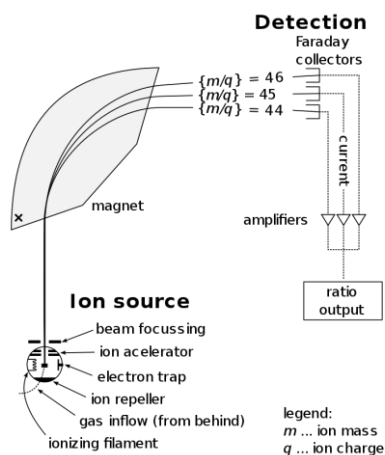


Figure 3.8. Principles of mass spectrometry[242].

### 3.2.2.4. EPR SPECTROSCOPY

EPR or ESR spectroscopy is the most direct technique to measure radicals in liquids[54]. This method uses unpaired electrons to detect radicals. Atoms or molecules with unpaired electrons are introduced in the magnetic field in which the magnetic moment of unpaired electron $m_s$ aligns parallel or antiparallel to the field ($m_s$=+1/2, -1/2). The splitting of energy levels of an electron into the hyperfine structure in a magnetic field is known as the Zeeman effect. The energy difference between two states of unpaired is directly proportional to the magnetic field, thus if the magnetic field B is finely tuned to resonate with the energetic states of electron (spin change), absorption of emission of a photon with energy h·v happens:

$$h \cdot v = \Delta E = g \cdot \mu_B \cdot B \hspace{3cm} \text{Eq.3.16}$$

Where g is g-factor, and $\mu_b$ Bohr magneton is characteristic of electrons. Accordingly, EPR analysis considers sampling the treated liquid and inserting it in a microwave resonator. As the measurement process takes a few minutes, short-living radicals have to be fixed in sampled liquid, and the spin trap realizes this. These

chemical compounds form stable EPR active adducts in interaction with radicals. EPR spectra are specific to the spin-trap adduct, which further allows recognition of radicals responsible for the adduct formation. The spin trap commonly used to trap and measure $^\bullet$OH, H radicals is DMPO. During the trapping, the adducts DMPO-OH and DMPO-H could be differentiated. Another way of measuring radicals is via the spin probe. RONS created in the liquid interact with a spin probe, usually nitroxide, where stable nitroxide radical is formed and measured. Spin probe often used to detect RONS is TEMPONE-H pre-calibrated with TEMP. Basic principles of radicals interaction with spin trap and spin probe and the example of EPR spectra is given in Figure 3.9.
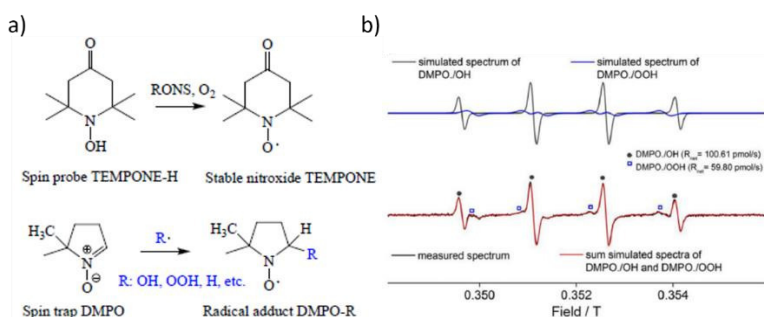


3.9. EPR/ESR spectroscopy principle: a) spin probe interaction with RONS[54], spin trapping of radicals; b) example of EPR spectra[76].

## 3.3. BIOLOGICAL DIAGNOSTICS

In this thesis biological effect of APPJ coupled with aerosol spray has been examined. Accordingly, few analytical techniques were employed to analyze biomaterials. The stability of charged macromolecules upon plasma treatments (proteins, biopolymers DNA, RNA, etc.) can be analyzed by the gel electrophoresis technique. Cell viability assay can determine plasma toxicity or its positive influence on cell growth. Colorimetric assays are used to quantify the viability of treated cells while staining assays can give information about cell morphology upon plasma treatment. Moreover, plasma impact on cell adhesion, migration, differentiation, and proliferation can be seen through early gene expression measured by polymerase chain reactions PCR.

### 3.3.1. AGAROSE GEL ELECTROPHORESIS

Gel electrophoresis is a method for analyzing macromolecules based on their size and charge. This method allows measuring the stability and fragmentation of the macromolecules such as plasmid DNA. The separation based on a molecule's size and charge occurs due to their time travel in the agarose gel in the electrical

field. The process of gel electrophoresis is carried out as follows. Firstly, the macromolecule of interest is extracted and stained. Then, the solution is deposited into perforations formed in the agarose gel. The agarose gel plays the role of a porous matrix through which molecules can move. Next, voltage is applied on the opposite ends of the agarose gel matrix, and negatively charged plasmid DNA and its fragments move through it to reach a positively charged anode. After a certain run time in the electrical field, stained plasmid DNA in the gel matrix is exposed to UV light and imaged. The recognition of fragments is usually done by calibration with macromolecules of the known size and charge and their parallel movement through the same matrix (calibration ladder or marker). Factors that can affect the migration of nucleic acids through the gel are gel concentration (gel-pores size), size of DNA, used voltage, ionic strength of the solvent (buffer), and concentration of the dye used to stain the macromolecule. Schematics of the gel electrophoresis technique are presented in Figure 3.10.
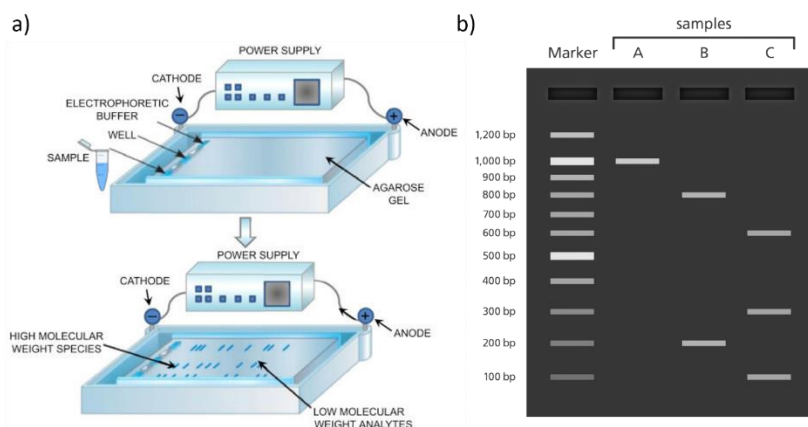


Figure 3.10. Principles of gel electrophoresis: a) experimental method; b) typical image of the gel[243].

Gel electrophoresis is widely used in biochemistry, genetic, and radiative science. For example, stability and fragmentation of the synthetic macromolecule plasmid DNA are broadly studied via gel electrophoresis[244].

### 3.3.2. *IN VITRO* STUDIES

*In vitro* (in glass) studies are experiments performed on isolated cells and seeded in Petri dishes or well plates. Experiments on cells assume the first step evaluation before *in vivo* and the clinical study. In this thesis, experiments on fibroblasts L929 cell lines are performed. The proliferative aspect of plasma has been evaluated employing viability assays. Impact on cell morphology and effectiveness

82

of cell-permeabilization and drug introduction into cells have been imaged by fluorescence microscope.

### 3.3.2.1. COLORIMETRIC ASSAYS: CELL VIABILITY

Cell viability assays often consider colorimetric assays, and the principles follow chemical colorimetric assays. In these types of assays, a reagent is added to the treated cells. Metabolically active-viable cells react with a reagent, resulting in the solution color change. Depending on the assay, fluorescence or absorbance of the solution is measured with a spectrophotometer. One of the most commonly used assays to measure metabolically active cells is one based on MTT (3-(4,5-dimethylthiazol-2-yl)-2,5-diphenyltetrazolium bromide). For example, MTT tetrazolium reduction assay is based on the penetration of positively charged MTT into eukaryotic cells and the interaction with them. Only viable cells with active metabolism will convert yellow-colored MTT to the purple formazan and relative absorbance at 570 nm. The limitation of broadly used MTT assay is its low sensitivity, 200-1000 cells per well.

Presto Blue is a popular assay to measure cell viability with high sensitivity, detecting 20 cells/well (96-well plate) after only 10 minutes of incubation. Presto Blue is a reduction, resazurin-based assay. Upon entering a living cell, non-fluorescent blue-colored resazurin is reduced to the fluorescent red-colored resorufin. Accordingly, resazurin-resorufin conversion is proportional to metabolically active cells. Visualization of the main principles of cell viability assay is given in Figure 3.11 (a).

### 3.3.2.2. FLUORESCENCE MICROSCOPY – CELL MORPHOLOGY

A fluorescence microscope measures fluorescence from cells when these are correctly stained. These microscopes usually have a magnification power of 100X and a 10-100 nm resolution. With fluorescence microscopy morphology of alive and dead cells, expressions of adhering gens and signaling proteins expressed in cells and their differentiation can be imaged. Live/dead, or viability/cytotoxicity kit is popular among researchers. It uses two reagents, calcein-AM (1 mg/mL) and ethidium homodimer-1 (1 mg/mL), interacting with live and dead cells. Upon their interaction, alive cells are stained green ($\lambda$=530 nm), and apoptotic or dead cells are stained red ($\lambda$=600 nm), as shown in Figure 3.11 (b). Incubation of samples with added reagents is very short, approximately 10 minutes. However, before exposure to the fluorescent microscope, samples should be kept in the dark.
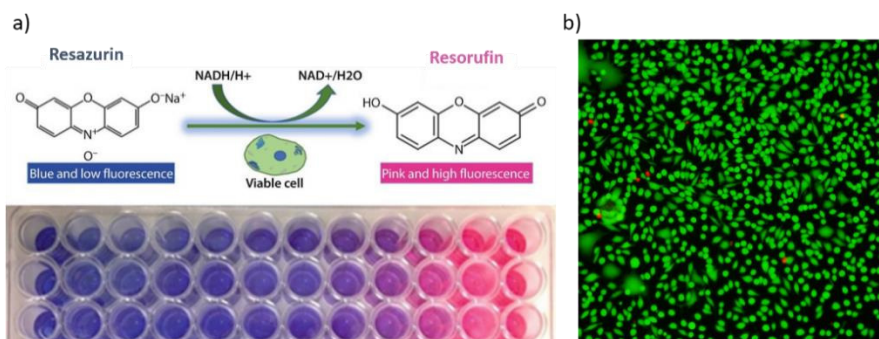
Figure 3.11 a) Cell viability resazurin-based colorimetric assay[245],
b) Live and dead cells staining with calcein (green) and ethidium homodimer (red).

### 3.3.3. POLYMERASE CHAIN REACTION (PCR)

PCR uses short DNA sequences called primers to select the portion of the genome to be amplified. In this laboratory technique, the temperature of a sample is repeatedly raised and lowered (20-40 times) to permit different temperature-dependent reactions–DNA denaturation and enzyme-driven DNA replication. Two main reagents are two (3'-5') DNA primer sequences-short, single-strand DNA fragments. These are complementary sequences to the target DNA and polymerase-enzyme that catalyze DNA synthesis (heat resistant). A polymerase chain reaction occurs as it follows:

1) Denaturation of template DNA: In the first step of PCR analysis, two strands of sampled DNA are thermally (T≈95°C) broken during the denaturation.

2) Annealing: In the next step, the temperature is lowered (50-65°C) so that primers can bind to each single-strand of the complementary sequences of DNA.

3) Synthesizing: Two complementary DNA strands are templates for DNA polymerase. During PCR, DNA generated uses itself as a template for replication resulting in a chain reaction in which the original DNA is exponentially amplified. The schematic of PCR is given in Figure 3.12.
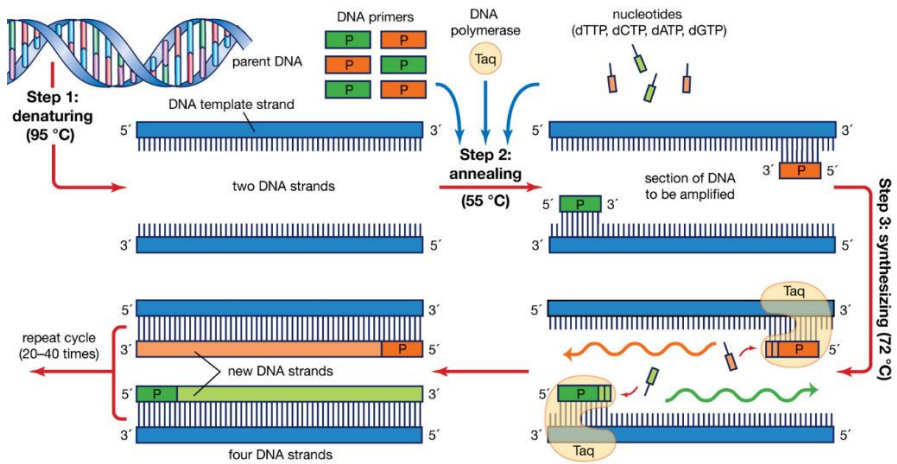
Figure 3.12. Principle of polymerase chain reaction PCR[246].

In this thesis, expressions of 10 different genes are measured via PCR in treated cells. Measured genes that have been chosen play an essential role in wound healing. For example, tendencies of connective tissue fibroblast cells to adhere, migrate, communicate with other cells and matrix, differentiate, and proliferate upon plasma treatment are hereby measured.

# CHAPTER 4: PHYSICAL DIAGNOSTIC OF THE LARGE SIZE ANNULAR SHAPE ATMOSPHERIC PRESSURE PLASMA JET

The results of Chapter 4 are published in the following international journal:

## 4.1. INTRODUCTION

In Chapter 4, a novel design of a non-thermal atmospheric pressure plasma jet has been presented as an alternative to existing cold plasma devices designed for biomedical applications. The RF annular shape plasma reactor is designed and constructed for safe wound healing and topical drug introduction assisted by plasma. Drawbacks of existing devices summarized in Chapter 2 are meant to be overcome by designing a larger, cold, stable plasma jet in Ar with the controlled interaction with aerosol. The first stop on the long journey towards clinical application concerns evaluating this plasma device is safe to be used in contact with human skin. Accordingly, in Chapter 4, diagnostics of an annular shape, RF APPJ in Ar, has been performed and discussed. In the first instance, electrical characterization has been implemented to evaluate discharge stability and uniformity while operating under atmospheric conditions. Secondly, plasma deposited power has been calculated, and the characteristic electric field, electron density, and electron temperature in plasma have been estimated.

Further, safety for human skin has been evaluated by means of gas temperature diagnostics. Special attention has been given to this aspect of plasma as plasma temperature plays a crucial parameter in the end application of cold plasma. To this end, the gas temperature of plasma has been measured utilizing three different methods having different interpretations of gas temperature in plasma. Hereby, presented results are of fundamental and application significance and will witness further on the plasma potentials.

## 4.2. PLASMA DIAGNOSTICS OF AN ANNULAR SHAPE RF APPJ IN ARGON

Low-temperature atmospheric pressure plasmas are a powerful source of chemically active species that are used for different heat-sensitive material processing or even in gas cleaning and synthesis and chemical synthesis, materials surface functionalization, cleaning, etching, coating, etc. [247-248]. Interest in these plasmas as a tool increased over the years due to various applications in plasma medicine. Their capabilities to generate reactive oxygen and nitrogen species (ROS, RNS) enabled them to be used for the inactivation of microorganisms, stimulate cell proliferation, tissue regeneration, or even inactivate cells by initializing apoptosis [249]. During the last years, two basic plasma device principles were established in medical research and application [250-252], known as dielectric barrier discharge (DBD) and atmospheric pressure plasma jet (APPJ). The safe application of plasma requires the generation of stable and reproducible plasma capable of operating at atmospheric conditions.

Furthermore, plasma needs to be cold (under temperatures that could induce skin burnings) and electromagnetic compatible (there should be no EM coupling between source and substrate) [249]. APPJs are especially interesting due to plasma effluent created in surrounding air being suitable for direct treating of substrates [253-254]. The fact that plasma is in direct contact with air makes plasma physics and chemistry of atmospheric pressure jets rather complex and brings several complications into its evaluations with plasma diagnostics.

A set of experimental plasma diagnostics is needed to design a source that meets previous requirements. For this reason, the present chapter focuses on the electrical and temperature characterization of argon atmospheric pressure radio-frequency plasma jet. The plasma source is designed in so-called co-axial electrode geometry, first introduced by Selwyn et al. [255] and Döbele et al. [256]. In contrast to the aforementioned works where discharge in He was studied, an attempt is made in the current study to generate stable plasma in Ar gas. It has to be noted that for industrial and medical applications, cold plasmas in argon have an advantage over expensive He gas. However, the design of the reactor should enable safe and stable operation, which is often not the case for APPJs operating in Ar because of filaments formation [6]. The source developed here is based on works [5, 255, 257], and it is an RF plasma up-scaled in the form of a ring-shaped jet of 14 mm diameter operating in pure Ar under atmospheric conditions. The source is intended to be used for skin treatment to support safe and fast wound healing and plasma/aerosol assisted topical drug introduction. Accordingly, it is constructed so that simultaneous application of water-soluble pharmaceutical compounds and plasma is possible. This chapter aims to study the source operating in Ar and suitable for combination with an aerosol, investigate its electrical characteristics, and compare temperature diagnostic methods applied to accurately measure gas temperature ($T_g$) in the plasma effluent. The most convenient way to measure gas temperature in non-equilibrium plasmas is the rotational optical emission spectroscopy (OES) of molecules. Temperature diagnostics by optical emission spectroscopy is well examined for rotational lines of the same vibrational band for $N_2$ transition $C^3\Pi_u \rightarrow B^3\Pi_g$ (0,2) and OH transition $A^2\Sigma + \rightarrow X^2\Pi_i$ (0,0) [258-259]. This technique is based on the fact that plasma fulfills the rotational-translational equilibrium described by the Maxwell-Boltzmann distribution of populated rotational levels. However, in atmospheric pressure plasmas, due to quenching effects and rovibrational coupling of states, overpopulation of higher rotational levels has been noticed in many cases. This overpopulation is manifested as non-Boltzmann behavior resulting in overestimation $T_g$[235]. The complexity of optical emission spectra analysis for gas temperature determination is coupled with a low spatial resolution of the method due to the line of sight detection. This is also a method disadvantage, and its validity needs to be improved by other techniques such as laser radiation scattering. Better

spatial resolution and higher sensitivity are obtained by the Rayleigh scattering with a scattered signal intensity directly proportional to heavy particle density. The method of laser scattering has been applied to measure gas temperature in high-pressure arc[260] and recently to APPJs[261]. The approximation of the negligible effect of plasma on the gas flow is not always valid.

In many cases, the gas flow is strongly affected by plasma and even is controlled by the discharge as done, e.g., in plasma actuators [262-263]. To confirm the negligible effect of plasma on gas dynamics, the Rayleigh temperature measurements are validated by Raman scattering spectroscopy. The advantage of the Raman scattering technique is based on the inelastic scattering of laser light on molecules in ground states and is independent of gas-phase dynamics [264]. Armed with this data, we were able precisely to determine the set of operational conditions at which the RF jet is safe for treatment of skin, and at the same time re-validate spectroscopy methods capability for gas temperature measurements at conditions of RF APPJ propagating in ambient air.

## 4.3. MATERIALS & METHODS

In the presented chapter, RF plasma jet for treatment large size objects and compatible with direct injection of an aerosol is studied. The main focus is given on the analysis of the RF plasma jet electrical characteristics and operational window for stable operation in diffuse $\alpha$ mode. Combining different methods, we studied the gas temperature Tg as a key parameter for biomedical applications. Chosen methods are applied in a way that they cannot affect the properties of the plasma. They are considered non-invasive, whereas $T_g$ in the plasma afterglow is determined by three different spectroscopic techniques; optical emission spectroscopy (OES), Rayleigh, and Raman scattering spectroscopy. The application of methods is based on the analysis of various physical processes, which allows comparison and validation of diagnostic methods in the high-pressure non-equilibrium discharges.

### 4.3.1. RF PLASMA JET AND ITS ELECTRICAL CHARACTERISATION

The plasma source presented in Figure 4.1 consisted of two coaxial electrodes with an internal one made as a hollow cylinder of $d_{in}$= 10 mm and $d_{out}$= 12 mm. The inner electrode from stainless steel, powered by RF voltage, was surrounded by a grounded external electrode of 14 mm diameter. The grounded outer electrode was made of aluminum. As can be seen from Figure 4.1, the conical reductions were made in the source body for practical reasons of the source installation and its holding. Additionally, conical reduction in the lowest part of the source was made of a size that fits in standard 12-well plate for bio-tests. The plasma source was powered with RF generator CESAR 136 (Advanced Energy Industries),

operating at 13.56 MHz with an L-type matching box. The inter-electrode gap of 1 mm width and 10 mm length was formed by the reduction of the grounded electrode diameter from 20 mm to 14 mm, as shown in Figure 4.1 (b).
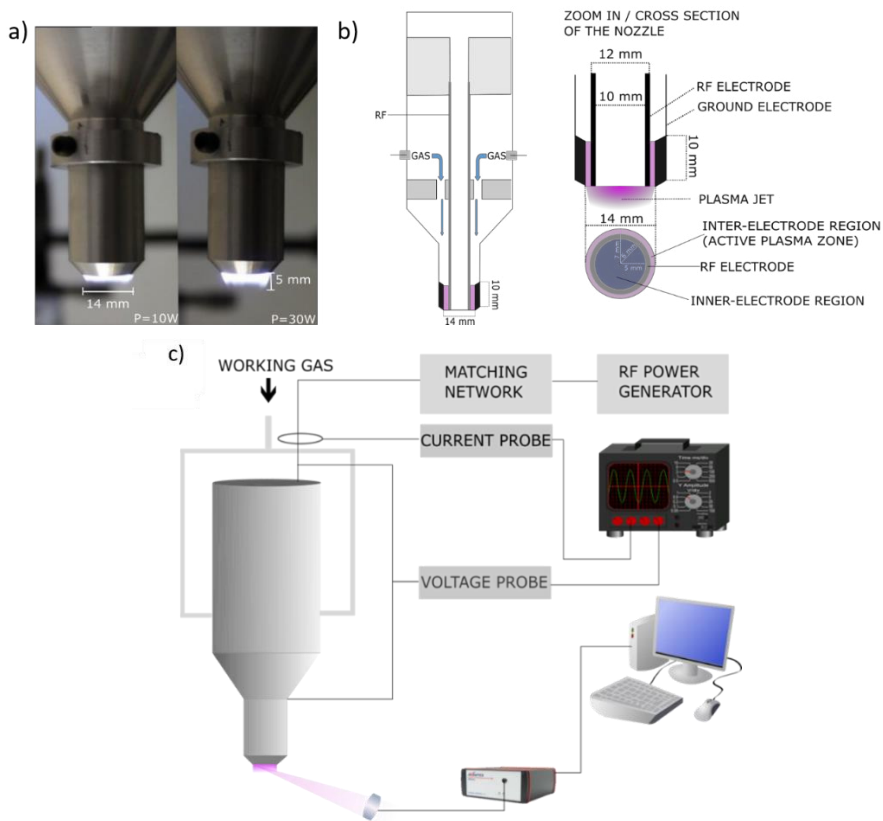


Figure 4.1. a) Visual view of the jet effluent in ambient air indicating the effluent formation of a length of 5 mm for the highest RF power applied at Ar flow of 2 SLM; b) Cross-section of the reactor, enlarged nozzle and its cross-section with indicated regions of interest c) Experimental set-up schematics used for optical and electrical characterization of RF plasma jet.

The gas was fed into the gap through two inlets mounted symmetrically 10 cm above the electrodes that ensure a laminar flow of the gas at the outlet of the source. For purposes of plasma diagnostics $N_2$ (99.999% purity) or dry air (78.999% $N_2$ and 21% $O_2$) were added to the gas mixture in an amount of 0.05-0.2% of argon flow. This small amount of admixing gas ensured that the effect of admixing gas was negligible on the electrical and temperature properties of the discharge. Depending on the jet application, argon flow was chosen of 2, 3, and 4 SLM, corresponding to Reynolds numbers 120, 180, and 240 indicating the laminar gas flow. In the case of

90

gas flow higher than 4 SLM, the discharge cannot be sustained in stable mode. Electric current and voltage of the discharge were measured with an IV probe (Vigilant) and were recorded with an oscilloscope (LeCroy Wavesurfer). Fast imaging with 5 ns resolution in single-shot mode was performed with the use of Hamamatsu ICCD camera with a band-pass filter with a transparency of 10 nm full width at half maxima (FWHM) centered at 750 nm. The camera was placed in front of the plasma jet and focused on the edge of the nozzle. ICCD camera was synchronized with RF generator using a delay generator Stanford Research DG535. The visual image of the plasma effluent, a cross-section of the reactor, and the nozzle with indicated regions of interest and experimental setup for electrical and optical characterization of the plasma jet are presented in Figure 4.1 (a, b).

### 4.3.2. OPTICAL EMISSION SPECTROSCOPY

APPJs are non-equilibrium plasmas with present constituents that have different temperatures (electronic $T_e$, vibrational $T_{vib}$, translational $T_t$, and rotational temperature $T_{rot}$). In the case of non-equilibrium atmospheric plasmas, the rotational temperature can be used as an indicator of the gas translational temperature due to the very high frequency of the collisions leading to establishing of the equilibrium between different rotational states of the colliders. Indeed as the lifetime of the molecules in the excited states is normally significantly larger than the characteristic time between collisions, the rotational temperature of the excited state is usually a good representation of the gas temperature [235, 258]. Accordingly, the establishing of the gas temperature in APPJ involves the determination of the $T_{rot}$ of present molecules. Most atmospheric pressure plasma diagnostics are based on the use of emission from OH(A) states or $N_2$ as an indicator of $T_{rot}$, considering their presence in many atmospheric pressure plasmas. OES temperature measurements are based on relative intensity measurements of rotational lines in the same vibrational band. Following Boltzmann distribution of rotational states, it is possible to directly infer translation temperature from rotational temperature. Here, the measurements of the gas temperature were done from partially rotationally resolved emission from OH radicals transition $A^2\Sigma+\rightarrow X^2\Pi_i$ (0,0) with a maximum of emission around 309 nm [87, 258] as well as from $N_2$ $C^3\Pi_u\rightarrow B^3\Pi_g$ (0,2) band with a maximum at 380 nm. Molecule rotational spectra were recorded using an Avantes spectrometer with a resolution of 0.05 nm with optical fiber directed to the effluent where plasma properties have been measured. Considering axial symmetry of the plasma source, plasma radiation is expected to be collected from the region corresponding to the inter-electrode area, e.g., for an area at 6 to 7 mm across the jet, as shown in Figure 4.1 (b).

OES is an experimentally simple, noninvasive, none expensive well as a fast method for estimation of the plasma parameters. Despite its simplicity, the method provides a line of sight measurement of the $T_g$ and relies on the approximation that

$T_g$ is equivalent to $T_{rot}$ of the excited states. Such an approach can lead to pitfalls and drastic overestimation of the gas temperature[235]. Typically the use of OH (A) emission leads to an overestimation of gas temperature due to non-Boltzmann behavior of the rotational states with high J numbers ($J>12$)[87, 259]. However, using $N_2$ emission can also result in incorrect estimates of the gas temperature, especially in the case of discharges operating in Ar gas[53]. Since this thesis is focused on accurate temperature measurements of the plasma jet, two direct methods of plasma diagnostics by laser scattering were applied to validate OES results. Laser-based spectroscopy methods, namely Rayleigh and Raman scattering spectroscopy, overcome the disadvantages of the OES method. Both methods are well spatially resolved, based on elastic laser scattering on heavy particles (Rayleigh) or inelastic laser scattering (Raman), and capable of direct measurements of translation temperature of ground states.

### 4.3.3. RAYLEIGH SCATTERING LASER SPECTROSCOPY

Rayleigh scattering spectroscopy is an active spectroscopic method based on the elastic scattering of laser light on heavy particles. A detailed description of the Rayleigh scattering theory is found in Ref[238, 265]. The intensity of the scattered light depends on the intensity and polarisation of the incident light and the density of the scatterers' $n_g^i$.

$$I \sim \sum_i \sigma^i n_g^i = \sum_i \sigma^i \frac{p^i}{k_B T_g}$$

Eq.4.1

Where $\sigma^i$ is the Rayleigh scattering cross-section of the light on the i scatterer, and $p^i$ is the partial pressure of the scatterer in the gas mixture. The direct dependence of the scattering signal on the density of heavy particles allows using the method for spatial and temporal resolved gas temperature measurements. For plasma temperature measurements, two signals in the same conditions need to be recorded: reference signal $I_0$ in working gas without plasma at referent temperature $T_0$ and the signal from the plasma $I_p$ with unknown $T_g$. Accordingly, the temperature $T_g$ is calculated as:

$$T_g = \frac{I_0}{I_P} T_0$$

Eq.4.2

A recorded scattered signal originates from different heavy particles present in the discharge. For example, in argon plasma operating in ambient air following species are considered: Ar, $N_2$, and $O_2$. Since these species have a similar

cross-section for Rayleigh scattering, the signal can be considered independent of the mixture and air entrainment in the effluent [266].

For temperature measurements, pulsed Nd: YAG laser (Litron nano-S) was used at a wavelength of 532 nm. The repetition rate was 10 Hz, the energy of the pulse was set to 8 mJ, and the pulse duration was 8 ns. Laser beam had a Gaussian shape with a diameter of 8 mm. At 532 nm light scattered cross-sections on Ar atoms, and the air is $4.5 \cdot 10^{-27}$ and $5.245 \cdot 10^{-27}$ respectively in units $cm^2$/molecule [238]. Fast imaging gated Hamamatsu digital camera with 532 nm filter with FWHM of 10 nm was used to record a scattered signal from the region of interest when plasma was OFF and ON to measure the signal $I_0$ and $I_p$, respectively. The synchronization between the laser pulse and the camera gate unit was achieved using the Stanford Research DG535 delay generator. The experimental setup for Rayleigh scattering spectroscopy is shown in Figure 4.2 (a).
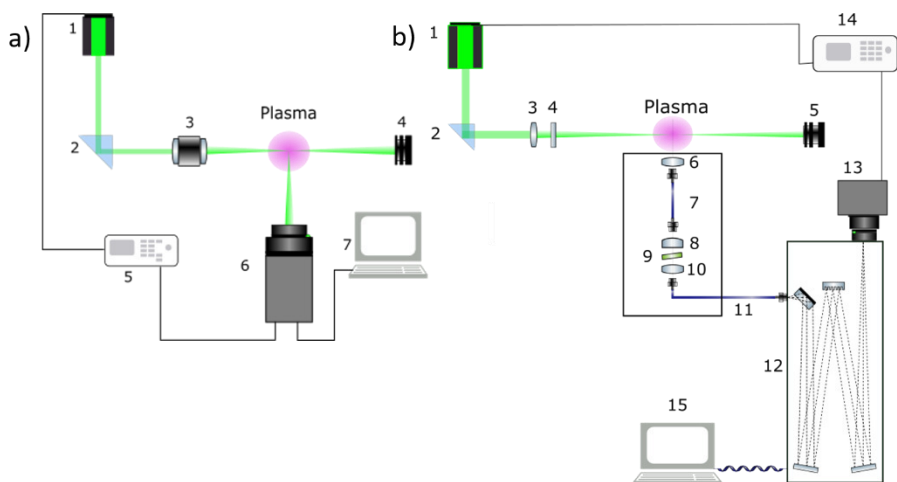


Figure 4.2. Experimental schematic of setup for: a) Rayleigh scattering spectroscopy with 1-Nd:YAG laser at 532 nm, 2-90 degree rotation prism, 3-telescope, 4-beam dump, 5-delay generator, 6-camera, and 7-PC; b) Raman scattering spectroscopy with 1-Nd:YAG laser at 532 nm; 2-prism; 3-lens f=500 mm; 4-polarizer ; 5-beam dump; 6,10 - collecting lens f=50 mm; 7,11- optical fiber with diameter of 300 μm; 8- collimation lens f=30 mm; 9- BNF 532 nm; 12-Monochromator; 13- ICCD camera; 14-delay generator; and 15-PC.

Quartz prism was used to deflect the direction of beam propagation for 90°. After deflection, the beam was reduced using the Edmund Optics telescope of power 10X, so the beam diameter in the plasma region was 0.8 mm. Temperature measurements were done at a distance of 1.5 mm from the nozzle in the effluent

with spatial resolution along with the jet better than 50 μm. The rationality in choice of the distance is dictated by biomedical applications of the developed source as typically treated objects are located at 1.5 mm from the nozzle. Experiments were carried out in ambient air. Only the region of interest, defined later on in the chapter, was used for Rayleigh scattering analysis. To perform a proper comparison of the Rayleigh scattering results with space averaged results of the OES, the Rayleigh signal was averaged over 1 mm region corresponding to the inter-electrode region of elevated temperature. It has to be emphasized that Eq. 4.1 and 4.2 are applicable only in a case when the electrical discharge operation is not affecting the gas flow dynamics. Otherwise observed Rayleigh signal during plasma operation has to be attributed not only to change of the $T_g$ but also to change of $p^i$ in Eq. 4.2 This appears due to the plasma effect on the gas flow. To this end, the applicability of the Rayleigh scattering method applied for $T_g$ measurements were furthermore validated by the Raman laser scattering. Since RF APPJ is designed to be used for medical treatments, all experiments were carried out in conditions as close to a real situation as possible without any shielding gas. As it is known, the Mie scattering can strongly affect both Rayleigh and Raman measurements. To suppress the Mie scattering effect, only an area underneath the nozzle free of Mie scattering was analyzed in laser scattering tests.

### 4.3.4. RAMAN LASER SCATTERING SPECTROSCOPY

Raman scattering spectroscopy is based on inelastic scattering of laser light on molecules, and for this purpose, dry air was added at 0.2 v.% to the feed gas. A spectrum consists of two symmetrical wings called Stokes and Anti-Stokes components with lines shifted relative to central incident wavelength ($\lambda_L$). The challenging task of the rotational Raman spectroscopy is very low scattering signal intensity and partial overlap of the central lines with about $10^4$ times higher Rayleigh signal that requires filtration of the elastically scattered light out to avoid saturation of the detector. Details of the Raman scattering spectroscopy are found in the literature [264, 267-269]. Since Raman rotational spectra are a characteristic of a specific molecule, the spectra are species-dependent, and so the method is free of the disadvantage of Rayleigh scattering spectroscopy. Wavelengths of Anti-Stokes and Stokes component for transitions J-J' are calculated using the expression [270]:

$$\lambda_{J-J'} = \lambda_L + \frac{\lambda_L^2}{hc} B_v((J'^2 + J') - (J^2 + J)) \qquad \text{Eq. 4.3}$$

Here h and c are the Planck constant and the speed of the light, respectively, $B_v$ rotational constant of molecules $N_2$ and $O_2$, J and J' are quantum numbers of initial

and final rotational state. The light intensity of Raman transition J-J' is calculated as [271]:

$$I_{J-J'} = Cn_J \frac{d\sigma_{J-J'}}{d\Omega}$$

Eq. 4.4

Where C is the experimental constant, $n_J$ is the density of molecules in states J, and $d\sigma_{J-J'}/d\Omega$ is a differential cross-section for transition J-J'. The density of molecules in state J is given as [272]:

$$n_j = \frac{n}{Q}(2J + 1)\, g_J\, e^{-\frac{B_v J(J+1)}{kT}}$$

Eq. 4.5

where n is a density of Raman active molecules, the partition function Q as expressed by[273]:

$$Q = (2I + 1)^2 \frac{kT}{2B_v}.$$

Eq. 4.6

The $g_j$ is nuclear spin degeneracy, and I nuclear spin quantum number. Differential cross-section for perpendicularly scattered light is [271]:

$$\frac{d\sigma_{J-J'}}{d\Omega} = \frac{64}{45}\frac{\pi^4}{\varepsilon_0^2} b_{J-J'} \frac{\gamma^2}{\lambda_{J-J'}^4},$$

Eq. 4.7

where the Placzek-Teller coefficient for diatomic molecules is given as:

$$b_{J-J'} = \frac{3(J+J')(J+J'+2)}{8(2J+1)(J+J'+1)}$$

Eq. 4.8

And $\gamma^2$ is the anisotropy of equilibrium polarizability tensor [274]. For diatomic molecules, allowed transitions are $\Delta J=\pm 2$ (positive sign for Stokes and negative sign for anti-Stokes components), whereas all molecular constants for both $N_2$ and $O_2$ are given in Table 4.1.

Table 4.1. Molecular constants of $N_2$ and $O_2$ were used to simulate the Raman signal [269].

| Parameter | $N_2$ | $O_2$ |
|---|---|---|
| $B_v$ (eV) | $2.467 \cdot 10^{-4}$ | $1.783 \cdot 10^{-4}$ |
| $\gamma^2$ ($F^2 m^4$) | $3.95 \cdot 10^{-83}$ | $1.02 \cdot 10^{-82}$ |
| $g_j$ (odd/even) | 3/6 | 1/0 |
| I | 1 | 0 |

Transmission Bragg Notch Filter BNF (OptiGrate) was used as a narrow band filter to reduce the Rayleigh scattered light by at least $10^3$ times. The laser light at 532 nm was focused with a plan-convex lens of f=500 mm 1.5 mm below the nozzle, the same distance as in the case of the Rayleigh scattering spectroscopy. Line integrated scattered signal along of the jet width (radius of 7 mm) was collected with a lens of f=50 mm and focused on the fiber of diameter 300 μm. The other end of the fiber was used as a point light source to perform collimation of the scattered light, which plays a crucial role in the filtration via BNF. Filter BNF-532 is designed in that way that 532 nm light is filtered if the light passes filter by the angle of 6±1°. Recently this method of Raman scattering spectroscopy using volume Bragg grating as a notch filter was applied [264, 275]. After passing the filter, the light is collected with a lens and projected to 0.75 m spectrometer Zolix Omni-λ. The 1200 grooves/mm grating (blazed on 500 nm) is used to resolve the Raman spectrum with a resolution better than 0.11 nm. The spectrum is recorded via the ICCD Andor camera synchronized with the laser. The laser energy was set at 20 mJ, and 16000 laser shots were accumulated for each recording of the Raman scattering spectra. The rotational temperature was calculated by comparing the experimental spectra with simulation using Eq. 4.3-4.8. Fitting parameters were the density of the scatterers, the laser energy, resolution of the spectrometer, and $T_g$. The experimental setup for Raman scattering spectroscopy is exhibited in Figure 4.2 (b). It has to be noted that in comparison with Rayleigh scattering, the method of Raman scattering detection is devoid of the disadvantage of results dependence on gas flow dynamics. The method relies on collective inelastic scattering of light by particles. Correspondingly, the effect of plasma on gas flow is neglected, which makes it a perfect candidate to validate Rayleigh scattering. It has to be noted that Raman scattering-based calculated temperatures are averaged along the laser line passing through the plasma and thus only used for validation of the Rayleigh results, which also are averaged over the same region of interest. Taking into account the region of averaging of the Raman signal, direct comparison of the gas temperature measured by OES method and Raman scattering is not feasible and not considered in the current study.

## 4.4. RESULTS & DISCUSSIONS

### 4.4.1. ELECTRICAL CHARACTERISATION OF RF PLASMA JET

The electrical discharge was sustained by the application of RF forward power in the developed APPJ at a level below 30 W. At RF input power above 30 W, the discharge was transferred to γ-mode. This manifests as highly localized discharge, which is sustained primarily by a secondary emission of the electrons from hot contact spot-localized to one of the electrodes. Through this thesis, only α-mode

uniform discharge was studied. The discharge is formed at the lowest power just on the edge of the electrodes. The increase of the power to 30 W leads to expansion of the discharge, propagating over the whole length of the electrode, which is 10 mm long, as indicated in Figure 4.1. A similar expansion of the RF plasma has also been noticed in our previous work on co-planar RF plasmas [276].

Further increase of the power leads to the discharge transformation to γ-mode. In α-mode at the power of 30 W, the discharge fills the whole area between the electrodes. The V-I characteristics of the discharge are presented in Figure 4.3 (a). Power dissipation in the discharge when plasma is off and on is shown in Figure 4.3 (b) based on the methodology described in Ref[51]. According to measurements, the plasma source stable operating range is from 10 W (minimum RF power to sustain plasma) to 30 W (γ-mode transition). In the case of adding nitrogen/air to the gas flow, due to optical emission spectroscopy measurements, the α-mode is still in the range of power from 13 W to 30 W. Length of the visible effluent depends on power (see Figure 4.1.), it is 2.5 - 5 mm, corresponding to a minimum and maximum power. An example of the discharge appearance in α- and γ-mode is presented in onsets in Figure 4.3.
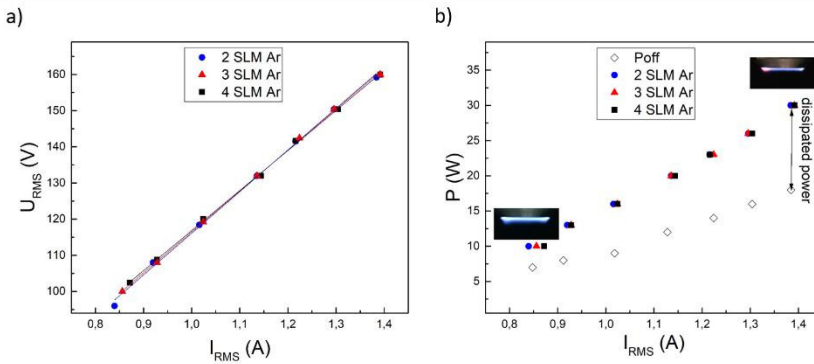


Figure 4.3. Electrical characterization of RF jet (a). I-V characteristics of the RF plasma jet operating in α-mode recorded with increasing the RF forward power from 10 to 30 W; (b) Forwarded power with gas flow, and forward power without gas flow (P$_{OFF}$) as a function of the current, with a visual representation of the discharge in α- and γ-mode.

It is interesting to note that an increase in the gas flow rate from 2 to 4 SLM has very little impact on the electrical characteristics of the plasma source. However, at a flow rate above 4 SLM, the discharge sustaining in a stable regime is not possible, and plasma is randomly completely extinguished or transferred to γ-mode. There is a small increase of V$_{RMS}$ value for the lowest power range from 96 to 102 V with an increase in the flow rate from 2 to 4 SLM. However, the current of the jet in α-mode

is independent of the gas flow, with current density in the range of 0.2-0.37 A/cm$^2$ for all working powers. Considering the almost linear V-I characteristic of the discharge with a positive slope of 110 V/A, it can be expected that the plasma operates in the glow–like mode sustained by Ohmic electrons heating[3]. This indicates that the main ionization processes are driven by fast electrons accelerated in the oscillating RF field [277]. Sustained RF glow discharge is characterized by a constant V/I phase difference of about 88° that implies the stability of α-mode and discharge capacitive character. The reason for a slight deviation of -2° from the pure capacitive coupling is due to decreasing capacitive contribution and increase of the resistive one with an increase of the power similar to observations of others [278-279]. An observation of stable α-mode formation in argon plasma has also been found for plasma jet described in [280]. The evolution of plasma constituents during an RF cycle was experimentally studied using fast imaging of the discharge emission presented in Figure 4.4. For this purpose, the fast imaging camera was used with a maximum transparent filter at 750 nm, which corresponds to Ar I transition $4p(^2P^0_{1/2}) \rightarrow 4s(^2p^0_{1/2})$. This is an excited state with a radiative lifetime of $\tau \approx 22$ ns [281], reduced to less than 5 ns due to quenching at high pressures. This intensive line is therefore suitable for RF imaging because the lifetime of atoms in excited levels is shorter than the duration of the RF cycle of 73 ns, and so the emission of Ar I should be directly related to the electron kinetics in the discharge. Emission of OH $A^2\Sigma+ \rightarrow X^2\Pi_i$ transition was also recorded, but no temporal evolution within RF cycle is noticed due to longer radiative lifetime of OH radicals $\tau \approx 0.6$-0.7 μs. Imaging of APPJ, presented in Figure 4.4 (a, b) was performed for five different time points during the RF cycle corresponding to applied voltage: $V_{RF} = 0$ ($T_1 = 0$ ns), $V_{RF} = +V_0$ ($T_2$ =18,44 ns) , $V_{RF} = 0$ ($T_3 = 36,87$ ns), $V_{RF} = -V_0$ ($T_4 = 55,3$ ns) and $V_{RF} = 0$ ($T_5 = 73,74$ ns). The imaged bulk plasma was uniform in all the time frames, whereas the formed sheath exhibited a strong emission near the RF electrode. The sheath width is calculated from the image corresponding to the highest argon emission near the RF electrode when its voltage reaches a negative amplitude, as indicated in Figure 4.4 (b). The sheath is here considered to be a width of the illuminating zone near the electrode where Ar I emission drops by 90% from the peak intensity $I_{peak}$. Moreover, the RF imaging indicates a higher intensity of Ar I lines in the electrode area (sheaths) with respect to the bulk plasma (Figure 4.4). The length of the developed sheath, corresponding to time 55.4 ns, is estimated to be around 200 μm, which is well in agreement with the results of particle-in-cell (PIC) simulation of RF plasmas operating at high current [282].
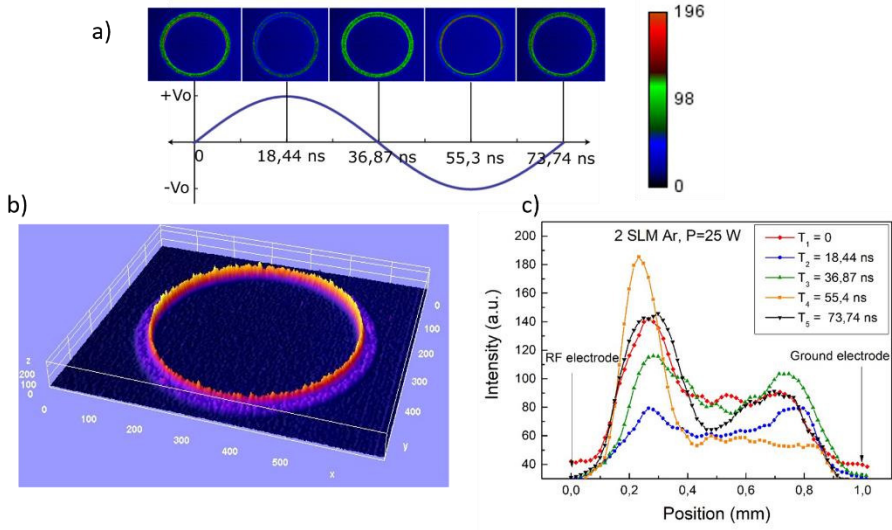
Figure 4.4. Time-resolved imaging of the RF APPJ with 5 ns exposure time in single-shot mode: a) The images are recorded through a band-pass filter of 10 nm FWHM centered at 750 nm corresponding to Ar I emission. Time of the records is indicated in the offsets; b) 3D map of intensity for a case of 55.4 ns time frame with an indication of the sheath formed near powered electrode; c) intensity distribution in the inter-electrode gap and near RF powered and ground electrodes.

It should be noticed that in contrast to symmetrical sheath formation observed in PIC simulation, the sheath in APPJ is strongly asymmetrical with a barely visible sheath formed at the ground electrode (virtual cathode at 18.4 ns) and very strong sheath at RF powered electrode (virtual cathode at 55.4 ns). Stronger light emission on the RF electrode is also noticed in our earlier work with RF planar discharge [7]. This effect is partially explained because the APPJ electrodes system is asymmetrical with a 5:6 ratio of electrode areas. However, the area ratio of the electrodes cannot fully explain the observed strong asymmetry of the discharge. Correspondingly other processes, unknown at the moment, can have an important contribution to the asymmetry, and additional research is required, which is out of the scope of this thesis. The presence of the sheath in RF plasma can have a strong impact on the stabilization of the discharge and generation of uniform α-mode plasma without filaments or transition to γ-mode.

Opposite to atmospheric pressure DBDs sustained in the kHz frequency range in Ar, which usually operates in filamentary mode, our APPJ is a uniform-stable plasma operating in diffuse α-mode. This is an advantage of the source, especially in biomedical treatments. Operation of the discharge in diffuse α-mode requires a mechanism to stabilize the discharge and suppress heating instabilities which

otherwise would result in the transition of the discharge to γ-mode of operation. Sustaining of the plasma in α-mode is analyzed based on the balance between processes of dissociation/recombination and diffusion of ions $Ar_2^+$ and electrons in the bulk of the discharge[67]. When recombination processes are dominant, the steady α- mode switches to filamentary γ-mode sustained by the secondary electron emission from the electrodes. If diffusion processes are dominated over recombination, then one can conclude that the heating dissipation is suppressed and uniform α-mode is realized. In self-sustained low ionization degree discharges, as one studied here, a major loss of the input RF power P dissipated in the discharge of volume V is because of elastic processes. Correspondingly, the electron density in bulk is estimated using power balance for free electrons in the plasma, assuming only elastic collisions as [283]:

$$\frac{P}{V} = n_e \cdot n_{Ar} \cdot \frac{3m_e}{m_{Ar}} \cdot k_{el} \cdot T_e$$
Eq. 4.9

In Eq. 4.9, the term responsible for heating of the gas is neglected as $T_g$ is much lower in comparison with $T_e$. Parameters n, m, T are the density, mass, and temperatures of species, respectively. Coefficient $k_{el}$ stands for the rate coefficient of elastic collisions between electron and argon atoms obtained from BOLSIG+ for characteristic electric fields E/N 1, 5, 10, 50, and 100 Td (1Td=$10^{-21}$ Vm$^2$ ). Maximum energy density is considered as 30 MW/m$^3$ based on the results presented in Figure 4.3 (b). On the other hand, the self-sustaining operation of the discharge should fulfill the ionization/ recombination balance[274]:

$$10^{-14} n_e n_{Ar} e^{-\frac{E_i}{kT_e}} = n_+ n_e k_d$$
Eq. 4.10

Here $k_d$ stands for dissociative recombination rate and is typical of $10^{-14}$ m$^3$s$^{-1}$[284]. Considering the condition of quasi-neutrality, Eq.4.10 is simplified to the ionization balance equation:

$$n_e = n_{Ar} e^{-\frac{E_i}{kT_e}}$$
Eq. 4.11

Where $E_i$ is the first ionization energy of $Ar_2$ as $Ar_2^+$ is a dominant molecular ion APPJ at atmospheric pressure. The dependence of electron density on $T_e$ for the range of characteristic values for atmospheric pressure plasmas (few eV) is presented in Figure 4.5, indicating the steady-state value for $n_e$=3.2·$10^{18}$ m$^{-3}$ and $T_e$=1 eV for the experimental condition of 5 Td. This very rough estimation of plasma

parameters is in good agreement with previous works of our group based on COMSOL simulation and continuum radiation calculations [7, 285].
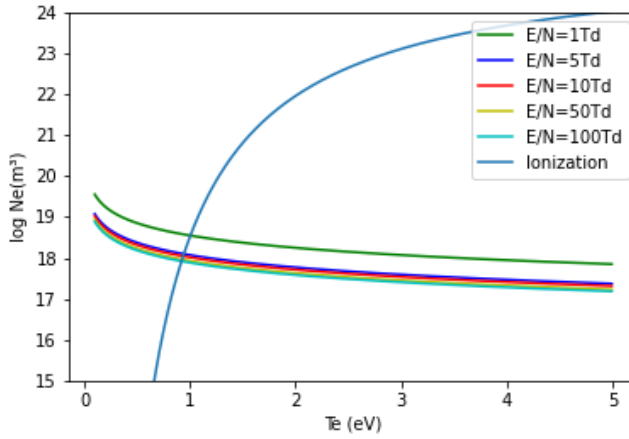


Figure 4.5. Electron density and temperature estimation plots from power and ionization/recombination balance. Curves for reduced E/N in the range 1-100 Td represents power balance due to elastic collisions.

The power and ionization/recombination balance results can be used to estimate characteristic times for both diffusion and recombination of charged particles. Obviously, in the high-pressure plasmas, the dominant processes of charge particle loss are dissociative recombination of electrons with $Ar_2^+$ ions and diffusion of particles from the bulk[286]. Dissociative recombination is described as:

$$Ar_2^+ + e^- \leftrightarrow Ar + Ar \qquad\qquad \text{Eq. 4.12}$$

has a characteristic time given as:

$$\tau_{diss} = \frac{1}{n_e \cdot k_{e-i}} \qquad\qquad \text{Eq. 4.13}$$

Where $k_{e-i}$ is a coefficient describing the electron-ion recombination, on the other hand, characteristic time for argon cluster ions to leave plasma due to diffusion can be expressed as:

$$\tau_{diff} = \left(\frac{l}{2.4}\right)^2 \cdot \frac{e}{\mu k T_e} \qquad\qquad \text{Eq. 4.14}$$

Where l is characteristic diffusion length and $\mu$ is $Ar_2^+$ mobility in argon[3]. With the use of $n_e$ and Te, calculations are estimated from Figure 4.10. indicate that

$\tau_{diss}$ is close to 4.5 µs. This is about 30-times faster than diffusion processes with $\tau_{diff}$ ≈140 µs. Such a large difference between $\tau_{diff}$ and $\tau_{diss}$ should lead to thermal instabilities and transfer of the RF discharge to γ-mode. This contradicts experimental results and leads to the conclusion that another process of RF discharge stabilization should exist [287]. Both estimations of $\tau_{diff}$ and $\tau_{diss}$ are made for the bulk plasma.

In contrast to DBDs or pulsed plasmas operating at high pressure, the sheath regions near the electrodes are formed in the RF APPJ, as presented in Figure 4.4. The sheath plays an essential role in discharge sustaining and can stabilize α-mode regime. High electrical potential in the sheath repeals fast electrons directing them to the bulk. PIC simulation of Lieberman *et al.* [282] has demonstrated electron density decrease in the sheath. Sheath behavior even at high pressure is similar to Child-Langmuir sheath in low pressure capacitive coupled RF discharges. Reduction of $n_e$ affects processes of dissociation/recombination lead to an increase of $\tau_{diss}$.

On the other hand, PIC simulation exhibits a high reduced field E/N in sheaths estimated to be 1 MV/m[282]. This increases ion mobility which causes a decrease of $\tau_{diff}$ and leads to discharge stabilization in the sheath, where condition $\tau_{diff} \sim \tau_{diss}$ is reached. The sheath effect in stabilizing the RF APPJ is important for sustaining the discharge in a uniform mode that is a key issue for the generation of low-temperature active media for the biomedical application of the plasmas.

## 4.4.2. TEMPERATURE CHARACTERISATION BY OES METHOD

The RF source presented in this study was developed for trans-epidermal drug delivery. In respect to its targeted application, the source requires to fulfill; (i) a safe operation without initiating thermal damage to the tissue in contact with the plasma, (ii) the compatibility with aerosol injection, and (iii) the ability of a large area treatment. The gas temperature in plasma is considered a key parameter for its application. To this end, a well-known technique based on OES gas temperature measurements was applied. The method is based on rotational temperature calculations of OH $A^2\Sigma+ \rightarrow X^2\Pi_i$ (0,0) and $N_2$ $C^3\Pi_u \rightarrow B^3\Pi_g$ (0,2) molecules from the partially resolved rot-vibrational bands. In the first case, $T_g$ was measured in the power range of 10 W-30 W for Ar flow of 2, 3, and 4 SLM from OH partially rotationally resolved band. The LIFBASE simulation and its comparison of the measured spectra are presented in Figure 4.5 (a). In the second case, the $N_2$ transition $C^3\Pi_u \rightarrow B^3\Pi_g$ (0,2) was used for rotational molecular temperature calculation based on MassiveOES software [288] where only linear part of the Boltzmann plot has been taken into account, similar as in Ref [87]. The Boltzmann plot for J numbers in the range of 4-20 was used to analyze $N_2$ radiation and obtained from the Boltzmann plot slope temperature is presented in Figure 4.6 (b).
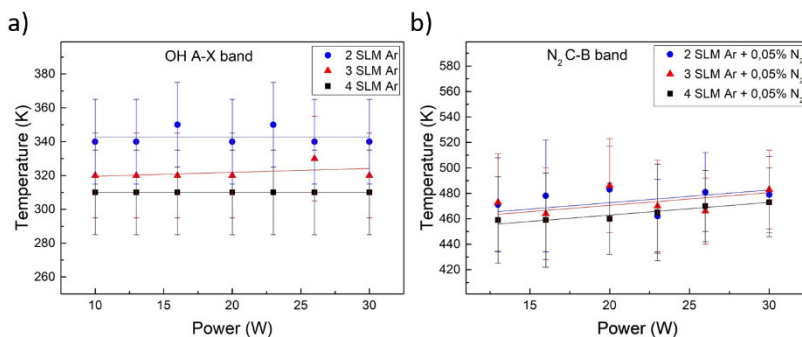
Figure 4.6. The gas temperature in plasma calculated via (a) LIFBASE software fitting of OH (A-X) band for different gas flow and RF forward power; (b) calculated via Boltzmann plot of $N_2$ transition (C-B) with the use of MassiveOES [288].

The OH rotational temperature of the effluent of Ar plasma which propagates into the ambient air was estimated to be in a range of 310 - 350 K, at a distance of 1.5 mm from the nozzle. Interestingly, the RF power increase had a negligible impact on the rotational temperature of OH(A) radicals, which is in agreement with previous results from our group [276]. This is explained by the increase of RF power in $\alpha$-mode, which results in plasma expansion between the electrodes along with the gas flow and the effluent that leads to almost constant power density W/cm$^3$ [276]. OES measurements presented in Figure 4.6 (a,b) are line-of-sight integrated across the effluent, correspondingly providing the spatially averaged value of $T_g$. In the case of $N_2$ admixing up to 0.2%, no change in visual appearance or V-I characteristic of the discharge was detected. However, the rotational temperature estimated from the linear slope of the Boltzmann plot indicates $T_g$ in the range of 450-480 K. It has to be noted that $N_2$ distribution shows Boltzmann behavior for rotational levels up to J=20 with the temperature indicated in Figure 4. 5(b). Whereas fitting the vibrational band 0-2 with J numbers up to 32 leads to an unrealistically high rotational temperature of 580-680 K. Correspondingly, only the range of rotational numbers J=4-20 with linear Boltzmann slope was analyzed. The results of Figure 4.5 indicate a discrepancy between $T_g$ obtained from OH(A-X) emission and $N_2$(C-B). Moreover, there was almost no tendency in $T_g$ as a function of gas flow in the case of use $N_2$ band emission. In several studies [53, 235] it was indicated that often encountered issue in non-equilibrium plasmas is the energy transfer from argon metastable atoms in Ar($^3P_2$) and Ar($^3P_0$) states to $N_2$(X) producing electronically excited $N_2$(C) molecules, which are not in equilibrium with the rest of the molecules. As this reaction is a near resonance process, it is often a dominant production mechanism of $N_2$ excited states in Ar discharges with small additions of $N_2$ or air [235]. The effect of Ar metastable energy transfer to $N_2$ species is noticeable by introducing

N$_2$ to the feeding gas, as shown in Figure 4.7. With the addition of N$_2$ to the working gas, there is an increase in the intensity of nitrogen lines (second positive system) and reduction of argon lines from transition 4p-4s. This behavior can be related to an efficient energy transfer from argon excited states to nitrogen species inducing overpopulation of N$_2$ (C) level and non-Boltzmann distribution.
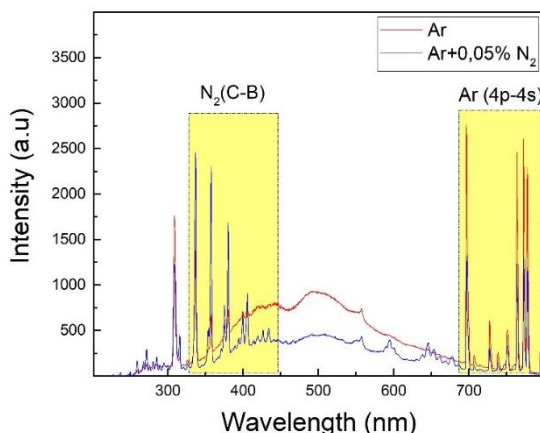


Figure 4.7. Example of RF APPJ spectra in pure argon (red) and argon in mixture with 0.05% of nitrogen (blue).

This fact can lead to the overestimation of gas temperature from the N$_2$ band. This could then be a reason for the discrepancy of results in our study. On the other hand, the use of OH(A-X) emission as a proper indicator of T$_g$ is also very questionable [87, 289] and has to be revalidated based on direct methods of neutrals translation temperature detection. To this end, the two other methods based on laser scattering detection are applied. However, they cannot be applied in a case when an aerosol spray is injected into the plasma. For this reason, we used them only to validate the OES results and unrevealing insights into the gas heating inside the RF plasma jet.

## 4.4.3. TEMPERATURE CHARACTERISATION BY THE LASER SCATTERING

The Rayleigh scattering allows direct measurement of gas density proportional to T$_g$ through Eq. 4.2 with a high spatial and temporal resolution. A typical example of the Rayleigh scattering image taken with the ICCD camera in pure Ar plasma of 10 W at a 1.5 mm distance from the nozzle is given in Figure 4.7 (a). Only part of the signal free of Mie scattering, indicated by dotted area ROI in Figure 4.8 (a), was analyzed. No laser synchronization with RF voltage was applied as no

temporary dependence of $T_g$ is expected because the characteristic time of the RF signal (T≈74 ns) is too short for gas heating to follow the RF cycle. Spatially resolved gas temperatures in Ar and Ar+N$_2$ plasma effluent are presented in Figure 4.8 (b,c) for a case of RF power of 20 and 30 W in Ar and Ar+N$_2$ mixtures, respectively. Based on the spatially resolved profile of $T_g$, it can be assumed that gas temperature is constant along the jet radial cross-section at a power below 20 W. Higher $T_g$ in a position that corresponds to space between the electrodes was noted at higher power, as indicated in Figure 4.8 (b). The slight asymmetry of the temperature (see Figure 4.8 (b, c)) is explained by the very small misalignment of the electrodes, which results in the shorter gap and correspondingly more intensive discharge in that location. This effect was also observed during fast imaging (see Figure 4.4. time frame 55.4 ns bottom part of the inter-electrode gap).
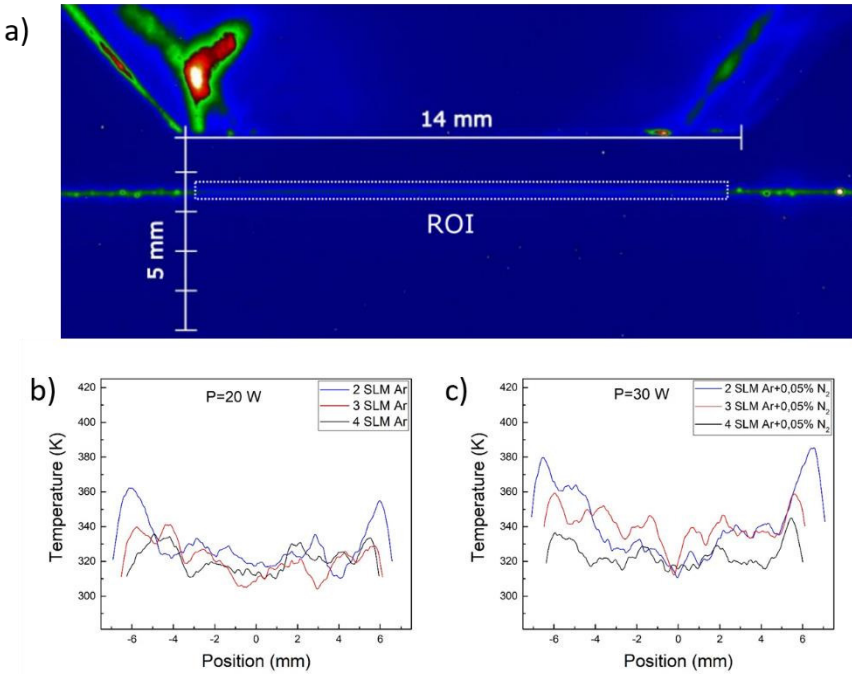


Figure 4.8. Rayleigh scattering of the laser light of 532 nm at a 1.5 mm distance from the nozzle. a) The image was taken with an ICCD camera of the laser beam passing through Ar plasma for P=10W. The dotted area represents the region free of Mie scattering and only this region was analyzed for the temperature estimations; b) Spatially resolved temperature measurements via Rayleigh scattering (Ar gas) at plasma power of 20 W; c) Spatially resolved temperature measurements via Rayleigh scattering (Ar+N$_2$ gas) at plasma power of 30 W.

The Rayleigh radial resolved signal presented in Figure 4.8 (b) was averaged along the regions corresponding to plasma effluent formed in the inter-electrode area, e.g., a region of 1 mm width located at the position from 6 to 7 mm for 2 SLM flow. It has to be emphasized that the position of the maximum of the gas temperature depends on the gas flow, and a shift towards the inner-electrode region was observed with an increase of the flow, as shown in Figure 4.8. Due to the shift of the high-temperature region, the area of the Rayleigh signal averaging has been adjusted depending on the flow, keeping the width of the averaging at 1 mm. Described methodology of the Rayleigh signal averaging was applied to determine space averaged $T_g$, which can be directly compared with OES measurements presented in Section 4.3.2. Obtained results for both Ar and Ar+N$_2$ mixtures as a function of gas flow rate and forward RF power are exhibited in Figure 4.9. Temperature profile analysis shows uniform temperature distribution at the lowest power of 10 W. With increasing input power, a higher temperature region corresponding to the effluent region starts to be noticeable, as shown in Figure 4.8 (b, c). As expected, the highest temperature difference is for the lowest flow. With increasing flow, the shape of the effluent is more conical, and there is effective heat transfer towards the middle of the plasma jet leading to thermalization and a more uniform temperature profile.
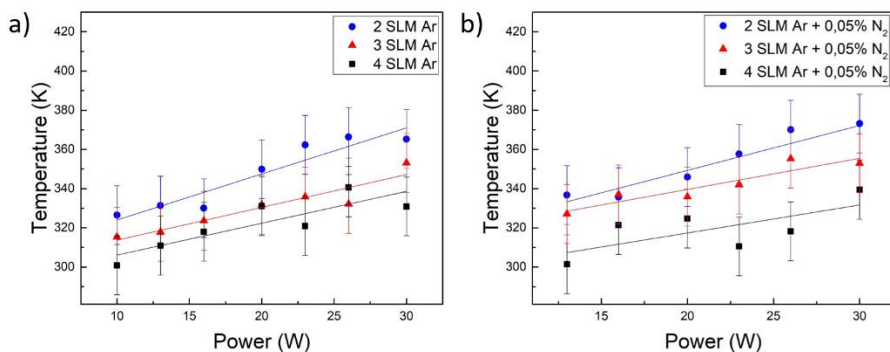


Figure 4.9. The gas temperature $T_g$ corresponds to the inter-electrode region analyzed by averaging the Rayleigh scattering signal in a) Ar gas; b) Ar+N$_2$ mixture.

Obtained results indicate that $T_g$ in both Ar and Ar+0.05% N$_2$ plasma is in the range of 300-370±15 K, depending on applied flow and power. Figure 4.7 (c) confirms an approximation of the negligible impact of the N$_2$ admixing used for OES experiments on $T_g$. The method of Rayleigh scattering has higher sensitivity in comparison to OES, and $T_g$ can be estimated with an uncertainty of ±15 degrees. This allows seeing an effect of input RF power on gas temperature which was undetectable in OES measurements. As presented in Figure 4.9 (a, b), the RF power

increase results in an almost linear increase in the gas temperature of the effluent. The maximum increase of temperature was found for the lowest flow rate of Ar gas due to less effective heat transfer at 2 SLM. The radial averaged value of $T_g$ measured by the Rayleigh scattering is in good agreement with the OES method based on OH(A-X) emission. On the other hand, disagreement with results obtained through $N_2$ emission is almost 100 K for all conditions. This leads to a conclusion of strong overestimation of $T_g$ in a case of utilization of emission of the second positive system of $N_2$ for determination of $T_g$.

Despite the good agreement of the Rayleigh scattering results and OES method based on OH(A-X) emission, the elastic laser scattering is not free of well-known intrinsic problem: the scattering is dependent on the species density, and so it requires the validity of a condition that gas flow dynamics is not affected by plasma. In this study, the aforementioned problem was checked. An effect of the gas flow dynamics on elastic scattering was validated by inelastic Raman scattering of the laser light on $N_2$ and $O_2$ molecules appearing in the effluent due to ambient air diffusion. Raman spectrum was measured in Ar plasma with 0.2% admixing of molecular gas (air) at a position of 1.5 mm beneath the nozzle. It has to be noted that due to the Bragg grating used to filter out the Rayleigh line at 532 nm, the detection scheme presented in Figure 4.2 (b) has a low radial resolution. To this end, a spatially averaged Raman signal was detected and compared with the Rayleigh scattering results. As mentioned earlier, Raman signal-based gas temperature was only used to validate the applicability of the Rayleigh scattering method to clarify the effect of the discharge on the gas flow dynamics. Accordingly, spatially averaged Raman signal over the region indicated as ROI in Figure 4.8 (a) was used as an indicator of the average temperature of the plasma jet effluent. Furthermore, it was compared with Rayleigh scattered signal averaged over the same length.

The strongest influence of plasma on gas flow dynamics is expected at the lowest gas flow and high power. Due to this reason, the Raman spectroscopy was performed at 2 SLM Ar flow. For calculation of $T_g$ from Raman spectra, theoretical spectra were fitted to experimental. Input parameters were the resolution of the spectrometer, $N_2$ and $O_2$ density, and $T_g$. Both anti-Stokes and Stokes signals were observed, but only this part of the Raman spectra was analyzed due to the stronger Stokes signal. The experimental and fitted Stokes components of Raman spectra are presented in Figure 4.10.
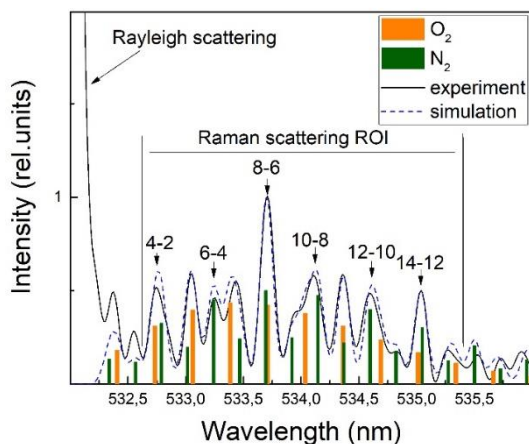
Figure 4.10. Examples of normalized experimental and simulated Raman spectra (Stokes component) for Ar plasma with 0.2% molecular gas admixing for RF forward power of 15 W. Raman components attributed to $O_2$ and $N_2$ are presented with red and green color with an indication of the rotational numbers of the lines.

During experiments, it was found that the first three lines in Stokes components with $J \leq 3$ were partially affected by a strong Rayleigh signal which was still presented even after filtration by a single BNF-532 filter. All three lines were excluded from the fitting procedure as well as lines above 535.2 nm (corresponding to J>14) as the S/N ratio was too low for high J number lines due to low lines intensity. The Raman spectrum fitting indicates $T_g$ of 320±25 K for 15 W RF power which is in good agreement with the Rayleigh scattering result of 330±15 K obtained by averaging the scattered signal over the ROI -7 to +7 mm, indicated in Figure 4.8 (a). Considering good agreement between Rayleigh and Raman spectroscopy results, it can be concluded that RF discharge in $\alpha$-mode does not affect the dynamics of the gas flow, and the method of Rayleigh scattering applies to similar plasmas.

As a summary, the rotational temperature measured by emission of OH(A) band well represents the gas temperature evaluated by the direct detection of Rayleigh scattering. The method based on emission spectroscopy of rovibrational bands of OH radicals can be used in future tests of the developed source in biomedical tests and treatment of skin surfaces where the applicability of other methods is technically challenging.

## 4.5. CONCLUSIONS

An annular-shape radio-frequency atmospheric pressure plasma jet was characterized with electrical and temperature diagnostics. The plasma device is designed for biomedical application in wound healing and topical drug delivery with the possible aerosol introduction through a hollow inner-electrode. For this reason, the aim was to obtain uniform and cold plasma to prevent any damages to the skin. The obtained results showed that this can be achieved with RF capacitive-coupled discharge operating in a uniform diffuse $\alpha$-mode at RF power below 30 W. To explain the stability of a uniform $\alpha$-mode of the discharge, processes of diffusion and recombination were analyzed. It is proposed that stabilization of the discharge operation in $\alpha$ mode is achieved due to the presence of the sheath.

Gas temperature in plasma is determined using the OES technique based on the rotational temperature of OH radicals $A^2\Sigma + \rightarrow X^2\Pi_i$ (0,0) band and $N_2$ $C^3\Pi_u \rightarrow B^3\Pi_g$ (0,2) band. The temperature obtained by the fitting method of OH $A^2\Sigma^+$-$X^2\Pi$ (0,0) band indicated $T_g$ of 340, 320, and 310 K for the flow of 2, 3, and 4 SLM of Ar. Considering the biomedical limit (333 K$\approx 60^0$ C during the short treatment time), it can be concluded that the safe operating range of the APPJ is above 2 SLM. However, the measurements for $N_2$ and OH bands yield discrepant results of almost 100 K, where the highest temperatures of 450-480 K are obtained in the case of $N_2$. For this reason, the temperature measurements by the OES technique were revalidated by two other independent techniques based on laser scattering. Rayleigh scattering has shown uniform temperature distribution at RF forwarded below 20 W, while at higher powers inner-electrode region is noticeable for low flow. For higher flow than 2 SLM, mixing with the middle part starts to be significant, resulting in more effective heat transfer from plasma jet to ambient air and more uniform temperature distribution. Radially averaged $T_g$ determined by the Rayleigh method is in good agreement with OH temperature determined by emission spectroscopy. The assumption of the negligible effect of plasma ignition on gas flow dynamics and so on results of the Rayleigh scattering has been validated by Raman scattering. It was revealed that both methods agree well with OES results based on OH (A-X) measurements. The low gas temperature of the RF plasma source combined with uniform and diffuse afterglow and the possibility of the source coupling with aerosol injection is considered beneficial for a variety of biomedical applications, including topical drugs injection and wound healing.

The next chapter presents the results of extensive diagnostics performed on plasma-initiated gas and liquid chemistry. The most important short- and long-living species are measured. Special attention is given to the influence of aerosol droplets' presence in plasma effluent on plasma initiated chemistry in the gas and liquid phase.

## 5.1. INTRODUCTION

The performance of cold plasmas employed in biomedicine or plasma medicine is determined by their capability to produce a wide range of reactive oxygen and nitrogen species (RONS). Modifying RONS production is typically accomplished by changing plasma feeding gas composition or adding shielding gases. In Chapter 5, RONS initiated chemistry, and the modification of generated species has been investigated. Alteration of RONS chemistry has been accomplished by adding the aerosol droplets into plasma effluent, while other parameters remained the same. Accordingly, a detailed examination of short- and long-living species production in treated liquid has been studied combining advanced diagnostic techniques. In addition, the total oxidative power of plasma has been evaluated through the oxidation of amino acid cysteine. The results presented in Chapter 5 impact both applications of plasma-aerosol systems and their design. Therefore, the following study can be of fundamental importance for investigating plasma effluent-aerosol interaction.

## 5.2. MODIFICATION OF PLASMA CHEMISTRY INITIATED BY THE PLASMA-AEROSOL SYSTEM

The unique feature of cold physical plasmas (CPP) to produce a mixture of highly reactive species mimicking the multi-ROS reactive oxygen species inflammatory environment is central to the plasma medicine theme. Since the first reports in the mid-nineties show that CPP sources can successfully inactivate bacteria, the field expanded significantly [19, 290]. Numerous plasma sources were developed for the decontamination of biotic/abiotic surfaces, deposition of bioactive coatings, and manipulation of eukaryotic cells and tissues [250, 291-292]. CPPs show several direct and indirect effects in biological models, inducing cell signaling, proliferation, apoptosis, or senescence depending on the treatment intensity ("dose") [293]. Currently, research focuses on applications such as chronic and acute wound healing, (pre-) cancerous lesions, and other conditions involving the immune system [294-299]. The design of cold plasma sources for biomedical applications evolves in two major directions: Dielectric Barrier Discharges (DBD) [36, 300] and Atmospheric Pressure Plasma Jets (APPJ) configuration [76].

Of special interest for fundamental and biomedical practice are cold plasma reactors in direct contact with liquid since many biological samples are inevitably covered with a liquid layer. Different reactor designs to study plasma-liquid interaction are developed and reviewed in [83], e.g., jets in direct contact with liquid, with a liquid electrode, surface discharges, gas-phase plasma with dispersed phase (aerosols), and discharges in bubbles. The introduction of liquids into electric discharges is mainly driven by the motivation to induce or enhance the plasma

chemistry and change the production of reactive species OH, O, $H_2O_2$ [301]. Moreover, with the introduction of aerosols into plasma, the effective interaction area between plasma and liquid increases, followed by a change in species production. For purposes of increasing interaction area and energy efficiency, water spray has been injected into argon and air plasma for purposes of adherent bacterial inactivation [302]. Cold RF plasma interaction with a controlled flow of micrometer droplets has been reported in [303] focused on the effects on droplets' size and velocity distribution after their transport through plasma (t≈100 μs).

Moreover, detailed research on the passage of a single isolated microdroplet (t≈10 ms) through cold diffuse RF plasma has been reported[304]. Controlled plasma-aerosol interaction presents a promising tool for fundamental quantitative studies on the production of water-derived species and their supervised deposition and delivery, which is of high importance for biomedical applications of plasmas. Due to the lack of systematic studies of plasma-induced chemistry in the presence of aerosols and, on the other hand, increased research interest in plasmas for biomedical application, we commit this thesis to a detailed study on how micro-droplets presence in the effluent can change the plasma chemistry.

Accordingly, a plasma jet coupled with aerosol spray was developed for two potential applications: (i) wound healing with controlled production of reactive species by injection of aerosol; (ii) drug delivery, where the drug is dissolved in aerosol or applied on a surface of the wound and plasma/aerosol treatment enhanced delivery of the drug to the patient. The presented RF sustained annular-shaped plasma jet uses an argon working gas and operates in ambient air [305]. Its coaxial geometry allows the introduction of an aerosol into the discharge effluent. This design facilitates the direct and controlled interaction of micro-droplets with the plasma effluent before reaching the (biological) target, modulating the generation of active species due to a large gas-liquid interface and opening the potential to introduce compounds or drugs for delivery to the target via the aerosol. Moreover, we have shown that aerosol injection into plasma effluent results in the temperature decrease of a treated Biobrane sample from 102.4°C to 59.4°C for working power 30 W and from 73.2°C to 48°C for 20 W power during 1 min treatment on distance 5 mm from plasma nozzle and [306]. A decrease in plasma gas temperature with the introduction of microdroplets for maximal 10°C has also been recently reported in [307]. The gas temperature drop in plasma coupled with aerosol is an essential point for biomedical applications when the heating level should be below the human-safe limit. To this end, a thorough understanding of the physics and the chemistry of this modular source is desired to determine future key points for an application both in the biomedical and in the technological scenario. So far, the biochemical potential of the plasma source has not been studied in detail, especially the impact of the RF

argon jet on the aerosol droplet carrying organic molecules remains to be determined.

Besides the primary species and radiation produced in the plasma core, species that can be generated in contact with air and water are of special interest for targeted applications. Among these are the reactive oxygen species (ROS): superoxide $O_2^{\bullet-}$, hydrogen peroxide $H_2O_2$, hydroxyl radical $^{\bullet}OH$, singlet oxygen $^1O_2$, atomic oxygen O, ozone $O_3$, and the reactive nitrogen species (RNS): atomic nitrogen radical $^{\bullet}N$, nitric oxides $N_xO_y$, peroxynitrite $ONOO^-$, nitrous and nitric acid with the corresponding ions ($HNO_2/NO_2^-$, $HNO_3/NO_3^-$). The species differ in their reactivity, affecting the lifetime and specificity of detection. Most of them occur regularly in physiological processes of living tissues, often involved in signaling processes [55, 308]. Biological reactivity of species reflects in oxidative changes of sensor molecules or – in case of excess – other biomolecules such as proteins or lipids [309]. The resulting outcome is still underexplored, but it has been observed that the oxidation of proteins changes their immunogenicity. In autoimmune type I diabetes patients, autoantibodies targeting experimentally oxidized insulin were detected [310]. It can be assumed that the introduction of covalent modifications in biomolecules is one mechanism behind the observed biomedical effects of CPPs. Thus, the biochemical impact of a given plasma source is relevant. Biomolecules such as peptides or amino acids are a suitable model to investigate the reactive species produced or deposited in a target by a given plasma source and, on the other hand, reveal the chemical structures most sensitive to the attack of reactive oxygen and nitrogen species RONS [311-314].

In this chapter, an established model system that employs the amino acid cysteine as the tracer molecule has been chosen to scavenge RONS generated by the RF plasma source. Cysteine is a key amino acid controlling structure, location, and functionality of proteins by its different oxidation states [315]. The applicability of the model has been validated using the argon plasma jet kINPen and the helium micro-plasma COST jet [311, 314]. By employing liquid chromatography and high-resolution mass spectrometry, the model can qualify and quantify the major cysteine derivatives produced by the interaction with the plasma-derived species. Besides the treatment of cysteine solutions with various power and distance settings, especially the direct interaction between cysteine in the aerosol droplets and the plasma effluent was investigated. Furthermore, electron paramagnetic resonance (EPR; $^{\bullet}OH$, $O_2^{\bullet-}$, $^{\bullet}H$, $^{\bullet}O$, $O_3$, $^1O_2$), ion chromatography (IC, $NO_2^-$ and $NO_3^-$ ions), and a colorimetric $H_2O_2$ assay were used to detect the deposition of short and long-lived reactive species into the liquid phase. Based on these data, the mechanisms of species generation and the role of aerosol injection on ROS and RNS production are discussed.

In this thesis, a special design of argon RF APPJ coupled with aerosol droplets injection was used. The safe, stable, and uniform operation of the source that is important for plasma medicine was shown in Chapter 4[305]. Hereby, in this chapter, special attention is given to the effects of plasma-aerosol direct interaction on the plasma efficiency of liquid media treatment. Correspondingly, varieties of diagnostic techniques were applied to support the study on chemical characterization of the source operation in ambient air with and without an aerosol. Optical emission spectroscopy (OES) and Fourier transform IR spectroscopy (FTIR) has been used to give insight into the composition of species in the plasma gas phase and plasma-aerosol medium. In the next step, the treated liquid target was analyzed in terms of liquid chemistry with colorimetric assays, ion chromatography (IC), and electron paramagnetic resonance (EPR) spectroscopy, focusing on a model of cysteine oxidation in the presence of plasma and plasma in contact with the aerosol.

### 5.3.1. DESIGN OF PLASMA REACTOR

The plasma reactor was constructed in geometry to introduce aerosol droplets in the effluent. Plasma jet in annular shape 1 mm thick with external diameter $d_{ex}$=14mm was generated in coaxial hollow-electrode geometry. The RF-powered inner electrode was made of corrosion-resistant stainless steel, while an external grounded electrode was aluminum. All experiments were carried out for two applied powers further indicated as "low" P=20 W, and "high" P=30 W. Low and high power settings correspond to dissipated power in the discharge of 8 and 12 W, respectively, as estimated and demonstrated in Chapter 4[305]. The high power is a maximum discharge power when RF plasma exists in $\alpha$ mode of operation. In the operational range reported here, gas temperature in plasma effluent was 330(±15) K for 20 W and 350(±15) K for 30 W, while electron temperature and density were previously estimated to be 1 eV and $3.2 \cdot 10^{18}$ m$^{-3}$ [305] (see Chapter 4). On the top of the reactor, a NexTgen ultrasonic spraying nozzle was installed (Figure 5.1(a)). Plasma forming gas argon was fixed at 3 SLM corresponding to maximal gas velocity in the effluent of 1.4 m/s. The flow rate was previously verified to generate uniform diffuse discharge in α-regime in a laminar gas flow regime (Figure 5.1(b)). For more details, see Chapter 4. The flow rate of aerosol liquid to be sprayed was controlled with a syringe pump at a flow of 0.1 mL/min. The optimal value of flow rate was chosen, assuring a uniform and reproducible spray during a treatment time between 10 and 60 s. The aerosol was injected into the affluent and did not pass through the active plasma formed between the electrodes (Figure 5.1). The mean size of the aerosol droplets was 22 (±0.825) μm, determined based on the datasheet provided by the company SinapTec, NexTgen Ultra Sonic platform. Additionally, 1 SLM flow of

Ar gas was applied through the central electrode to push droplets downwards with a velocity of 0.2 m/s to prevent aerosol condensation inside the plasma source during the treatment time and formation of large droplets due to condensation.
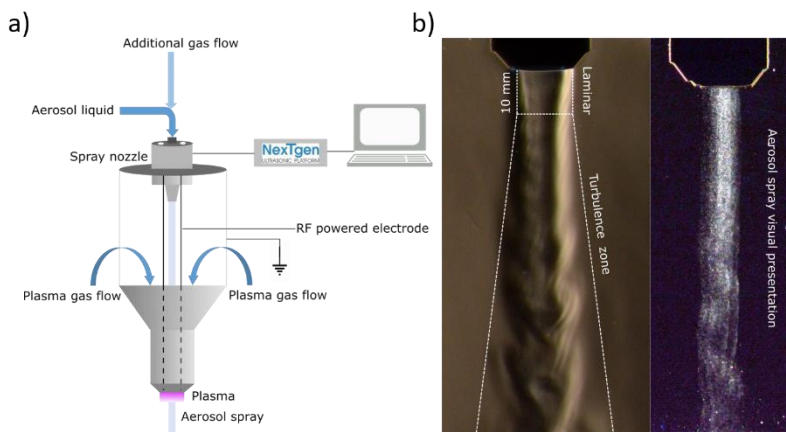


Figure 5.1. a) General view of the plasma jet reactor with aerosol injection and enlarged cross-section of the nozzle, b) Visual view of the gas flow obtained by Schlieren imaging indicating two zones of different gas flow regimes (on the left) and visual view of the aerosol spray (on the right).

## 5.3.2. SPATIAL RESOLVED OPTICAL EMISSION SPECTROSCOPY (OES)

Optical emission spectroscopy can be a qualitative method to give insight into the composition of exciting species present in plasma. Emission from excited species in plasma effluent has been measured in the 250-900 nm range. The Ocean Optics spectrometer with a resolution of 1.7 nm was used to record emission spectra from the plasma effluent. Spectral sensitivity of the spectrometer, transparency of the fiber, and collection optics were calibrated with an Oriel model 63355 quartz tungsten-halogen lamp. The light emitted by the plasma effluent was collected with a fiber (d=200 μm) located 2 mm away from the region of interest resulting in an acceptance angle corresponding to the spatial resolution of 1 mm. This arrangement of the spectral measurements prevents the collection of the radiation from the discharge region and ensures that only light emission from the effluent was recorded. Line-of-sight measurements were performed to record spectra for three positions perpendicular to the jet's axis, 2 mm from the nozzle in visible plasma effluent, 6 mm from the nozzle, and 8 mm away from the nozzle – far effluent. The effluent was imaged using a Hamamatsu ICCD camera (5 μs exposition, 1000 integration), coupled to band-pass filters with a transparency of 10 nm full width at

half maxima FWHM centered at 751 and 298 nm corresponding to Ar I and OH(A-X) emission, respectively.

### 5.3.3. FOURIER-TRANSFORM INFRARED SPECTROSCOPY (FTIR)

FTIR high-resolution spectroscopy was performed with the use of a Matrix-MG2 spectrometer of 0.5 cm$^{-1}$ resolution to detect and estimate the absolute concentration of the most abundant long-living compounds generated in the gas phase with and without the aerosol. The spectrometer coupled with a multi-pass cell of 5 m was calibrated for $H_2O$, $N_2O$, $N_2O_5$, $NO$, $NO_2$, $O_3$ compounds with a sensitivity of 0.1 ppm. Gas from the plasma was directed in a tube through which dry air was circulating in flow range 0.5-1 SLM to simulate an open atmosphere operation. Once aerosol was introduced in the plasma, trapped gas was filtrated through quartz wool to reduce water droplets entering the FTIR system to a minimum while having only a limited impact on the detected RONS. In pilot experiments, filtering was found unavoidable. To minimize the effect of quartz wool, all experiments were performed after reaching steady-state (T=5 min). The FTIR spectra were averaged 30 times in progression mode and recorded in the wavenumber range of 800-6200 cm$^{-1}$.

### 5.3.4. SAMPLES PREPARATION AND TREATMENTS OF LIQUIDS

For mass spectrometry analysis, 1 mM solutions of cysteine amino acid (L-Cysteine, Sigma Aldrich) were prepared fresh daily. The pH was stabilized at pH 7.4 by the use of 5 mM phosphate buffer (HPLC-MRM analysis) or 5 mM ammonium formate (direct infusion shotgun HRMS). For electron paramagnetic resonance (EPR) experiments, the spin trap/spin probe was solubilized in 5 mM phosphate buffer. In pilot experiments, a volume of 1.5 mL sample in a 6-well plate was optimal.
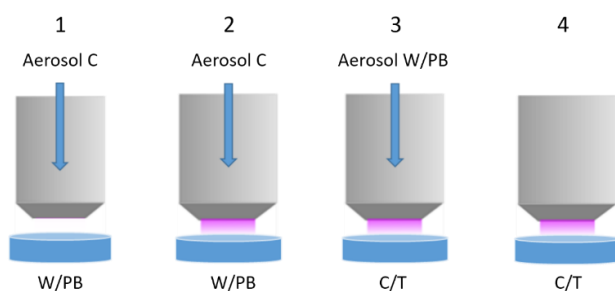


Figure 5.2. General experimental setups. Ultrasonic aerosol used in setups 1 to 3. Plasma off conditions (setup 1) was used as background control. Abbreviations: C for cysteine, T for trapping trap/spin probe, W for water, and PB for phosphate buffer.

Cysteine oxidation was investigated for plasma power of 20 and 30 W, treatment time variation (10, 35, 60 s), and distance variation of a target from the effluent (2, 6, 12 mm). Target was the treated (and tracer-enriched) liquid collected for chemical analysis, namely mass spectrometry, EPR, IC, and colorimetric assays. Treatment time reported in this study is the exposure time of plasma treatment of 1.5 mL liquid sample by the setups shown in Figure 5.2. Four different set-ups, including or excluding aerosol injection, were used (Figure 5.2/Table 5.1). For some experiments, the aerosol was generated from a 1 mM cysteine solution and collected for analysis into either empty well plates or wells filled with 1.5 mL water with estimated dilution and final concentrations c=11 μM, c=37.5 μM, and 62.5 μM during 10, 35, and 60 s treatments. Evaporation of the aerosol droplets in the effluent was not taken into account since imaging showed a negligible effect in the considered distances (see Figure 5.1. (b)). However, droplets may partially be evaporated during the transport to the treated liquid. Correspondingly, the chemical analysis performed in this chapter represents the integral effect of droplets and gas-phase water molecules on the plasma-induced chemistry. Overall aerosol loss due to evaporation in the effluent on the distance up to 15 mm from the nozzle has been estimated low, as seen from the almost constant intensity of the visible aerosol jet Figure 5.1(b).

Table 5.1. Overview of the plasma treatment protocol. PBS = phosphate-buffered saline; spin trap/spin buffer = 2 mM BMPO or 100 mM TEMPD (see Figure 5.2)

| Set-up | Aerosol liquid | Target liquid | Power (watt) | Distance (mm) | Treatment time (s) |
|--------|----------------|---------------|--------------|---------------|--------------------|
| 1 | 1 mM cysteine in water (C) | water (W) or phosphate buffer (PB) | 0 (control) | | |
| 2 | 1 mM cysteine in water (C) | water (W) or phosphate buffer (PB) | | 2, 6, 12 | 10, 35, 60 |
| 3 | water (W) or phosphate buffer (PB) | 1 mM cysteine in water (C) / spin trap in PBS (T) | 20, 30 | | |
| 4 | No aerosol | 1 mM cysteine in water (C) / spin trap in PBS (T) | | | |

The aerosol injection into the plasma effluent considerably changed the surface area of the effluent/liquid interaction. Knowing that the mean diameter of

the spherical aerosol droplet is 22 µm, the calculated mean volume and surface of the droplet are respectively 5575 µm$^3$ and 1520 µm$^2$. Assuming a droplet mean volume and aerosol flow rate, liquid 0.1 mL/min (1.66 µl/s ) estimated droplet formation rate is $3 \times 10^5$ droplets/s. Subsequently, the effective interaction area of droplets with the plasma effluent was calculated to be $4.5 \times 10^3$, $1.6 \times 10^4$, and $2.7 \times 10^4$ mm$^2$ for the treatment of 10, 35, and 60 s, respectively. It has to be noted that aerosol droplets interact with plasma only during a short time when passing through the effluent (2 mm or 6-10 ms).

In comparison, an area of up to 500 mm$^2$ is treated in condition 4 (6-well plate, 2 mm distance). Despite the laminar flow in the first 10 mm, of both plasma feeding gas Ar with velocity 1.4-1.8 m/s and flow of aerosol droplets with velocity 0.2-0.35 m/s, once the target is placed below the nozzle, laminar behavior cannot be granted. Placement of the liquid target in the direction of gas and droplets flow acts as a perturbation resulting in switching to turbulent behavior and effective mixing of effluent with droplets in the region between the nozzle and liquid target. Unfortunately, the actual number of the droplets coming in contact with plasma effluent and interacting with effluent is difficult to estimate. This would involve experimental PIV (Particle Image Velocimetry) laser technique or particle tracing simulation in COMSOL modeling platform, which is out of the scope of the current study.

### 5.3.5. HIGH-PRESSURE LIQUID CHROMATOGRAPHY & MASS SPECTROMETRY (HPLC-MS)

Qualitative high-resolution mass spectrometry analysis was achieved by directly infusing the cysteine solutions into a TripleTOF 5600 (Sciex, Darmstadt, Germany). 10 µL/min of solutions were infused using a Turbo V ion source, using optimized parameters (negative polarity, curtain gas 35 psi, gas1 20 psi, gas2 25 psi, capillary temperature 150 °C, spray voltage 4.5 kV). The spectra were acquired in a mass range of 30 to 400 mass to charge ratio (m/z). Quantitative analysis was achieved by high-pressure liquid chromatography-mass spectrometry coupling. An Infinity II 1290 system (Agilent Technologies, Waldbronn, Germany) was equipped with a HILIC 2.1 mm x 100 mm Acquity Amide Column (130 Å pore size, 1.7 µm particle size, Waters, Manchester, United Kingdom) and a respective pre-column (2.1 mm x 5 mm). Using 400 µL flow rate and an 18 min gradient of A (10 mM ammonium formate plus 0.15% formic acid in water) and B (85% acetonitrile, 10 mM ammonium formate buffer pH 3), the baseline separation of cysteine, cystine, cystine sulfonic acid, and cysteine-S-sulfonate was achieved (Sigma, Deisenhofen, Germany). The details of the gradient are resumed in Table 5.2. A qTRAP 5500 triple quadrupole instrument (Sciex) was used in the Multiple Reaction Monitoring (MRM) strategy for

detection and quantification. All compounds were analyzed in positive ion mode, and specific transitions were monitored in the MRM experiments (Table 5.3). External calibration curves were prepared. All samples were injected or infused twice (technical duplicates).

Table 5.2. The chromatographic gradient was used for the HPLC-MS characterization of cysteine derivatives.

| Time (min) | B phase (%) |
|---|---|
| 0 | 99 |
| 6.1 | 94 |
| 10 | 82 |
| 14 | 70 |
| 14.1 | 99 |
| 18 | 99 |

Table 5.3. MRM method used for the HPLC-MS characterization of cysteine derivatives.

| Compound | Elution time (min) | MRM-transition (m/z) | CE (eV) | Dwell (ms) |
|---|---|---|---|---|
| Cysteine | 4.71 | 122 → 76 | 20 | 200 |
| Cystine | 12.16 | 241 → 152 | 20 | 200 |
| Sulfonic acid | 8.54 | 170 → 124 | 10 | 200 |
| Sulfinic acid | 9.57 | 154 → 74 | 10 | 200 |
| *S*-sulfonate | 5.09 | 202 → 120 | 10 | 200 |

### 5.3.6. ELECTRON PARAMAGNETIC RESONANCE SPECTROSCOPY (EPR)

Spin trap enhanced electron paramagnetic resonance spectroscopy (EPR, EMXmicro, Bruker Biospin GmbH; X-band 9.75 GHz; magnetic field up to 0.65 T) using the Xenon software in addition with the spin counting module (Bruker Biospin GmbH) was applied to quantify radicals/reactive oxygen species. The following instrument parameters were used: modulation frequency 100 kHz, modulation amplitude 0.1 mT, microwave power 5.024 mW, receiver gain 30 dB, and a time constant of 0.01 ms. 5-tert-Butoxycarbonyl-5-methyl-1-pyrroline-N-oxide (BMPO, Dojindo Laboratoire, Japan) – a spin trap for $^•OH$, $O_2^{•-}$, $^•H$, was dissolved in 5 mM phosphate buffer to a final concentration of 2 mM, and 2,2,6,6-tetramethyl-4-piperidone (TEMPD, Sigma Aldrich) – spin probe for $^•O$, $O_3$, $O_2(a^1\Delta_g)$, was dissolved in the same system to a final concentration of 100 mM. For all experiments, an untreated sample was measured prior to the plasma treatment. More details on the measurement procedure can be found in [316-319].

### 5.3.7. HYDROGEN PEROXIDE ASSAY

Hydrogen peroxide ($H_2O_2$) was detected via a colorimetric assay. 10 µL of the sample were incubated for 15 minutes with 100 µL of reagent, consisting of a solution of xylenol orange, sorbitol, and ammonium ferrous (II) sulfate (Pierce™ Quantitative Peroxide Assay Kit, Thermo Scientific). In aqueous solutions, sorbitol and hydrogen peroxide react to form peroxyl radicals, which oxidize $Fe^{2+}$ to $Fe^{3+}$. This induces a color change of xylenol orange, detectable at 595 nm through a spectrophotometer (Infinite M200 Pro plate reader, Tecan, Männedorf, Switzerland). Each sample was analyzed in triplicate. The assay delivers a linear response between 0.78 and 50 µM $H_2O_2$, and the concentration of $H_2O_2$ could be determined safely starting from 2.3 µM.

### 5.3.8. ION CHROMATOGRAPHY (IC)

Nitrite ($NO_2^-$) and nitrate ($NO_3^-$), as well as sulfite ($SO_3^-$) and sulfate ($SO_4^-$), were quantified via ion chromatography (ICS-5000, Thermo, Dreieich, Germany). For separation, a weak ion exchange column (IonPac AS23 2 x 250 mm) and respective precolumn (2 x 50 mm IonPac AG23) were used (Thermo Scientific). The ions were separated in 25 min isocratic run, at a flow rate of 0.25 mL/min, using 80 mM $HCO_3^-$ and 450 mM $CO_3^{2-}$ buffer as mobile phase. External calibration curves were measured for all ions using the Seven-Anion standard (Dionex/Thermo Scientific) or sodium sulfite analytical standard (Sigma Aldrich, Deisenhofen, Germany). Each sample of three different experiments was injected in duplicate.

### 5.4.1. ACTIVE SPECIES GENERATION IN THE EFFLUENT

Spatially resolved emission spectroscopy results for the plasma effluent in three different positions 2, 6, and 8 mm from the nozzle, in pure argon plasma and plasma in contact with aerosol, are shown in Figure 5.3.
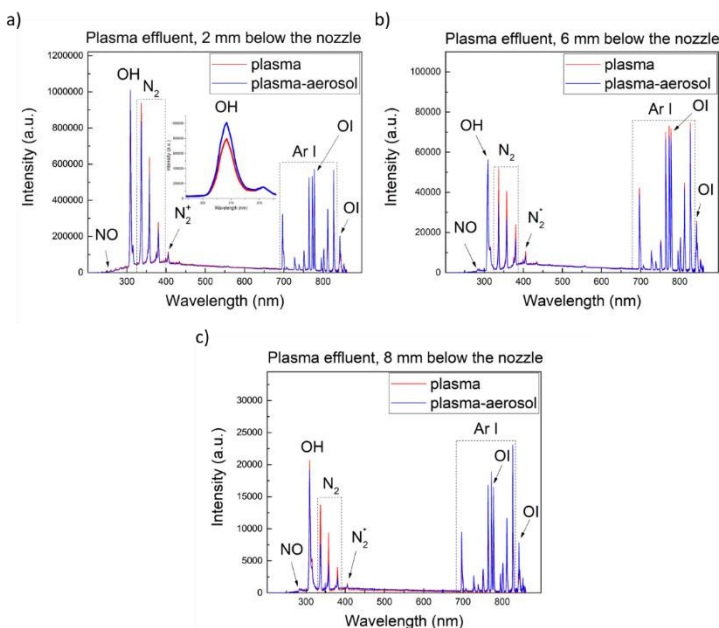


Figure 5.3. Overview of Ar plasma jet emission without the use of aerosol (red) and plasma emission when in contact with aerosol (blue) in a range of 250-900 nm in the effluent positions corresponding to a) 2 mm, b) 6 mm, and c) 8 mm below the nozzle, P=30 W.

The effluent emission in ambient air mainly consists of radiation of excited species Ar, O I, OH(A-X) radicals, and $N_2$ (C-B), as marked in Figure 5.3. However, weak emission from NO molecules has also been detected below 300 nm. The observed continuum appearing in the region 300-600 nm is ascribed to the Bremsstrahlung radiation and $NO_2$ chemiluminescence as explained in detail in our work on similar RF discharge operating in a planar geometry [285]. All spectra were recorded along with effluent, where the interaction of aerosol with effluent took place. Emission intensity was highest in close vicinity to the nozzle (Figure 5.3(a)) and exponentially decreased with the distance. In argon plasmas operating under ambient conditions, the energy transfer from $Ar^*$ to $N_2$ is an important and effective process, and it can be used as an indicator of plasma interaction with air. Energy transfer is expected to be high as soon as excited Ar atoms leave the active plasma

volume and collide with the surrounding air, corresponding to a case presented in Figure 5.3. In all three positions (Figure 5.3) entrance of $N_2$ in the plasma, effluent can be seen as its excitation. The presence of the aerosol in the effluent leads to an increase of OH radicals emission intensity of more than 25% in position closest to the nozzle, indicating a probable increase in OH radicals production by water aerosol injection (see the inset in Figure 5.3 (a)). The intensity of NO excited molecule emission is higher in Ar plasma without aerosol. In addition to a changed formation of NO due to gas-phase chemistry, partial absorption of NO emission as for UV radiation below 300 nm[63] and direct quenching of NO radicals could not be excluded based on OES measurements and may be underestimated in this condition.

The plasma chemistry in the far effluent, especially when aerosols are introduced, is mainly driven by VUV/UV radiation generated in plasma between electrodes and emitted in the direction of gas flow. The VUV/UV emission has been recorded from the plasma (Figure 5.4).
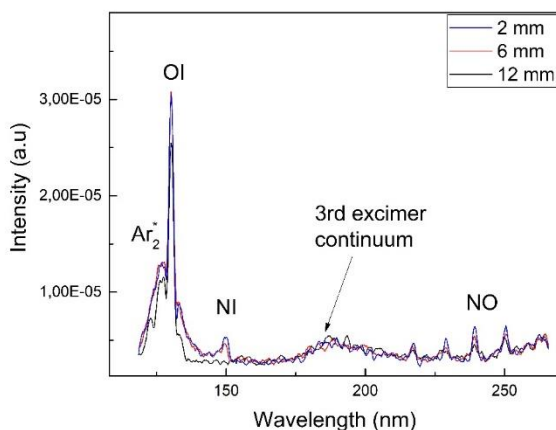


Figure 5.4. VUV/UV spectra of annular shape plasma jet recorded from plasma zone (inter-electrode region) for three distances from the edge of visible effluent: 2 mm (blue), 6 mm (red), and 12 mm (black). Plasma working power was 30 W.

As expected in argon-driven plasmas, argon excimers $Ar_2^*$ on 126 nm and atomic oxygen OI 130 nm radiation is dominating VUV/UV spectra of the plasma. It has to be emphasized that due to the high abundance of monoatomic gas Ar with respect to the ambient air in the direction of the emission detection, VUV/UV photons are detected far as 12 mm from the edge of the visible effluent (14 mm from the electrode). As VUV/UV spectra have been recorded only axially from a region between the electrodes and no UV emission has been detected from the plasma

effluent, aerosol effect on UV emission has been not considered due to technical limitations. Namely, simultaneous spraying of aerosol on the UV spectrometers window and detection of UV radiation would lead to the condensation and formation of the liquid layer on the spectrometers window and consequent absorption. It has been reported[63] that excimer radiation emitted at 126 nm will be absorbed by 99% in a water layer as thin as 4.6 μm based on Lambert-Beer law, while experimentally, 50% absorption has been measured in 200 μm water layer for photons λ<180 nm.

The effluent has been imaged for Ar and OH emission using ICCD to examine potential changes in plasma dynamics behavior and plasma radiation with aerosol injection. It has to be kept in mind that the significance of the data can be challenged since the presence of the droplets may result in quenching effects. Additionally, both optical techniques do not give information about the absolute densities of the observed species. Despite some noticeable changes in OES revealed in the case of aerosol injection, an overall impact of the aerosol on the plasma effluent is relatively weak and mainly attributed to a drop in Ar I lines and an increase of OH emission. The low impact of the aerosol was also confirmed by the effluent imaging presented in Figure 5.5 for both Ar I and OH (A-X) emission.
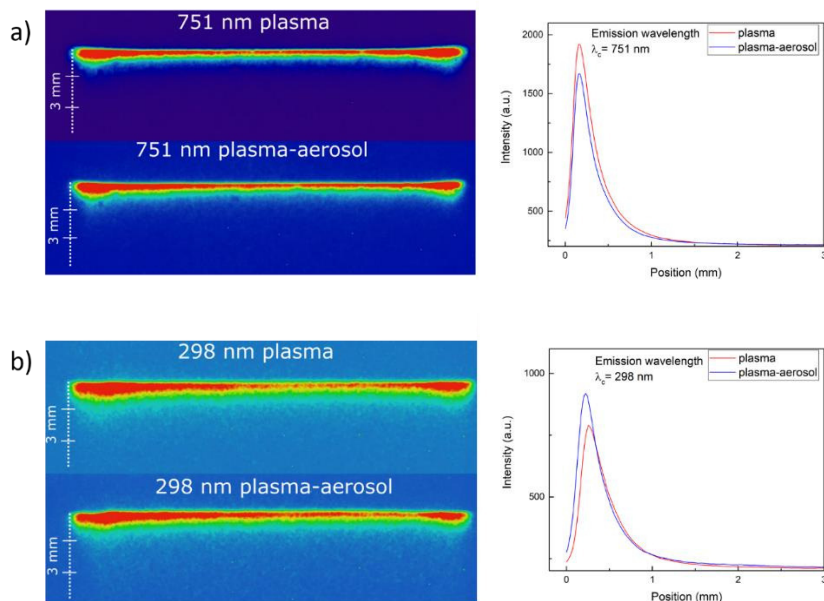


Figure 5.5. Plasma effluent imaging at two different wavelengths: a) 751 nm (Ar I emission); b) 298 nm (OH emission) at RF input power P=30 W.

In both conditions, with and without aerosol injection, the radiation profile is very similar, indicating a low impact of the aerosol on excited species production that well agrees with OES results. Visible emission of the effluent at 750 nm and 280 nm is detected only 1 mm below the nozzle (Figure 5.5), which can be assigned to a low signal-to-noise ratio of the camera SNR=10.

With the use of FTIR, low production of ozone, below 20 ppm in the gas phase, was confirmed for all plasma and plasma-aerosol conditions. FTIR spectra of Ar jet and jet in contact with water aerosol under operating power 20 W are presented in Figure 5.6. Rotationally resolved spectra of water molecule bending vibrations 1400-2000 cm$^{-1}$ and stretching vibration 3600-4300 cm$^{-1}$, 5100-5600 cm$^{-1}$ are dominant in all conditions, while ozone peak located at 1051 cm$^{-1}$, can also be seen in Ar plasma after 5 minutes of operation. In argon plasma without aerosol, a simultaneous decrease of water content and an increase of ozone has been noted from $c(H_2O)$=400 ppm and $c(O_3)$=1.04 ppm to $c(H_2O)$=230 ppm and $c(O_3)$=9.5 ppm at 20 W RF power after 5 minutes of operation. At the water concentration of $c(H_2O)$=400 ppm, a significant change in plasma chemistry as reported in [320] was expected. The high amount of $H_2O$ at the beginning of the experiments was attributed to the adsorption of water vapor on gas Teflon tubes and the metal body of the jet. The water amount was decreased during the operation. In addition, access to the ambient atmosphere to the reactor when not in use allowed potential adsorption of water on the electrodes. Gas temperature and wall temperature were close to the room temperature (T≈300 K), and no substantial heating of the device due to the presence of plasma has been noticed. During the measurement, slow removal of the absorbed water from the walls due to the presence of gas flow occurs. Gas temperature effect on water concentration is negligible, and there is very little gas heating in this device. At higher RF power of 30 W, higher $c(O_3)$=12.7 ppm was observed after 5 minutes of operation, indicating a positive effect of the discharge power on $O_3$ production. This trend was not observed when aerosol was introduced: the humidity of the trapped gas was significantly higher $c(H_2O)$=1175 ppm increasing to $c_2(H_2O)$=1500 ppm during the same time of 5 min, while ozone concentration was constant at $c(O_3)$=3.5 ppm. The observed lower ozone concentration in the case of aerosol introduction is very probable due to the quenching of O atoms (precursor of $O_3$ production) by $H_2O$ with the formation of OH radicals. No presence of any traces of $N_xO_y$ products was revealed, which agrees with OES results where NO is shown to be very weak, see Figure 5.3. This observation indicates that the generation of reactive nitrogen species in RF plasma operation in the air with and without aerosol is very ineffective and can be neglected in analyzing the plasma-initiated chemistry in a liquid target.
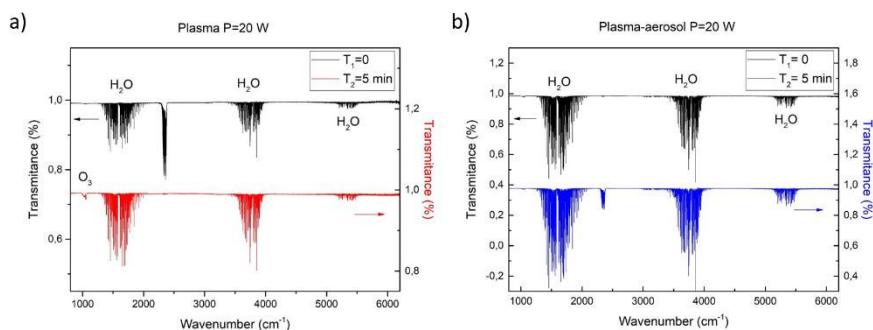
Figure 5.6 FTIR spectrum in the range 800-6200 cm$^{-1}$ of a) argon plasma jet, b) plasma jet in contact with aerosol at power P=20W.

## 5.4.2. DEPOSITION/PRODUCTION OF RONS IN TREATED LIQUIDS

Due to the importance of plasma-induced chemical processes in liquid media for biomedical applications, a chemical analysis of RONS in liquid was performed. Short-lived reactive species, such as atomic oxygen ($^{\bullet}O$), singlet oxygen ($^{1}O_2$), ozone ($O_3$), hydroxyl radicals ($^{\bullet}OH$), superoxide anion radicals ($O_2^{\bullet-}$), and hydrogen radicals ($^{\bullet}H$) were analyzed via EPR. The deposition of long-lived reactive species in the treated liquid target was investigated by ion chromatography (nitrite, $NO_2^-$ and nitrate, $NO_3^-$) and a colorimetric assay (hydrogen peroxide, $H_2O_2$).

## 5.4.2.1. SHORT-LIVED REACTIVE SPECIES

Figure 5.7 presents measured BMPO peaks and the simulated BMPO-adducts for 60 s treatment on the distance 12 mm. Using BMPO as a spin trap, hydroxyl radicals ($^{\bullet}OH$), superoxide anion radicals ($O_2^{\bullet-}$), and atomic hydrogen ($^{\bullet}H$) were detected in the liquid target after treatments with plasma and plasma-aerosol as presented in Figure 5.8. The measured concentrations of BMPO-OH represent ≈ 0.6% of the accumulated hydroxyl radical concentration during the treatment according to the published trapping efficacies [321], and 90% of the less reactive and more easily trapped superoxide anion radical (BMPO-OOH) [322]. For the hydrogen atoms (BMPO-H), no trapping efficacy for BMPO is reported. Given a similar lifetime in the gas phase, a trapping efficacy similar to $^{\bullet}OH$ radicals may be assumed. Therefore, significant amounts of hydroxyl radicals ($^{\bullet}OH$) and hydrogen atoms were detected, along with considerably lower amounts of $O_2^{\bullet-}$.
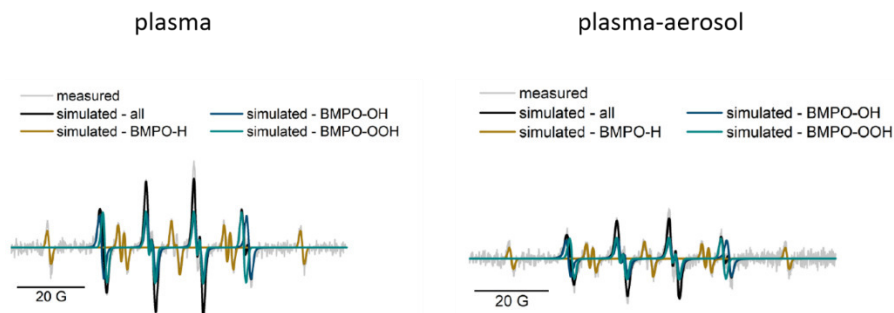
Figure 5.7. Spectra of the measured BMPO peaks and the different simulated BMPO-adducts for plasma and plasma-aerosol t=60 s and d=12 mm treatment.

Interestingly, the observed species concentrations as a function of treatment time and distance are similar, suggesting a common origin of the three species. All the three radicals can be formed most likely by the interaction of water molecules with gas-phase species, such as Ar metastables [323-326], radicals (e.g., $^\bullet$O), or ozone decay products [327-329]. However, ozone formation is not favored in the discharge, as FTIR data showed trace amounts only. In Figure 5.4, VUV/UV emission from the plasma ring has been presented as a function of the distance from the nozzle to the optical detector. Interestingly, in the direction of the gas flow, a high level of VUV emission from $Ar_2^*$, O I, and N I states has been still detected on the longest distance of 12 mm, suggesting an important role of VUV radiation on plasma driven liquid induced chemistry at long distances to the target. Namely, photolysis of the water can be induced by radiation from plasma below 180 nm originating from argon excimers $Ar_2^*$ ($\lambda$=126 nm), atomic oxygen OI ($\lambda$=130 nm), and nitrogen NI ($\lambda$=149 nm) and can be responsible for the formation of ROS in the liquid phase.

In the presence of the aerosol, a slightly lower deposition of $^\bullet$OH, $O_2^{\bullet-}$ and $^\bullet$H in the liquid bulk was observed, pointing towards the aerosol droplets acting as scavenger partners for high reactive/energetic species. Especially (V)UV radiation below 180 nm, leading to the photolysis of water because of intensive radiation of $Ar_2^*$ excimers and OI and NI emission, is absorbed due to the presence of the droplets. Similarly, the generation of other species is quenched due to the large effective interaction area of the aerosol droplets with the effluent in comparison to a treated liquid bulk (see Section 5.3.4). The effect of UV radiation above 200 nm on liquid chemistry is considered to be low with and without aerosol due to water transparency for such radiation and low level of emission in that region (see Figure 5.4 region 200-300 nm).

Since no spin probes were injected by the aerosol route, these OH radicals were lost to recombination and other secondary reactions and did not contribute to the EPR signals of the liquid bulk, leading to its reduction in the presence of the droplets. This indicates that the de-novo formation of species occurs mostly at the gas-liquid interface of a droplet or bulk liquid, outcompeting the deposition of species formed in the gas phase. This assumption is supported by previous works, where $^\bullet$OH formed in the gas phase due to humidity was not transported in the liquid [330-331]. Alongside, a transport of $^\bullet$H and $O_2^{\bullet-}$ by the droplets to the liquid bulk was not observed and the species decayed before reaching the spin traps/spin probes.
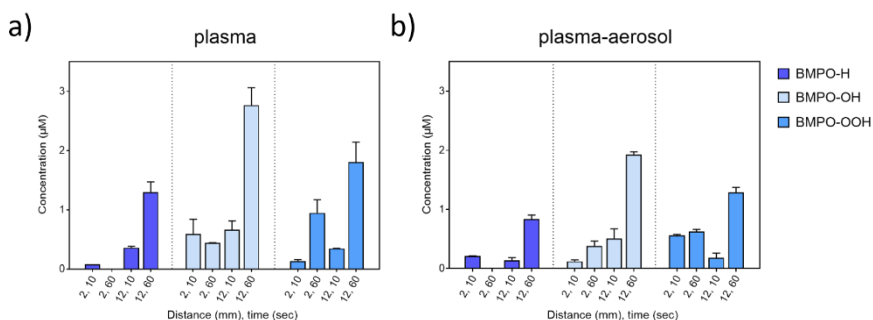


Figure 5.8. BMPO-adduct concentrations after a) plasma and b) plasma-aerosol treatment for 10 and 60 s, 1.5 mL water, at 2 and 12 mm distance. RF power of 30 W. Trapping efficacies are not considered ($^\bullet$H unknown, $^\bullet$OH 0.6 %, and $O_2^{\bullet-}$ 90 %).

Further insight into RONS production was realized by examining the deposition of $O_3$, $^1O_2$, and $^\bullet$O were measured using TEMPD. In contrast to BMPO, TEMPD is a spin probe, which means it reacts with reactive species without binding the species to itself. Therefore, it is not giving a characteristic spectrum for different species, and identification is not possible [317, 332]. However, when considering the species with different lifetimes, useful information could be obtained. In Figure 5.9, the detected and simulated peaks of the TEMPD-adduct are given for 60 s and 2 mm treatment distance.
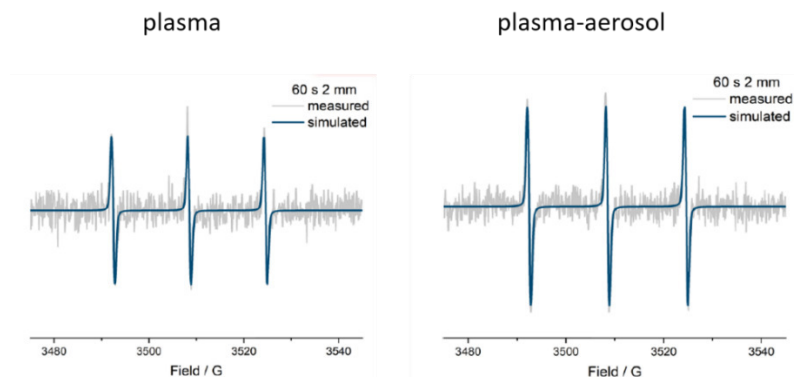
Figure 5.9. Spectra of the measured TEMPD-HCl peaks and the different simulated TEMPD-adduct for plasma and plasma-aerosol t=60 s and d=2 mm treatment.

In contrast to the BMPO-adducts, the detected concentrations decreased with increasing treatment distance and increased with treatment time (Figure 5.10). For 12 mm distance, no signal was detected indicating that long-lived ozone is not relevant for this plasma source. Since the formation of $O_3$ takes place via a three-body reaction of $O_2$ and $^•O$ with a third partner [317, 333], the concentrations usually increase with higher distances [317, 334]. However, as shown by FTIR spectroscopy data (Section 5.4.2), the ozone formation in the gas phase was low (12.7 ppm maximum with an applied plasma power of 30 W), probably due to the low density of molecular oxygen in the effluent required for $O_3$ production [335]. In contrast, signals at 2 and 6 mm show the presence of short-lived atomic ($^•O$) and/or singlet oxygen ($O_2(a^1\Delta_g)$) that are exclusively generated in the gas phase, via a reaction between argon metastables and $O_2$ [52, 333, 336].
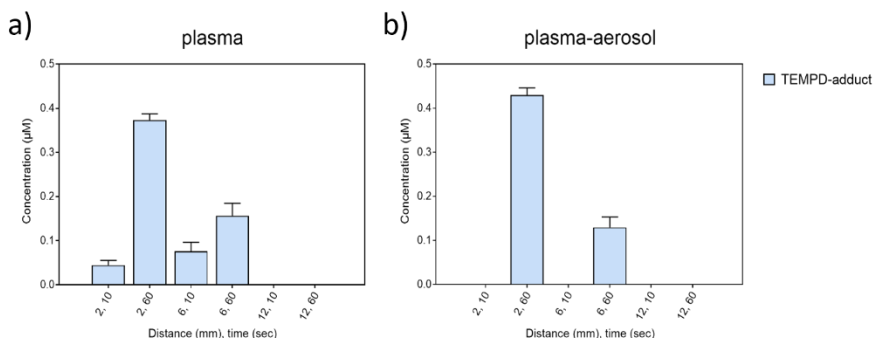


Figure 5.10. TEMPD-adduct concentrations for the detected species after different treatment times (10, 60 s) for 2, 6, and 12 mm: a) with and b) without the aerosol presence.

128

Atomic oxygen is highly reactive and reacts with $^\bullet$OH, yielding $HO_2^\bullet/O_2^{\bullet-}$ [331], or with $H_2O$ yielding two $^\bullet$OH radicals. It has a short lifetime under ambient atmosphere conditions and is quickly quenched, forming molecular oxygen and ozone. This explains the absence of TEMPO active ROS for 12mm distance and a small but detectable amount of product for 2 and 6 mm and 10 s treatment in dry/non-aerosol conditions. Indeed, the presence of aerosol could scavenge the deposition of $^\bullet$O by interacting with the water droplets in the gas phase[337-338]. The second (less abundant) candidate responsible for the EPR signal of TEMPD in both plasma with and without aerosol is $O_2(a^1\Delta_g)$. The slight increase of TEMPD-adduct in the presence of the aerosol may suggest transport of $O_2(a^1\Delta_g)$ in the aerosol droplets when distances and transfer times are short (2 mm $\approx$ 10 ms), however, given the lifetime of 20 μs the contribution of the transport is limited.

### 5.4.2.2. LONG-LIVED REACTIVE SPECIES

The long-lived reactive species hydrogen peroxide ($H_2O_2$), nitrite ($NO_2^-$), and nitrate ($NO_3^-$) were quantified (Figure 5.11). Nitrite and nitrate can be considered final stable products of the short-lived nitrogen species, such as peroxynitrite, $^\bullet$NO, or $^\bullet$NO$_2$ radicals [318-319]. In the same way, hydrogen peroxide, an almost ubiquitous product of cold plasma discharges formed, e.g., by the recombination of $^\bullet$OH radicals or disproportion of superoxide anion radicals [318-319]. The deposited amount of $H_2O_2$ was significant, also in comparison with other plasma sources [311, 339]. This reflects an intensive production of $^\bullet$OH radicals in the gas and/or liquid phase. In contrast, the deposition of nitrite and nitrate was below the average, indicating a strong dominance of oxygen species, which is in agreement with the FTIR results. The presence of aerosol reduced the deposition of $NO_x^-$ ions further, indicating that primary species, namely $N_xO_y$ molecules, are generated in the plasma region and not in the plasma/aerosol droplets interface. Additionally, the low solubility of $N_xO_y$ in aqueous media contributes to the observation.

The presence of the aerosol suppressed the deposition of $H_2O_2$ significantly in comparison to plasma-only treatments. In the presence of the aerosol, an increased deposition with time was observed, while in its absence, an inverse relationship appeared. This decay of $H_2O_2$ in plasma-only conditions could be due to (V)UV radiation-driven photo-dissociation in liquid or the reaction of $H_2O_2$ with atomic oxygen at the interphase. The argon-specific excimer on 126 nm emits UV radiation capable of cleaving H-O bonds. For longer distances, deposition decreased due to the lifetime of the precursor species OH and $O_2^-$ and decay and competitive reactions occur.
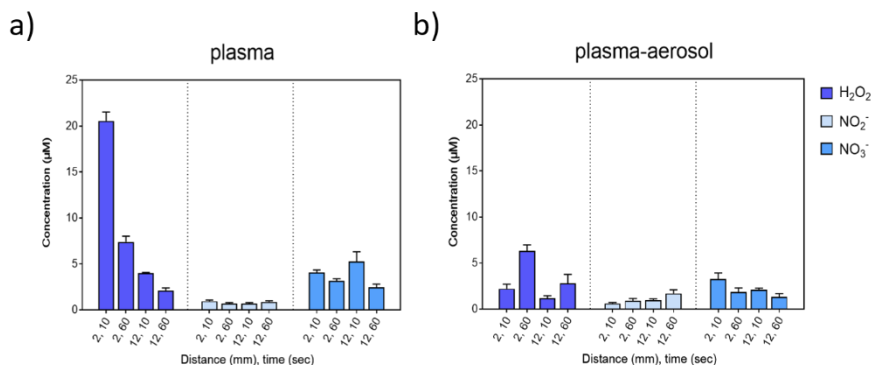
Figure 5.11. Hydrogen peroxide ($H_2O_2$), nitrite ($NO_2^-$), and nitrate ($NO_3^-$) concentrations for the detected species after different treatment times (10, 60 s) for 2 and 12 mm: a) with and b) without the aerosol presence.

Among these, the discussed interaction between OH radicals and atomic oxygen is most prominent. Furthermore, the photo-dissociation of long-lived species (or their precursors, e.g., $^\bullet NO_2$) occurring by increasing the treatment time could contribute to their decomposition in liquid both for N-containing species [340-341] and for hydrogen peroxide [340, 342-345], mainly due to Ar excimers radiation ($\lambda_{MAX}$ = 126 nm), see Figure 5.4. To support this hypothesis, the high amount of species from water photolysis in long distances with plasma-only, shown in Figure 5.7. Even on long distances (12 mm) away from the effluent, there is a significant amount of VUV/UV detected (Figure 5.4). Ar excimer intensity drops only 20% from shortest (2 mm) to longest considered distance (12 mm). Consequently, it has to be noted that on longer treated distances (12 mm), UV radiation has a leading role in plasma-induced liquid chemistry. As previously discussed, the impact of radiation, as well as other reactive species in the gas phase (e.g., $^\bullet O$ and $^1O_2$), is reduced by the presence of aerosol. This is a crucial observation considering that VUV/UV radiation can impact the density of long-living species in the liquid media. However, it has to be mentioned that (V)UV may also have a negative effect due to a direct impact on biological samples, e.g., via lipid or protein photo-oxidation. Correspondingly, aerosol injection seems to be an effective method to control the amount of (V)UV radiation reaching the target and plasma-induced chemistry in the liquid phase.
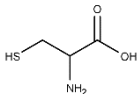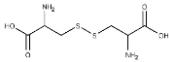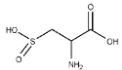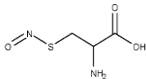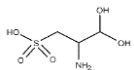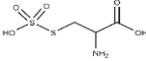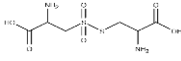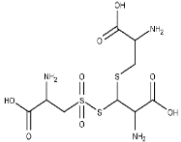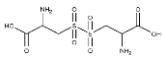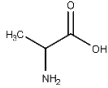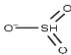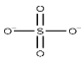
### 5.4.3. CYSTEINE OXIDATION IS MODULATED BY THE AEROSOL

Significant oxidation of cysteine was observed with the thiol group as the main target (Table 5.4). Depending on the treatment, oxidation levels of cysteine

vary: for short treatments, compounds with a lower oxidation number of sulfur dominate, such as cystine (2), cysteine sulfinic acid (3), cysteine *S*-sulfonate (6), and cysteine sulfoxides (7-9). These intermediates are not stable and are further oxidized by strong oxidizing conditions (e.g., long treatments, short distances), resulting in compounds with high oxidation states of sulfur, such as cysteine sulfonic acid (5) and sulfate (13), both end products of the cysteine oxidation pathway[311]. Some of the products indicate the presence of certain reactive species[346]: cystine for the presence of $H_2O_2$, cysteine-*S*-sulfonate for $^\bullet$OH radicals, cysteine sulfonic acid for gas-phase ROS ($^\bullet$O, $^1O_2$), and cysteine sulfinic acid for both short-lived ROS ($^\bullet$O, $^1O_2$) and water-derived $^\bullet$OH. Control measurement excluded the effects of argon flow on cysteine. For the treatment of liquid targets without cysteine in the aerosol, a direct electron transfer was excluded since the effluent did not touch the liquid. The impact of heat was estimated by control tests performed by incubating cysteine for 1 min at 100 °C. A conversion of 17% cysteine to cystine was observed, and no other cysteine products were detected.

Species such as $O_2^{\bullet-}$ could not be detected by using this model due to their low reactivity towards the thiol moiety in a physiological pH. While the anion sulfite $SO_3^-$ is potentially involved in the formation pathway of the *S*-sulfonate [347-349], the sulfate ion $SO_4^-$ is formed by over-oxidation of cysteine. Those two and the cysteine fragment alanine could be formed by plasma-derived (V)UV radiation alone via cleavage of the C-S bond and subsequent oxidation of the SH radical [350-352].

Table 5.4. Major cysteine derivatives induced by plasma treatment

| | Name | Formula | [M-H]⁻ (m/z) | Reactive species* | Structure |
|---|---|---|---|---|---|
| 1 | Cysteine (RSH) | $C_3H_7NO_2S$ | 120.0119 | none |  |
| 2 | Cystine (RSSR) | $C_6H_{12}N_2O_4S_2$ | 239.016 | $^\bullet OH$, $H_2O_2$ |  |
| 3 | Cysteine sulfinic acid (RSO₂H) | $C_3H_7NO_4S$ | 152.0017 | $^\bullet OH$, $^\bullet O, ^1O_2$ |  |
| 4 | S-nitrosocysteine (RSNO) | $C_3H_5N_2O_3S$ | 149.0021 | $^\bullet NO$, $N_2O_3$, $^\bullet NO_2$, $ONOO^-$ |  |
| 5 | Cysteine sulfonic acid (RSO₃H) | $C_3H_7NO_5S$ | 167.9967 | $^\bullet O$, $^1O_2$, $O_3$ |  |
| 6 | Cysteine S-sulfonate (RSSO₃H) | $C_3H_7NO_5S_2$ | 199.9687 | $^\bullet OH$ |  |
| 7 | Cysteine disulfoxide I (RSO₂RS) | $C_6H_{12}N_2O_6S_2$ | 271.0056 | $^\bullet OH$, $H_2O_2$ |  |
| 8 | Cysteine disulfoxide II (RSO₂RSSR) | $C_9H_{16}N_3O_8S_3$ | 390.0100 | $^\bullet OH$, $H_2O_2$, $^\bullet O$, $^1O_2$, $O_3$ |  |
| 9 | Cysteine disulfoxone (RSO₂RSO₂) | $C_6H_{10}N_2O_8S_2$ | 301.9879 | $^\bullet OH$, $H_2O_2$ |  |
| 10 | Alanine (R) | $C_3H_7NO_2$ | 88.03985 | Radicals, photolysis |  |
| 11 | Sulfite (SO₃⁻) | $SO_3$ | 79.95681 | Radicals, UV, ROS |  |
| 12 | Sulfate (SO₄⁻) | $SO_4$ | 95.95173 | Radicals, UV, ROS |  |

The observed cysteine derivatives varied significantly with applied plasma power, treatment time, and distance. Quantitative data were obtained by using multiple reaction monitoring (MRM). The key molecules in the cysteine oxidation pathway (cysteine – RSH (1), cystine – RSSR (2), cysteine $S$-sulfonate – RSSO$_3$H (6), sulfinic acid – RSO$_2$H (3), and sulfonic acid - RSO$_3$H (5)) were quantified by HPLC-MS in absolute units. The MRM technique is both sensitive and specific, relying on the detection of specific fragment ions.
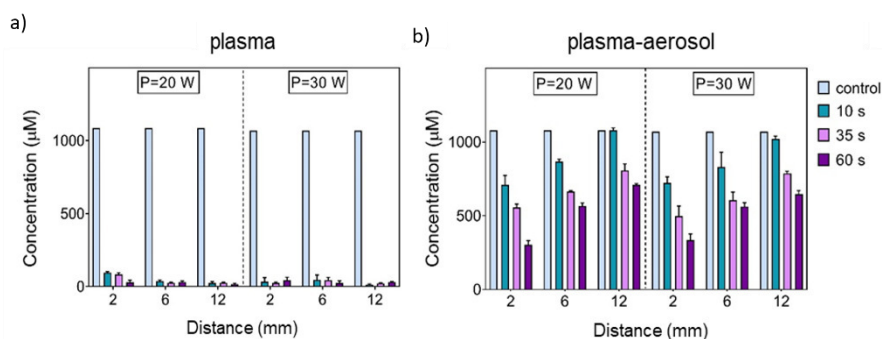


Figure 5.12. Absolute cysteine concentration after treatment of a cysteine solution by a) plasma and b) plasma-aerosol. Power (20/30 W) and distance (2/6/12 mm) were modulated. Water injection into the plasma source massively changed reactive oxygen species output – the cysteine turnover is decreased markedly. See text. Mean of three independent experiments +SD.

Without aerosol injection, a strong distance and treatment time-independent cysteine oxidation was observed (Figure 5.12). Almost complete oxidation of the available cysteine was observed, and the residue was below 5%. In contrast, the presence of aerosol droplets reduced the oxidation efficacy markedly, and the residual cysteine ranged between 100 % (20 W, 12 mm, 10 s) and 30 % (30 W, 2 mm, 60 s). This indicates a "softer discharge" with a sharply decreased output of reactive oxygen species. The short-lived gas-phase species O and $^1$O$_2$ are quenched by the presence of the water, and at the droplets surface, water is cleaved, forming $^\bullet$OH radicals that do not survive the travel time (10 ms/2 mm).

In contrast, when cysteine solutions are treated plasma (without aerosol injection), the local formation of $^\bullet$OH and $^\bullet$H by radiation and impact of argon metastables is promoted (see EPR data), and the additional impact of the short-lived gas-phase species atomic O and $^1$O$_2$ leads to the observed strong cysteine oxidation (Figure 5.13). Their presence is distance-dependent; the significant drop of the

cysteine-S-sulfonate (6) at 12 mm distance proves the limited availability of atomic oxygen at the gas-liquid interface and subsequently $^\bullet$OH radicals in accordance with previous results [346].



Figure 5.13. Absolute concentrations of cysteine derivatives after treatment by plasma (cysteine in target) at 30 W power. Time and distance were modulated. Mean of three independent experiments +SD.

The formation of highly oxidized cysteine derivatives was still substantial at 12 mm distances. This highlights the potential of the RF jet to produce reactive species surviving 6 mm and more travel distance such as singlet oxygen and (V)UV radiation (see Figure 5.4). With these elements replacing the atomic oxygen, changes related to the distance were less significant than in the plasma-aerosol mode (Figure 5.14). Cystine could be generated by recombination of thiyl radicals (RS$^\bullet$) formed in reaction with $^\bullet$OH and $^\bullet$H or by reaction with $H_2O_2$ [353-354]. The synergistic effect of singlet oxygen and radiation is possibly reflected in sulfite and sulfate production. Indeed, radiation (vacuum UV) impacts cysteine molecules yielding C-S breakage (bond energy 272 kJ mol$^{-1}$) [340]. The formed product could be further oxidized by oxygen species, e.g., singlet oxygen, to sulfate.

In the presence of the aerosol, the yield of the observed products changed, with some decreased (Table 5.4, compounds 2, 6, 12), others increased (Table 5.4, compound 11) or remained at a similar level as under non-aerosol conditions (Table 5.4, compounds 3, 5). Obvious is a significant influence of the treatment distance, showing an inverted correlation with the product yield (e.g., cysteine sulfonic acid (5)). The pattern confirms the scavenging role of aerosol droplets in the effluent area

for radiation and short-lived oxygen species. The resulting •OH radicals are lost with distance leading to the observed loss in the yields of •OH-dependent derivatives (RSSR, RSSO$_3$H). Such, the formation of cysteine-S-sulfonate (Table 5.4, compound 6) occurred almost 10 fold lower in the aerosol condition. In the presence of aerosol droplets, the formation of the stable derivative cysteine sulfonic acid (RSO$_3$H) increased with treatment time and decreased significantly with the distance. In contrast, the distance was of minor impact in the plasma treatment (Figure 5.13). Backed up by the EPR data (Figure 5.8, 5.10) and the H$_2$O$_2$ deposition (Figure 5.11), atomic oxygen and singlet oxygen represent the most likely candidates to explain this formation pattern. Only small amounts of H$_2$O$_2$ and OH radicals are deposited in the aerosol mode at short distances. In contrast, TEMPD-adducts show the occurrence of singlet oxygen for both conditions and the presence of atomic oxygen at short distances/plasma-only conditions, along with the formation of cysteine sulfonic acid. The transport of $^1$O$_2$ in the liquid droplets might occur for short distances, yielding to the high concentrations of sulfonic acid in this case. This assumption is not fully backed by the EPR data (Figure 5.10); however, due to the fact that the reaction probability with the respective spin probe/label does not allow absolute quantification, the transport might not be reflected to a full extent. The $^1$O$_2$ deposition further leads to the decay of intermediate products (RSO$_2$H, RSSO$_3$H), yielding sulfonic acid (RSO$_3$H) for long treatments.
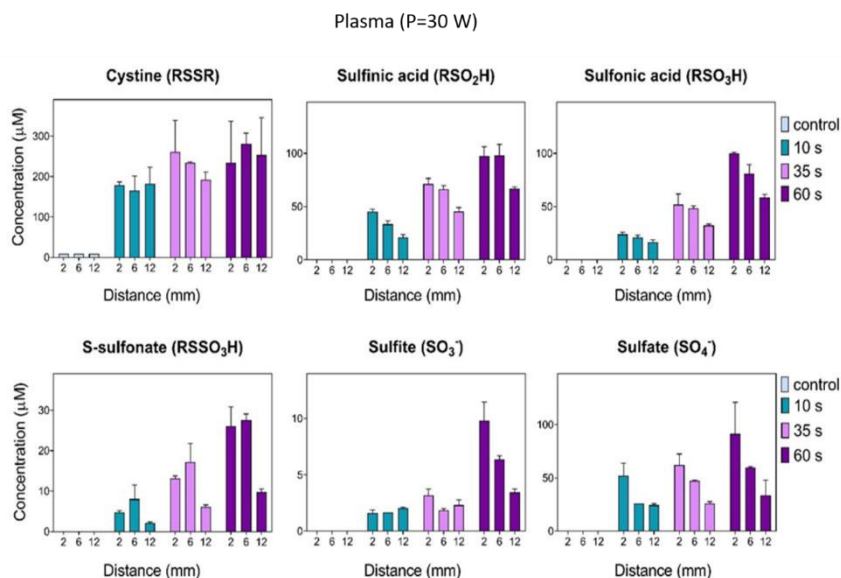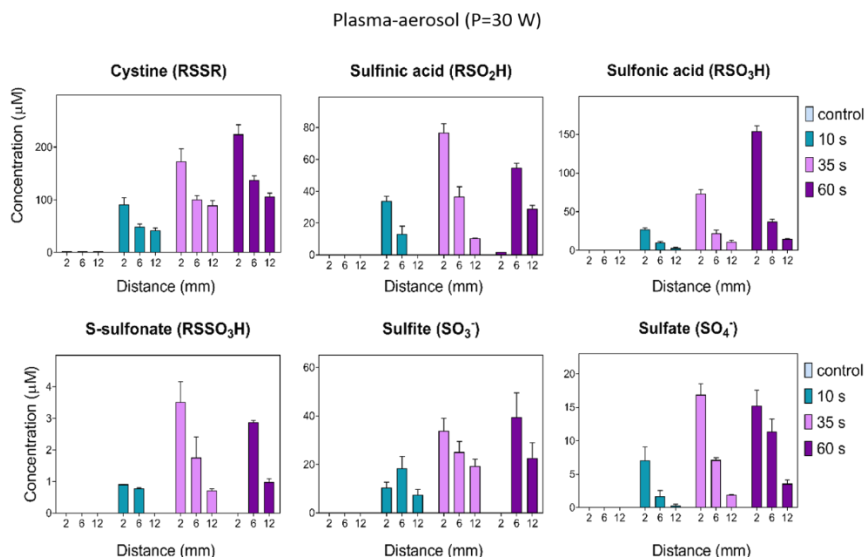


Figure 5.14. Absolute concentrations of cysteine derivatives after treatment by plasma with aerosol (cysteine in target) at power 30 W. Time and distance were modulated. Mean of three independent experiments +SD.

An interesting and not fully resolved pattern is present for the two ions sulfite and sulfate, that both represent fragmentation products of cysteine. They can be formed by different pathways, including the impact of (V)UV radiation. The decrease of sulfate deposition in the presence of aerosol confirms the role of the droplets as scavengers for radiation and reactive species. Absolute concentrations of cysteine derivatives obtained during low power, P=20 W plasma, and plasma-aerosol treatment are given in Appendix.

### 5.4.4.2. LIQUID CHEMISTRY INDUCED IN THE AEROSOL DROPLETS

The plasma-induced chemistry in the aerosol droplets was investigated to determine the reactive species formed inside and what their fate is during the transport (Figure 5.15).
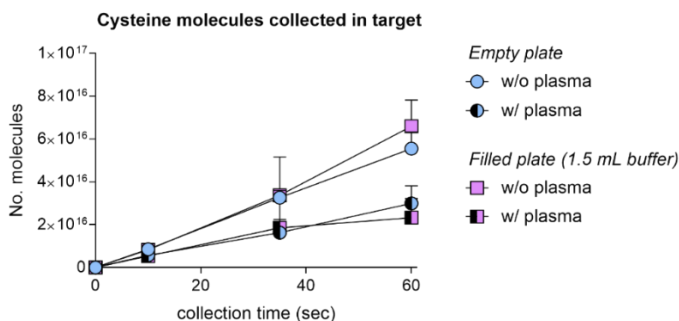


Figure 5.15. Cysteine turnover in aerosol droplets passing the plasma source with plasma off (full symbols) or plasma on (divided symbols) collected into empty wells (circles) and water-filled wells (squares). Plasma power 30 W, 2 mm distance to the target (setup 1 and 2). Cysteine oxidation occurs in the droplet during the passage of the effluent.

When introducing cysteine into the aerosol droplets, a significant extent of oxidation was observed. The extent depended on the traveling time – with a longer distance between nozzle and target (either dry collection into plate or water), yielding stronger cysteine oxidation. For the 2 mm case, when aerosol droplets remain approximately 10 ms in the effluent zone, 37 % ± 1.4 and 39 % ± 1.8 of the available cysteine was oxidized. This impact was independent of collection time (10 s – 60 s), indicating that the majority of the reactions take place during the droplets transport to the target and not in the collection liquid/the droplet formed during collection. When quantifying the major cysteine derivatives for diverse distances and collection times (Figure 5.16), similar cysteine derivatives as for the treatment of a cysteine solution were observed. For longer distances, slightly higher amounts of the

sulfinic acid (RSO$_2$H) and the S-sulfonate (RSSO$_3$H) were observed while the dominant product, cysteine sulfonic acid, remained unchanged. This sulfonic acid is a marker for short-lived gaseous ROS (e.g., O, $^1$O$_2$, [346]) showed a distance-insensitive behavior and accumulated during treatment time - its formation. However, this only occurred during the passage through the active plasma jet zone emphasizing the interaction of the gas phase species with the surface of the droplets (Ar excimers and (V)UV photons, $^\bullet$O, $^1$O$_2$). The formation of OH radicals seems to extend beyond the visible effluent zone (2 mm) for some time, as the increased formation of RSO$_2$H and RSSO$_3$H with distance suggests. These results confirmed the potential carrier role of droplets in short distances, as well as their scavenging role towards radiation and reactive species in longer distances in favor of the production of water homolysis species (Figure 5.13).
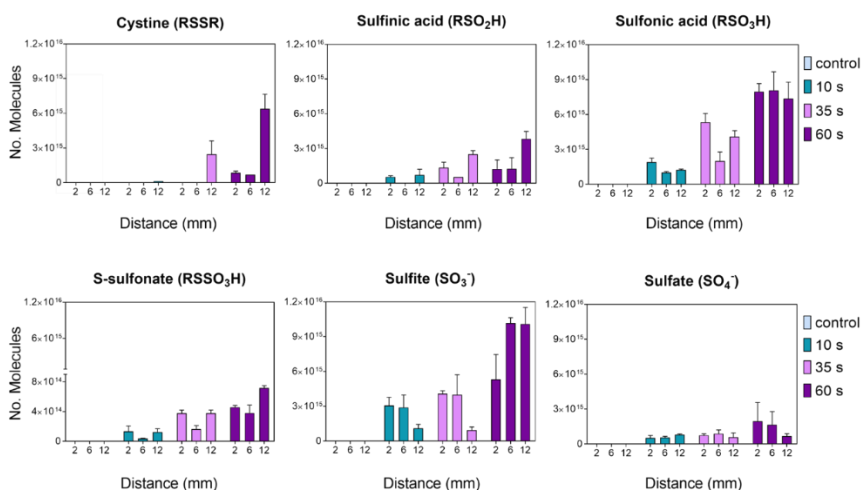


Figure 5.16. Major cysteine conversion products were observed in cysteine-enriched aerosol droplets. Plasma power 30 W (cysteine in aerosol), collected in water-filled wells. The absolute number of molecules deposited is given. The limited impact of distance indicates that most reactions occur in the droplets.

### 5.4.4.3. CYSTEINE CONVERSION PATHWAYS BY RONS

In this chapter, plasma interaction with liquid phase was investigated in 3 different model systems, namely, (i) plasma with cysteine in liquid target; (ii) plasma with aerosol and cysteine in liquid target; (iii) plasma interaction with cysteine-enriched aerosol injection into the effluent. The effectiveness of different setups in cysteine oxidation and its conversion into derivatives are recalibrated in percentages % for clearer comparison (Figure 5.17). Additionally to the schematic of the cysteine

oxidation, a complete overview for different treatment distances is summarized in Table 5.5.
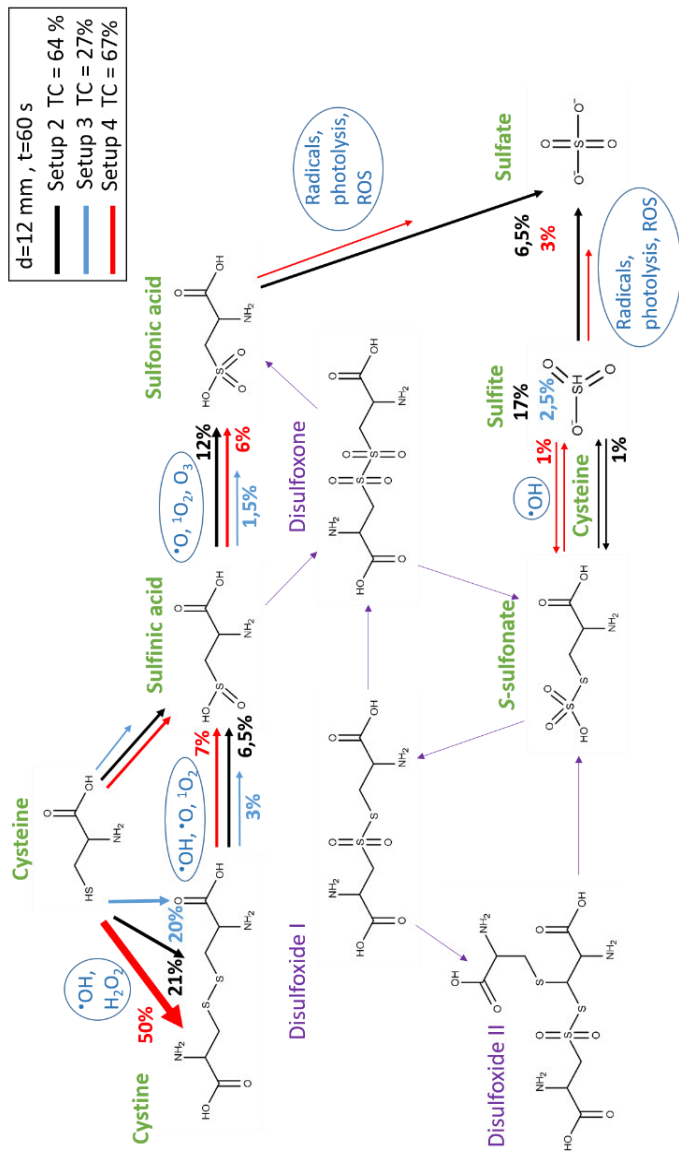


Figure 5.17. Cysteine oxidation pathway example and its total conversion for experimental parameters P = 30 W, d = 12 mm, t = the 60s. Generation of six major cysteine derivatives in Setup 2 (cysteine in aerosol, black), Setup 3 (plasma with aerosol-cysteine in target, blue), and Setup 4 (plasma-cysteine in target, red) is presented in percentage for better comparison of processes. The quantified derivatives are labeled in green color.

As expected, the conversion of cysteine is highest for the direct plasma treatment of a cysteine-containing target liquid. In this case, the distance is of little importance, and conversion is still massive at 12 mm. In contrast, when the discharge is injected with water droplets, the cysteine oxidation drops significantly even for a 2 mm distance and further with increasing distance to the nozzle (Table 5.5). When the aerosol is enriched with cysteine, the observed product portfolio indicates that most of the reactions occur in the droplet during the passage of the visible effluent (10 ms/2 mm). The increase of the metastable cysteine products S-sulfonate and sulfinic acid with increasing distance show a residual formation of hydroxyl radicals beyond the effluent visible margins. A summary of the model and the observations made are presented in Figure 5.18.

Table 5.5. Cysteine conversion into six quantified derivatives during the treatment time of 60 s for treatment distances 2, 6, and 12 mm from effluent in Setups 2, 3 and 4.

| Setup | Treatment distance (mm) | Cysteine conversion (%) |
|---|---|---|
| Setup 2 Plasma treatment of cysteine in aerosol liquid | 2 | 45 |
| | 6 | 50 |
| | 12 | 64 |
| Setup 3 Plasma-aerosol treatment of cysteine in liquid target | 2 | 60 |
| | 6 | 43 |
| | 12 | 27 |
| Setup 4 Plasma treatment of cysteine in liquid target | 2 | 78 |
| | 6 | 83 |
| | 12 | 67 |
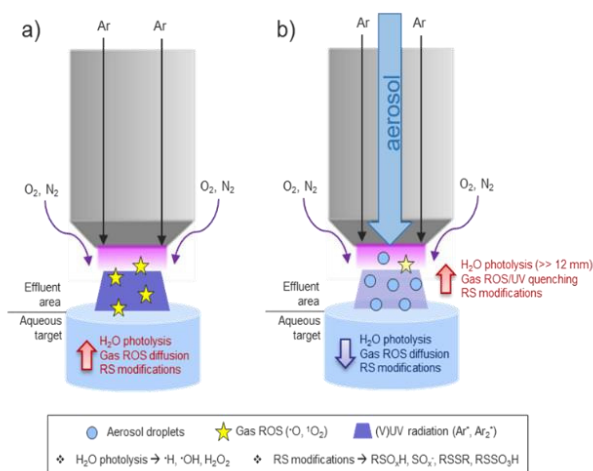
Figure 5.18. Schematic representation of initiated chemistry of treated liquid by plasma (a) and plasma with aerosol droplets in the effluent area (b).

## 5.5. CONCLUSIONS

RF plasma jet in combination with aerosol injection in the effluent has been developed for biomedical purposes, namely as a support in the field of chronic wound healing and transdermal drugs delivery. In this chapter, the emphasis has been made on the effect of the aerosol injection in effluent on induced RONS chemistry in the treated liquid. The chemistry at plasma/liquid interface and liquid chemistry induced in the effluent area and liquid target of an RF plasma jet was analyzed using cysteine as a bait molecule, particularly focusing on the role of aerosol droplets in the effluent. The deposition of $^\bullet OH$, $O_2^{\bullet -}$, and O, $^1O_2$, and $O_3$ was measured via EPR, and the long-lived species $H_2O_2$, $NO_2^-$, and $NO_3^-$ were quantified by colorimetric assays and ion chromatography. Data analysis revealed that UV radiation (e.g., VUV of Ar excimers), followed by short-lived reactive oxygen species (e.g., $^\bullet O$, $^1O_2$), are the dominant active elements in the studied RF plasma jet. Acting directly on the liquid target or the aerosol droplets, cysteine oxidation products and water photolysis products ($^\bullet OH$, $^\bullet H$) were observed.

By controlling distance, treatment time, and the presence of aerosol droplets, the liquid phase chemistry can be adjusted in a wide range. Short-lived gaseous species (e.g., $^\bullet O$, $^1O_2$) were detected predominantly for short distances, and in parallel, distinct cysteine oxidation products were observed, confirming ROS potential biological impact. In the presence of aerosol droplets, the impact of these species was diminished significantly, yet cysteine sulfonic acid, a marker for gas-phase ROS at the gas-liquid interface, was still detected. Taking the EPR data into account, it was concluded that singlet oxygen $^1O_2$ prevails for middle and long distances (6 - 12 mm) and in the presence of aerosol. The impact of (V)UV radiation

140

on the liquid target was strong, leading to photo-dissociation of water molecules as well as cysteine and the formation of short-lived radicals (e.g., $^\bullet$OH, $^\bullet$H, SH), as confirmed by EPR and the detection of sulfite/sulfate by mass spectrometry. Again, the presence of aerosol droplets in the effluent quenched the (V)UV photons and related reactions in the target. Instead, water molecules in the droplets were attacked, forming, e.g., OH radicals at the droplets gas-liquid interface. The transport of species formed in or solvated by the droplets was found to be of minor importance. This hypothesis was confirmed by introducing cysteine solution directly in the form of aerosol droplets and the observation of cysteine derivatives produced predominantly by OH radicals (cystine, sulfinic acid, cysteine-*S*-sulfonate). The impact of (V)UV radiation was observed by the formation of sulfite from cysteine-containing droplets.

In conclusion, the chemical potential of the investigated RF plasma jet coupled with aerosol allows it to be tuned in a wide range, proposing its application for various biomedical purposes. The intense synergistic effects of radiation and short-lived gaseous species achieved by using the plasma-only mode could be relevant for cancer treatment. In contrast, softer conditions, including aerosol droplets, could limit the impact of radiation and other gaseous radical species and be of interest in the wound care field and delivery of drugs through the skin where any possible side effect of VUV/UV has to be avoided.

In the next chapter, a detailed investigation of VUV/UV emission from plasma is carried out. Learning about the high photochemical activity of Ar plasma, the biological effect of UV radiation has to be established and well understood. Accordingly, plasma UV radiation is filtered out, exposing biomaterials to its flux. Potential biological risks of plasma and  UV radiation from plasma are studied in biomolecules, cells, and tissues. Finally, as a result, we use obtained knowledge of selective ROS quenching and UV absorption property of aerosol to customize safe plasma treatment.

# CHAPTER 6: PLASMA DAMAGE CONTROL – FROM BIOMOLECULES TO CELLS AND TISSUES

The results of Chapter 5 are published in the following international journal:

## 6.1. INTRODUCTION

In Chapter 6, the role of aerosol in plasma effluent has been examined as having a role in plasma damage control. Special attention studied here has been given to the importance of UV radiation in biological treatments. It has been shown that vacuum UV (VUV) radiation cannot be considered to be absorbed in Ar plasmas, but it rather propagates along medically important distances. To this end, protection in the form of an aerosol curtain has been proposed to scavenge the potentially damaging effect of VUV radiation in living tissues. The biological effect of plasma has been studied on biomolecule plasmid DNA, fibroblast cells in a wet and dry environment, and living tissue.

## 6.2. AEROSOL CURTAIN AS A DAMAGE CONTROL AGENT DURING TREATMENTS OF BIOLOGICAL TARGETS – BIOMOLECULES, CELLS, AND TISSUES

A key focus of today's medical research is in finding alternative healing methods for chronic diseases in order to decrease the use of medicines and solve the problem of pathogen resistance to drugs[95] (e.g., antibiotics in chronic wound healing therapy). Cold atmospheric pressure plasma (CAP) shows great perspective to be used as a therapeutic alternative for treating stubborn wounds in diabetic patients[175, 355-356]. CAP-assisted wound-healing is accomplished through simultaneous bacterial wound decontamination[357-358], induced coagulation[359-360], and stimulation of cell proliferation[361-362], resulting in healthy wound closure and no scarring[170]. Although a powerful source of radiation, particles, and electric field, the therapeutic efficiency of CAP is mostly ascribed to reactive oxygen and nitrogen species (RONS) production[363] and their effect on biomolecules[82, 364-365] and cells[366-368]. RONS $^\bullet$OH, $O_2^{\bullet-}$, $H_2O_2$, $ONOO^-$ cause oxidative damage and modification of cell membrane, proteins, lipids, and DNA[369], while $^\bullet$NO plays an important role in cell signaling by signal transduction mediators or by triggering molecules[55]. Therefore, the biological effect of CAP associated with RONS is often expressed through redox signaling and oxidative stress on essential macromolecules in prokaryotic and eukaryotic cells or their liquid surroundings[137, 370].

CAP radiation—vacuum ultraviolet (VUV) and ultraviolet (UV)—is helpful in heat-sensitive surface sterilization and decontamination[64, 371]. Having energy in the range of 4–12 eV, VUV and UV photons can dissociate crucial molecules present in a liquid medium and create free radicals $^\bullet$O, $^\bullet$N, $^\bullet$H, $^\bullet$OH in the surrounding cells. The contribution of VUV/UV radiation to RONS-driven inactivation of Escherichia coli in He/$O_2$ X-jet has been shown to enhance $O_3$ and water ion formation and bacterial inactivation[64]. Crucially, during plasma treatments of wounds, VUV/UV radiation reaches human skin. Therefore, its well-known genotoxic effect must be

evaluated[372]. Exposure of human skin to VUV/UV light causes DNA strand damage leading to crosslinking of pyrimidines, formation of stable thymine dimers, and mutation of skin cells[373]. Plasma radiation in the UVA ($\lambda$=315–400 nm, E<3.9 eV), UVB ($\lambda$=280–315 nm, E=3.9–4.4 eV), and UVC ($\lambda$=100–280 nm, E=4.4–12.4 eV) ranges is known to have different levels of biological impact related to genotoxic and carcinogenic effects[374]. Having different energies, UVC, UVB, and UVA have different penetration depths (1.5–60 $\mu m$[375]) in human skin, causing different biological effects[376]. UVB and UVA have been widely examined, and the health consequences of UV exposure are well known. Higher energy UVB is considered more carcinogenic than UVA; however, its mechanisms of action are different[377]. It has been shown that UVB-fingerprint DNA damage is located mainly in keratinocytes in the stratum granulosum, while DNA damage caused by UVA radiation is located in melanocytes in the basal layer of the epidermis. Radiation from atmospheric plasma is often neglected when studying plasma–sample interactions. This follows the assumption that energetic photons are mainly absorbed in ambient air or added diatomic gases ($O_2$[378]). Given a large amount of data and reporting on VUV/UV-caused DNA damage, it is clear that the harmful biological effects of UVA, UVB, and UVC must be considered in all plasma treatments and avoided accordingly.

Safe plasma treatment and careful dosage management of delivered species are essential. The high temperature during plasma treatment, high RONS flux, and energetic UV emissions can lead to cell and tissue damage and must be controlled[211]. Moreover, recent advances in biomedical sciences employ APPJs to locally functionalize and activate scaffolds for enhanced cell adhesion and controlled tissue growth[379] or 3D bio-print biomolecules and cells[380]. Following the development of APPJs based biomedical technologies, safe and controlled plasma treatment is required when operating with biomaterials. Therefore, in this chapter, a systematic investigation of the biological role of UV radiation from plasma its contribution to the plasma–target interface and interface control has been carried out.

One antibiotic-free, alternative wound healing approach is treatment by atmospheric pressure plasma jets (APPJs), wherein numerous reactive species are generated[165, 168, 381-382]. This study takes previous research a step further, presenting plasma-tailored wound therapy where drugs in the form of an aerosol are locally applied together with the plasma, and their topical penetration is accordingly promoted. Aerosol introduction in the plasma effluent in general decreases the temperature of the treated object[307]; introduced droplets evaporate in the effluent, having a cooling effect on the treated target (approximately 25 °C during 1 min plasma treatment). Moreover, aerosol droplets in the effluent change the plasma chemistry[383] and can limit the flux of UV plasma radiation towards the target, as shown in Chapter 5.

The presented RF plasma jet with aerosol injection has been developed for medical purposes to promote the healing process of chronic wounds and to enhance topical drug delivery. First, a detailed VUV/UV emission study has been performed and described. The effect of plasma and VUV/UV radiation ($\lambda > 115$ nm) have been examined on a fluorescent compound to define plasma–target interface and aerosol effects. Experiments with biological targets, biomolecules, cells, and tissues are described and analyzed in the next section. Respectively, the stability of plasmid DNA is studied under plasma exposure and VUV/UV radiation. Plasmid DNA serves as an excellent model to describe and quantify plasma interaction with biomolecules, and it is commonly used as an assay for genotoxicity[384]. *In vitro* experiments have been performed to study fibroblast cell proliferation in suspension 24 h and 72 h post-plasma treatments. To stress the biological importance of VUV/UV radiation emitted from plasma during the plasma treatments, the attached fibroblast cells without the medium were treated, and the effect of aerosol presence was evaluated. In the last section, a demonstration of mouse skin treatment with RF APPJ coupled with aerosol is presented, and safety aspects and treatment limitations are discussed.

## 6.3. MATERIALS & METHODS

### 6.3.1. ARGON APPJ COUPLED WITH AEROSOL

The design of the low-temperature argon plasma jet coupled with aerosol injection is presented in Figure 6.1 and described in Chapters 4,5 [385]. Powered and grounded electrode coaxial geometry allowed the formation of a plasma ring of 7 mm external and 6 mm inner radius, and effluent length 2–3 mm; photography of the plasma effluent can be seen in Figure 6.1 (a). The discharge was generated in pure argon 3 SLM flow in low (20 W) and high (30 W) power mode. The aerosol could be optionally introduced through the central hollow electrode into the plasma effluent, as shown on the enlarged nozzle scheme (Figure 6.1 (b)). Distilled water was used as an aerosol and was injected at a flow rate of 0.1 mL/min to a NexTgen ultrasonic spraying nozzle where it dispersed into micro-droplets of diameter $d \approx 20$ μm. Additional Ar gas flow of 1 SLM was added to the central gas channel to guide aerosol transport to the target and assure uniform and condensation-free operation of the jet. In this geometry, the aerosol droplets were only introduced into the plasma effluent. Accordingly, plasma parameters were not changed in the presence of the aerosol.
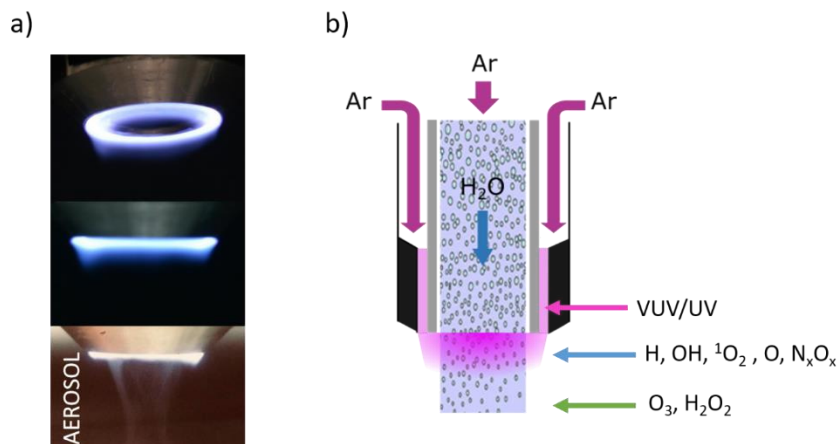
Figure 6.1. APPJ coupled with aerosol: a) photography of plasma jet; b) enlarged scheme of plasma nozzle and related species.

### 6.3.2. EXPERIMENTAL METHODOLOGY AND PLASMA TREATMENT

VUV/UV emission from plasma is primarily studied employing emission spectroscopy. Further investigation of the radiation effect on biological samples and its controllability with aerosol injection into effluent is carried out through a systematic set of experiments:

1) Plasma–target interface visualization and localization of VUV/UV emitters
2) Effect of plasma and VUV/UV radiation on plasmid DNA
3) Effect of plasma and VUV/UV radiation on mouse fibroblast cells
4) Effect of plasma-aerosol combination on mouse skin

The UV radiation from the plasma jet was investigated for three wavelength ranges. Total VUV/UV radiation was observed through a magnesium-fluoride ($MgF_2$) filter, transparent starting from $\lambda>115$ nm. A quartz optical filter was used for the detection of emission $\lambda>180$ nm from the source. Finally, UVA radiation was detected using a Pyrex glass filter, transparent above $\lambda>320$ nm. The transparency curve of the filters as a function of wavelength has been presented in Figure 6.2. The difference between transparencies of the three filters in the overlapping range of passing-through wavelengths is approximately 5% ($\Delta T\approx5\%$). Due to the qualitative character of this study and relative measurements of VUV/UV emission from plasma, no further correction on filters sensitivity has been made.
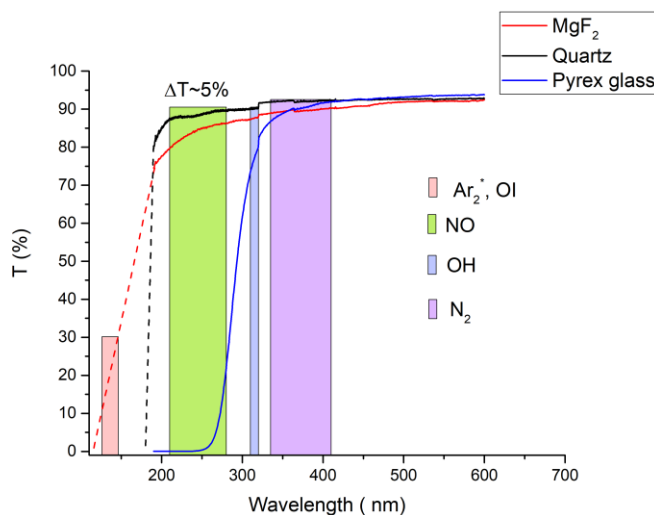
Figure 6.2. Transparency of the filters used in the study: $MgF_2$ – red, Quartz – black, and Pyrex glass – blue as a function of wavelength; wavelengths of the most important emitters considered in this study are presented.

The difference between transparencies of the three filters in the overlapping range of passing-through wavelengths is approximately 5% ($\Delta T \approx 5\%$). Due to the qualitative character of this study and relative measurements of VUV/UV emission from plasma, no further correction on filters sensitivity has been made.

To separate the radiation effect from the integral plasma effect and test the impact of aerosol presence on the plasma–sample interface, treatments were organized in five setups. Accordingly, the samples were treated with: 1) Plasma; 2) Plasma-aerosol; 3) Plasma VUV/UV $\lambda > 115$ nm; 4) Plasma VUV/UV $\lambda > 180$ nm; 5) Plasma VUV/UV $\lambda > 320$ nm. Moreover, the effect of power P=20, 30 W, treatment distance d=5, 8, 14 mm, and treatment time t=10, 35, 60, 120, 240 s were tested. It should be noted that the plasma effluent was 2 mm long and was not in direct contact with the treated substrate or biological samples. An overview of the experimental methodology is presented in Figure 6.3.

Figure 6.3. Experimental methodology. Schematics of plasma; plasma–aerosol and plasma VUV/UV treatment protocols. Performed analyses were respectively: 1) fluorescence imaging of the plasma-treated compound dichlorofluorescein (DCF); 2) stability of treated plasmid DNA using gel electrophoresis; 3) viability of treated fibroblast cells post-plasma treatment; 4) skin damage imaging.

### 6.3.3. VUV/UV SPECTROSCOPY AND RADIATION FROM ARGON APPJ

The VUV/UV spectra of APPJ in the range 115–350 nm along 14 mm (axial scanning) and across 20 mm (radial scanning) were recorded by the system presented in Figure 6.5 (a). The spectroscopic system consisted of a 200 mm focal distance monochromator with 1200 g/mm grating blazed on 50 nm (McPherson 234/302) and photomultiplier-tube PMT (Hamamatsu R2228). The grating was driven by step motor scanning with the wavelength scanning step of 0.3 nm. PMT detector was connected to the acquisition unit pico-amperemeter (Keithley 6485).

VUV/UV spectrometer was evacuated down to $10^{-6}$ mbar with Edwards turbo station vacuum system. $MgF_2$ window of the spectrometer inlet port provides detection of VUV/UV light emitted at wavelength down to 115 nm with transparency better than 70%. The plasma reactor was mounted on the X-Y translational stage for precise axial and radial scanning of the radiation emitted from the jet. For spatially resolved scanning of VUV/UV radiation emitted from the plasma, a slit of the monochromator was directly illuminated, as shown in Figure 6.5 (a). The slit was open at 100 μm, corresponding to a resolution of 1.3 nm at wavelength 130 nm. Emission of the main VUV/UV lines have been radially monitored to localize species generated in the plasma: argon excimers $Ar_2^*$ with a maximum of emission at 126 nm, atomic oxygen OI at 130 nm, and molecular nitrogen $N_2^*$ band with a maximum at 337 nm. Radial scanning has been performed along 20 mm, 10 mm left and right from the center of the nozzle with a 1 mm step. VUV/UV emission from the jet has been recorded only from the plasma active zone, as shown in Figure 6.5. Emission from the effluent was not possible to measure as the signal was below the detection limit. Accordingly, in this geometry, no VUV/UV emission from plasma together with aerosol was possible to measure. Aerosol deposition on the spectrometer window would lead to window contamination with water droplets, followed by the detection error and gradual dissolution of $MgF_2$. Mechanisms of excitation and ultraviolet photon emission detected and considered in this chapter are summarized in Table 6.1.

VUV/UV radiation filtration has been implemented by using optical filters $MgF_2$ λ>115 nm, Quartz λ>180 nm and Pyrex glass λ>320 nm. Transparency of the filters as a function of wavelength 190-600 nm has been recorded with spectrophotometer while the 110-190 nm range was extrapolated knowing the lower wavelength limitation of a filters transparency provided by the company, shown in Figure 6.2.

Following the qualitative character of this study and the interest in the localization of VUV/UV emitters, no absolute calibration of the VUV/UV system was made. Accordingly, intensities are presented in arbitrary units (a. u.).

Table 6.1. Mechanisms of UV emitters generation and their emission in Ar plasma.

| Emitters | | Emitter formation mechanisms | UV emission | $\lambda_{MAX}$ (nm) | $E_{hv}$ (eV) |
|---|---|---|---|---|---|
| UV A | $N_2{}^*$ | $e + N_2(X) \rightarrow N_2(C) + e$ <br> $N_2(A) + N_2(A) \rightarrow N_2(C) + N_2(X)$ | $N_2(C) \rightarrow N_2(B) + hv$ | 337 | 3.68 |
| UV B | OH | $e + H_2O^+ \rightarrow OH(A) + H$ | $OH(A) \rightarrow OH(X) + hv$ | 309 | 4.01 |
| | $NO_\gamma$ | $O + N_2(A) \rightarrow NO + N \Rightarrow$ <br> $e + NO(X) \rightarrow NO(A) + e$ | $NO(A) \rightarrow NO(X) + hv$ | 280 | 4.42 |
| UV C | N I | $Ar(4s) + N_2(A) \rightarrow Ar + N + N \Rightarrow$ <br> $e + N \rightarrow N(2p) + e$ | $N(2p) \rightarrow N(2p_0) + hv$ | 174 | 7.12 |
| | N I | $Ar(4s) + N_2(A) \rightarrow Ar + N + N \Rightarrow$ <br> $e + N \rightarrow N(2p) + e$ | $N(2p) \rightarrow N(2d_0) + hv$ | 149 | 8.32 |
| | N I | $Ar(4s) + N_2(A) \rightarrow Ar + N + N \Rightarrow$ <br> $e + N \rightarrow N(4_p) + e$ | $N(4p) \rightarrow N(4s_0) + hv$ | 119.5 | 10.4 |
| | O I | $e + O_2 \rightarrow O + O + e \Rightarrow$ | $O(3p) \rightarrow O(3s_0) + hv$ | 130 | 9.53 |

| | $e + O \rightarrow O(3p) + e$ | | | |
|---|---|---|---|---|
| O I | $e + O_2 \rightarrow O + O + e \Rightarrow$ <br><br> $e + O \rightarrow O(1d) + e$ | $O(1d) \rightarrow O(1d_0) + h\nu$ | 115 | 10.8 |
| $Ar_2{}^*$ | $e + Ar \rightarrow e + Ar^* \Rightarrow$ <br><br> $Ar^* + 2Ar \rightarrow Ar + Ar_2^*$ | $Ar_2^* \rightarrow 2Ar + h\nu$ | 126 | 9.8 |
| H I | $e + H_2O \rightarrow OH + H + e \Rightarrow$ <br><br> $e + H \rightarrow H(2s) + e$ | $H(2s) \rightarrow H(2p_0) + h\nu$ | 121.5 | 10.2 |

Imaging the oxidized fluorescent compound dichlorofluorescein (DCF) upon plasma exposure was employed to define the plasma–target footprints. During the interaction of plasma with the fluorescent target, DCF was oxidized. The plasma print contribution of VUV/UV radiation on the treated object oxidation and the aerosol effect on the plasma–sample interface was visualized. Experiments were carried out on the two fluorescent probes: 2',7'- dichlorofluorescein diacetate (DCFH$_2$)–DA non-fluorescent (not shown here) and 2',7'- DCF fluorescent. DCF assay is widely used to evaluate cellular stress in intracellular redox biology[386-387]. The experimental protocol for the extracellular DCF redox assay used in this chapter has been described in detail elsewhere[388]. For plasma print imaging, 500 µl of the probe was loaded on the porous polymeric PET fabric samples (representative of the skin surface) and immediately exposed to plasma. After the treatment, the samples were visualized under exposure to UV light at 254 nm radiation, and fluorescence patterns were recorded with a Nikon D3000 camera. To avoid any possible effect of sample heating, fluorescence control tests with sample heating up to 280 °C were performed. It was confirmed that DCF is thermally stable. This offers assurance that all chemical changes of DCF observed in tests were due to oxidation of the dye owing to the presence of RONS or VUV/UV emitted from the plasma, and any heating effect can be neglected. In Table 6.2. an overview of species that are expected to be responsible for dye oxidation and fluorinated product generation is presented.

Table 6.2. Map of the species expected to be responsible for DCF oxidation in corresponding setups: 1) Plasma; 2) Plasma-aerosol; 3) Plasma VUV/UV  λ>115 nm; 4) Plasma VUV/UV  λ>180 nm; 5) Plasma VUV/UV  λ>320 nm.

| Set-up | RONS | | | | | | | | VUV/UV emitters | | | | | |
|---|---|---|---|---|---|---|---|---|---|---|---|---|---|---|
| | $^1O_2$ | $O_2^{\bullet-}$ | $^\bullet O$ | $O_3$ | $NO_x$ | $^\bullet OH$ | $^\bullet H$ | $H_2O_2$ | $Ar_2^*$ | OI | NI | NO (A) | OH (A) | $N_2^*$ |
| 1 | + | + | + | + | + | + | + | + | + | + | + | + | + | + |
| 2 | + | + | + | + | + | + | + | + | + | + | + | + | + | + |
| 3 | | | | | | | | | + | + | + | + | + | + |
| 4 | | | | | | | | | | | | + | + | + |
| 5 | | | | | | | | | | | | | | + |

153

### 6.3.5. EFFECT OF PLASMA AND VUV/UV RADIATION FROM PLASMA ON PLASMID DNA

Plasmid DNA has been used as a model biomolecule to study extracellular DNA damage[212, 231]. Damage of this biomolecule is commonly used in radiation assays to study DNA damage of ionizing radiation[244]. Accordingly, fitting methods have been developed to follow the kinetics of plasmid damage and quantify its fragments attributed to single-strand break (SSB) and double-strand break (DSB)[384]. Plasmid encoding green fluorescence protein (GFP) under the control of the CMV promoter and neomycin resistance gene (pEGFP-N1, Clontech, Basingstoke, UK) was exposed in this thesis to plasma treatment and plasma-originated VUV/UV radiation. 10 μg of plasmid DNA was dissolved in 1.5 mL distilled water or phosphate-buffered saline (PBS) and placed into 60 mm Petri dishes. After the treatment, 20 μL suspension was extracted and mixed with 4 μL of loading buffer (Gel Loading Dye, Purple, 6x, no SDS, BioLabs Inc.). The mixture was loaded into 1% agarose gel together with a molecular weight ladder (Supercoiled DNA Ladder, BioLabs Inc.). Gel electrophoresis ran for 50 min powered by a voltage of 100 V. The gel was stained (with SYBR™ Gold nucleic acid gel stain, Invitrogen, Thermo Fisher Scientific) for 30 min, rinsed with distillated water and imaged by a Vilber Imaging Device (Collégien, France).

### 6.3.6. EFFECT OF PLASMA AND VUV/UV FROM PLASMA ON MOUSE FIBROBLAST CELLS

The biological effect of the jet was qualitatively and quantitatively investigated on mouse fibroblast cells. The L929 cell line originates from mouse skin tissue and, as such, presents a good model for studies on plasma–skin interaction. In this chapter, the integral plasma biological effect and separated VUV/UV radiation effect on cells was examined in terms of cell proliferation 24 and 72 h post-plasma treatment. Treatment times were varied in the range of 10–240 s to validate and optimize the plasma and VUV/UV effect on cell proliferation. In addition, to study the plasma effect, the aerosol injection was investigated concerning cell proliferation. The potential cytotoxic or proliferative impact of RF plasma and VUV/UV emission generated by the discharge on cells was investigated by Presto Blue and imaging of the cell confluence.

#### 6.3.6.1. L929 CELL LINE VIABILITY VIA PRESTO BLUE ASSAY

The plasma effect on mouse embryonic fibroblast cell line L929 was studied with Presto Blue assay. L929 murine fibroblasts (American Type Culture Collection, Manassas, VA, USA) were cultured in an advanced minimum essential medium (AMEM; Gibco, Thermo Fisher Scientific), supplemented with 5% fetal bovine serum (FBS; Gibco), 10 mL/l L-glutamine (GlutaMAX; Gibco), 100 U/mL penicillin

(Grünenthal, Aachen, Germany) and 50 μg/mL gentamicin (Krka, Novo Mesto, Slovenia) in a 5% $CO_2$ humidified incubator at 37 °C.

For cell viability assay, 1 x $10^6$ L929 cells were suspended in a 1.5 mL cell medium (MEM without phenol red, Gibco) to assure uniform treatment without spillage due to gas flow. After the treatment, 1000 L929 cells from each experimental group were plated in a 0.1 mL cell culture medium in 96-well plates (Corning Inc., Corning, NY, USA). Four replicates were used for each experimental group. All treatments were repeated in triplicate. Cells were incubated at 37 °C in a 5% $CO_2$ humidified incubator for up to 3 days. 24 h and 72 h after the treatment, 10 μL of Presto Blue® viability reagent (Thermo Fisher Scientific) was added to the wells, and 1 h later, fluorescence intensity was measured with a microplate reader (Cytation 1, BioTek Instruments). Cell viability of experimental groups was normalized to the control group of the corresponding day.

### 6.3.6.1.1. STATISTICAL ANALYSIS

All the results are presented with a standard error of the mean value. One-way ANOVA (t-test) statistical analysis was performed in GraphPad Prism 9 (GraphPad Software, Inc., CA, USA) to access statistically significant differences between experimental groups. Significance levels $P < 0.05$ (*), $P < 0.01$ (**), $P < 0.001$ (***), and $P < 0.0001$ (****) were tested among all experimental groups.

### 6.3.6.2. QUALITATIVE STUDY OF PLASMA TREATMENT ON ATTACHED CELLS

Plasma impact on cell viability and its pattern has also been examined when the surface of the attached cells was treated without the liquid medium. It is known that VUV/UV radiation completely absorbs at wavelengths below 200 nm in a cell medium of 200 μm thickness[63]. This indicates that plasma treatment of cells in a liquid medium is not representative of a realistic scenario when fibroblast cells are in contact with RONS/UV radiation. In the following tests, special attention was given to investigating the VUV/UV radiation effect on cells. One day prior to the treatment, 4 x $10^5$ cells were plated in 60 mm Petri dishes. Before the treatment, the cell culture medium was removed, and cells were treated as described above. Immediately after the treatment, a fresh cell culture medium was added, and treated cells were incubated at 37 °C in a 5% $CO_2$ humidified incubator for 24 h. After 24 h, the treated cells were imaged using Cytation 1 (BioTek Instruments). Confluence analysis of imaged Petri dishes was used to estimate the adherent cell percentage.

### 6.3.7. EFFECT OF PLASMA AND AEROSOL ON TISSUE: SKIN DAMAGE MODEL

Plasma-caused direct and indirect skin damage was tested on mouse skin. For this purpose, 10-week old female Balb/c mice (Charles Rivers) were plasma-treated in plasma effluent (d = 14 mm) for 35 and 60 s in the flank region. To assure safe treatment (T<42 °C), skin temperature was monitored with a thermal camera (Workswell WIC 640) in the temperature range 25 °C–150 °C and with a sensitivity of 0.03 °C; corresponding infrared (IR) image is presented in Figure 6.10(a, right). All procedures were performed in compliance with the guidelines for animal experiments of the EU directive (2010/63/EU) and with permission from the Veterinary Administration of the Ministry of Agriculture, Forestry, and Food of the Republic of Slovenia (U34401-1/2015/43). Mice were housed in pathogen-free conditions with 12 h light cycles and provided food and water ad libitum. At the end of the experiment, mice were humanely sacrificed by cervical dislocation. A day prior to plasma treatment, mice were shaved and depilated on the left and right flank. Mice were initially anesthetized with 150 μL intraperitoneal injection containing a mixed solution of 10 mg/mL ketamine (affiliation) and 1 mg/mL xylazine (affiliation) diluted in saline. Immediately after plasma treatment, mice were placed under a stereomicroscope (ZeissStereoLumar.V12, Zeiss, Jena, Germany). The first image was taken immediately after the treatment; the rest followed at 24 h and 48 h post-treatment. For the images taken 24 h and 48 h post-treatment, mice were firstly anesthetized with inhalation anesthesia in an induction chamber using a 2% isoflurane (Forane, AbbVie) mixture with oxygen. Under the stereomicroscope, they remained anesthetized under a constant supply of inhalation anesthesia delivered through an inhalation tube.

## 6.4. RESULTS & DISCUSSIONS

### 6.4.1. ORIGIN AND LOCALIZATION OF THE MAIN VUV/UV EMITTERS CONSIDERED IN BIOLOGICAL EXPERIMENTS

VUV/UV emission from argon plasma is dominantly characterized by the emission of argon excimers $Ar_2^*$. However, contributions to total VUV/UV emission are expected from molecular bands NO, OH, $N_2^*$ as a result of air and water penetration in plasma and atomic lines OI, Hα, NI. Dissociation energies with corresponding radiation wavelengths of crucial molecules leading to VUV/UV radiation from APPJs in Ar gas are summarized in Table 6.1. VUV/UV radiation emitted along the axial line from a plasma jet operating in ambient air at 30 W RF power and distances 5, 8, and 14 mm from the spectrometer optical port is presented in Figure 6.5 (b). Radial profiles of VUV/UV emission from the species $Ar_2^*$,

OI, and $N_2^*$ along with the 20 mm radial line are shown in Figure 6.5 (c). High intensities of OI and OH lines are mainly caused by water impurities in the feeding argon gas tubes. Nevertheless, the appearance of NO, NI, and $N_2^*$ is related to air intrusion into the plasma effluent, mainly in the region free of plasma, the inner electrode area. Atomic oxygen OI and argon excimer $Ar_2^*$ emission are the dominant VUV/UV emission of the jet, originating from the plasma region as shown in the radial profile representation, see Figure 6.5 (c).
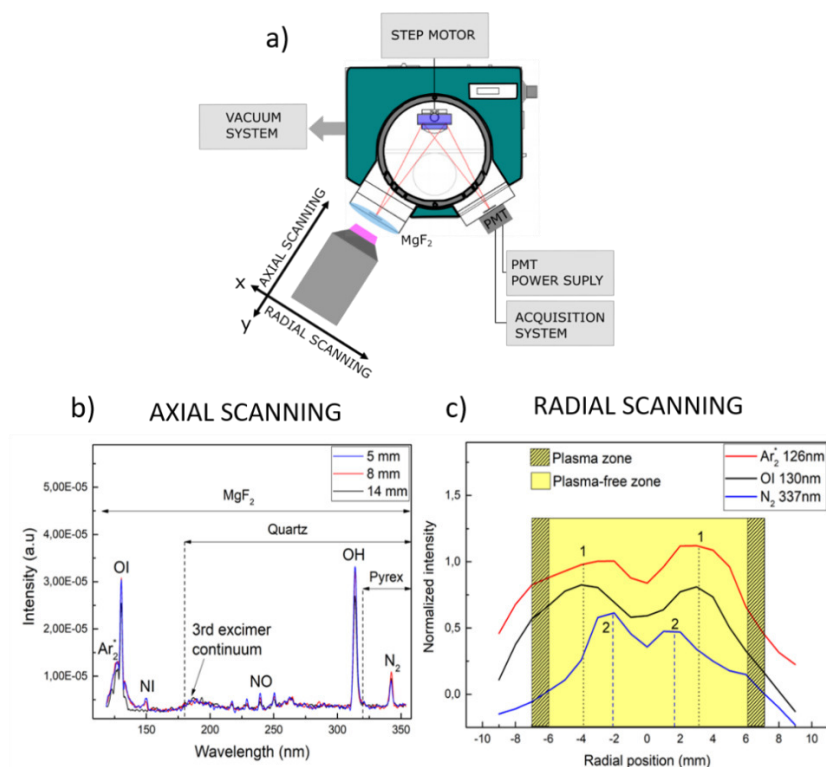


Figure 6.5. VUV/UV radiation from plasma detected in arbitrary units (a.u.): a) VUV/UV emission spectroscopy experimental setup; b) VUV/UV emission from APPJ generated in 3 SLM Ar, P = 30 W at distances 5, 8, and 14 mm from the optical port; c) radial profile of VUV/UV emission of $A_2^*$(red), OI (black), and $N_2^*$ (blue) at 5 mm axial distance. Points 1 and 2 correspond to the maximum of excimer and $N_2^*$ emission.

Scanning UV emission from the RF argon plasma jet in three positions (5, 8, 14 mm) along the axis showed no significant intensity drop with distance ($\Delta I \approx 15\%$). This result is important as VUV/UV radiation is expected to be absorbed in ambient air, and often its presence and potential risk in biomedical applications are

neglected. For the optimal treatment distance of 14 mm from the plasma nozzle, VUV/UV emission was still detected as photons traveled in the direction of argon gas flow. For safe human application and customization of biomedical plasma jets, the problem of inevitable VUV/UV plasma radiation presence should be considered and accordingly solved.

Radial position differences in the maximal emission of OI, $Ar_2^*$, and $N_2^*$ (1,2) indicate different spatial origins of the species and mechanisms of their excitation. Expectedly maximal emission of argon $Ar_2^*$ and oxygen species OI (1) is shifted with respect to $N_2^*$ emission (2) and clearly corresponds to the plasma region between the electrodes where excitation is caused by fast electrons (Table 6.1). Nitrogen excitation is associated with air intrusion in the plasma-free region, and it is consequently confined in the central area (0), as shown in Figure 6.5. (c). Opposite to OI, $Ar_2^*$ excitation of $N_2^*$ happens in close proximity to the plasma effluent. VUV/UV radiation from the jet in any direction except the front view results in a drastic emission decrease, clearly indicating that radiation is almost exclusively formed inside the plasma between the electrodes.

### 6.4.2. PLASMA–TARGET INTERFACE VISUALIZATION AND MAPPING OF THE SPECIES

In this chapter, the plasma–target interface is visualized during plasma treatment by means of fluorescence imaging. A plasma oxidation print on the fluorescent compound and the contribution of three plasma radiation ranges—respectively λ>115 nm, λ>180 nm, and λ>320 nm—are presented in this section. The effect of aerosol presence on the plasma–sample interface is also examined and visualized. It has to be emphasized that fluorescence imaging of the plasma print only gives qualitative results of the oxidized area. Nevertheless, this method provides sufficient information on the acting range of plasma and oxidative species localization. Upon exposure of the samples to the plasma, DCF is oxidized in the area that corresponds to the plasma zone (Figure 6.3). DCF is oxidized in the area where RONS and UV photons from the plasma reach and interact with the sample. This interface area is recognized employing fluorescence imaging and appears as degradation of fluorescent dye (green to blue). In the below-presented images, the edge between plasma and plasma-free regions is not always clearly distinguishable. This can be associated with the entrainment of air into plasma effluent and the contribution of RONS (e.g., $^\bullet NO$, $^\bullet OH$, $H_2O_2$) to DCF oxidation in the plasma-free region.

As expected, higher plasma power results in stronger oxidation in all conditions, as shown in the plasma and plasma–aerosol DCF oxidation map in Figure 6.6. In addition, longer treatment time and shorter distances result in stronger dye

oxidation due to stronger plasma impact, as demonstrated for the treatment time effect for d=5 mm and treatment distance effect for t=35 s in Figures 6.6.
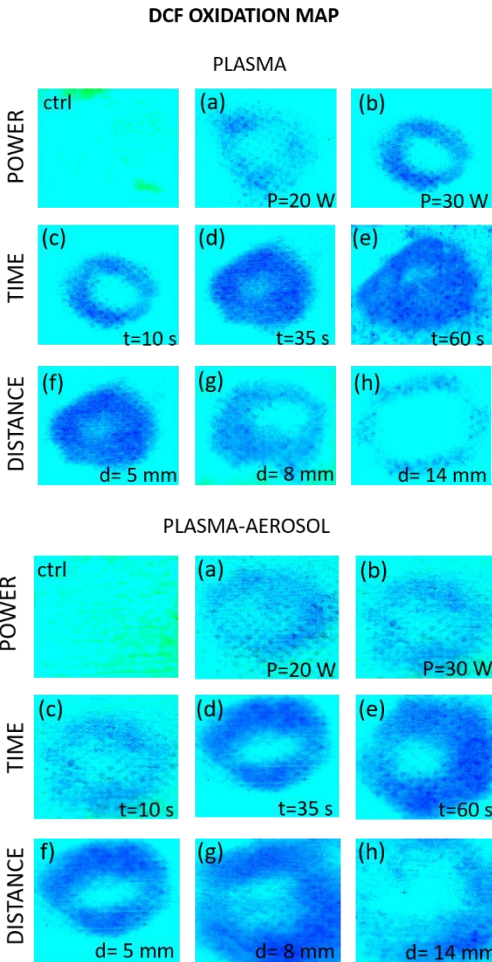


Figure 6.6. DCF oxidation map in plasma (upper) and plasma–aerosol treatments (bottom): power effect for t = 35 s, d = 5 mm plasma treatment; time effect for P = 30 W, d = 5 mm plasma treatment; distance effect for P = 30 W, t = 35 s plasma treatment. Image contrasts have been edited for better representation and comparison purposes. W x H of the presented samples is 35 mm x 30 mm.

DCF oxidation initially starts in the area that corresponds to the inter-electrode region and, with increasing treatment duration, expands towards the center, probably due to species diffusion. An annular-shaped plasma pattern is more

recognizable for higher power, while for lower power, the pattern is more diffuse. This is explained by the fact that species transport to the sample is dependent on plasma specific energy input (W × s/l), as well as increased air entrainment at lower plasma power, previously shown in Chapter 4 via Rayleigh scattering [385]. With increasing treatment distance, a decrease of the effective treatment area is evident, accompanied by an increase of the plasma-free zone, see Figure 6.6 (h). This is associated with the decrease of both RONS and VUV/UV photons reaching the target. Nevertheless, even at distances as long as 14 mm, considerable oxidation of DCF is visible.

The oxidation effect of filtered VUV/UV radiation from the plasma is weakened with respect to the total plasma effect. A comparison of the contributions of different plasma components to DCF oxidation is presented in Figure 6.7.
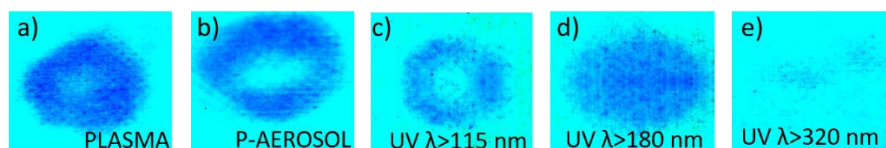


Figure 6.7.  DCF oxidation map in filtered treatment P = 30 W, d = 5 mm, t = 35 s: a) plasma, b) plasma–aerosol, c) plasma VUV/UV λ>115 nm, d) plasma VUV/UV λ>180 nm, e) plasma VUV/UV λ>320 nm. Image contrasts have been adjusted for better representation and comparison purposes. W x H of the presented samples is 35 mm x 30 mm.

VUV/UV radiation (λ>115 nm) affects the dyed sample, with the formation of patterns as presented in Figure 6.7 (c). VUV/UV radiation results in the formation of a well-defined annular-shape footprint revealing the dominant contribution of emission from argon excimers $Ar_2^*$, OI generated only in the inter-electrode gap. Emission from NO, OH, and $N_2^*$ molecules filtered by the quartz filter (Figure 6.7 (d)) has localization in the whole area of the jet, including the plasma-free zone. Finally, Pyrex glass filtered λ>320 nm UVA radiation mainly emitted by $N_2^*$ excited states has a negligible effect on dye decomposition (Figure 6.7 (e)). The effect of VUV/UV radiation has well-defined localization corresponding to the emission of radiative species generated in the inter-electrode area, with the size of the pattern matching the size of the jet.

The plasma–target interface has been visualized as the oxidized pattern of fluorescent compound DCF appearing because of VUV/UV radiation and RONS. The interaction between plasma and solid target starts in the plasma region and expands towards the plasma-free zone and external area due to species diffusion. VUV/UV radiation λ>115 nm and λ>180 nm from the plasma has a significant effect on the

oxidation of the DCF target. Interface imaging shows that VUV/UV emissions from Ar$_2$* and OI originate from the plasma ring. However, nitrogen species are introduced into the plasma effluent due to mixing with ambient air and diffusion towards the plasma-free zone; emissions of N$_2$ and NO are mainly detected in the plasma-free region, inside of the plasma ring.

The aerosol presence effect is noticeable in both the plasma-free zone and plasma zone (Figure 6.6 (b)). The plasma-free zone area that corresponds to the aerosol inflow is well screened from the oxidative effect of species localized in this area. In the plasma zone, aerosol presence results in weaker oxidation of the DCF sample but increased interactive area. Weaker oxidation can be ascribed to oxidative species quenched by aerosol droplets while the increased oxidized area is probably due to species-promoted diffusion in the direction of the gas flow.

In addition to our experimental results, modeling attempts have been made to confirm ambient air diffusion into the region controlled by plasma and the impact of aerosol on the interface area. Solid target treatment with heated argon gas in the corresponding flow geometry is simulated by the COMSOL Multi-Physics platform; model presented in SI in detail. In this 2D axial symmetry stationary model, only gas flow dynamics without plasma are assumed, and no chemical reactions are considered. Laminar flow of 3 SLM heated argon (340 K) is introduced between the electrodes flowing out in the air environment and hitting the solid target, as presented in Figure 6.8 (a). Streamlines of the argon velocity field in ambient air and air convective air flux in argon laminar flow are simulated and presented in Figure 6.8 (a, b) to explain air species penetration into the plasma effluent.
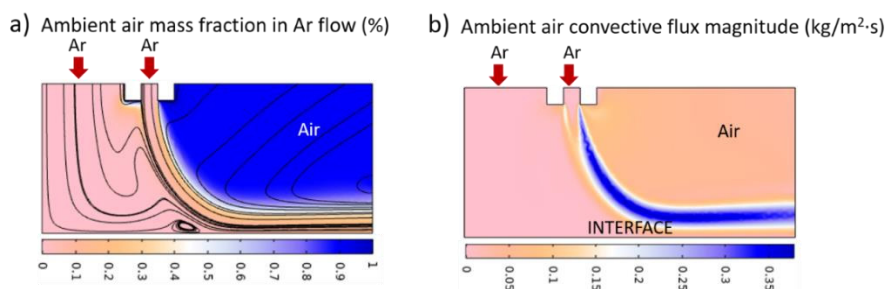


Figure 6.8 COMSOL model of plasma feeding argon in an annular-shape APPJ geometry 8 mm above the solid target: a) ambient air mass fraction (BLUE) in Ar flow (PINK) and argon velocity streamlines; b) ambient air (BLUE) convective flux magnitude simulated to confirm argon mixing with ambient air and incorporation of air species into argon flow and their consequent deposition in the interface area

Moreover, with the stationary laminar flow model, time-resolved visualization of aerosol droplets during 100 ms in the 6 mm interface area is

presented in Figure 6.9. This simple model considers only 100 water droplets of 20 µm diameter in the argon gas flow deposited on the solid target.

Ar velocity field and aerosol trajectory
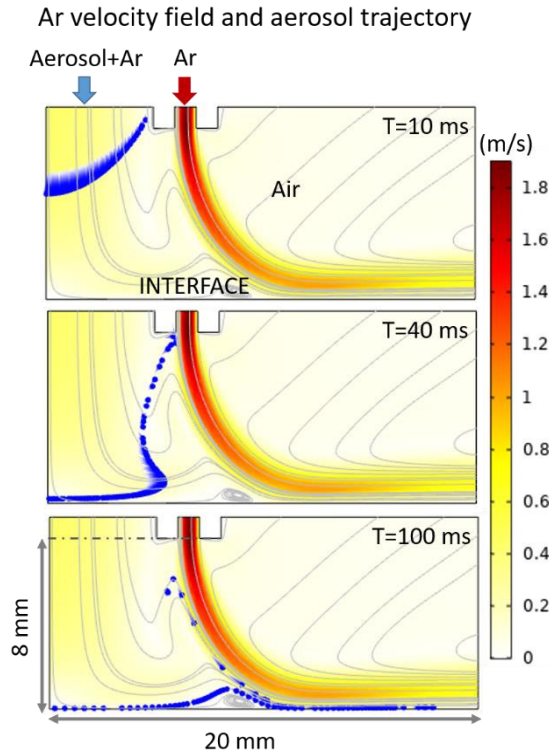


Figure 6.9 COMSOL model of time-resolved aerosol trajectory visualized at moments 10 ms (top), 40 ms(middle), and 100 ms (bottom) in the laminar Ar flow.

Even though argon flow is laminar, upon hitting the target, it forms swirls while mixing with ambient air and introduces air-originating species into the plasma region. Ambient air species can diffuse into the argon jet at lower velocity points, shown in Figure 6.8 (b). In this way, these can be introduced into a plasma and plasma region and consequently deposited on a treated surface. However, the gas flow model does not confirm air species presence in the inner plasma-free region. It must be emphasized that plasma changes gas flow dynamics[389], and absolute matching without including plasma into the model is impossible. A particle trajectory tracing model is used to introduce aerosol droplets into the model to explain their effect on the interface area. The model confirms the screening effect of aerosols in the plasma-free region (direction of aerosol injection), partial interaction with plasma feeding gas, and their spreading along with the interface in the direction of gas flow. The modeled spatial distribution of particles in the interface region can

explain the absorption of UV photons emitted in the direction of these droplets. Accordingly, the highest screening effect is in the plasma-free region. However, attenuation of UV flux can be expected in the plasma region as well due to the spreading of droplets with the gas flow (Figure 6.8 (c)). Aerosol presence in plasma effluent has been shown to absorb VUV/UV radiation and quenches some oxidative species (O, $O_3$) but also promotes transport of soluble RONS ($^1O_2$)[383], already demonstrated in the previous chapter. Moreover, promoted diffusion of soluble species in the direction of the gas flow increases the effective interactive area between plasma and the target, as visible in the experiments and COMSOL simulation.

### 6.4.3. PLASMA AND PLASMA VUV/UV RADIATION EFFECT ON BIOMOLECULES: PLASMID DNA

Damage of plasmid DNA due to exposure to oxidizing and ionizing agents is shown to be a good approximation for cell DNA damage before reparation processes start[212, 390-391]. The effect of an argon plasma jet coupled with aerosol and VUV/UV radiation from plasma was examined on plasmid DNA. Typically, commercial plasmid DNA (>90%) exists in supercoiled (SC) form. Another two heavier fragments were noticed in the non-treated plasmid DNA sample, as shown in the gel electrophoresis image (Figure 6.10 (a, b) (ctrl). Heavier fragments are normally relaxed or open circular (OC), linear (LIN), and heavy dimers (HD) due to plasmid DNA breaking and crosslinking[392-393]. The genotoxic effect of plasma was tested on plasmid dissolved in water in PBS, shown in Figure 6.10 (a) and Figure 6.10 (b), respectively. However, plasmid DNA dissolved in water upon plasma exposure underwent irregular cutting, and the yields of fragments could not be compared. Plasmid DNA was exposed to the effect of plasma, filtered UV radiation, and plasma–the aerosol combination at a distance of 6 mm and for 35 s in six plasma treatments. In agreement with previously reported results in Ref[212], the plasmid is more stable upon plasma exposure when dissolved in PBS due to the scavenging effect of the buffered solution. This is presented as a concentration of its original SC form relative to the control shown in Figure 6.10 (c). It can be seen that in the treated samples (1–6), the relative concentration of the original SC form decreases while the relative concentrations of fragments of higher molecular weight increase, Figure 6.10 (d). As previously reported in[212, 390], exposure of plasmid DNA to ionizing radiation or oxidative species from plasma results in damage of its original plasmid form, and plasma can damage plasmid DNA through SSB or DSB. According to a robust curve fitting model[384], the appearance of OC and LIN plasmid conformations can be directly associated with SSB and DSB processes.
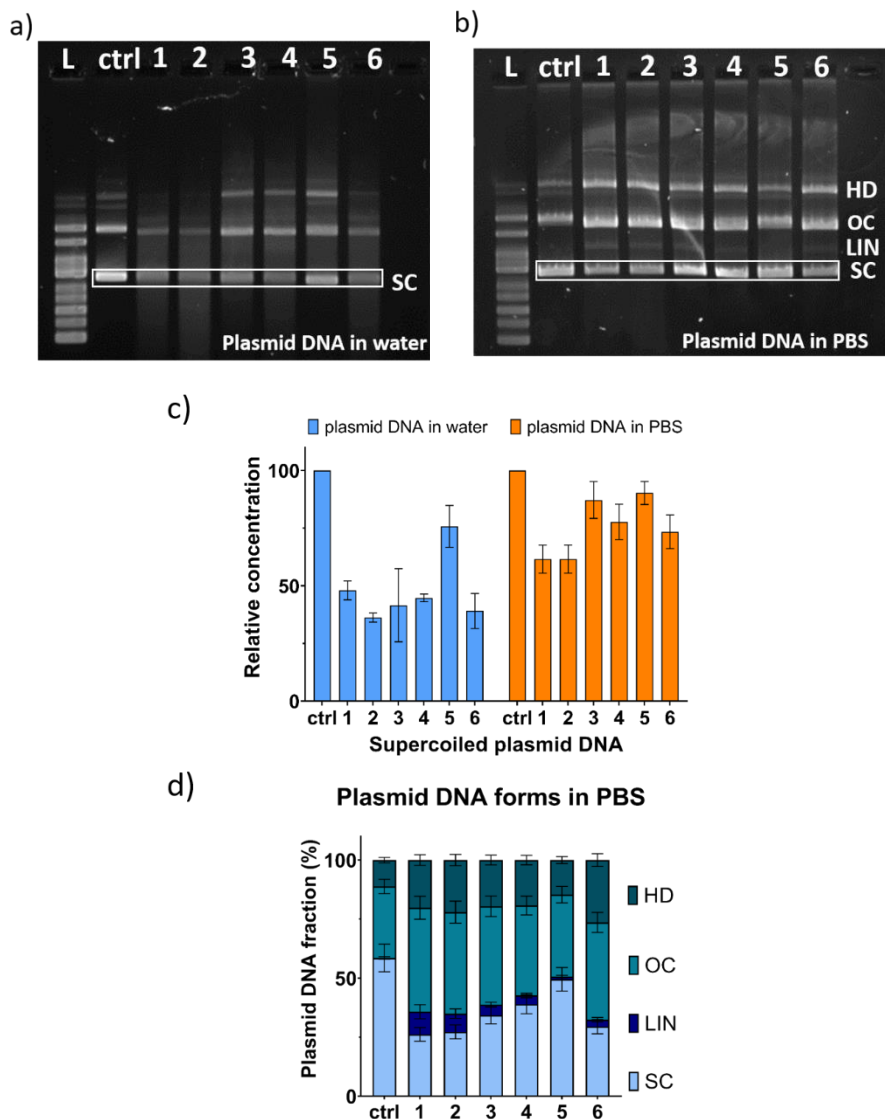
Figure 6.10 Image of gel electrophoresis of plasmid DNA treated in plasma treatments 1–6 in a) water and b) PBS. Column L refers to Ladder, Ctrl – untreated sample, 1- Plasma treatment P=20 W; 2- Plasma treatment P=30 W; 3- Emission λ>115 nm; 4 - Emission λ>180 nm; 5- Emission λ>320 nm; 6- Plasma–aerosol P=20 W in the treatment condition d=6 mm and t=35 s. c) Stability of plasmid original SC form when dissolved in water/PBS in corresponding treatments (1–6). d) Yields of plasmid forms SC, LIN, OC and HD in treatments (1–6) in PBS.

In all of the plasma treatments, the yield of original plasmid form SC decreases with the increase of fragments OC, LIN, and HD, indicating damage of plasmid DNA. The OC plasmid form appears in all of the treatments (1-6). However, the yield of the LIN form, which can be correlated with DSB processes[384], was the highest during plasma treatment. It is important to notice that the LIN plasmid form was not detected in the control sample and its appearance strongly correlates with the genotoxic effect of plasma. Accordingly, the appearance of this fragment was used to estimate the contribution of plasma radiation to the total genotoxic effect of plasma. Emitted energetic radiation from argon plasma has been shown to have a significant effect on plasmid DNA damage and must be considered in biomedical applications. The genotoxic effect of the plasma radiation λ>180 nm is estimated to contribute about 70% to the total plasma effect in the scavenging PBS environment and cannot be neglected in biomedical applications. The relative quantification of plasmids fragments is based on image analysis, and no correction of filters transparency has been made, hereby must be mentioned that the transparency of the quartz has a strong rising edge on 180 nm with the T≈90 %. As expected, plasmid DNA damage was lowest during UVA treatment (5). Simultaneous exposure to radicals and radiation from plasma has the strongest damage effect on plasmid DNA. However, VUV/UV radiation plays an important role in argon plasma treatments and therefore cannot be neglected. To further investigate the biological effect of VUV/UV radiation in plasma treatments, fibroblast cells in a cell medium were treated. Their viability 24 h and 72 h post-treatment were measured.

## 6.4.4. EFFECT OF PLASMA AND VUV/UV FROM PLASMA ON FIBROBLAST SURVIVAL WITH AND WITHOUT MEDIUM

### 6.4.4.1 PLASMA AND VUV/UV RADIATION IMPACT ON FIBROBLAST IN THE LIQUID ENVIRONMENT

Results of the viability of L929 cells treated with plasma, plasma together with aerosol, and UV radiation filtered out from plasma are shown in Figure 6.10. The integral plasma effect on fibroblast cells has been tested regarding treatment time for distances of 5, 8, and 14 mm from the nozzle. Statistical analyses show no difference in cell survival between the control group and group that corresponds to short plasma treatments (t<60s). Accordingly, these treatments have been defined as a safe operational range. However, overexposure of the cells in longer plasma treatments (t=240 s) resulted in a cytotoxic effect (d=5 mm) 24 h post-plasma treatment and (d=5, 8 mm) 72 h post-plasma treatment (Figure 6.11 (a)). Although no statistical difference between control and other experimental groups after 24 h has been recognized, the difference between short (t<60 s) and longer time (t>60 s) treatments is obvious (*,**). The treatment distance effect was mild, and there was

no statistical difference between experimental groups 5, 8, and 14 mm. Nevertheless, different behavior trends between short (t<60 s) and longer time (t>60 s) treatments were observed for 5, 8, and 14 mm treatments. At short distanced = 5/8 mm treatments, cell proliferation differences are more obvious, especially when comparing short (t<60 s) and longer time (t>60 s) treatments. In the case of treatments in the far effluent (d=14 mm), the difference of mean cell viability in terms of treatment time is less distinguishable. Mean cell proliferation, measured 72 h after the treatments, and corresponding significant differences have been presented to preserve visibility of results; used notation is given in Table 6.3. For example, experimental group D corresponding to d=5 mm and t=60 s is significantly different from control group A with a significance level ** p<0.001, but also with other experimental groups B, G, H, L, M, N as noted in the table with indicated significant differences.

Table 6.3. Experimental groups and their affiliations are presented in Figure 6.11.

| Experimental group | Affiliation |
| --- | --- |
| Control | A |
| 5 mm | B (10 s), C (35 s), D (60 s), E (120 s), F (240 s) |
| 8 mm | G (10 s), H (35 s), I (60 s), J (120 s), K (240 s) |
| 14 mm | L (10 s), M (35 s), N (60 s), O (120 s), P (240 s) |

The low dependence of mean cell proliferation on treatment distance suggests that dominant biologically active species are long-living RONS and VUV/UV radiation from plasma. Based on COMSOL calculation of gas velocity field, species capable of reaching the target are identified as those with the lifetime t≈25–70 ms: NO, OH, $^1O_2$, $O_3$, and $H_2O_2$. The aerosol injection into plasma effluent results in VUV/UV radiation absorption. This mode of operation, therefore, provides safe and controlled deposition of plasma-generated species and radiation into the environment of treated biological objects. The safe range of operation previously confirmed in plasma treatments (10–60 s) has been re-examined for the case of plasma with aerosol treatment, presented in Figure 6.11(b). Cell proliferation measured 24 h after plasma–aerosol treatment shows no significant statistical difference between the experimental group and control. This result confirms the safe range of operation and provides an opportunity to design further plasma-assisted medical treatments where cell viability must not be affected e.g. plasma-assisted topical drug delivery.
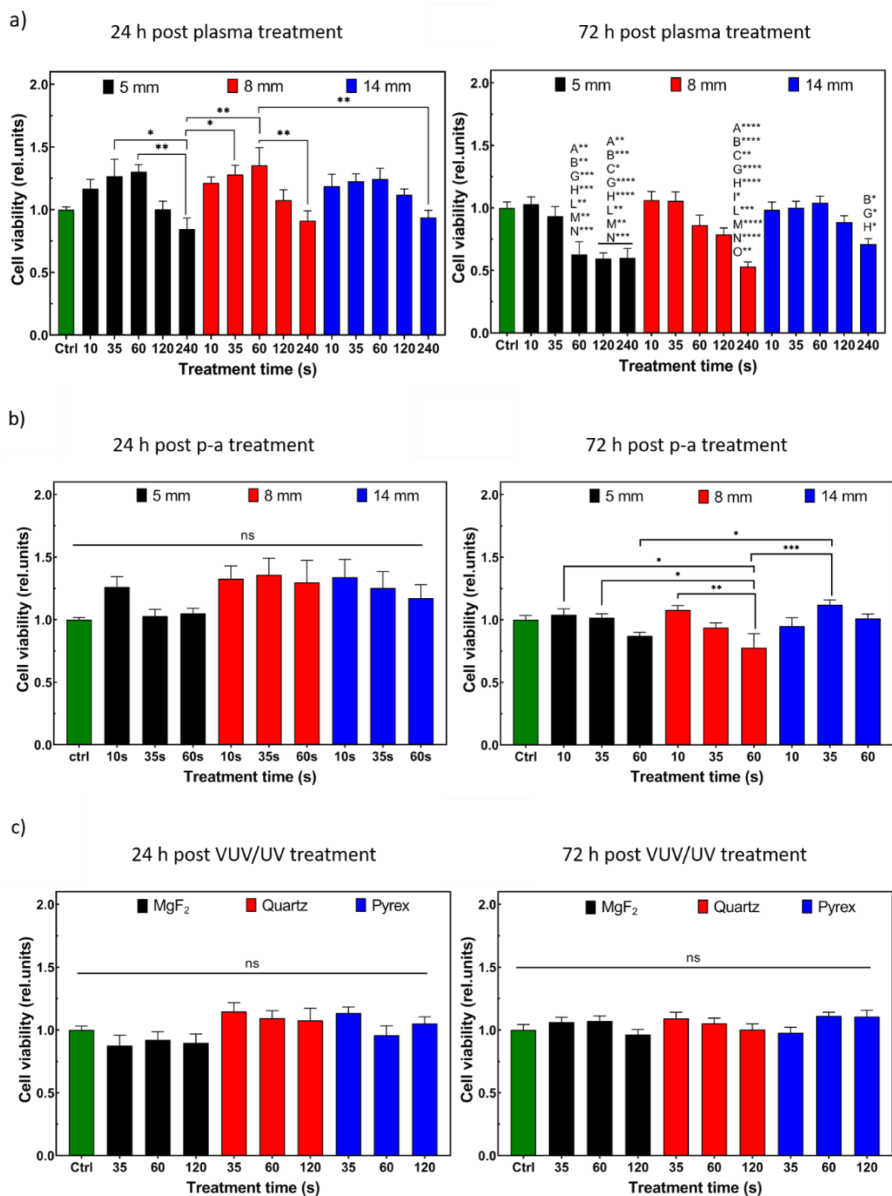
Figure 6.11. Cell viability measured 24 h and 72 h with respect to the untreated sample (GREEN) after treatment with a) plasma and b) plasma–aerosol at distances 5 (BLACK), 8 (RED), and 14 mm (BLUE) away from the nozzle; c) VUV/UV radiation from plasma at a fixed 8 mm distance with filtered out λ>115 nm (BLACK); λ>180 nm (RED); and λ>320 nm (BLUE). Mean results are presented ±SE, * p<0.05, ** p<0.01, *** p<0.001, and ****p<0.0001.

In Figure 6.11(c), relative cell survival is presented in the case of cell exposure to UV radiation from plasma at a distance of 8 mm from the nozzle. Cells were exposed to UV light of different energy as explained earlier, filtered out from integral plasma radiation with MgF$_2$ glass λ>115 nm, quartz glass λ>180 nm, and Pyrex glass λ>320 nm. No significant difference between cell survival of the experimental groups due to VUV/UV emission from plasma was observed 24 h and 72 h after plasma radiation treatment. The small contribution of VUV/UV radiation to the total plasma effect in terms of cell viability has been attributed to its almost 100% absorption in the cell medium of all photons with wavelength below 200 nm[63]. Indeed, as shown in section 6.3.1., the VUV/UV part of the spectrum has a dominant contribution of Ar$_2^*$, OI, and NI species. However, due to the strong absorption of VUV/UV photons in liquid media, the direct effect of these photons on cell survival is almost negligible.

## 6.4.4.2. PLASMA/VUV/UV IMPACT ON L929 CELL CULTURE IN A DRY ENVIRONMENT: ESTIMATION OF PLASMA−CELL INTERFACE

In many real scenarios of plasma treatment, tissues are directly exposed to plasmas with a limited amount of liquid around them, e.g., direct contact with the skin during plasma-assisted topical drug introduction or skin therapy. Correspondingly, the role of the liquid environment and water presence on the plasma–cell interaction has been tested on the attached cells without the cell medium. To evaluate the impact of VUV/UV photons on fibroblast and estimate the range of the plasma–cell interface in a dry environment, 10$^5$ attached L929 cells were treated at a fixed 8 mm distance from the reactor's nozzle under plasma power of 20 W. As in earlier experiments, samples were treated with plasma, plasma with aerosol, VUV/UV radiation λ>115 nm, λ>180 nm, and λ>320 nm. The results are shown in Figure 6.12 for all used conditions. Samples were exposed for a long treatment time of 120 s to ensure easy differentiation of dead/alive cells.
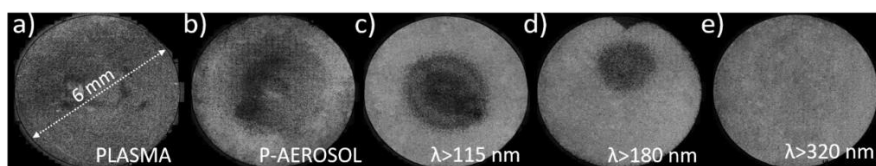


Figure 6.12. Attached cells in 6 mm Petri dish treated for 120 s at a distance of 8 mm with: a) plasma, b) plasma with aerosol, c) UV radiation λ>115 nm from the plasma, d) UV radiation λ>180 nm from the plasma, and e) UV radiation λ>320 nm from the plasma.

The light grey color corresponds to an area covered by live/attached cells, while darker spots correspond to areas where cells are dead/detached. Every image presented in Figure 6.12 is an accumulation of microscopic images obtained from the well moved under the reader, explaining some slight distortions to the images. The images show different acting ranges of plasma treatments and VUV/UV radiation only. In plasma treatment, including both RONS and radiation (see Figure 6.12 (a)), almost the whole surface has been affected by plasma treatment. This larger interface area between plasma and cells can be ascribed to both VUV/UV radiation below the nozzle (Figure 6.12 (c, d)) and RONS carried with the gas flow and expanding along with the whole dry sample. Confluence analyses of imaged attached cells without the cell medium show a strong contribution of VUV/UV photons from plasma to the total plasma cytotoxic effect. However, the range of interaction differs. It is estimated that VUV/UV radiation $\lambda > 115$ nm emitted from plasma acts on cells with a contribution of almost 80% (see Figure 6.12 (c)), while radiation above $\lambda > 180$ nm has a slightly lower cytotoxic effect (Figure 6.12 (d)). It is important to notice a different pattern of the treated area with radiation $\lambda > 115$ nm and $\lambda > 180$ nm (Figure 6.12 (c, d)). Both radiation patterns are characterized by a shared central area that is considered to originate from the species generated in the air (NO, OH, $N_2^*$). However, the treatment pattern corresponding to radiation $\lambda < 115$ nm has an additional ring around the central part that can be assigned to the plasma ring and UV radiation generated from an inter-electrode area ($Ar_2^*$, OI). To determine the absolute cytotoxic efficiency of different VUV/UV emissions on the attached cells, absolute calibration of the VUV/UV system has to be made, and a filter transparency curve is applied.

When aerosols are introduced into the plasma effluent, the plasma–cell interface is distributed over a smaller region, and cell survival increases by about 10% (Figure 6.12 (b)). A different effect from an aerosol presence on the plasma–fluorescent target and plasma–cell interfaces is because different plasma-generated species participate in DCF oxidation and more complex cell inactivation. Compared to the integral plasma effect on the attached cells in a dry environment, introducing aerosol droplets into the central part results in a higher degree of localized cytotoxicity. A strong cytotoxic effect in the central region can be ascribed to the higher concentration of water-derived species, probably short-living $^\bullet$OH, as no diffusion outside the plasma region can be recognized here. Water-derived species such as $^\bullet$O, $HO_2^\bullet$, $H_2O_2$, and $^\bullet$OH cause lipid membrane peroxidation[79]. A lower flux of plasma species (short treatment) enhances membrane permeability which allows cell transfection, such as targeted drug delivery into cells[231]. On the other hand, the high flux of the plasma species such as $^\bullet$OH (long exposure) can cause cell membrane rupture followed by cell leakage and necrosis. Accordingly, $^\bullet$OH driven membrane rupture in this long exposure of the attached cells to the plasma-aerosol (cytotoxic

effect of APPJ is expressed in treatments longer than 60 s) is the most probable scenario. This effect is of great interest for studying plasma-assisted cellular transfection and molecular delivery. Nevertheless, a smoother averaged effect from the plasma coupled with aerosols in dry-environment cell treatments is confirmed. Aerosol assistance to decrease plasma damage of biological targets during the treatment simultaneously employs: 1) plasma temperature decrease, 2) lower oxidative stress, and 3) VUV/UV radiation control. One more exciting point of the plasma-aerosol system is the change of plasma chemistry on the molecular level above the interface with the target. This is important for controlled treatments of porous bio-materials or printing of biomolecules, hydrogels, and cells.

More importantly, opposite to the negligible effect of VUV/UV radiation on fibroblast cell proliferation in the medium, a strong VUV/UV effect is found on attached cells without the medium. As expected, the interaction of VUV/UV radiation with cells in a dry environment is localized in the region below the plasma nozzle (Figure 6.12 (c, d)). Experiments on the attached cells without the medium stress the importance of VUV/UV emission from medical plasma devices during skin treatments. It has been shown that the radiation from the plasma has an instant and cytotoxic effect on cells that can influence the plasma therapy procedure and has a long-lasting negative impact if not adequately controlled.

### 6.4.5. PLASMA DAMAGE CONTROL FOR TISSUES – EVALUATION

In the final stage of our study, we evaluated the in vivo biomedical applicability of our plasma jet coupled with aerosol. A short 35 s skin treatment at a 14 mm distance from the plasma nozzle was shown to be safe for further biomedical applications, as shown in Figure 6.13 (a). Under these conditions, treated skin temperature stayed below a safe level of 42 °C and microscopic images 24 h post-plasma treatment showed no indirect damage in the flank region, see Figure 6.13 (b) (35 s). During the plasma treatments, skin temperature increased to 46.4 °C in 60 s time, and oedema appeared (accumulation of fluid in the interstitium) shown in Figure 6.13 (b) (60 s). Correspondingly, for further in vivo applications for wound healing and topical drug introduction, only short plasma–aerosol treatment (35 s) can be considered. It has to be emphasized that only treatments in combination with aerosols were performed here, as previously proved that such treatments are safe for cells. Aerosol spraying during plasma treatment assures lower skin temperature and partial absorption of VUV/UV radiation in droplets (effluent) and the liquid layer (skin). However, during overexposure (60 s), treated flanks suffer indirect damage (24 h post-treatment) caused by the high flux of UV radiation and RONS[211]. The damaged region on the skin corresponds to the plasma ring region; see Figure 6.13 (b) (60 s, Mouse 2). Species expected to be generated from the plasma ring are

mainly RONS from plasma ($^\bullet$O, $^\bullet$OH)[211] and VUV/UV emission of Ar$_2$$^*$ and OI (Section 6.3.1.). Although no risks of skin damage were reported regarding UV emission OH λ=310 nm in short argon plasma treatments [394], this study has shown the effect of VUV/UV photons Ar$_2$$^*$ λ=126 nm and O I λ=130 nm must not be neglected. In argon plasma jets, UV photons propagate further than typical distances considered in plasma treatments (~10 mm). Accordingly, the emission must always be considered and flux-limited for safe use.
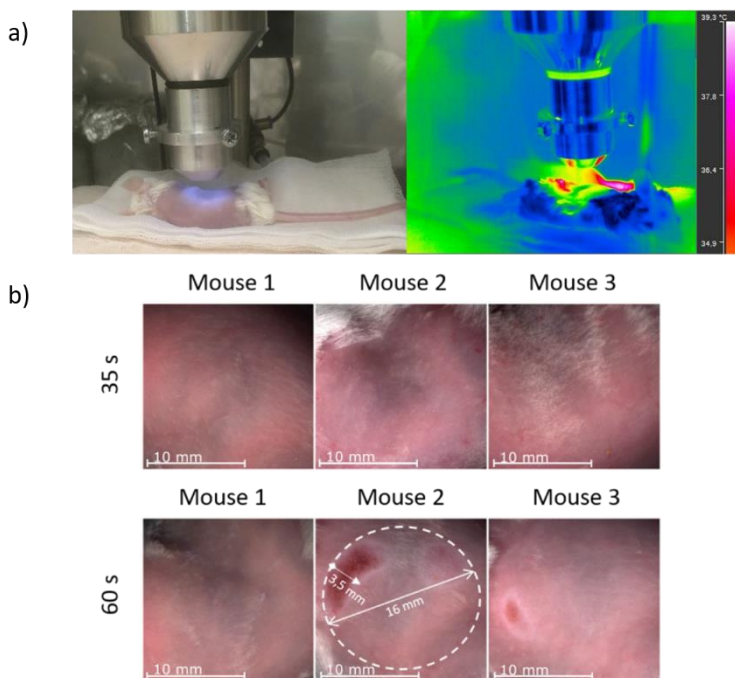


Figure 6.13 a) Plasma treatment of a mouse (left) and IR image of temperature distribution on the treated flank during plasma treatment P = 20 W, t = 35 s, d = 14 mm (T$_{MAX}$ = 39.3 °C). b) Mice flanks 24 h post-plasma treatment P = 20 W, d = 14 mm, t = 35 s (T$_{MAX}$=39.3 °C) and t = 60 s (T$_{MAX}$ = 46.4 °C).

## 6.5. CONCLUSIONS

Possible side effects during biomedical plasma applications have been discussed in this chapter. VUV/UV emission from a plasma jet and its possible negative impact on biological samples, as well as a method to improve safety by aerosol injection, has been demonstrated and analyzed. It has been found that plasma UV radiation is localized in the inter-electrode region and dominated by argon excimer Ar$_2$$^*$ λ = 126 nm and OI λ = 126 nm. Air intrusion in the plasma effluent occurs in the plasma-free region resulting in a weak emission of N$_2$$^*$. VUV/UV

emission has only been detected in the direction of gas flow but as far as 14 mm away from the plasma nozzle. Localization of the main VUV/UV emitters has been confirmed through a fluorescent imaging technique of the plasma–DCF interface. Additionally, this technique has allowed us to image the effect of aerosol presence on the plasma–target interface. It has been found that aerosol injection into plasma effluent has an overall soothing effect (lower oxidation power of plasma) while changing the interface area. Plasma and the VUV/UV radiation effect have been studied on plasmid DNA. The genotoxic effect of VUV/UV radiation (λ>115 and λ>180 nm) from plasma contributes approximately 70% to the total plasma effect. *In vitro* tests on the fibroblast cells in a liquid medium have shown no significant cytotoxic effects of the plasma and plasma–aerosol in treatments shorter than 60 s. UV radiation showed no impact on cell proliferation when treated in a liquid medium due to the total absorption of the VUV part of the spectra in the liquid surrounding. However, a strong and instant cytotoxic effect for cells without media has been noticed. An important role of radiation λ>115 nm on attached cell survival rate has been observed, with an 80% contribution to the integral plasma effect. Aerosol injection in the plasma effluent increased attached cell survival and changed the interaction between plasma and cells. Introduced aerosol plays an essential role as an absorbing medium for VUV/UV radiation, and consequently, it is proposed to control the dosage of radiation during treatment. The cooling effect and the VUV/UV radiation absorption effect of aerosol injection in plasma effluent have been tested *in vivo*. This combination has been proven safe for skin treatments in short treatments (t<60 s). To this end, an annular shape plasma jet coupled with an aerosol can be used under defined safe conditions for skin treatment, e.g., wound healing and topical introduction of molecules. In addition, findings expressed in this study are important for other aspects of APPJs biomedical application where controlled interaction with biomaterials, biomolecules, and cells is required, e.g., bio-printing controlled drug delivery. The high potential of the plasma-aerosol system in cutting-edge plasma biomedical technology is presented in this study.

The introduction of aerosol into plasma effluent has been shown to play a protective role during biomedical treatments. Moreover, this multiphase combination offers the possibility to change the interface between plasma and target. This can be of interest in localized, topical delivery for promoted wound healing. In the next chapter, the first steps have been made towards combined plasma treatment for wound healing and drug delivery. Moreover, wound healing aspects have been examined in the following study by proliferation assays and expression of genes crucial in wound healing model *in vitro*. Plasma and plasma-aerosol have been successfully employed to permeabilize fibroblast cells and introduce modeled drugs locally.

# CHAPTER 7: PLASMA WOUND HEALING ENHANCED BY DRUG DELIVERY – *IN VITRO* MODEL

Ivana Sremački, Mahtab Asadian, Nathalie De Geyter, Christophe Leys, Liesbet Geris, Anton Nikiforov

"*Potentials of the plasma-aerosol system for wound healing advanced by drug introduction: in vitro study.*"
In preparation.

## 7.1. INTRODUCTION

In the final chapter of this thesis, the potentials of the plasma-aerosol system for enhanced wound healing have been studied *in vitro*. The leading idea was to combine the well-known proliferative effects of plasma with induced cell-permeabilization and drug delivery. Accordingly, extensive cell study has been performed to mimic fibroblast behavior upon plasma treatment during wound healing. Cell tendency to migrate, adhere, communicate with other cells and extracellular matrix, proliferate and differentiate after the plasma treatment has been presented in this chapter. Lastly, local cell permeabilization and transfection of model drug utilizing plasma jet assisted by aerosol have been demonstrated and discussed on an *in vitro* model.

## 7.2. PLASMA WOUND HEALING: *IN VITRO* STUDY

Normal healing of a wound can be described by four time-overlapping phases hemostasis, inflammation, proliferation, and remodeling. In a normal wound upon skin injury, fibroblasts activate, dermal fibroblasts migrate into damaged tissue, adhere to the provisional extracellular matrix, and proliferate[395]. In the remodeling phase, rearrangement of extracellular matrix ECM happens, and the presence of transforming growth factor TGF-β induces fibroblast differentiation into myofibroblasts [396]. Finally, in the last stage, myofibroblasts are undergoing apoptosis. Depending on a patient's history and condition, some healing stages can be prolonged or shifted, and abnormal or chronic wounds can be developed. Abnormal or chronic wounds appear to be a global problem impacting the population worldwide due to the growing number of diabetic patients (≈20% increase in 10 years)[92]. Studies show that one-third of diabetic patients develop diabetic foot ulcers during their lifetime, half of those develop an infection wherein worst-case scenario 17% of the infected DFU results in amputation[93]. In conventional wound care treatments, wounds are initially cleaned or debrided and covered with topical dressings (antibiotics, collagen)[105]. Due to the extended healing of abnormal wounds, advanced technologies have been developed to promote their recovery. Among them are negative pressure therapy (debridement), hyperbaric oxygen chamber (wound oxygenation)[108], RF electromagnetic field stimulation (*in situ* NO production)[110]. Recently, bioengineered therapies got attention in healthcare society. The most promising are cellular[113] and acellular, e.g., extracellular matrix ECM- and growth factor GF-based therapies[118]. However, existing wound care technologies are costly (6-10 000 euro/annually[95]) and must be applied frequently. Accordingly, future development concerns effective and alternative economic approaches.

To this end, cold atmospheric plasmas CAP show great potential for their employment in wound healing[166, 397]. Cold atmospheric plasmas are chemically and physically reactive mediums, producing charged particles, metastables, radicals, reactive oxygen and nitrogen species RONS, and ultraviolet UV radiation. Biomedical application of atmospheric pressure plasmas is often associated with their reactive oxygen and nitrogen species RONS production and explained by redox biology[398]. RONS-induced changes in intracellular chemistry are critical for cell homeostasis, signaling including energy metabolism, gene expressions, immune responses, cell cycles, growth (GF and TGF- β1 release[162]), and apoptosis[77]. Biological effects of plasmas have been studied globally, and their coagulative[360], antibacterial[137, 142], and proliferative effects have been revealed[44, 163, 362]. These attributes suggest that CAPS should be an excellent candidate for alternative wound care technologies[37, 166]. Although the wound healing aspects of many CAPs have been confirmed *in vitro, in vivo*, and in clinical trials, the roles of RONS from plasmas remain unclear and must be addressed. Accordingly, additional investigation of RONS healing pathways is highly desired.

Wound healing has been studied on one of the world's most famous and medically certified plasma devices kINPen®MED argon plasma jet[76, 180]. The evaluation of kINPen®MED effectiveness in wound healing *in vivo* has been shown that plasma alone has a positive effect on wound closure[87]. This effect was enhanced by 20% when combining 30 s plasma treatment with the addition of nebulized bioactive agents such as collagen and hyaluronic acid (40μl). More recently, in the first randomized clinical trials, kINPen®MED was engaged in the treatment of DFU in 45 patients[185]. 30 s/cm$^2$ Ar plasma jet shown to increase wound closure by 50 % after 9 days, 8 treatments in 14 days, 5 consecutive days, 3 treatments every other day with respect to the controlled group. However, clinical trials of plasma in chronic wound healing have shown no significant effect on removing clinical infection and wound sterilization. Appropriately, CAP has a real perspective to be used in future wound care technologies; however, more likely not solely but combined with drug delivery for the enhanced effect.

Medicaments are conventionally delivered orally and by injection; however, interest in topical and transdermal delivery seems to increase. Topical and transdermal drug deliveries are non-invasive techniques based on drug intracellular or transcellular penetration through the epidermis (d≈150 μm) and dermis (d≈2 mm) to blood vessels. The main advantage of drug delivery through the skin is its direct entrance to blood circulation without gastrointestinal and liver degradation. However, the issue of drug delivery through the skin is the stratum corneum acting as a barrier. Therefore, only small and lipophilic molecules can be delivered by their passive diffusion.

On the other hand, therapeutically efficient dosages of larger molecules can be delivered by one of the enhancement techniques. In the past two decades, electroporation[217] has received the most considerable attention. Electroporation is used clinically to enhance the delivery of drugs, chemotherapeutics[223], genes (DNA vaccine, RNA transfection[225]). This technique uses high voltage short pulses (100-1500 V, 1-100 ms) to disrupt the lipid bilayer and create transient pathways to deliver larger molecules (10 Da-1 MDa) and larger dosages. Topical delivery of drugs by electroporation is highly effective yet not applicable to patients with pacemakers and anticoagulant therapy. Accordingly, medical alternatives are needed to fill in the gaps existing in current topical and transdermal delivery technologies and applications.

In this chapter, the not-yet-examined ability of a cold atmospheric plasma CAP jet is brought to the light to answer the existing issues concerning promoted plasma wound healing advanced with drug delivery. The design and biomedical aspects of the CAP jet have been studied previously utilizing physical[305], chemical[383], and biological[399] diagnostics to evaluate its applicability in plasma medicine. Significant advantages of here discussed atmospheric pressure plasma jet APPJ coupled with aerosol are shown to be its stability, low temperature, reproducibility, and ability to manipulate ROS and UV radiation flux towards the biomaterial enabling safe and controlled medical treatment. Accordingly, in the current chapter we study plasma advanced healing *in vitro*, concretely plasma assisted connective tissue fibroblast cell proliferation and controlled intracellular drug introduction. In the simplified *in vitro* wound healing model we demonstrate synergic ability of a CAP to enhance fibroblast proliferation and permeabilize cells to promote drug delivery. Fibroblast viability and proliferation after plasma treatment has been studied by means of staining and colorimetric assays. In addition, treated fibroblast have been subjected to PCR test in order to study expression of genes crucial in wound healing. Accordingly, expression of upregulating genes concerning cell migration, adhesion, cell-cell/matrix signaling cell, and fibroblast differentiation towards myofibroblasts have been measured post plasma treatment. Nitrogen gas $N_2$ has been added to the feeding gas argon to study the biological effect of reactive oxygen ROS and reactive nitrogen species RNS in wound healing *in vitro* models. Emphasis is placed on the potential role of an APPJ in fibroblast-cell permeabilization and the local introduction of a drug carrier (dextran).

## 7.2.1. MODIFICATION OF RONS PRODUCTION IN PLASMA TREATMENTS: N$_2$ GAS AND AEROSOL ADDITION

Atmospheric pressure plasma jet APPJ coupled with aerosol employed in this thesis has been designed for plasma-assisted wound healing[305, 383, 399]. It has been shown that oxygen-driven ROS chemistry dominates Ar plasma jet generated in

ambient air and that photo-induced chemistry is relevant for this jet. Previously, liquid chemistry initiated by APPJ has been studied, and the possibility of modifying ROS species generation/deposition in treated liquid by aerosol addition into plasma effluent. RONS generated in a plasma-treated liquid have a crucial role in *in vitro* studies, considering that the liquid layer always covers cells. Aerosol has shown to be a good tool for the spatial modification of production and deposition of RONS and, accordingly, manipulating the plasma interface. Moreover, its biological effects mirror safer treatment due to the partial ROS quenching and UV absorption.

ROS production control can also be modified by adding $N_2$ into Ar feeding gas. A low amount of 0.05% of $N_2$ does not affect the stability and temperature of the plasma jet[305]. However, boosted production of RNS is to be expected. The addition of nitrogen gas favors NO production in the gas phase and downstream reaction products $NO_2^-$, $NO_3^-$ in the liquid phase[400]. For nitrate and nitrite production, atomic oxygen O and superoxide $O_2^-$ are consumed. Improved performances of argon jet on angiogenesis, blood flow in the wound, epithelization, and wound contraction are closely related to the higher concentration of RONS (RNS) in the wound bed[179]. Biologically crucial RONS produced in treated liquid are measured before *in vitro* experiments. The overview of the dominant species produced by APPJ in liquid treated at a distance of 10 mm is given in Table 7.1.

Table 7.1. RONS produced or deposited to treated liquid by APPJ (d=10 mm, t=10-60 s)

| Plasma | OH | $O_2^-$ | $H_2O_2$ | $NO_2^-$ | $NO_3^-$ |
|--------|-----|---------|----------|----------|----------|
| Ar | 0.5-2.8 uM | 0.2-1.8 uM | 4-2 uM | 1-2 uM | 5-3 uM |
| Ar/$N_2$ | ↘ | ↘ | ↘ | ↗ | ↗ |
| Ar-aerosol | 0.5-2 uM | 0.1-1.2 uM | 1-3 uM | 1 uM | 2-1 uM |
| Ar/$N_2$-aerosol | ↘ | ↘ | ↘ | ↗ | ↗ |

## 7.3. MATERIALS & METHODS

*In vitro* wound healing model employing advanced plasma treatment has been studied in this chapter. The plasma reactor used for this purpose is a large size ($d_{out}$=14 mm) annular shape plasma jet operating in 3 SLM (standard liter per minute) Ar and admixture 3 SLM Ar+0.05% $N_2$. A hollow inner powered electrode (RF 13.56 MHz), aerosol microdroplets d≈20μm can be introduced into plasma effluent for RONS and UV flux modification towards the target. Detailed design of plasma reactor

can be found in the previous chapters[305]. In this chapter, fibroblast cells L929 cell line have been treated in cell medium to study plasma impact on :

I. Cell viability, proliferation, and gene expressions concerning migration, adhesion, signaling, and differentiation, respectively

II. Cell-permeabilization and model drug introduction into fibroblast cells

Cells were treated at a 10 mm distance from the effluent of low power ($P_{dissipated}$=8 W) pure Ar, Ar+0.05% $N_2$, Ar-aerosol, and Ar+$N_2$-aerosol plasma. Short treatment times are defined in advance, 10, 35, and maximal 60 s. The methodology of performed experiments designed to study plasma wound healing and drug introduction *in vitro* is presented in Figure 7.1.
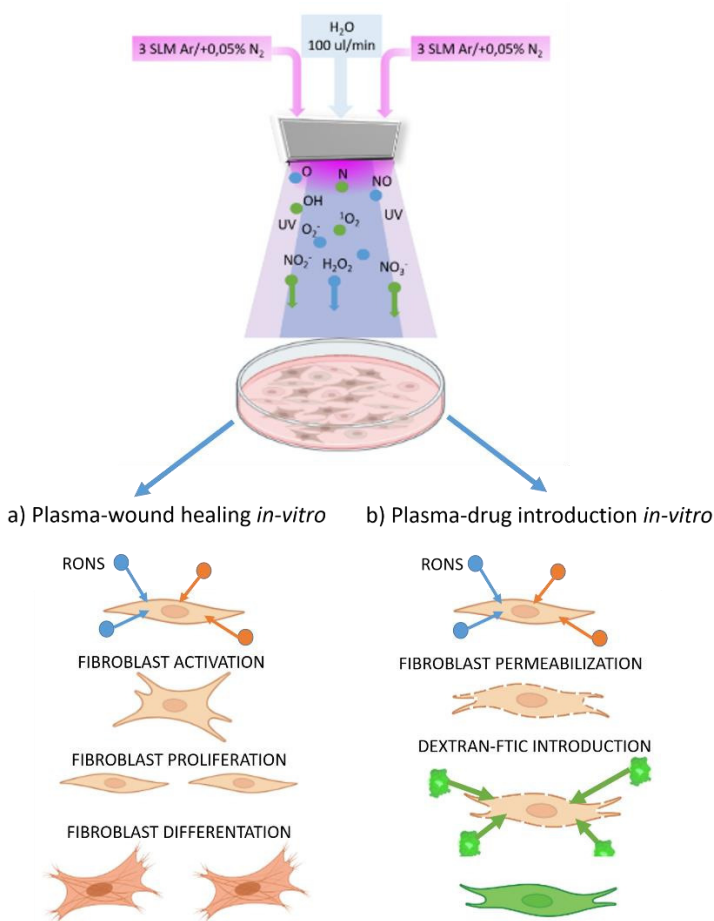


Figure 7.1. Experimental schematic of plasma treatments of fibroblast cells for a) promoting fibroblast proliferation and differentiation; b) inducing fibroblast permeabilization and dextran introduction.

The plasma interaction with fibroblasts was studied through their proliferation and differentiation, as shown in Figure 7.1 (a). For this purpose, plasma-treated cells were subjected to colorimetric and staining assays after the treatment. Moreover, expressions of genes relevant to wound healing are measured by PCR. Ultimately, the cell-permeabilization upon interaction with plasma was studied by fluorescence microscopy after dextran-FTIC is introduced into permeabilized cells, Figure 7.1 (b).

### 7.3.1. CELL PROLIFERATION: PRESTO BLUE COLORIMETRIC ASSAY

Proliferative plasma effect on mouse embryonic fibroblast cell line L929 was studied cell viability with Presto Blue assay. The L929 murine fibroblasts was cultured in an advanced minimum essential medium (AMEM; Gibco, Thermo Fisher Scientific), supplemented with 5% fetal bovine serum (FBS; Thermo Fisher), 10 mL/l L-glutamine (GlutaMAX; Thermo Fisher), 100 U/mL penicillin and 50 µg/mL streptomycin (Sigma Aldrich) in a 5% $CO_2$ humidified incubator at 37°C.

For cell viability assay, $1 \times 10^6$ L929 cells were suspended in 1.5 mL cell media (AMEM) to assure uniform treatment without spillage due to the gas flow. After the treatment, 1000 L929 cells from each experimental group were plated in a 0.1 mL cell culture medium in 96-well plates. Duplicates were used for each experimental group. All treatments have been repeated in triplicates. Cells were incubated at 37°C in a 5% $CO_2$ humidified incubator for up to 7 days. Day 1, 3, and 7 after the treatment, 10 µL of Presto Blue® viability reagent (Thermo Fisher Scientific) was added to the wells. Two hours later, fluorescence intensity was measured with a microplate reader (Cytation 1, BioTek Instruments). Cell viability of experimental groups was normalized to the control group of the corresponding day.

#### 7.3.1.1. STATISTICAL ANALYSIS

All the results were presented with a standard error of the mean value. One-way ANOVA (t-test) statistical analysis has been performed in GraphPad Prism 9 (GraphPad Software, Inc., CA, USA) to access statistically significant differences between experimental groups. Significance levels $P<0.05$ (*), $P<0.01$(**), $P<0.001$(***), and $P<0.0001$(****) have been tested among all experimental groups.

### 7.3.2. CELL VIABILITY AND MORPHOLOGY: LIVE/DEAD STAINING

As a complementary evaluation of cell viability in addition to morphology visualization, a live/dead viability/cytotoxicity kit (Invitrogen) was used. Prior to the staining, the supernatant was removed, and the cells were rinsed twice with phosphate-buffered saline (PBS). Next, the staining was done by incubating the cells

in the staining solution (0.5 µL 4 mm Calcein AM in anhydrous DMSO solution and 2 µL 2 mm ethidium homodimer in DMSO: $H_2O$ (1:4 v/v) in 1 mL PBS) for 20 min at room temperature in the dark. Finally, the cells were visualized with a fluorescence microscope (Olympus IX 83) using the appropriate filters.

### 7.3.3. EXPRESSION OF GENES CRUCIAL IN WOUND HEALING

In this thesis, some of the genes known to play a role in wound healing are measured 6 h, 24 h, and 48 h post 35 s plasma treatment. Measured genes are concerning cell migration (paxillin α and focal adhesion kinase), cell adhesion (collagen 1A1 and syndecan 1), cell-cell/matrix signaling (talin and vinculin), cell proliferation index KI-67, and fibroblast differentiation towards myofibroblasts (α-smooth muscle actin). Gene names and primer sequences are given in Table 7.2.

#### 7.3.3.1 QUANTITATIVE REAL-TIME POLYMERASE CHAIN REACTION (QRT-PCR)

Total RNA from fibroblast cells (L929) was extracted utilizing the Nucleospin RNA II kit (Macherey-Nagel). The cells from one well were pooled together, and total RNA was isolated using QIAshredder (Qiagen) continued by RNeasy Mini Kit (Qiagen). This analysis was performed with at least three replicates per condition. RNA quality and concentration were evaluated with NanoDrop 2000 (Thermo Scientific), and the PrimeScript™ RT reagent kit (Takara) was utilized for cDNA synthesis. qRT-PCR was carried out utilizing SYBR® Green (Life Technologies) with Rotor Gene® 6000 (Qiagen), and relative differences in expression were measured using the $2^{-\Delta\Delta Ct}$ method normalized to the housekeeping gene Glyceraldehyde-3-Phosphate Dehydrogenase (GAPDH)[401]. All protocols were performed according to the manufacturer's protocol.

Table 7.2. Gene expression in plasma-treated fibroblasts was measured in this thesis.

| Gene name | Gene ID | Primer sequences (3`- 5`) |
|---|---|---|
| Paxillin | *PXNα* | ACT TGA CCG GCT GTT ACT GG |
| | | GGG CTC GAT TCG GCT TCA T |
| Focal adhesion kinase | *FAK* | GAG TAC GTC CCT ATG GTG AAG G |
| | | CTC GAT CTC TCG ATG AGT GCT |
| Syndecan 1 | *SDC1* | AAC GGG CCT CAA CAG TCA G |
| | | CCG TGC GGA TGA GAT GTG A |
| Syndecan 4 | *SDC4* | TTT GCC GTT TTC CTG ATC CTG |
| | | TTG CCC AAG TCG TAA CTG CC |
| Collagen 1a1 | *COL1A1* | GCT CCT CTT AGG GGC CAC T |
| | | ATT GGG GAC CCT TAG GCC AT |
| Collagen IV | *COLIV* | GGC CCC AAA GGT GTT GAT G |
| | | CAG GTA AGC CGT TAA ATC CAG G |
| Vinculin | *VCL* | GCT TCA GTC AGA CCC ATA CTC |
| | | AGG TAA GCA GTA GGT CAG ATG TG |
| Talin 1 | *TLN1* | ATG TTA GAC GGA ACG GTG AAG A |
| | | CAA TTC GGG CAC AAA TGG TCA |
| KI-67 | *Ki-67* | AATCCAACTCAAGTAAACGGGG |
| | | TTGGCTTGCTTCCATCCTCA |
| α-smooth-muscle actin | *αSMA* | CCC AGA CAT CAG GGA GTA ATG G |
| | | TCT ATC GGA TAC TTC AGC GTC A |

181

### 7.3.4. CELL PERMEABILITY MEASUREMENT: FTIC DEXTRAN INTRODUCTION AND DETECTION

Labeled dextrans-FTIC (fluorescein isothiocyanate) 4, 10, 40, and 70 kDa (Sigma Aldrich) were used to evaluate the permeabilization of the cell upon plasma treatment. For the cell permeabilization experiments, $10^5$ fibroblast cells (L929 cell line) were seeded 1 day before the experiments into 6-well plates to reach confluence 80-90%. Culturing and incubation has been done as explained above. The optimal concentration of the dextran-FTIC solution in PBS has been determined to be 37.5 mg/mL for fluorescence microscopy of stained cells. Prior to the plasma treatment, the cell medium was removed from adhered cells, and 500 ul of 1:1 dextran/phenol red-free medium (MEM, Gibco, Thermo Fisher) 18.75 mg/mL solution has been deposited[231]. Cells with dextran in cell medium have been treated at a distance of 10 mm with Ar, Ar+0.05% $N_2$, Ar-aerosol, and Ar+$N_2$-aerosol plasma. After 35 s treatment, 1.5 mL of fresh medium AMEM was added to de cells, dextran together with cell medium was removed, and cells 3 times rinsed with 1.5 mL of fresh AMEM. Immediately after the plasma treatment, the fluorescence of dextran incorporated in cells was detected by fluorescence microscopy (Olympus IX 83) in an appropriate wavelength. Control samples were treated 35 s with plasma feeding gas flow but no plasma, following the same rinsing protocol. Well, plates have been imaged in the mosaic style and 4X magnification.

### 7.4. RESULTS & DISCUSSIONS

In this chapter, plasma-assisted wound healing and cell-permeabilization have been demonstrated *in vitro*. Cell viability and proliferation have been measured by staining and colorimetric assays, respectively. Additionally, processes triggered in fibroblasts during a tissue injury and their consequent behavior are examined by measuring relevant gene expressions after plasma treatment. Finally, a new aspect of plasma – localized drug delivery into the treated fibroblasts has been studied. The driving idea of this study was to boost the proliferative effect of plasma by combining it with cellular drug delivery.

### 7.4.1. FIBROBLASTS VIABILITY AND PROLIFERATION AFTER PLASMA TREATMENT – WOUND HEALING: *IN VITRO* MODEL

Fibroblasts' proliferation increases after being treated with $P_{depossited}=8$ W plasma effluent during the short treatment times 10, 35, and 60 s, previously evaluated as safe noncytotoxic[399]. Fibroblasts were treated with different plasma feeding gases as explained earlier (Ar, Ar/$N_2$, Ar-aerosol, and Ar/$N_2$-aerosol) and compared with the untreated sample (ctrl), as presented in Figure 7.2 (a).
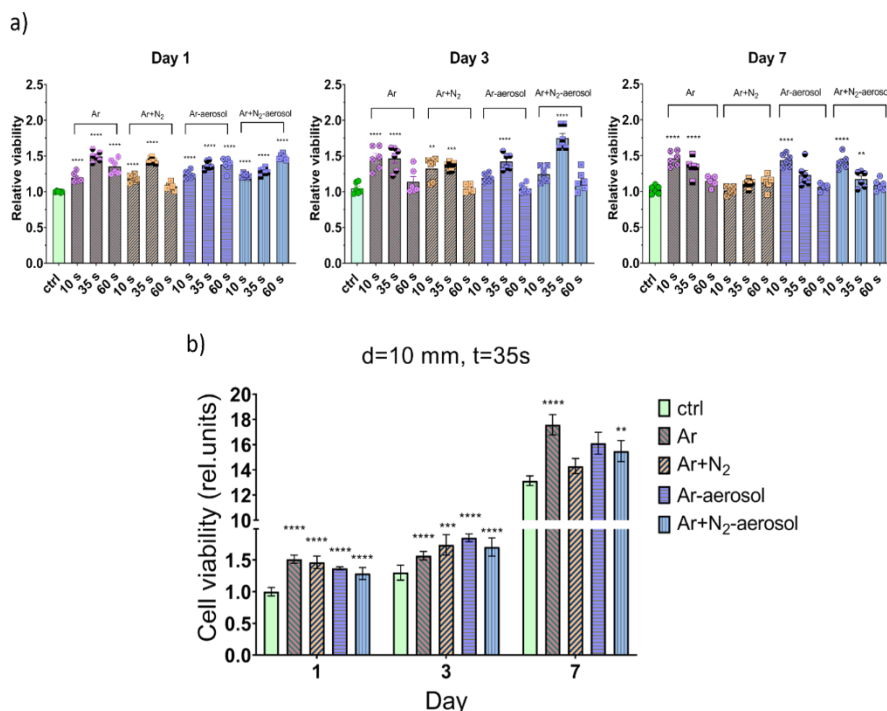
Figure 7.2. *In vitro* study on the cell proliferation and viability: a) Fibroblast proliferation after treated with plasma quantified relative to the untreated sample via Presto Blue assay (day 1, day 3, and day 7), b) Daily proliferation of plasma-treated fibroblast in different treatments for 35s.

In general, all plasma-treated cells under study show higher viability values than the control group. This indicates an enormously increased L929 cell adhesion and proliferation upon plasma treatment compared to the untreated cells. In addition, as all plasma-treated cells, regardless of treatment conditions, showed cell viability above 75% (if each ctrl is considered as 100%), all plasma treatment conditions can be considered as non-toxic according to literature[402]. The proliferation of cells induced by plasma can be explained through oxidative stress that cells are experiencing after being exposed to plasma RONS. Namely, many cells respond to mild oxidative stress by proliferating[81]. In other words, ROS from plasma has been shown to promote fibroblast growth factor (FGF-2) release, the main mechanism of plasma-induced cell proliferation[163]. The cells' ROS- responsive behavior is explained by cells' tendency to adapt to the oxidative stress by upregulation of the defense system. This may result in partial/complete protection from damage or overprotection and resistance development[81].

As shown in Figure 7.2, no significant difference in cell proliferation among different experimental groups is noticed. However, different behavior in cell proliferation could be seen in experimental groups by alternating treatment times 10, 35, and 60 s. Figure 7.2 also shows that the proliferation of plasma-treated fibroblast on day 1 seems to be highest (50 % relative to the control) for the experimental groups treated for a longer time of 35-60 s. Cell treated for 35-60 s exhibited enhanced proliferation as a response to the moderate flux of RONS and their oxidative stress. However, during the following days (until day 7), their growth rate decreased, probably due to their adaptation to the introduced RONS environment (see Figure 7.2(a), day 1 and day 7 for 60 s). The proliferation of experimental groups treated with low plasma dosage (10-35 s) shows the opposite behavior. Regardless of carrier gas, cells treated with the lower dosage of RONS gradually increased proliferation and adaption to the RONS environment. The maximal proliferation reached 50 % relative to the control on day 7 (see Figure 7.2 (a), day 7 for 10s).

Although results presented in Figure 7.2 provide essential quantitative information on the behavior of fibroblast cells after plasma treatment, the cell viability has also been visualized by the use of live/dead assay. Stained fibroblasts on day 1 and day 3 after the plasma treatment are shown in Figure 7.3 (for day 7, see Appendix 3).
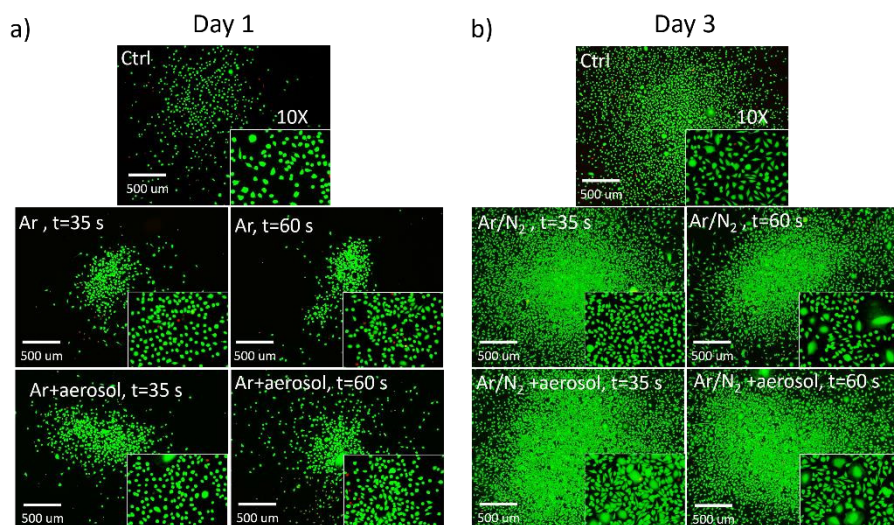


Figure 7.3. Live (green)/Dead (red) staining (magnification 4X and 10 X) a) day 1 : Control; Ar plasma t= 35 s (left) and t=60 s (right); Ar+aerosol plasma t= 35 s (left) and Ar+aerosol plasma t= 60 s (right). b) day 3: Control; Ar/N$_2$ plasma t= 35 s (left) and t=60 s (right); Ar/N$_2$+aerosol plasma t= 35 s (left) and t= 60 s (right).

Fluorescence staining of fibroblasts has shown a high survival rate of plasma-treated cells, especially in the case of 10 and 35 s treatment for all experimental groups. For the best representation, only two experimental groups, medium and long plasma exposure (35 and 60 s) are presented for all used carrier gases. Figure 7.3 (a) reveals that one day after seeding, the untreated cells show living cells with a more rounded morphology suggesting poorer cell adhesion than the plasma-treated conditions. In contrast, on all plasma modified fibroblasts, a higher number of living cells can be observed with a more spread-out morphology proving the excellent initial adhesion of these cells. Cell attachment to the substrate and to other cells is mediated by cell-adhesion molecules (CAMs) referred to as integrin and cadherin, respectively. However, CAMs can be easily damaged by overexposure to ROS-induced oxidative stress associated with oxidation of the adhesion proteins located on the exterior of the cell[403]. Additionally, 3 days after culturing, more adhered fibroblasts are characterized in the plasma-treated samples by more flattened morphology. This morphology corresponds to the differentiated fibroblasts (myofibroblasts) observed on tissue culture polystyrene plates and might be thus an indication of excellent cell differentiation. The differentiation of the cells upon plasma treatment has been additionally checked with gene expressions and presented in the next section. The achieved results indicate a stimulatory effect of 35 s on cell adhesion and proliferation for the 10 mm distance employed in the gas plasma treatments. Therefore, these plasma treatment parameters (35 s and 10 mm) were used for subsequent experiments.

## 7.4.2. GENE EXPRESSIONS IN PLASMA-TREATED CELLS: WOUND HEALING *IN VITRO* MODEL

After a tissue injury, cells migrate towards it, adhering to the wound bed to proliferate and repair the damage. The proliferation phase of a wound is followed by the matrix remodeling, differentiation of fibroblasts into myofibroblasts, and finally, healthy scarring without fibrosis. Although the healing effect of CAPs in wound healing is already demonstrated *in vivo* and clinically, underlying molecular mechanisms regulating fibroblast migration, adhesion, and differentiation remain unclear. In the recent combined *in vitro/in vivo* studies with CE plasma device kINPen®MED has been shown that tissue regeneration utilizing cold plasma is accompanied by regulation of focal adhesion, matrix remodeling, and tissue oxygenation[161]. In the mentioned study ROS are shown to be crucial for activation (phosphorylation) of the integrin adhesions (focal adhesion kinase, paxillin); alterations of structural proteins and actin organization, improved deposition of ECM protein collagen, and the formation of new cell-matrix contacts. However, the effect of RONS, more specifically RNS, remains unknown. RNS, mainly NO, plays an

essential role in cell signaling; nonetheless, cell proliferation pathways are entirely ascribed to ROS in atmospheric plasmas.

To this end, we have studied plasma-induced cellular responses critical in wound healing by measuring expressions of genes responsible for migration and adhesion, cell-cell/matrix contact achievement, proliferation, and finally, differentiation. Integrins and syndecans are transmembrane matrix receptors tightly linked to cell motility. As shown in Figure 7.4, a simplified model, cell-matrix interaction is realized as a response of injured tissue in proliferation and remodeling stages.
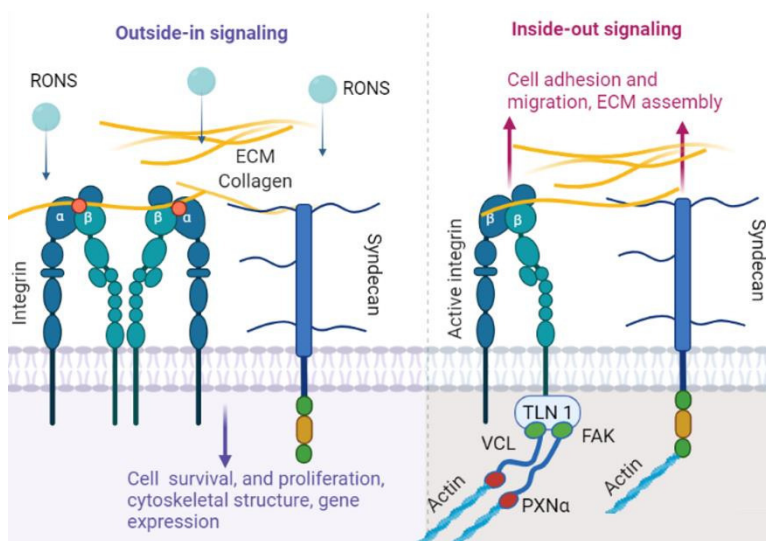


Figure 7.4. Visualization of cell-matrix communication realized through integrin focal adhesions and syndecans.

In this chapter, integrin focal adhesions expression of genes were measured, respectively vinculin and talin - structural proteins, paxillin and focal adhesion kinase – signaling proteins, collagen I and IV, and syndecans 1 and 4. It is known that collagens are the most abundant ECM proteins secreted by cells (beside elastin), and these play a vital role in the remodeling stage of the wound healing process. Besides allowing direct contact of cell with ECM, syndecan 1,4 proteins clustering with other proteins such as HER2, α6β4 integrin, αvβ3,5 promotes wound healing, cell invasion, survival, and angiogenesis[404].

Gene expressions have been measured 6 h, 24 h, and 48 h after the plasma treatment Ar, Ar/N$_2$, Ar-aerosol, and Ar/N$_2$-aerosol. Normalized gene expressions to the control value 1 in early (6 h post plasma) and late measurements (48 h post

plasma) are presented in the form of a heat map in Figure 7.5 (a, b). Separate graphs for all measured genes in three-time points are shown in Appendix 4.
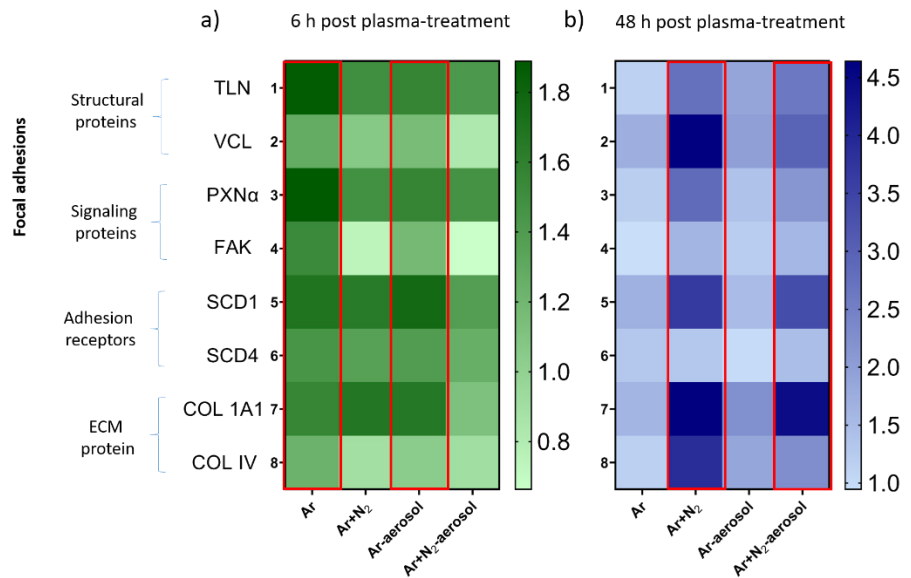


Figure 7.5. Gene expressions of talin, vinculin, paxillin, focal adhesion kinase, syndecan 1, 4, and collagens I, IV are measured: b) 6h after plasma treatment and c) 48 h after plasma treatment. Measured genes have been normalized to GAPDH, results presented in the heat map have been normalized to control.

It has to be emphasized that almost all measured upregulating genes concerning the ability of cells to migrate and adhere are overexpressed in plasma-treated cells (see Figure 7.5 (a, b)). Essential to notice are different trends of expressed genes, indicating the high dependency of the cell fate on the plasma conditions (either carrier gas or with/without aerosols) and the post-plasma treatment time. Namely, 6 h after the plasma treatment, the expression level of measured genes (for all the markers) is more pronounced after Ar and Ar-aerosol plasma treatment (Figure 7.5 (a), red marks). In argon feeding gas plasma, reactive oxygen species ROS and UV radiation are dominant reactants. Most of the ROS species present in the plasma are short-living species $^\bullet OH$, $^\bullet O$, $^1O_2$, $O_3$[383] followed by long-living $H_2O_2$ (10 µM).

On the other hand, the addition of only 0.05 % of $N_2$ to gas plasma resulted in the highest gene upregulation measured 48 h after plasma treatments (see Figure 7.5 (b), red marks). The addition of $N_2$ to the Ar gas enhances NO downstream long-living products such as $NO_2^-$, $NO_3^-$. Late focal adhesions gene expressions in cells treated with plasma enriched with $N_2$ can be explained by post-discharge evolution

of long-living species liquid chemistry[405]. Under acidic conditions post-discharge and presence of protonium ion $H^+$, the concentrations of $NO_2^-$ and $H_2O_2$ species decrease during hours after the treatment, resulting in post plasma generation of $NO_3^-$ [405]. However, this post plasma behavior is often present in plasma-activated water (PAW) and it is used for bacterial decontamination. In the neutral environment (pH≈7) another reaction yielding $NO_3^-$ is more likely to occur. In nitrogen-mixtures plasmas, short-living peroxynitrite ion $ONOO^-$ is commonly produced in the liquid phase[406-407]. $ONOO^-$ is created in the spontaneous reaction between nitric oxide $^•NO$ and superoxide $O_2^{-}$[52] (Eq. 7.1). This reaction has great physiological importance and acts as a second messenger in redox cell signaling[408].

$$NO + O_2^- \rightarrow ONOO^- \qquad\qquad \text{Eq. 7.1}$$
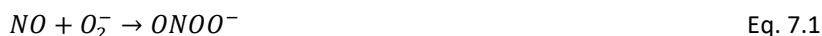
Under neutral conditions in the biological environment enriched with carbon dioxide, $CO_2$ molecule scavenges peroxynitrite yielding a short-living nitrosoperoxycarbonate anion $ONOOCO_2^-$ (Eq.7.2). This ion decomposes quickly wherein nitrate $NO_3^-$ and carbon dioxide $CO_2$ are generated[409] (Eq.7.3).

$$ONOO^- + CO_2 \rightarrow ONOOCO_2^- \qquad\qquad \text{Eq.7.2}$$

$$ONOOCO_2^- \rightarrow NO_3^- + CO_2 \qquad\qquad \text{Eq.7.3}$$

Moreover, the synergetic selective cytotoxic effect of three long-living species abundant in plasma-activated medium $H_2O_2$, $NO_2^-$ and $NO_3^-$ is demonstrated on the cancerous cells (c>150 μM)[410]. The synergetic effect of $H_2O_2$ and $NO_2^-$ has also been shown by promoting normal cell proliferation and migration when the concentrations are below the cytotoxicity level (c≈10-30 μM)[411]. Although the importance of $NO_2^-$ ion is seen as a reservoir of NO signaling molecules, no enhanced mechanisms of $H_2O_2$ and $NO_2^-$ species in the plasma-activated medium are speculated.

As no additional treatment has been carried out, the late upregulation of the focal adhesions genes and collagens observed after $Ar/N_2$ plasma treatment is explained through the cell interaction with long-living $NO_2^-$ and $NO_3^-$. This means 1) total consumption after 48 h of nitrates and nitrites produced by plasma during the operation or 2) post-discharge activity of the cell medium and prolonged generation of species.

## 7.4.2.1 CELL-MATRIX INTEGRIN-BASED ADHESION PROTEINS, ECM PROTEINS, PROLIFERATION, AND DIFFERENTIATION MARKERS

A previous study reported that changes in vinculin and talin levels improve intracellular signaling and intercellular connections, which are essential for wound closure[161]. Moreover, the study hypothesizes that vinculin is a plasma-regulated switch in the dynamics of focal adhesions and a valuable target for optimizing the care of non-wounds. Indeed, extracellular matrix proteins and integrins perceive extracellular signals from plasma-induced active species through activation of vinculin and talin, which are associated with actin and integrin stimulations. Such changes are then passed to signaling proteins by changing protein kinase phosphorylation levels (e.g., focal adhesion kinase) as a decisive factor of cellular responses. These responses improve cell migration toward the wound site, enhancing re-epithelialization and further matrix deposition. The results confirm that talin and vinculin will increase upon alternation in cellular architectures under oxidative stress (Figure 7.5). Plasma ROS (in early cell culture, 6 h) and RONS (in late cell culture time, 48h) induce upregulation of talin with the relative folds 2 and 3 and vinculin with the relative folds 2 and 4.5 (Ar plasma 6 h, Ar/N$_2$ plasma 48 h).

Compared with the expression under other conditions, higher expression of focal adhesion kinase and paxillin is observed for ROS-dominating plasma (Ar and Ar-aerosol) after 6 h (relative folds 1.5 and 2) and RNS (RONS)-dominating plasma (Ar/N$_2$ and Ar/N$_2$-aerosol) after 48 h (relative folds 1.5 and 3), indicating that our findings are congruent (see Appendix 4 (c,d)). Moreover, the SDC1 (relative fold 2, 1.5 (Figure Appendix 4 (e))) level increased during short incubation (6 h) using Ar carrier gas (with/without aerosol). The values obtained for long incubation times (48 h) are higher than those of other experimental groups when nitrogen is included in the plasma gas carrier (relative fold 3). This suggests that Ar-plasma-induced ROS (in short post-discharge time) and Ar/N$_2$ plasma-induced RONS (in long post-discharge time) tune extracellular signal transfer across the cell surface to the cytoskeleton. Such a transfer would influence the activation of various intracellular signaling cascades through stimulation of SDCs. The aforementioned higher expression level of SDC 1,4 allows direct contact of the cells with ECM (see Figure 7.4). Moreover, syndecans (SDC 1,4) have an important role when clustering with other proteins such as HER2, α6β4 integrin, and αvβ3,5 which stimulates cell invasion, survival, and angiogenesis. Similar to our results for L929, Schmidt et al.[161] also found upregulation of both growth factor co-receptors (SDC1/4) during 24 h after the Ar plasma-assisted treatments in primary dermal fibroblasts. This was associated to increased cell migration and growth factor uptake.

A previous study reported fibroblast proliferation is associated with a collagen-rich ECM reconstitution[161]. Indeed, fibroblast survival increases in response to external stimulation (induced by plasma modification) from the

microenvironment, and this increase is manifested by the secretion of ECM components (e.g., collagens), see Figure 7.5 (a, b) and Figure Appendix 4 (g, h)). Compared with the expression level observed for untreated cells, the expression level of collagens COL1A1 and COL IV is significantly higher for plasma-modified fibroblasts. Precisely in ROS dominating plasma (Ar and Ar-aerosol), COL1A1 and COL IV are upregulated up to 2 relative folds (6h), while in RONS dominating plasma (Ar/$N_2$ and Ar/$N_2$-aerosol), the upregulation of this ECM collagens increases above 4 relative fold.

As explained in the previous section, upon plasma exposure, most of the cells are viable at all three-time points; however, the proliferation rate increases more slowly in the early cell culture (between days 1 and 3) than in the long cell culture (between day 3 and 7) (Figure 7.2(b)). Messenger ribonucleic acid (mRNA) transcripts of the marker associated with proliferation Ki-67 is therefore screened for three different time points (6, 24, and 48 h incubation post plasma activation). The corresponding results (see Figure 7.6 (a)) revealed that Ar-plasma-induced ROS (with/without aerosol) leads to a downregulation of ki-67 from 6 h to 48 h. This indicates that the impact of ROS species on the proliferation rate of L929 is less favorable in the initial two days of culturing than under other plasma conditions. In contrast, Ar/$N_2$plasma-induced RONS (with/without aerosol) results in upregulation of the proliferation-related marker, thereby revealing numerous proliferating L929 during the first two days. These results suggest that the alternation in proliferation after 48 h was induced by incorporating long-lived nitration species rather than by incorporating short-lived oxygen species.

As previously explained, the differentiation of fibroblasts into myofibroblasts is considered the last step in the proliferation and remodeling stages of the healthy wound healing process. Assessing the influence of each plasma treatment on the fibroblast-to-myofibroblast transition stage is therefore important. To this end, the expression of myofibroblasts-related marker α-smooth muscle actin (α-SMA) is examined. Unlike, focal adhesions maximally upregulated 48 h after the Ar/$N_2$ plasma treatment, the α-SMA differentiation marker is highly upregulated in the first 6 h after the pure Ar plasma treatment (with/without aerosol), see Figure 7.6 (b). The α-SMA expression level in the Ar plasma-treated cells is almost four times higher than that of the untreated cells. This indicates that the differentiation of fibroblasts into myofibroblasts is mainly induced by short- and long-living ROS, although the effect of the former on the differentiation stage is more prominent than that of the latter. The improvement in fibroblast differentiation is attributed to the stimuli effect of plasma-induced ROS in GF secretion.
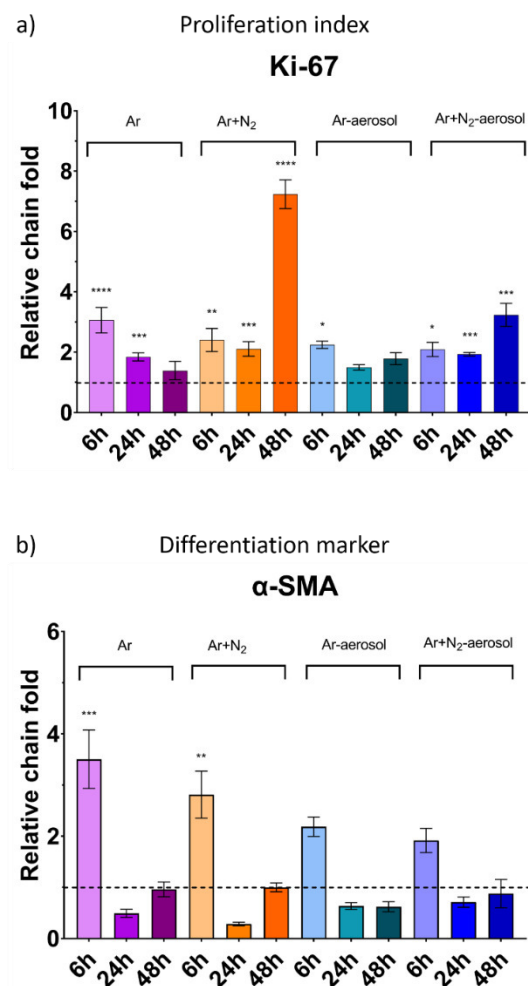
Figure 7.6. a) Gene expression of a proliferative index Ki-67 and b) Gene expression of differentiation marker α-smooth muscle actin indicating fibroblast differentiation towards myofibroblasts, 6 h, 24 h, and 48 h after the plasma treatments presented relative to the GAPDH control (1).

Previous studies have reported that fibroblasts release TGF, an essential factor for differentiation, upon exposure to an oxidative stress[163, 412]. In conventional therapies, TGFs are added as a therapeutic to improve the proliferation of cells[118, 120], which is often achieved by adding a high concentration of TGF to culture media. This high-concentration has negative effects such as cell toxicity (in some cases), quick cell saturation, and waste of expensive GFs. However, our results revealed the excellent effect of plasma modification on the fibroblast-to-myofibroblast transition

stage (in the absence of wound-healing related GF), indicating an outstanding potential application of these techniques.

APPJ can trigger fibroblast responses (namely, focal adhesions, proliferation, and differentiation) associated with healthy wound healing. Maximal upregulation of focal adhesions and proliferative index Ki-67 has been measured 48 h after an Ar/N$_2$ plasma treatment, indicating the importance of RONS nitrites and nitrates in triggering cellular wound healing responses. However, the differentiation of cells is mainly triggered by ROS species. The effect of plasma on wound healing can be boosted by the additional introduction of drugs into cells. Accordingly, the study presents an *in vitro* transcellular topical drug introduction model. The main results demonstrate prospects of plasma utilization in the medical field.

### 7.4.3. PLASMA-AEROSOL ADVANCED WOUND HEALING *IN VITRO* MODEL: DRUG INTRODUCTION

Plasma has been shown to stimulate cell proliferation during short treatment times 10-35 s during tested 7 days after the plasma treatment. In this research, one additional step has been made to combine the positive effect of plasma having on cell proliferation and differentiation with induced cell permeabilization followed by drug introduction. Accordingly, labeled dextran has been used as a modeled drug carrier[231, 413]. Dextrans are non-toxic biopolymers consisting of a few D-glucose molecules joined in longer chains of varying lengths. The average molecular weight of dextran is a key property of the biopolymer that determines the size of the molecules in an aqueous solution. In this thesis, dextrans with molecular weights 4, 10, 40, and 70 kDa with corresponding hydrodynamic radii approximately 1, 1.9, 4.8, 6.5 nm are employed to study the permeabilization of fibroblast upon plasma treatment. Dextrans are labeled with green fluorescence protein FTIC and accordingly, it is easy to detect their fluorescence once FTIC is covalently bound to the targeted cell. Dextrans are used in pharmacology and medicine (microinjection[414], ultrasound cavitation[415], electrophoresis[416]) to trace drug delivery as these molecules cannot freely penetrate the cells. To this end, dextrans are perfect candidates to test cell permeabilization upon plasma treatment and transcellular drug delivery. Plasma delivery of dextran to fibroblast cells has been carried out with Ar, Ar/N$_2$ plasma, and Ar, Ar/N$_2$ plasma-aerosol system. Cells were exposed for 35 s to the plasma at a 10 mm distance from the effluent. Full plate imaging by permeable cells fluorescence for smallest dextran molecule is shown in Figure 7.7 (a). Obviously, dextran is delivered locally-only in plasma-treated cells, while untreated cells remained unstained. No significant qualitative difference between localized delivery of dextran into fibroblasts with Ar and Ar/N$_2$ plasmas have been noticed. However, a significant difference in localized delivery of dextran to permeabilized cells has been seen when employing gas plasmas and plasmas

assisted with aerosols, see Figure 7.7 (a). In addition, plasma-aerosol cell permeabilization and different size dextran delivery are shown in Figure 7.7 (b).
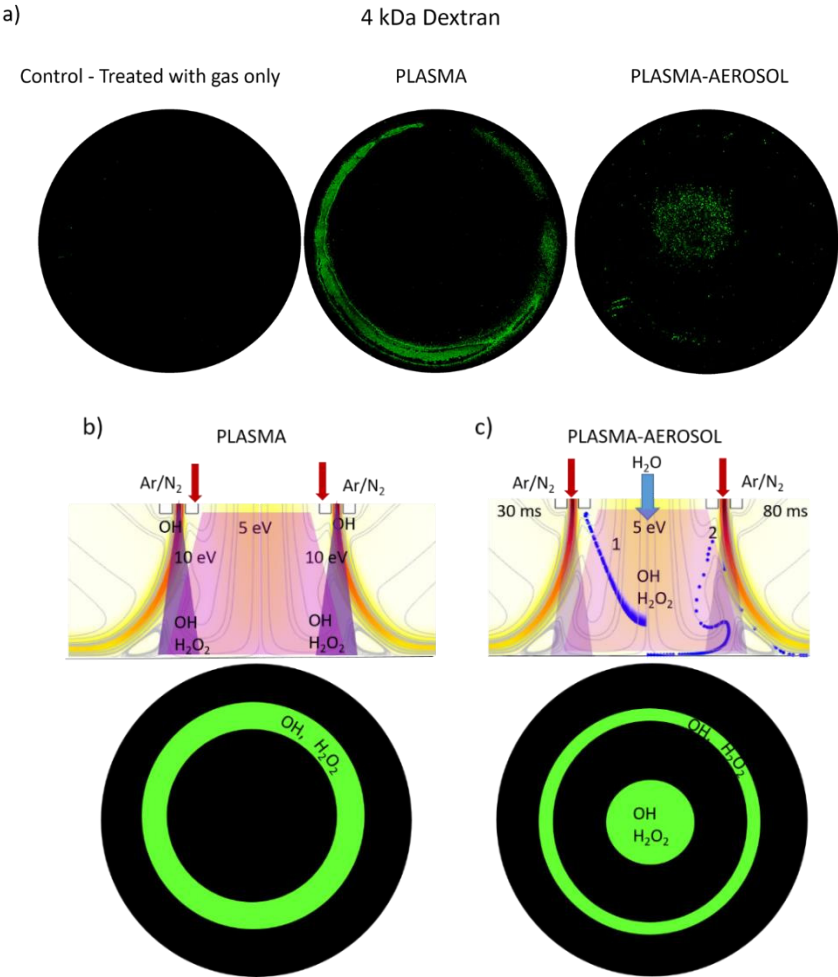


Figure 7.7. a) 4 kDa Dextran introduction into plasma-induced permeable cells. Schematics of localized cell permeabilization and dextran delivery via b) plasma and c) plasma-aerosol treatment.

In the case of plasma treatment fibroblasts, localized cell-permeabilization and the introduction of dextran happens in the annular region of the plasma ring. On the contrary, upon plasma-aerosol cell-permeabilization, dextran introduction occurs in the area corresponding to the aerosol. In the previous research on cell-permeabilization by He RF plasma jet[231], two possible mechanisms have been proposed to cause cell-membrane poration: cell charging induced by heavy ions[417]

and lipid peroxidation of the membrane by •OH radicals and $H_2O_2$[403]. The first one has been shown to play an essential role in the direct treatments with FE-DBD, where treated cells are directly exposed to the heavy ions from the plasma[66]. In plasma jets, ions and electrons recombine shortly after exiting the nozzle and thus are considered to have no/or minor role in the permeabilization of cells in this research. On the other hand, •OH radicals and $H_2O_2$ are abundantly created in APPJ in contact with water[304] and reasonably considered to play a major role in transient pore creation by lipid peroxidation of herby plasma-treated cells.

Different plasma localized dextran delivery patterns correspond to the plasma chemistry change once aerosol droplets are introduced into plasma effluent. During the treatment with Ar or $Ar/N_2$ plasma, •OH is generated as a dissociation product of water impurities in feeding gas (plasma), ambient air (close effluent), the aqueous layer covering the cells (UV radiation). The dominant reactions happening in Ar jet operating under humid conditions are presented with Equations 7.4-7.8 as follows[52]:

$$Ar_2^+ + H_2O \rightarrow 2Ar + H_2O^+ \ \rightarrow \ H_2O^+ + e^- \rightarrow OH + H \qquad \text{Eq. 7.4}$$

$$Ar_2^+ + H_2O \rightarrow OH + ArH^+ + Ar \qquad \text{Eq. 7.5}$$

$$Ar(4s[3p_2]) + H_2O \rightarrow Ar + OH + H \qquad \text{Eq. 7.6}$$

$$H_2O \xrightarrow[5\ eV]{hv} OH + H \qquad \text{Eq. 7.7}$$
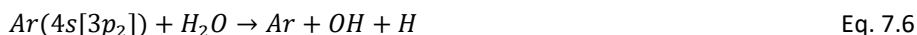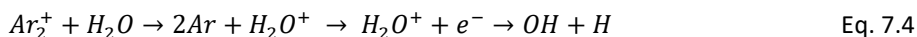
In the far effluent •OH radicals tend to recombine in three-body collisions, forming long-living $H_2O_2$ clusters.

$$OH + OH + M \rightarrow H_2O_2 + M \qquad \text{Eq. 7.8}$$

In the presence of Ar, $N_2$, $O_2$, $H_2$, $H_2O$, and $O_3$[52], •OH radicals dimerize in $H_2O_2$ (Eq. 7.8). Considering intense UV radiation Ar excimers and atomic oxygen ($E_{hv} \approx 10$ eV) from plasma ring contribution of photodissociation must not be neglected ($E_{diss}=4.4$ eV for O-H bond) (Eq. 7.7).

Introduction of aerosols in plasma effluent translates dominating plasma chemistry translates from plasma to plasma effluent. The favorable interaction of plasma with aerosol droplets over an aqueous target is explained by a larger effective interface[83, 383]. Considering the pattern of localized cell permeabilization, drug-delivering molecules, namely •OH and $H_2O_2$ originate from the aerosol. Controlled effluent interaction with aerosol results in •OH radicals and $H_2O_2$ generation, which

are shielded and safely transferred[90] to the cells covered by the dextran layer see Figure 7.7 (c(1)). As this interaction occurs in the plasma-free region, the interaction of water droplets and RONS/UV radiation generated in the air is limited, resulting in lower $^{\bullet}OH$ and $H_2O_2$ concentrations. Although most of the cell-permeabilization in plasma-aerosol treatments happens using activated aerosols (Figure 7.7 (c,1)), weaker and not always obvious permeabilization occurs partially in the plasma ring region Figure 7.7 (c,2). Possibly, partial diffusion of micro-droplets or water vapor towards the external ring region of plasma effluent (Figure 7.7 (c)) can impact the formation of $^{\bullet}OH$ radicals by quenching precursors, e.g., electrons and Ar metastables. Other mechanisms can be assigned to the complete photolysis of water vapor in the plasma effluent region by high energy UV photons emitted from the inter-electrode region and further quenching of atomic oxygen, as shown in equation Eq.7.8-9 :

$$H_2O \xrightarrow[8.8\,eV]{h\nu} 2H + O$$
<div align="right">Eq.7.9</div>

Further, different sizes of dextran have been investigated for plasma-induced cell permeability and transient membrane poration. Cell permeabilization by means of plasma and plasma coupled with aerosol is presented in Figure 7.8 (b). and Figure 7.8 (b). Dextran of the lowest molecular weight was the most efficiently incorporated in permeabilized cells, see Figure 7.8 (a).

Accordingly, the fluorescence of 4 kDa dextran labeled with FTIC was detected with the highest intensity. During the plasma treatment, the smallest nanopores (d≈1 nm) have been created along the whole plasma ring (d≈22 mm). In contrast, larger pores (1.9-6.5 nm) corresponding to the introduction of larger dextrans 10, 40, and 70 kDa have occurred in 50-25% of the plasma ring length. This might be due to the slight decentralization of electrodes, as reported in Chapter 4, Section 4.4.3. Cell permeabilization utilizing plasma combined with aerosol has shown the same trend in FTIC fluorescence of 4, 10, 40, and 70 kDa dextrans, see Figure 7.8 (b). The intensity of dextran-FTIC fluorescence decreased with the increase in molecular mass and size.

A previous study on HeLa cells permeabilization cells by He RF plasma jet[231] also reported the size limitation of molecules that can be introduced. In this study creation of pores smaller than 6.5 nm was shown, and transfection of 6 nm plasmid DNA with efficiency 30 %. AC plasma[228] was studied. Pores created by He jet were limited to introducing the smallest dextrans 4 and 10 kDa[231]. Moreover, 20 % efficiency gene transfection of plasmid DNA (4.7kbp≈10-13 nm[230]) was realized with 1-3 s air AC (40 kHz)[228]. The study reports the creation of transient pores in cell lines HeLa, epithelial, connective tissue HT-1080, breast tissue MCF7 and bone marrow

cells SH-SY5Y. Advantages of employing cold plasma for gene transfection were highlighted to be relatively high efficiency, low cell mortality compared to electroporation (transfection efficiency ≈38%, cell mortality ≈11%), simple procedure, and no need for special reagents.

a) Different dextrans introduced in cells upon Ar plasma treatment
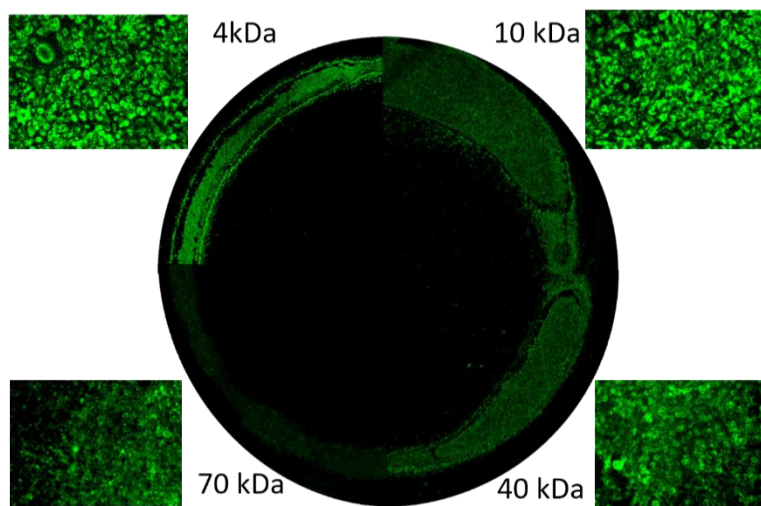


b) Different-size introduction in cells upon plasma treatment
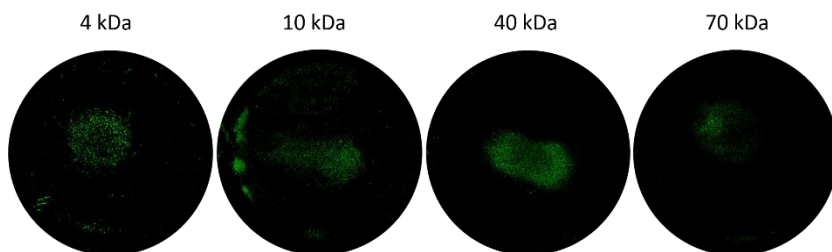


Figure 7.8. a) Ar plasma induced and b) Ar plasma-aerosol induced localized cell permeabilization and introduction of 4, 10, 40, 70 kDa dextrans. For better representation, the brightness of all the images was increased by 50%.

This chapter has given attention to the localized drug delivery and its manipulation by spatial change of delivery molecules $^{\bullet}OH$, $H_2O_2$ concentrations.

Nevertheless, it has to be mentioned that the operation limitation of the plasma-aerosol device still needs to be carefully defined when cells are covered by a limited amount of liquid (drug). Long exposure of the cells surrounded by a limited amount of liquid film to plasma is followed by cell detachment (high flux of RONS delivery), which can be seen in some regions of plasma-treated cells. Detachment of cells during longer drug delivery plasma treatment can be avoided by aerosol introduction, as shown in our previous research[399]. The introduction of aerosol in plasma changes the spatial chemistry of drug delivery molecules and localized drug delivery. To this end, plasma/plasma-aerosol drug delivery therapy offers a great potential to modify and perform local drug delivery.

## 7.5. CONCLUSIONS

This chapter discusses the potential of the atmospheric pressure plasma-aerosol system in wound healing- in vitro. Special attention has been given to the joined effect of plasma to promote cell proliferation and introduce drugs for enhanced wound healing. The proliferative and permeable effect of Ar, Ar/N$_2$ plasmas with and without aerosol have been demonstrated on fibroblast cells (L929). It has been shown that all forms of short plasma treatments t<60 s studied here promote cell proliferation 10-40% and have a noncytotoxic effect on fibroblast cells. Plasma triggers molecular responses in treated cells concerning better adhesion, signaling, proliferation, and differentiation. This has been demonstrated in the overexpression of genes which play an essential role in a wound-healing model (proliferation and remodeling phase). Upregulation of genes focal adhesions (cell migration, adhesions) and those crucial for ECM communication is triggered by both ROS (H$_2$O$_2$) and RNS (NO$_2^-$, NO$_3^-$). However, plasma-assisted differentiation of fibroblasts into myofibroblasts, crucial in the last stage of wound healing and healthy scarring, is triggered by ROS.

Moreover, aspects of plasma-driven wound healing enhanced by drug delivery *in vitro* are discussed here. Dextran delivery into cells treated with APPJ is realized through cell membrane lipid peroxidation by $^{\bullet}$OH radicals and H$_2$O$_2$. Two patterns of dextran delivery reported here concern differently localized cell-permeabilization upon plasma and plasma-aerosol treatment. It has been shown that the introduction of aerosol into plasma effluent changes the spatial distribution molecules $^{\bullet}$OH and H$_2$O$_2$ the local introduction of dextran. This learning is also essential for localized chemical activation, coating deposition, polymerization, etc. In addition, conclusions can be drawn concerning the plasma aerosol interaction. Aerosol introduction in plasma effluent favors interaction with aerosol and translates plasma chemistry to the aerosol region. This knowledge can be helpful for *in situ* plasma modification of biomolecules and their delivery to the target.

# CHAPTER 8: GENERAL CONCLUSIONS & OUTLOOKS

## 8.1. CONCLUSIONS

This thesis discusses the biomedical applicability of an APPJ coupled with aerosol, concretely for wound healing and topical drug delivery. With that aim, throughout four chapters (Chapter 4 - Chapter 7), the plasma device's physical, chemical, and biological aspects are presented. Finally, considering points for improving existing medically certified plasma devices, we suggest a solution in plasma-aerosol configuration.

First, stability and temperature safety aspects of a large annular-shape RF APPJ in argon were investigated. Large-size ($d_{out} \approx 14$ mm) annular-shape APPJ in Ar gas is sustained in diffuse, $\alpha$-mode under power density 30 W/cm$^3$. The stabilization of the discharge uniform operation is ascribed to the presence of sheath. The gas temperature of the plasma jet was investigated utilizing three different diagnostic tools to validate its biomedical applicability. Rayleigh scattering can be successfully employed in this type of plasma characterization, giving gas temperature in the effluent in agreement with OH radical rotational temperature. To this end, biomedical application of APPJ jet is encouraged above 2 SLM Ar gas flow and below deposited power of 10 W. Under these experimental conditions, gas temperature in plasma jet is estimated to be 60°C.

Afterward, plasma-induced liquid chemistry was investigated to validate the biomedical applicability of this APPJ further. Reactive oxygen species-dominating character of Ar plasma jet operating under ambient conditions was shown. Namely, VUV/UV radiation followed by short-living species atomic oxygen O and singlet oxygen $^1O_2$ prevail plasma chemistry. Accordingly, the photolytic processes upon plasma UV radiation drive water-induced chemistry and the creation of species OH and $H_2O_2$. In this study, aerosol was introduced in plasma effluent to modify plasma chemistry. Aerosol presence in plasma effluent was shown to translate plasma chemistry in the aerosol region, resulting in lower oxidation power of plasma. Water droplets act as scavenging and absorption centers for radicals created in plasma and UV radiation. With the introduction of liquid micro-droplets, plasma jet favors interaction with aerosol due to the larger effective interface. This results in higher spatial selectivity of generated species.

A further concern of this research was the biological safety aspects of APPJ. In the following study, UV emission from the Ar plasma jet was filtered out, and its effect was tested on biological targets. For this purpose, we performed experiments on biomolecules, cells, and tissues. It was shown that the most intensive UV emission comes from argon excimers $Ar_2^*$ and atomic oxygen O located between electrodes (UV C). This emission is followed by nitrogen $N_2$(C-B) emission (UV A) located in the region where the plasma jet exits the nozzle and interacts with the air. Although plasma jet operates in ambient air, UV photons propagate in Ar flow and are

detected 14 mm below plasma nozzle ($I_{drop} \approx 25\%$). Therefore, UV radiation should be considered in biomedical treatments and accordingly handled. UV radiation showed a significant effect on the defragmentation of plasmid DNA. It contributes to the integral plasma effect with about 70 % to the single and double-strand break of plasmid DNA. Although the impact of UV radiation on fibroblast cells in liquid was shown to be negligible, a strong cytotoxic effect on the cells in a dry environment was confirmed. In this thesis was shown that aerosol affects the plasma biological properties.

In the first instance, it has been confirmed that aerosol changes the plasma-target interface. This was expected to be seen considering our previous study on plasma-induced chemistry. Aerosol injection in the plasma effluent increased the stability of plasmid DNA. Moreover, survival of cells in a dry environment and change in the interaction area between plasma and cells was accomplished by plasma coupling with aerosol. Introduced aerosol plays a vital role as an absorbing medium for VUV/UV radiation, and consequently, it is proposed as a tool to control the flux of radiation during treatment. This combination was proven safe for skin treatments in short treatments (t<60 s).

Finally, more investigations were carried out to study plasma-cell proliferation and to examine possibilities of plasma-assisted drug delivery. Enhanced plasma-wound healing, joined with drug introduction, was the driving idea of the final study. In these studies, fibroblasts were treated with plasma to define the proliferative range of plasma treatments. The proliferation of fibroblast cells was significant in short treatment 10, 35, and 60 s on 10 mm distance with $P_{diss}$=8 W Ar/Ar+$N_2$ plasma. Plasma was shown to cause upregulation of genes of vital importance in wound healing. Upregulation of the focal adhesions and collagens was mainly triggered by long-living RONS ($NO_x$ ions).

On the other hand, differentiation of fibroblasts into myofibroblasts probably occurs due to ROS actions. In the final studies in this thesis, special attention was given to investigating plasma-assisted cell permeabilization and drug introduction *in vitro*. This study has shown that plasma permeabilizes cells by lipid peroxidation of the cell membrane. This mainly occurs through the action of hydroxyl radical $^\bullet OH$ and hydrogen peroxide $H_2O_2$. Owing to our previous findings, spatial generation and concentration of species $^\bullet OH$ and $H_2O_2$ can be modified utilizing aerosol. The introduction of aerosol was shown to translate plasma chemistry in the aerosol region where cell-permeabilization happens. To this end, plasma and plasma coupled with aerosol offer great potential for localized drug delivery.

## 8.2. FUTURE OUTLOOKS

Although numerous biomedical perspectives of the plasma jet have been demonstrated in this thesis, more investigation is needed before its commercial use:

1) Knowing that aerosol affects plasma chemistry significantly, more investigation on plasma-aerosol interaction is of central importance. For this reason, further development of a more realistic computational model is desirable. To this end, Plasma Module COMSOL Mutliphyiscs should be coupled with the existing model. The computational modeling of the plasma-aerosol system offers an excellent opportunity to study droplet size and distribution for optimal interaction with plasma.

2) A critical point in future studies is to examine the bactericidal property of the plasma jet (e.g., Gram-negative/positive *Pseudomonas aeruginosa*/*Staphylococcus aureus*). Accordingly, plasma treatment should be defined for efficient inactivation of bacteria while promoting eukaryotic cell proliferation.

3) In this thesis, the first trials on cell permeabilization by plasma and drug delivery were done; however, more research on this topic is mandatory. Firstly, after the plasma-induced permeabilization, cell viability must be validated. After mild plasma treatment, nanopores creation of the cell membrane occurs, and the drug is delivered into a cell. However, exposure to the high flux of plasma species OH and $H_2O_2$ can result in cell-membrane disintegration and cell leakage (necrosis). Therefore, plasma-permeabilized cells must be subjected to a cell viability test.

4) Finally, the interaction of plasma effluent with the aerosol can modify biomolecules dissolved within the aerosol (UV radiation/RONS). Accordingly, if a drug is tailored to be delivered as an aerosol passing through plasma effluent, additional attention must be given to its possible modification.

Plasma (P=20 W)
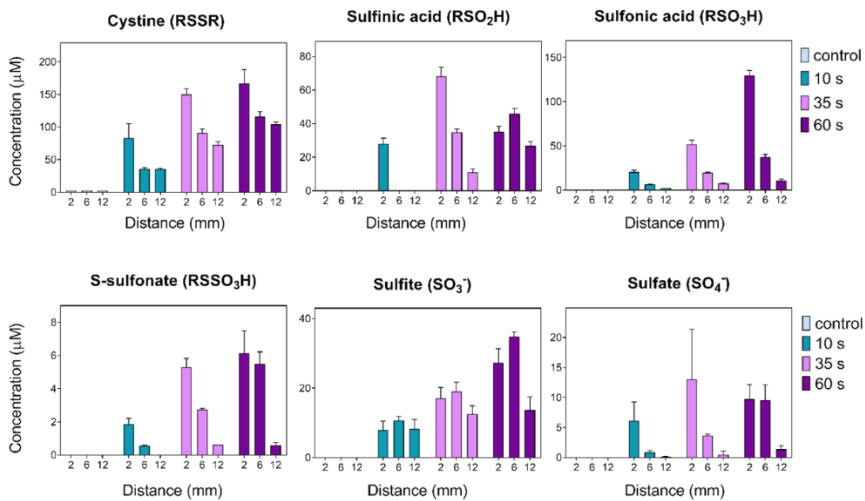


Appendix 1. Absolute concentrations of cysteine derivatives after treatment by plasma (cysteine in target) at power 20 W. Time and distance were modulated. Mean of three independent experiments +SD

Plasma-aerosol (P=20 W)
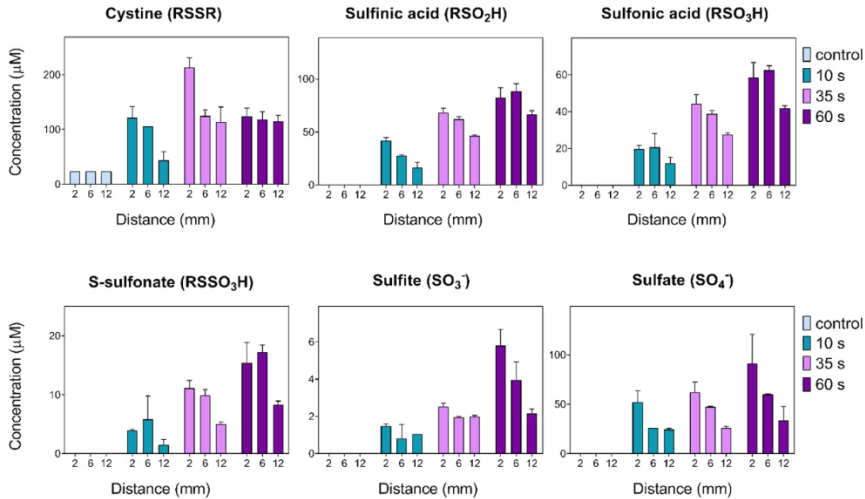


Appendix 2. Absolute concentrations of cysteine derivatives after treatment by plasma with aerosol (cysteine in target) at power 20 W. Time and distance were modulated. Mean of three independent experiments +SD.
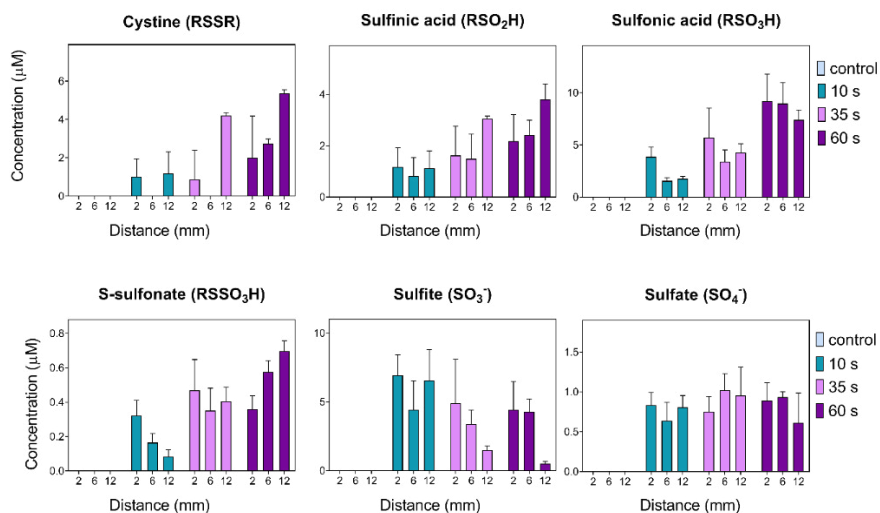
Appendix 3. Absolute concentrations of cysteine derivatives generated by the introduction of cysteine solutions (1 mM) in aerosol with plasma operating at power 20 W (cysteine in aerosol) collected in water-filled wells. The absolute number of molecules deposited is given. The limited impact of distance indicates that the majority of reactions occur in the droplets

Day 7
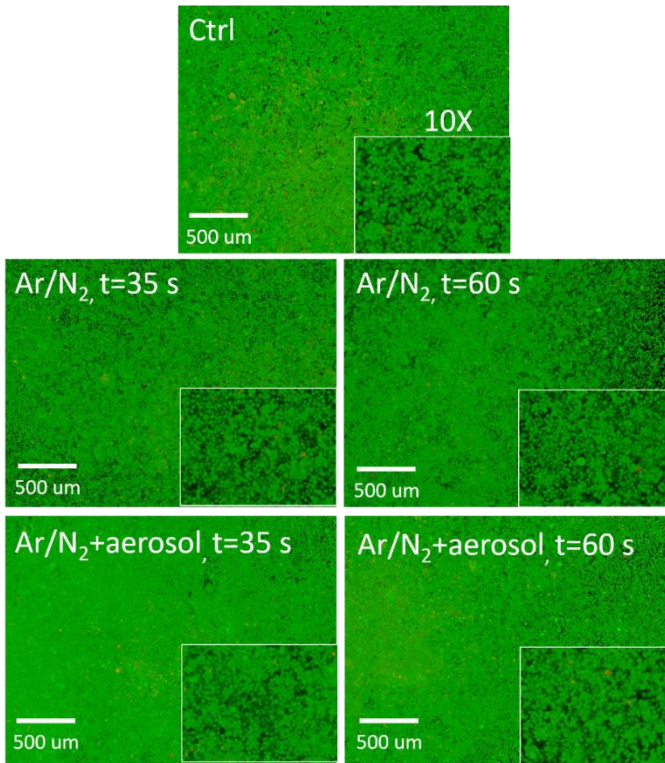


Appendix 3. Live (green)/Dead (red) staining (magnification 4X and 10 X) on day 7 :
Control;  Ar plasma t= 35 s (left) and t=60 s (right); Ar+aerosol plasma t= 35 s (left)
and Ar+aerosol plasma t= 60 s (right).
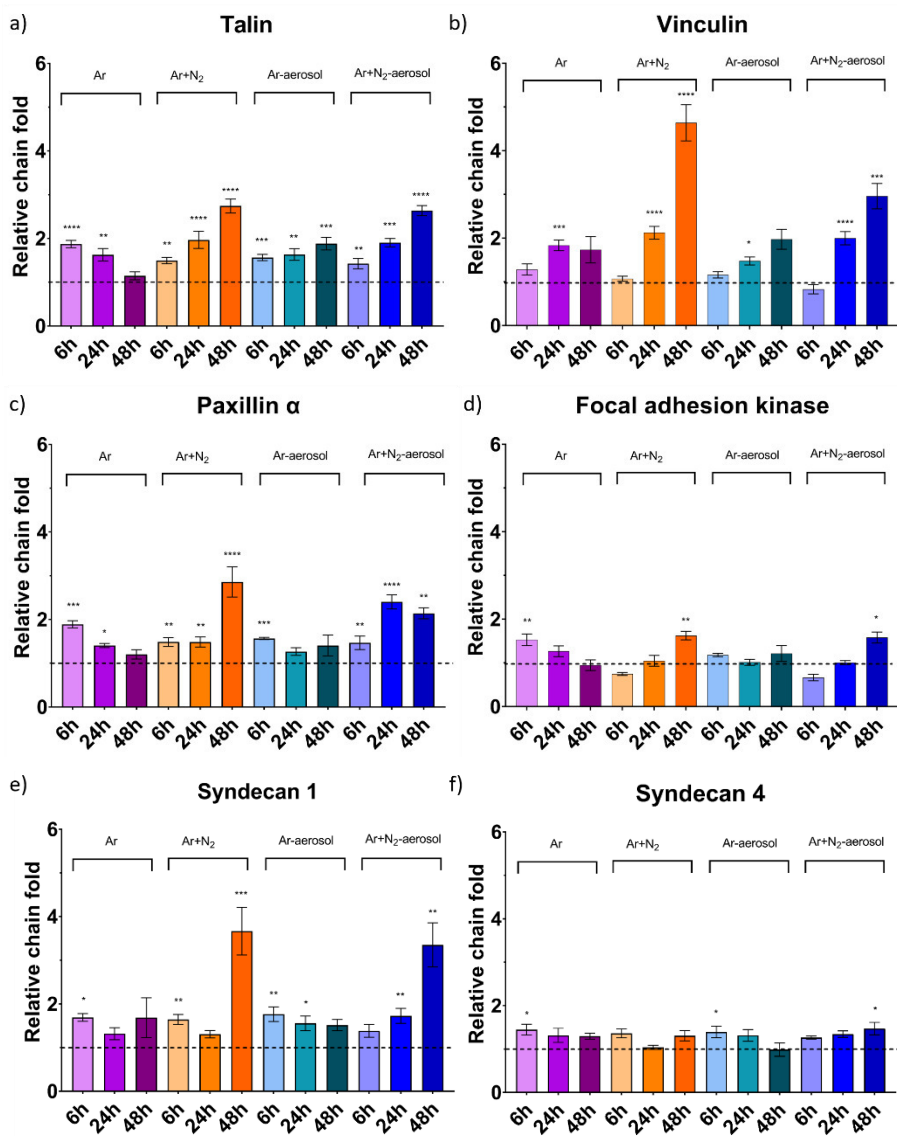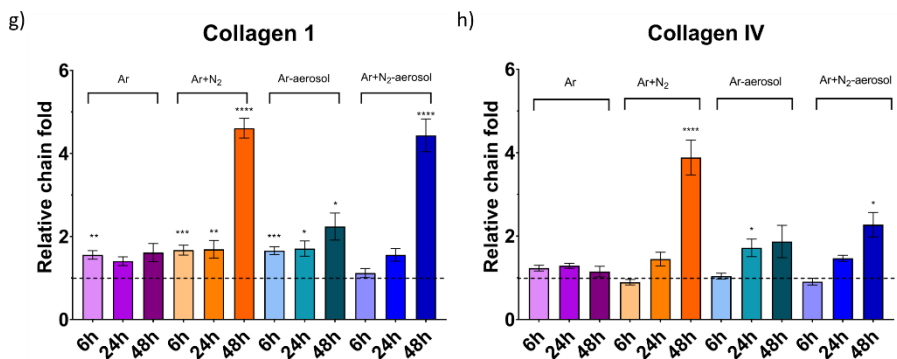
Appendix 3. Gene expression analysis; relative chain fold on the expression of: a) talin, b) vinculin, c) paxilin-α, d) focal adhesion kinase, e) syndecan 1, f) syndecan 4, g) collagen I, h) collagen IV measured 6h, 24 h, and 48 h after the Ar, Ar+N$_2$, Ar-aerosol and Ar+N$_2$-aerosol plasma treatment. Measured genes have been normalized to GAPDH (1).

## REFERENCES

1.      Chen, F. F., *Introduction to plasma physics*. Springer Science & Business Media: 2012.
2.      Tonks, L.; Langmuir, I., A general theory of the plasma of an arc. *Physical review* **1929,** *34* (6), 876.
3.      Lieberman, M. A.; Lichtenberg, A. J., *Principles of plasma discharges and materials processing*. John Wiley & Sons: 2005.
4.      Raizer, Y. P.; Allen, J. E., *Gas discharge physics*. Springer Berlin: 1997; Vol. 2.
5.      Schutze, A.; Jeong, J. Y.; Babayan, S. E.; Park, J.; Selwyn, G. S.; Hicks, R. F., The atmospheric-pressure plasma jet: a review and comparison to other plasma sources. *IEEE Trans. Plasma Sci.* **1998,** *26* (6), 1685-1694.
6.      Brandenburg, R., Dielectric barrier discharges: progress on plasma sources and on the understanding of regimes and single filaments. *Plasma Sources Science and Technology* **2017,** *26* (5), 053001.
7.      Wang, L.; Dinescu, G.; Deng, X.; Ionita, E.-R.; Leys, C.; Nikiforov, A. Y., Mechanisms of sustaining a radio-frequency atmospheric pressure planar discharge. *Plasma Sources Science and Technology* **2017,** *26* (7), 075012.
8.      Kogelschatz, U., Filamentary, patterned, and diffuse barrier discharges. *IEEE Trans. Plasma Sci.* **2002,** *30* (4), 1400-1408.
9.      Vervloessem, E.; Aghaei, M.; Jardali, F.; Hafezkhiabani, N.; Bogaerts, A., Plasma-Based N2 Fixation into NO x: Insights from Modeling toward Optimum Yields and Energy Costs in a Gliding Arc Plasmatron. *ACS Sustainable Chemistry & Engineering* **2020,** *8* (26), 9711-9720.
10.     Roth, J. R., *Industrial plasma engineering: Volume 2: Applications to nonthermal plasma processing*. CRC press: 2001; Vol. 2.
11.     Becker, K. H.; Kogelschatz, U.; Schoenbach, K.; Barker, R., *Non-equilibrium air plasmas at atmospheric pressure*. CRC press: 2004.
12.     Conrads, H.; Schmidt, M., Plasma generation and plasma sources. *Plasma Sources Science and Technology* **2000,** *9* (4), 441.
13.     Akishev, Y.; Grushin, M.; Napartovich, A.; Trushkin, N., Novel AC and DC non-thermal plasma sources for cold surface treatment of polymer films and fabrics at atmospheric pressure. *Plasmas and Polymers* **2002,** *7* (3), 261-289.
14.     Moshrefi, M. M.; Rashidi, F., Hydrogen production from methane decomposition in cold plasma reactor with rotating electrodes. *Plasma Chemistry and Plasma Processing* **2018,** *38* (3), 503-515.
15.     Gorbanev, Y.; Verlackt, C.; Tinck, S.; Tuenter, E.; Foubert, K.; Cos, P.; Bogaerts, A., Combining experimental and modelling approaches to study the sources of reactive species induced in water by the COST RF plasma jet. *Physical Chemistry Chemical Physics* **2018,** *20* (4), 2797-2808.
16.     Mintoussov, E.; Pendleton, S.; Gerbault, F.; Popov, N.; Starikovskaia, S., Fast gas heating in nitrogen–oxygen discharge plasma: II. Energy exchange in the afterglow of a volume nanosecond discharge at moderate pressures. *Journal of Physics D: Applied Physics* **2011,** *44* (28), 285202.

17.     Xia, G.; Chen, Z.; Saifutdinov, A. I.; Eliseev, S.; Hu, Y.; Kudryavtsev, A. A., Longer microwave plasma jet with different discharge performances originated by plasma–surface interactions. *IEEE Trans. Plasma Sci.* **2014,** *42* (10), 2768-2769.

18.     O'Neill, L.; O'Hare, L. A.; Leadley, S. R.; Goodwin, A. J., Atmospheric pressure plasma liquid deposition–a novel route to barrier coatings. *Chemical Vapor Deposition* **2005,** *11* (11-12), 477-479.

19.     Laroussi, M., Sterilization of contaminated matter with an atmospheric pressure plasma. *IEEE Trans. Plasma Sci.* **1996,** *24* (3), 1188-1191.

20.     Carton, O.; Ben Salem, D.; Bhatt, S.; Pulpytel, J.; Arefi-Khonsari, F., Plasma polymerization of acrylic acid by atmospheric pressure nitrogen plasma jet for biomedical applications. *Plasma Process. Polym.* **2012,** *9* (10), 984-993.

21.     Van Vrekhem, S.; Vloebergh, K.; Asadian, M.; Vercruysse, C.; Declercq, H.; Van Tongel, A.; De Wilde, L.; De Geyter, N.; Morent, R., Improving the surface properties of an UHMWPE shoulder implant with an atmospheric pressure plasma jet. *Scientific reports* **2018,** *8* (1), 1-11.

22.     Van Gils, C.; Hofmann, S.; Boekema, B.; Brandenburg, R.; Bruggeman, P., Mechanisms of bacterial inactivation in the liquid phase induced by a remote RF cold atmospheric pressure plasma jet. *Journal of Physics D: Applied Physics* **2013,** *46* (17), 175203.

23.     Guo, L.; Xu, R.; Gou, L.; Liu, Z.; Zhao, Y.; Liu, D.; Zhang, L.; Chen, H.; Kong, M. G., Mechanism of virus inactivation by cold atmospheric-pressure plasma and plasma-activated water. *Applied and environmental microbiology* **2018,** *84* (17).

24.     Kostov, K. G.; Borges, A. C.; Koga-Ito, C. Y.; Nishime, T. M. C.; Prysiazhnyi, V.; Honda, R. Y., Inactivation of Candida albicans by cold atmospheric pressure plasma jet. *IEEE Trans. Plasma Sci.* **2014,** *43* (3), 770-775.

25.     Vasilev, K.; Griesser, S. S.; Griesser, H. J., Antibacterial surfaces and coatings produced by plasma techniques. *Plasma Process. Polym.* **2011,** *8* (11), 1010-1023.

26.     Yoshinari, M.; Matsuzaka, K.; Inoue, T., Surface modification by cold-plasma technique for dental implants—Bio-functionalization with binding pharmaceuticals. *Japanese Dental Science Review* **2011,** *47* (2), 89-101.

27.     Albanese, A.; Licata, M. E.; Polizzi, B.; Campisi, G., Platelet-rich plasma (PRP) in dental and oral surgery: from the wound healing to bone regeneration. *Immunity & Ageing* **2013,** *10* (1), 1-10.

28.     Isbary, G.; Morfill, G.; Schmidt, H.; Georgi, M.; Ramrath, K.; Heinlin, J.; Karrer, S.; Landthaler, M.; Shimizu, T.; Steffes, B., A first prospective randomized controlled trial to decrease bacterial load using cold atmospheric argon plasma on chronic wounds in patients. *British Journal of Dermatology* **2010,** *163* (1), 78-82.

29.     Arndt, S.; Unger, P.; Wacker, E.; Shimizu, T.; Heinlin, J.; Li, Y.-F.; Thomas, H. M.; Morfill, G. E.; Zimmermann, J. L.; Bosserhoff, A.-K., Cold atmospheric plasma (CAP) changes gene expression of key molecules of the wound healing machinery and improves wound healing in vitro and in vivo. *PloS one* **2013,** *8* (11), e79325.

30.     Keidar, M.; Walk, R.; Shashurin, A.; Srinivasan, P.; Sandler, A.; Dasgupta, S.; Ravi, R.; Guerrero-Preston, R.; Trink, B., Cold plasma selectivity and the possibility of a paradigm shift in cancer therapy. *British journal of cancer* **2011,** *105* (9), 1295-1301.

31.     Winter, J.; Brandenburg, R.; Weltmann, K., Atmospheric pressure plasma jets: an overview of devices and new directions. *Plasma Sources Science and Technology* **2015,** *24* (6), 064001.

32.     Goldman, M.; Goldman, A.; Sigmond, R., The corona discharge, its properties and specific uses. *Pure Appl. Chem.* **1985,** *57* (9), 1353-1362.

33.     Massines, F.; Gouda, G., A comparison of polypropylene-surface treatment by filamentary, homogeneous and glow discharges in helium at atmospheric pressure. *Journal of Physics D: Applied Physics* **1998,** *31* (24), 3411.

34.     Kuraica, M. M.; Obradović, B. M.; Manojlović, D.; Ostojić, D. R.; Purić, J., Ozonized water generator based on coaxial dielectric-barrier-discharge in air. *Vacuum* **2004,** *73* (3-4), 705-708.

35.     Fridman, G.; Shereshevsky, A.; Jost, M. M.; Brooks, A. D.; Fridman, A.; Gutsol, A.; Vasilets, V.; Friedman, G., Floating electrode dielectric barrier discharge plasma in air promoting apoptotic behavior in melanoma skin cancer cell lines. *Plasma Chemistry and Plasma Processing* **2007,** *27* (2), 163-176.

36.     Xu, X., Dielectric barrier discharge—properties and applications. *Thin solid films* **2001,** *390* (1-2), 237-242.

37.     Laroussi, M., The Resistive Barrier Discharge: A Brief Review of the Device and Its Biomedical Applications. *Plasma* **2021,** *4* (1), 75-80.

38.     Laroussi, M.; Akan, T., Arc-free atmospheric pressure cold plasma jets: A review. *Plasma Process. Polym.* **2007,** *4* (9), 777-788.

39.     Walsh, J. L.; Kong, M. G., Contrasting characteristics of linear-field and cross-field atmospheric plasma jets. *Applied Physics Letters* **2008,** *93* (11), 111501.

40.     Kostov, K. G.; Nishime, T. M. C.; Castro, A. H. R.; Toth, A.; Hein, L. R. d. O., Surface modification of polymeric materials by cold atmospheric plasma jet. *Applied Surface Science* **2014,** *314*, 367-375.

41.     Zheng, X.; Chen, G.; Zhang, Z.; Beem, J.; Massey, S.; Huang, J., A two-step process for surface modification of poly (ethylene terephthalate) fabrics by Ar/O2 plasma-induced facile polymerization at ambient conditions. *Surface and Coatings Technology* **2013,** *226*, 123-129.

42.     Yim, J. H.; Rodriguez-Santiago, V.; Williams, A. A.; Gougousi, T.; Pappas, D. D.; Hirvonen, J. K., Atmospheric pressure plasma enhanced chemical vapor deposition of hydrophobic coatings using fluorine-based liquid precursors. *Surface and Coatings Technology* **2013,** *234*, 21-32.

43.     Narimisa, M.; Krčma, F.; Onyshchenko, Y.; Kozáková, Z.; Morent, R.; De Geyter, N., Atmospheric pressure microwave plasma jet for organic thin film deposition. *Polymers* **2020,** *12* (2), 354.

44.     Shi, X.-m; Xu, G.-m.; Zhang, G.-j.; Liu, J.-r.; Wu, Y.-m.; Gao, L.-g.; Yang, Y.; Chang, Z.-s.; Yao, C.-w., Low-temperature plasma promotes fibroblast proliferation in wound healing by ROS-activated NF-κB signaling pathway. *Current medical science* **2018,** *38* (1), 107-114.

45.     Yousfi, M.; Merbahi, N.; Sarrette, J.; Eichwald, O.; Ricard, A.; Gardou, J.; Ducasse, O.; Benhenni, M., Non thermal plasma sources of production of active species for biomedical uses: analyses, optimization and prospect. In *Biomedical engineering-frontiers and challenges*, IntechOpen: 2011.

46.     Castell, R.; Iglesias, E.; Ruiz-Camacho, J., Glow discharge plasma properties of gases of environmental interest. *Brazilian journal of physics* **2004,** *34* (4B), 1734-1737.

47.     Fricke, K.; Koban, I.; Tresp, H.; Jablonowski, L.; Schröder, K.; Kramer, A.; Weltmann, K.-D.; von Woedtke, T.; Kocher, T., Atmospheric pressure plasma: a high-performance tool for the efficient removal of biofilms. *PloS one* **2012,** *7* (8), e42539.

48.     Ahmed, K., Design and experimental investigations of electrical breakdown in a plasma jet device and applications. **2014**.

49.     Lu, X.; Naidis, G.; Laroussi, M.; Reuter, S.; Graves, D.; Ostrikov, K., Reactive species in non-equilibrium atmospheric-pressure plasmas: Generation, transport, and biological effects. *Physics Reports* **2016,** *630*, 1-84.

50.     Lu, X.; Fridman, A., Guest editorial the second special issue on atmospheric pressure plasma jets and their applications. *IEEE Trans. Plasma Sci.* **2015,** *43* (3), 701-702.

51.     Hofmann, S.; Van Gessel, A.; Verreycken, T.; Bruggeman, P., Power dissipation, gas temperatures and electron densities of cold atmospheric pressure helium and argon RF plasma jets. *Plasma Sources Science and Technology* **2011,** *20* (6), 065010.

52.     Van Gaens, W.; Bogaerts, A., Kinetic modelling for an atmospheric pressure argon plasma jet in humid air. *Journal of Physics D: Applied Physics* **2013,** *46* (27), 275201.

53.     Sobolev, N., Electron-excited molecules in a nonequilibrium plasma. *Moscow Izdatel Nauka* **1985,** *157*.

54.     Gorbanev, Y.; Privat-Maldonado, A.; Bogaerts, A., Analysis of short-lived reactive species in plasma–air–water systems: the dos and the do nots. ACS Publications: 2018.

55.     Schieber, M.; Chandel, N. S., ROS function in redox signaling and oxidative stress. *Current biology* **2014,** *24* (10), R453-R462.

56.     Schmidt-Bleker, A.; Winter, J.; Bösel, A.; Reuter, S.; Weltmann, K.-D., On the plasma chemistry of a cold atmospheric argon plasma jet with shielding gas device. *Plasma Sources Science and Technology* **2015,** *25* (1), 015005.

57.     Gorbanev, Y.; O'Connell, D.; Chechik, V., Non-thermal plasma in contact with water: The origin of species. *Chemistry–A European Journal* **2016,** *22* (10), 3496-3505.

58.     Toth, J. R.; Abuyazid, N. H.; Lacks, D. J.; Renner, J. N.; Sankaran, R. M., A plasma-water droplet reactor for process-intensified, continuous nitrogen fixation at atmospheric pressure. *ACS Sustainable Chemistry & Engineering* **2020,** *8* (39), 14845-14854.

59.     Snoeckx, R.; Bogaerts, A., Plasma technology–a novel solution for CO 2 conversion? *Chemical Society Reviews* **2017,** *46* (19), 5805-5863.

60.     Bruggeman, P.; Kushner, M. J.; Locke, B. R.; Gardeniers, J. G.; Graham, W.; Graves, D. B.; Hofman-Caris, R.; Maric, D.; Reid, J. P.; Ceriani, E., Plasma–liquid interactions: a review and roadmap. *Plasma sources science and technology* **2016,** *25* (5), 053002.

61.     Mori, M.; Hamamoto, A.; Takahashi, A.; Nakano, M.; Wakikawa, N.; Tachibana, S.; Ikehara, T.; Nakaya, Y.; Akutagawa, M.; Kinouchi, Y., Development of

a new water sterilization device with a 365 nm UV-LED. *Medical & biological engineering & computing* **2007,** *45* (12), 1237-1241.

62. Baxendale, J.; Wilson, J., The photolysis of hydrogen peroxide at high light intensities. *Transactions of the Faraday Society* **1957,** *53*, 344-356.

63. Jablonowski, H.; Bussiahn, R.; Hammer, M.; Weltmann, K.-D.; von Woedtke, T.; Reuter, S., Impact of plasma jet vacuum ultraviolet radiation on reactive oxygen species generation in bio-relevant liquids. *Phys. Plasmas* **2015,** *22* (12), 122008.

64. Schneider, S.; Lackmann, J. W.; Ellerweg, D.; Denis, B.; Narberhaus, F.; Bandow, J. E.; Benedikt, J., The role of VUV radiation in the inactivation of bacteria with an atmospheric pressure plasma jet. *Plasma Process. Polym.* **2012,** *9* (6), 561-568.

65. Lackmann, J.-W.; Schneider, S.; Edengeiser, E.; Jarzina, F.; Brinckmann, S.; Steinborn, E.; Havenith, M.; Benedikt, J.; Bandow, J. E., Photons and particles emitted from cold atmospheric-pressure plasma inactivate bacteria and biomolecules independently and synergistically. *Journal of the Royal Society Interface* **2013,** *10* (89), 20130591.

66. Dobrynin, D.; Fridman, G.; Friedman, G.; Fridman, A., Physical and biological mechanisms of direct plasma interaction with living tissue. *New Journal of Physics* **2009,** *11* (11), 115020.

67. Fridman, A., *Plasma chemistry*. Cambridge university press: 2008.

68. Kalghatgi, S. U. Mechanisms of interaction of non-thermal plasma with living cells. Drexel University, 2010.

69. Fridman, G.; Peddinghaus, M.; Balasubramanian, M.; Ayan, H.; Fridman, A.; Gutsol, A.; Brooks, A., Blood coagulation and living tissue sterilization by floating-electrode dielectric barrier discharge in air. *Plasma Chemistry and plasma processing* **2006,** *26* (4), 425-442.

70. Golda, J.; Held, J.; Redeker, B.; Konkowski, M.; Beijer, P.; Sobota, A.; Kroesen, G.; Braithwaite, N. S. J.; Reuter, S.; Turner, M., Concepts and characteristics of the 'COST Reference Microplasma Jet'. *Journal of Physics D: Applied Physics* **2016,** *49* (8), 084003.

71. Privat-Maldonado, A.; Gorbanev, Y.; Dewilde, S.; Smits, E.; Bogaerts, A., Reduction of human glioblastoma spheroids using cold atmospheric plasma: The combined effect of short-and long-lived reactive species. *Cancers* **2018,** *10* (11), 394.

72. Ellerweg, D.; Benedikt, J.; von Keudell, A.; Knake, N.; Schulz-von der Gathen, V., Characterization of the effluent of a He/O2 microscale atmospheric pressure plasma jet by quantitative molecular beam mass spectrometry. *New Journal of physics* **2010,** *12* (1), 013021.

73. Gorbanev, Y.; Golda, J.; Gathen, V. S.-v. d.; Bogaerts, A., Applications of the COST plasma jet: More than a reference standard. *Plasma* **2019,** *2* (3), 316-327.

74. Reuter, S.; Winter, J.; Schmidt-Bleker, A.; Schroeder, D.; Lange, H.; Knake, N.; Schulz-Von Der Gathen, V.; Weltmann, K., Atomic oxygen in a cold argon plasma jet: TALIF spectroscopy in ambient air with modelling and measurements of ambient species diffusion. *Plasma Sources Science and Technology* **2012,** *21* (2), 024005.

75. Jablonowski, H.; Sousa, J. S.; Weltmann, K.-D.; Wende, K.; Reuter, S., Quantification of the ozone and singlet delta oxygen produced in gas and liquid

phases by a non-thermal atmospheric plasma with relevance for medical treatment. *Scientific reports* **2018,** *8* (1), 1-12.

76.        Reuter, S.; Von Woedtke, T.; Weltmann, K.-D., The kINPen—a review on physics and chemistry of the atmospheric pressure plasma jet and its applications. *Journal of Physics D: Applied Physics* **2018,** *51* (23), 233001.

77.        Kamata, H.; Hirata, H., Redox regulation of cellular signalling. *Cellular signalling* **1999,** *11* (1), 1-14.

78.        Snezhkina, A. V.; Kudryavtseva, A. V.; Kardymon, O. L.; Savvateeva, M. V.; Melnikova, N. V.; Krasnov, G. S.; Dmitriev, A. A., ROS generation and antioxidant defense systems in normal and malignant cells. *Oxidative medicine and cellular longevity* **2019,** *2019*.

79.        Kohen, R.; Nyska, A., Invited review: Oxidation of biological systems: oxidative stress phenomena, antioxidants, redox reactions, and methods for their quantification. *Toxicologic pathology* **2002,** *30* (6), 620-650.

80.        Halliwell, B.; Gutteridge, J. M., *Free radicals in biology and medicine*. Oxford university press, USA: 2015.

81.        Davies, K. J., The broad spectrum of responses to oxidants in proliferating cells: a new paradigm for oxidative stress. *IUBMB life* **1999,** *48* (1), 41-47.

82.        Lackmann, J.-W.; Bruno, G.; Jablonowski, H.; Kogelheide, F.; Offerhaus, B.; Held, J.; Schulz-von der Gathen, V.; Stapelmann, K.; von Woedtke, T.; Wende, K., Nitrosylation vs. oxidation–How to modulate cold physical plasmas for biological applications. *PLoS One* **2019,** *14* (5), e0216606.

83.        Bruggeman, P. J.; Kushner, M. J.; Locke, B. R.; Gardeniers, J. G.; Graham, W.; Graves, D. B.; Hofman-Caris, R.; Maric, D.; Reid, J. P.; Ceriani, E., Plasma–liquid interactions: a review and roadmap. *Plasma sources science and technology* **2016,** *25* (5), 053002.

84.        Schoenbach, K.; Kolb, J.; Xiao, S.; Katsuki, S.; Minamitani, Y.; Joshi, R., Electrical breakdown of water in microgaps. *Plasma Sources Science and Technology* **2008,** *17* (2), 024010.

85.        Mededovic, S.; Locke, B., Primary chemical reactions in pulsed electrical discharge channels in water. *Journal of Physics D: Applied Physics* **2007,** *40* (24), 7734.

86.        Machala, Z.; Jedlovsky, I.; Martisovits, V., DC discharges in atmospheric air and their transitions. *IEEE Trans. Plasma Sci.* **2008,** *36* (4), 918-919.

87.        Bruggeman, P.; Schram, D.; Gonzalez, M. A.; Rego, R.; Kong, M. G.; Leys, C., Characterization of a direct dc-excited discharge in water by optical emission spectroscopy. *Plasma Sources Sci. Technol.* **2009,** *18* (2), 13.

88.        Aoki, H.; Kitano, K.; Hamaguchi, S., Plasma generation inside externally supplied Ar bubbles in water. *Plasma Sources Science and Technology* **2008,** *17* (2), 025006.

89.        Bruggeman, P.; Leys, C., Non-thermal plasmas in and in contact with liquids. *Journal of Physics D: Applied Physics* **2009,** *42* (5), 053001.

90.        Burlica, R.; Shih, K.-Y.; Locke, B., Formation of H2 and H2O2 in a water-spray gliding arc nonthermal plasma reactor. *Industrial & Engineering Chemistry Research* **2010,** *49* (14), 6342-6349.

91.      Nunan, R.; Harding, K. G.; Martin, P., Clinical challenges of chronic wounds: searching for an optimal animal model to recapitulate their complexity. *Disease models & mechanisms* **2014,** *7* (11), 1205-1213.

92.      Smet, S.; Probst, S.; Holloway, S.; Fourie, A.; Beele, H.; Beeckman, D., The measurement properties of assessment tools for chronic wounds: a systematic review. *International Journal of Nursing Studies* **2021**, 103998.

93.      Armstrong, D. G.; Boulton, A. J.; Bus, S. A., Diabetic foot ulcers and their recurrence. *New England Journal of Medicine* **2017,** *376* (24), 2367-2375.

94.      Wukich, D. K.; Raspovic, K. M.; Suder, N. C., Patients with diabetic foot disease fear major lower-extremity amputation more than death. *Foot & ankle specialist* **2018,** *11* (1), 17-21.

95.      Frykberg, R. G.; Banks, J., Challenges in the treatment of chronic wounds. *Advances in wound care* **2015,** *4* (9), 560-582.

96.      Pfalzgraff, A.; Brandenburg, K.; Weindl, G., Antimicrobial peptides and their therapeutic potential for bacterial skin infections and wounds. *Frontiers in pharmacology* **2018,** *9*, 281.

97.      Doebel, T.; Voisin, B.; Nagao, K., Langerhans cells–the macrophage in dendritic cell clothing. *Trends in immunology* **2017,** *38* (11), 817-828.

98.      Kolarsick, P. A.; Kolarsick, M. A.; Goodwin, C., Anatomy and physiology of the skin. *Journal of the Dermatology Nurses' Association* **2011,** *3* (4), 203-213.

99.      James, W. D.; Elston, D.; Berger, T., *Andrew's diseases of the skin E-book: clinical dermatology*. Elsevier Health Sciences: 2011.

100.    Lloyd, G.; Friedman, G.; Jafri, S.; Schultz, G.; Fridman, A.; Harding, K., Gas plasma: medical uses and developments in wound care. *Plasma Process. Polym.* **2010,** *7* (3-4), 194-211.

101.    Eming, S. A.; Martin, P.; Tomic-Canic, M., Wound repair and regeneration: mechanisms, signaling, and translation. *Science translational medicine* **2014,** *6* (265), 265sr6-265sr6.

102.    Kawasumi, A.; Sagawa, N.; Hayashi, S.; Yokoyama, H.; Tamura, K., Wound healing in mammals and amphibians: toward limb regeneration in mammals. *New Perspectives in Regeneration* **2012**, 33-49.

103.    Han, G.; Ceilley, R., Chronic wound healing: a review of current management and treatments. *Advances in therapy* **2017,** *34* (3), 599-610.

104.    Stojadinovic, A.; Carlson, J. W.; Schultz, G. S.; Davis, T. A.; Elster, E. A., Topical advances in wound care. *Gynecologic oncology* **2008,** *111* (2), S70-S80.

105.    Ziegler, K.; Görl, R.; Effing, J.; Ellermann, J.; Mappes, M.; Otten, S.; Kapp, H.; Zoellner, P.; Spaeth, D.; Smola, H., Reduced cellular toxicity of a new silver-containing antimicrobial dressing and clinical performance in non-healing wounds. *Skin pharmacology and physiology* **2006,** *19* (3), 140-146.

106.    Kim, J. J.; Franczyk, M.; Gottlieb, L. J.; Song, D. H., Cost-effective alternative for negative-pressure wound therapy. *Plastic and reconstructive surgery Global open* **2017,** *5* (2).

107.    Jonsson, K.; Hunt, T. K.; Brennan, S. S.; Mathes, S. J., Tissue oxygen measurements in delayed skin flaps: a reconsideration of the mechanisms of the delay phenomenon. *Plastic and reconstructive surgery* **1988,** *82* (2), 328-336.

108.     Kessler, L.; Bilbault, P.; ORTega, F.; Grasso, C.; Passemard, R.; Stephan, D.; Pinget, M.; Schneider, F., Hyperbaric oxygenation accelerates the healing rate of nonischemic chronic diabetic foot ulcers: a prospective randomized study. *Diabetes care* **2003,** *26* (8), 2378-2382.

109.     Kranke, P.; Bennett, M. H.; Martyn-St James, M.; Schnabel, A.; Debus, S. E.; Weibel, S., Hyperbaric oxygen therapy for chronic wounds. *Cochrane Database of Systematic Reviews* **2015,**  (6).

110.     Moffett, J.; Griffin, N. E.; Ritz, M. C.; George, F. R., Pulsed radio frequency energy field treatment of cells in culture results in increased expression of genes involved in the inflammation phase of lower extremity diabetic wound healing. *The Journal of Diabetic Foot Complications* **2010,** *2* (3), 57-64.

111.     Frykberg, R. G.; Driver, V. R.; Lavery, L. A.; Armstrong, D. G.; Isenberg, R. A., The use of pulsed radio frequency energy therapy in treating lower extremity wounds: results of a retrospective study of a wound registry. *Ostomy-Wound Management* **2011,** *57* (3), 22.

112.     Wang, C.-J.; Wu, R.-W.; Yang, Y.-J., Treatment of diabetic foot ulcers: a comparative study of extracorporeal shockwave therapy and hyperbaric oxygen therapy. *Diabetes research and clinical practice* **2011,** *92* (2), 187-193.

113.     Eaglstein, W. H.; Falanga, V., Tissue engineering and the development of Apligraf®, a human skin equivalent. *Clinical therapeutics* **1997,** *19* (5), 894-905.

114.     Falanga, V.; Margolis, D.; Alvarez, O.; Auletta, M.; Maggiacomo, F.; Altman, M.; Jensen, J.; Sabolinski, M.; Hardin-Young, J., Rapid healing of venous ulcers and lack of clinical rejection with an allogeneic cultured human skin equivalent. *Archives of dermatology* **1998,** *134* (3), 293-300.

115.     Kim, J. Y.; Suh, W., Stem cell therapy for dermal wound healing. *International journal of stem cells* **2010,** *3* (1), 29.

116.     Marston, W. A.; Hanft, J.; Norwood, P.; Pollak, R., The efficacy and safety of Dermagraft in improving the healing of chronic diabetic foot ulcers: results of a prospective randomized trial. *Diabetes care* **2003,** *26* (6), 1701-1705.

117.     Greaves, N. S.; Iqbal, S. A.; Baguneid, M.; Bayat, A., The role of skin substitutes in the management of chronic cutaneous wounds. *Wound repair and regeneration* **2013,** *21* (2), 194-210.

118.     Kiwanuka, E.; Junker, J.; Eriksson, E., Harnessing growth factors to influence wound healing. *Clinics in plastic surgery* **2012,** *39* (3), 239-248.

119.     Steed, D. L., Clinical evaluation of recombinant human platelet–derived growth factor for the treatment of lower extremity diabetic ulcers. *Journal of vascular surgery* **1995,** *21* (1), 71-81.

120.     Barrientos, S.; Brem, H.; Stojadinovic, O.; Tomic-Canic, M., Clinical application of growth factors and cytokines in wound healing. *Wound Repair and Regeneration* **2014,** *22* (5), 569-578.

121.     Hamdan, S.; Pastar, I.; Drakulich, S.; Dikici, E.; Tomic-Canic, M.; Deo, S.; Daunert, S., Nanotechnology-driven therapeutic interventions in wound healing: potential uses and applications. *ACS central science* **2017,** *3* (3), 163-175.

122.     Hoffman, A. S., Ionizing radiation and gas plasma (or glow) discharge treatments for preparation of novel polymeric biomaterials. *Polymers in medicine* **1984**, 141-157.

123. Cho, G.; Kang, H.; Choi, E.-H.; Uhm, H. S., Electric-shock-free coupling of double atmospheric-plasma jets. *IEEE Trans. Plasma Sci.* **2012,** *41* (3), 498-502.

124. Leber, B.; Mayrhauser, U.; Leopold, B.; Koestenbauer, S.; Tscheliessnigg, K.; Stadlbauer, V.; Stiegler, P., Impact of temperature on cell death in a cell-culture model of hepatocellular carcinoma. *Anticancer research* **2012,** *32* (3), 915-921.

125. Johanns, W.; Luis, W.; Janssen, J.; Kahl, S.; Greiner, L., Argon plasma coagulation (APC) in gastroenterology: experimental and clinical experiences. *European journal of gastroenterology & hepatology* **1997,** *9* (6), 581-587.

126. Kuo, S.; Tarasenko, O.; Chang, J.; Popovic, S.; Chen, C.; Fan, H.; Scott, A.; Lahiani, M.; Alusta, P.; Drake, J., Contribution of a portable air plasma torch to rapid blood coagulation as a method of preventing bleeding. *New Journal of Physics* **2009,** *11* (11), 115016.

127. Ueda, M.; Yamagami, D.; Watanabe, K.; Mori, A.; Kimura, H.; Sano, K.; Saji, H.; Ishikawa, K.; Hori, M.; Sakakita, H., Histological and Nuclear Medical Comparison of Inflammation After Hemostasis with Non-Thermal Plasma and Thermal Coagulation. *Plasma Process. Polym.* **2015,** *12* (12), 1338-1342.

128. Belov, S., Use of high-frequency cold plasma ablation technology for electrosurgery with minimized invasiveness. *Biomedical Engineering* **2004,** *38* (2), 80.

129. Shah, U. K.; Dunham, B., Coblation for tonsillectomy: an evidence-based review. *ORL* **2007,** *69* (6), 349-357.

130. Stoffels, E.; Kieft, I.; Sladek, R., Superficial treatment of mammalian cells using plasma needle. *Journal of Physics D: Applied Physics* **2003,** *36* (23), 2908.

131. Jacobs, P. T.; Lin, S.-M., Gas-plasma sterilization. ACS Publications: 1996.

132. Herrmann, H. W.; Selwyn, G. S.; Henins, I.; Park, J.; Jeffery, M.; Williams, J. M., Chemical warfare agent decontamination studies in the plasma decon chamber. *IEEE Trans. Plasma Sci.* **2002,** *30* (4), 1460-1470.

133. Laroussi, M.; Mendis, D.; Rosenberg, M., Plasma interaction with microbes. *New Journal of Physics* **2003,** *5* (1), 41.

134. Laroussi, M.; Richardson, J. P.; Dobbs, F. C., Effects of nonequilibrium atmospheric pressure plasmas on the heterotrophic pathways of bacteria and on their cell morphology. *Applied Physics Letters* **2002,** *81* (4), 772-774.

135. Birmingham, J. G.; Hammerstrom, D. J., Bacterial decontamination using ambient pressure nonthermal discharges. *IEEE Trans. Plasma Sci.* **2000,** *28* (1), 51-55.

136. Uhm, H. S.; Lim, J. P.; Li, S. Z., Sterilization of bacterial endospores by an atmospheric-pressure argon plasma jet. *Applied physics letters* **2007,** *90* (26), 261501.

137. Nasir, N. M.; Lee, B.; Yap, S. S.; Thong, K.; Yap, S. L., Cold plasma inactivation of chronic wound bacteria. *Archives of biochemistry and biophysics* **2016,** *605*, 76-85.

138. Daeschlein, G.; von Woedtke, T.; Kindel, E.; Brandenburg, R.; Weltmann, K. D.; Jünger, M., Antibacterial activity of an atmospheric pressure plasma jet against relevant wound pathogens in vitro on a simulated wound environment. *Plasma Process. Polym.* **2010,** *7* (3-4), 224-230.

139.    Laroussi, M.; Leipold, F., Evaluation of the roles of reactive species, heat, and UV radiation in the inactivation of bacterial cells by air plasmas at atmospheric pressure. *International Journal of Mass Spectrometry* **2004,** *233* (1-3), 81-86.

140.    Lee, S. J.; Ma, S.-H.; Hong, Y. C.; Choi, M. C., Effects of pulsed and continuous wave discharges of underwater plasma on Escherichia coli. *Separation and Purification Technology* **2018,** *193*, 351-357.

141.    Lee, K.-Y.; Park, B. J.; Lee, D. H.; Lee, I.-S.; Hyun, S. O.; Chung, K.-H.; Park, J.-C., Sterilization of Escherichia coli and MRSA using microwave-induced argon plasma at atmospheric pressure. *Surface and Coatings Technology* **2005,** *193* (1-3), 35-38.

142.    Laroussi, M., Low temperature plasma-based sterilization: overview and state-of-the-art. *Plasma Process. Polym.* **2005,** *2* (5), 391-400.

143.    Niedźwiedź, I.; Waśko, A.; Pawłat, J.; Polak-Berecka, M., The state of research on antimicrobial activity of cold plasma. *Polish journal of microbiology* **2019,** *68* (2), 153.

144.    Boudam, M. K.; Moisan, M.; Saoudi, B.; Popovici, C.; Gherardi, N.; Massines, F., Bacterial spore inactivation by atmospheric-pressure plasmas in the presence or absence of UV photons as obtained with the same gas mixture. *Journal of Physics D: Applied Physics* **2006,** *39* (16), 3494.

145.    Sato, T.; Miyahara, T.; Doi, A.; Ochiai, S.; Urayama, T.; Nakatani, T., Sterilization mechanism for Escherichia coli by plasma flow at atmospheric pressure. *Applied physics letters* **2006,** *89* (7), 073902.

146.    Shen, J.; Cheng, C.; Fang, S.; Xie, H.; Lan, Y.; Ni, G.; Meng, Y.; Luo, J.; Wang, X., Sterilization of Bacillus subtilis spores using an atmospheric plasma jet with argon and oxygen mixture gas. *Appl. Phys. Express* **2012,** *5* (3), 036201.

147.    Eto, H.; Ono, Y.; Ogino, A.; Nagatsu, M., Low-temperature sterilization of wrapped materials using flexible sheet-type dielectric barrier discharge. *Applied physics letters* **2008,** *93* (22), 221502.

148.    Choi, J. H.; Han, I.; Baik, H. K.; Lee, M. H.; Han, D.-W.; Park, J.-C.; Lee, I.-S.; Song, K. M.; Lim, Y. S., Analysis of sterilization effect by pulsed dielectric barrier discharge. *Journal of electrostatics* **2006,** *64* (1), 17-22.

149.    Hayashi, N.; Nakashima, T.; Yonesu, A., Sterilization of medical equipment using air torch plasma produced by microwave discharge. *IEEE Trans. Plasma Sci.* **2011,** *39* (11), 2976-2977.

150.    Timoshkin, I. V.; Maclean, M.; Wilson, M. P.; Given, M. J.; MacGregor, S. J.; Wang, T.; Anderson, J. G., Bactericidal effect of corona discharges in atmospheric air. *IEEE Trans. Plasma Sci.* **2012,** *40* (10), 2322-2333.

151.    Shaw, P.; Kumar, N.; Kwak, H. S.; Park, J. H.; Uhm, H. S.; Bogaerts, A.; Choi, E. H.; Attri, P., Bacterial inactivation by plasma treated water enhanced by reactive nitrogen species. *Scientific reports* **2018,** *8* (1), 1-10.

152.    Jablonowski, H.; Hänsch, M. A. C.; Dünnbier, M.; Wende, K.; Hammer, M. U.; Weltmann, K.-D.; Reuter, S.; von Woedtke, T., Plasma jet's shielding gas impact on bacterial inactivation. *Biointerphases* **2015,** *10* (2), 029506.

153.    Asghar, A. H.; Ahmed, O. B.; Galaly, A. R., Inactivation of E. coli using atmospheric pressure plasma jet with dry and wet argon discharges. *Membranes* **2021,** *11* (1), 46.

154.    Laurita, R.; Miserocchi, A.; Ghetti, M.; Gherardi, M.; Stancampiano, A.; Purpura, V.; Melandri, D.; Minghetti, P.; Bondioli, E.; Colombo, V., Cold atmospheric plasma treatment of infected skin tissue: evaluation of sterility, viability, and integrity. *IEEE Transactions on Radiation and Plasma Medical Sciences* **2017,** *1* (3), 275-279.

155.    Dobrynin, D.; Wasko, K.; Friedman, G.; Fridman, A. A.; Fridman, G., Cold plasma sterilization of open wounds: live rat model. *Plasma Medicine* **2011,** *1* (2).

156.    Plattfaut, I.; Besser, M.; Severing, A.-L.; Stürmer, E. K.; Opländer, C., Plasma medicine and wound management: Evaluation of the antibacterial efficacy of a medically certified cold atmospheric argon plasma jet. *International Journal of Antimicrobial Agents* **2021,** *57* (5), 106319.

157.    Traba, C.; Chen, L.; Liang, J. F., Low power gas discharge plasma mediated inactivation and removal of biofilms formed on biomaterials. *Current Applied Physics* **2013,** *13*, S12-S18.

158.    Fricke, K.; Koban, I.; Tresp, H.; Jablonowski, L.; Schröder, K.; Kramer, A.; Weltmann, K.-D.; von Woedtke, T.; Kocher, T., Atmospheric pressure plasma: a high-performance tool for the efficient removal of biofilms. **2012**.

159.    Modic, M.; McLeod, N. P.; Sutton, J. M.; Walsh, J. L., Cold atmospheric pressure plasma elimination of clinically important single-and mixed-species biofilms. *International journal of antimicrobial agents* **2017,** *49* (3), 375-378.

160.    Liu, J.-R.; Xu, G.-M.; Shi, X.-M.; Zhang, G.-J., Low temperature plasma promoting fibroblast proliferation by activating the NF-κB pathway and increasing cyclinD1 expression. *Scientific reports* **2017,** *7* (1), 1-12.

161.    Schmidt, A.; Liebelt, G.; Nießner, F.; von Woedtke, T.; Bekeschus, S., Gas plasma-spurred wound healing is accompanied by regulation of focal adhesion, matrix remodeling, and tissue oxygenation. *Redox biology* **2021,** *38*, 101809.

162.    Kalghatgi, S.; Friedman, G.; Fridman, A.; Clyne, A. M., Endothelial cell proliferation is enhanced by low dose non-thermal plasma through fibroblast growth factor-2 release. *Annals of biomedical engineering* **2010,** *38* (3), 748-757.

163.    Kalghatgi, S. U.; Fridman, A.; Friedman, G.; Clyne, A. M. In *Cell proliferation following non-thermal plasma is related to reactive oxygen species induced fibroblast growth factor-2 release*, 2009 Annual International Conference of the IEEE Engineering in Medicine and Biology Society, IEEE: 2009; pp 6030-6033.

164.    Liu, T.; Zhang, L.; Joo, D.; Sun, S.-C., NF-κB signaling in inflammation. *Signal transduction and targeted therapy* **2017,** *2* (1), 1-9.

165.    Arndt, S.; Schmidt, A.; Karrer, S.; von Woedtke, T., Comparing two different plasma devices kINPen and Adtec SteriPlas regarding their molecular and cellular effects on wound healing. *Clinical Plasma Medicine* **2018,** *9*, 24-33.

166.    Bekeschus, S.; von Woedtke, T.; Emmert, S.; Schmidt, A., Medical gas plasma-stimulated wound healing: Evidence and mechanisms. *Redox Biology* **2021**, 102116.

167.    Vasilets, V. N.; Shekhter, A. B.; Guller, A. E.; Pekshev, A. V., Air plasma-generated nitric oxide in treatment of skin scars and articular musculoskeletal disorders: Preliminary review of observations. *Clinical Plasma Medicine* **2015,** *3* (1), 32-39.

168.     Jacofsky, M. C.; Lubahn, C.; McDonnell, C.; Seepersad, Y.; Fridman, G.; Fridman, A. A.; Dobrynin, D., Spatially resolved optical emission spectroscopy of a helium plasma jet and its effects on wound healing rate in a diabetic murine model. *Plasma Medicine* **2014,** *4* (1-4).

169.     Chatraie, M.; Torkaman, G.; Khani, M.; Salehi, H.; Shokri, B., In vivo study of non-invasive effects of non-thermal plasma in pressure ulcer treatment. *Scientific reports* **2018,** *8* (1), 1-11.

170.     Wang, X.-F.; Fang, Q.-Q.; Jia, B.; Hu, Y.-Y.; Wang, Z.-C.; Yan, K.-p.; Yin, S.-Y.; Liu, Z.; Tan, W.-Q., Potential effect of non-thermal plasma for the inhibition of scar formation: a preliminary report. *Scientific reports* **2020,** *10* (1), 1-10.

171.     Yu, Y.; Tan, M.; Chen, H.; Wu, Z.; Xu, L.; Li, J.; Cao, J.; Yang, Y.; Xiao, X.; Lian, X., Non-thermal plasma suppresses bacterial colonization on skin wound and promotes wound healing in mice. *Journal of Huazhong University of Science and Technology [Medical Sciences]* **2011,** *31* (3), 390-394.

172.     Lou, B.-S.; Hsieh, J.-H.; Chen, C.-M.; Hou, C.-W.; Wu, H.-Y.; Chou, P.-Y.; Lai, C.-H.; Lee, J.-W., Helium/argon-generated cold atmospheric plasma facilitates cutaneous wound healing. *Frontiers in bioengineering and biotechnology* **2020,** *8*, 683.

173.     Nakajima, Y.; Mukai, K.; Komatsu, E.; Rahayu, H. S. E.; Nur, M.; Ishijima, T.; Enomoto, H.; Uesugi, Y.; Sugama, J.; Nakatani, T., A simple technique to improve contractile effect of cold plasma jet on acute mouse wound by dropping water. *Plasma Process. Polym.* **2015,** *12* (10), 1128-1138.

174.     Breathnach, R.; McDonnell, K. A.; Chebbi, A.; Callanan, J. J.; Dowling, D. P., Evaluation of the effectiveness of kINPen Med plasma jet and bioactive agent therapy in a rat model of wound healing. *Biointerphases* **2018,** *13* (5), 051002.

175.     Cheng, K.-Y.; Lin, Z.-H.; Cheng, Y.-P.; Chiu, H.-Y.; Yeh, N.-L.; Wu, T.-K.; Wu, J.-S., Wound healing in streptozotocin-induced diabetic rats using atmospheric-pressure argon plasma jet. *Scientific reports* **2018,** *8* (1), 1-15.

176.     Darmawati, S.; Rohmani, A.; Nurani, L. H.; Prastiyanto, M. E.; Dewi, S. S.; Salsabila, N.; Wahyuningtyas, E. S.; Murdiya, F.; Sikumbang, I. M.; Rohmah, R. N., When plasma jet is effective for chronic wound bacteria inactivation, is it also effective for wound healing? *Clinical Plasma Medicine* **2019,** *14*, 100085.

177.     Schmidt, A.; von Woedtke, T.; Vollmar, B.; Hasse, S.; Bekeschus, S., Nrf2 signaling and inflammation are key events in physical plasma-spurred wound healing. *Theranostics* **2019,** *9* (4), 1066.

178.     Kim, H. Y.; Kang, S. K.; Park, S. M.; Jung, H. Y.; Choi, B. H.; Sim, J. Y.; Lee, J. K., Characterization and effects of Ar/Air microwave plasma on wound healing. *Plasma Process. Polym.* **2015,** *12* (12), 1423-1434.

179.     Ngo Thi, M. H.; Shao, P. L.; Liao, J. D.; Lin, C. C. K.; Yip, H. K., Enhancement of angiogenesis and epithelialization processes in mice with burn wounds through ROS/RNS signals generated by non-thermal N2/Ar micro-plasma. *Plasma Process. Polym.* **2014,** *11* (11), 1076-1088.

180.     Bekeschus, S.; Schmidt, A.; Weltmann, K.-D.; von Woedtke, T., The plasma jet kINPen–A powerful tool for wound healing. *Clinical Plasma Medicine* **2016,** *4* (1), 19-28.

181. Shekhter, A.; Kabisov, R.; Pekshev, A.; Kozlov, N.; Perov, Y. L., Experimental and clinical validation of plasmadynamic therapy of wounds with nitric oxide. *Bulletin of Experimental Biology and Medicine* **1998,** *126* (2), 829-834.

182. Isbary, G.; Stolz, W.; Shimizu, T.; Monetti, R.; Bunk, W.; Schmidt, H.-U.; Morfill, G. E.; Klämpfl, T.; Steffes, B.; Thomas, H., Cold atmospheric argon plasma treatment may accelerate wound healing in chronic wounds: Results of an open retrospective randomized controlled study in vivo. *Clinical Plasma Medicine* **2013,** *1* (2), 25-30.

183. Klebes, M.; Ulrich, C.; Kluschke, F.; Patzelt, A.; Vandersee, S.; Richter, H.; Bob, A.; von Hutten, J.; Krediet, J. T.; Kramer, A., Combined antibacterial effects of tissue-tolerable plasma and a modern conventional liquid antiseptic on chronic wound treatment. *Journal of biophotonics* **2015,** *8* (5), 382-391.

184. Ulrich, C.; Kluschke, F.; Patzelt, A.; Vandersee, S.; Czaika, V.; Richter, H.; Bob, A.; Hutten, J. v.; Painsi, C.; Hüge, R., Clinical use of cold atmospheric pressure argon plasma in chronic leg ulcers: A pilot study. *Journal of wound care* **2015,** *24* (5), 196-203.

185. Stratmann, B.; Costea, T.-C.; Nolte, C.; Hiller, J.; Schmidt, J.; Reindel, J.; Masur, K.; Motz, W.; Timm, J.; Kerner, W., Effect of cold atmospheric plasma therapy vs standard therapy placebo on wound healing in patients with diabetic foot ulcers: a randomized clinical trial. *JAMA network open* **2020,** *3* (7), e2010411-e2010411.

186. Panngom, K.; Baik, K.; Nam, M.; Han, J.; Rhim, H.; Choi, E., Preferential killing of human lung cancer cell lines with mitochondrial dysfunction by nonthermal dielectric barrier discharge plasma. *Cell death & disease* **2013,** *4* (5), e642-e642.

187. Partecke, L. I.; Evert, K.; Haugk, J.; Doering, F.; Normann, L.; Diedrich, S.; Weiss, F.-U.; Evert, M.; Huebner, N. O.; Guenther, C., Tissue tolerable plasma (TTP) induces apoptosis in pancreatic cancer cells in vitro and in vivo. *BMC cancer* **2012,** *12* (1), 1-10.

188. Kim, S. J.; Chung, T.; Bae, S.; Leem, S., Induction of apoptosis in human breast cancer cells by a pulsed atmospheric pressure plasma jet. *Applied Physics Letters* **2010,** *97* (2), 023702.

189. Volotskova, O.; Hawley, T. S.; Stepp, M. A.; Keidar, M., Targeting the cancer cell cycle by cold atmospheric plasma. *Scientific reports* **2012,** *2* (1), 1-10.

190. Van der Paal, J.; Neyts, E. C.; Verlackt, C. C.; Bogaerts, A., Effect of lipid peroxidation on membrane permeability of cancer and normal cells subjected to oxidative stress. *Chemical science* **2016,** *7* (1), 489-498.

191. Keidar, M., A prospectus on innovations in the plasma treatment of cancer. *Phys. Plasmas* **2018,** *25* (8), 083504.

192. Vandamme, M.; Robert, E.; Lerondel, S.; Sarron, V.; Ries, D.; Dozias, S.; Sobilo, J.; Gosset, D.; Kieda, C.; Legrain, B., ROS implication in a new antitumor strategy based on non-thermal plasma. *International journal of cancer* **2012,** *130* (9), 2185-2194.

193. Freund, E.; Liedtke, K. R.; van der Linde, J.; Metelmann, H.-R.; Heidecke, C.-D.; Partecke, L.-I.; Bekeschus, S., Physical plasma-treated saline promotes an immunogenic phenotype in CT26 colon cancer cells in vitro and in vivo. *Scientific reports* **2019,** *9* (1), 1-18.

194. Brullé, L.; Vandamme, M.; Riès, D.; Martel, E.; Robert, E.; Lerondel, S.; Trichet, V.; Richard, S.; Pouvesle, J.-M.; Le Pape, A., Effects of a non thermal plasma treatment alone or in combination with gemcitabine in a MIA PaCa2-luc orthotopic pancreatic carcinoma model. *PloS one* **2012,** *7* (12), e52653.

195. Köritzer, J.; Boxhammer, V.; Schäfer, A.; Shimizu, T.; Klämpfl, T. G.; Li, Y.-F.; Welz, C.; Schwenk-Zieger, S.; Morfill, G. E.; Zimmermann, J. L., Restoration of sensitivity in chemo—resistant glioma cells by cold atmospheric plasma. *PloS one* **2013,** *8* (5), e64498.

196. Van Boxem, W.; Van der Paal, J.; Gorbanev, Y.; Vanuytsel, S.; Smits, E.; Dewilde, S.; Bogaerts, A., Anti-cancer capacity of plasma-treated PBS: effect of chemical composition on cancer cell cytotoxicity. *Scientific reports* **2017,** *7* (1), 1-15.

197. Zhou, X.; Cai, D.; Xiao, S.; Ning, M.; Zhou, R.; Zhang, S.; Chen, X.; Ostrikov, K.; Dai, X., InvivoPen: A novel plasma source for in vivo cancer treatment. *Journal of Cancer* **2020,** *11* (8), 2273.

198. Bernhardt, T.; Semmler, M. L.; Schäfer, M.; Bekeschus, S.; Emmert, S.; Boeckmann, L., Plasma medicine: Applications of cold atmospheric pressure plasma in dermatology. *Oxidative medicine and cellular longevity* **2019,** *2019*.

199. Emmert, S.; Brehmer, F.; Hänßle, H.; Helmke, A.; Mertens, N.; Ahmed, R.; Simon, D.; Wandke, D.; Maus-Friedrichs, W.; Däschlein, G., Atmospheric pressure plasma in dermatology: Ulcus treatment and much more. *Clinical Plasma Medicine* **2013,** *1* (1), 24-29.

200. Thiem, A.; Has, C.; Diem, A.; Klausegger, A.; Hamm, H.; Emmert, S., Wundtherapie mit kaltem Plasma bei Epidermolysis bullosa dystrophica. *Der Hautarzt* **2021**, 1-7.

201. Chutsirimongkol, C.; Boonyawan, D.; Polnikorn, N.; Techawatthanawisan, W.; Kundilokchai, T., Non-thermal plasma for acne and aesthetic skin improvement. *Plasma Medicine* **2014,** *4* (1-4).

202. Wirtz, M.; Stoffels, I.; Dissemond, J.; Schadendorf, D.; Roesch, A., Actinic keratoses treated with cold atmospheric plasma. *Journal of the European Academy of Dermatology and Venereology* **2018,** *32* (1), e37-e39.

203. Foster, K. W.; Moy, R. L.; Fincher, E. F., Advances in plasma skin regeneration. *Journal of cosmetic dermatology* **2008,** *7* (3), 169-179.

204. Borges, A. C.; Kostov, K. G.; Pessoa, R. S.; de Abreu, G.; Lima, G. d. M.; Figueira, L. W.; Koga-Ito, C. Y., Applications of Cold Atmospheric Pressure Plasma in Dentistry. *Applied Sciences* **2021,** *11* (5), 1975.

205. Li, Y.; Sun, K.; Ye, G.; Liang, Y.; Pan, H.; Wang, G.; Zhao, Y.; Pan, J.; Zhang, J.; Fang, J., Evaluation of cold plasma treatment and safety in disinfecting 3-week root canal Enterococcus faecalis biofilm in vitro. *Journal of endodontics* **2015,** *41* (8), 1325-1330.

206. Borges, A. C.; Lima, G. d. M. G.; Nishime, T. M. C.; Gontijo, A. V. L.; Kostov, K. G.; Koga-Ito, C. Y., Amplitude-modulated cold atmospheric pressure plasma jet for treatment of oral candidiasis: In vivo study. *PLoS One* **2018,** *13* (6), e0199832.

207. Han, X.; Klas, M.; Liu, Y.; Sharon Stack, M.; Ptasinska, S., DNA damage in oral cancer cells induced by nitrogen atmospheric pressure plasma jets. *Applied Physics Letters* **2013,** *102* (23), 233703.

208.     Cha, S.; Park, Y.-S., Plasma in dentistry. *Clinical plasma medicine* **2014,** *2* (1), 4-10.

209.     Reitberger, H. H.; Czugala, M.; Chow, C.; Mohr, A.; Burkovski, A.; Gruenert, A. K.; Schoenebeck, R.; Fuchsluger, T. A., Argon cold plasma–A novel tool to treat therapy-resistant corneal infections. *American journal of ophthalmology* **2018,** *190*, 150-163.

210.     Misyn, F.; Gostev, V., Cold" plasma application in eyelid phlegmon curing. *Diagnostics and treatment of infectious diseases* **2000.**

211.     Kos, S.; Blagus, T.; Cemazar, M.; Filipic, G.; Sersa, G.; Cvelbar, U., Safety aspects of atmospheric pressure helium plasma jet operation on skin: In vivo study on mouse skin. *PloS one* **2017,** *12* (4), e0174966.

212.     O'connell, D.; Cox, L.; Hyland, W.; McMahon, S.; Reuter, S.; Graham, W.; Gans, T.; Currell, F., Cold atmospheric pressure plasma jet interactions with plasmid DNA. *Applied Physics Letters* **2011,** *98* (4), 043701.

213.     Kim, G.; Kim, W.; Kim, K.; Lee, J., DNA damage and mitochondria dysfunction in cell apoptosis induced by nonthermal air plasma. *Applied Physics Letters* **2010,** *96* (2), 021502.

214.     Isbary, G.; Köritzer, J.; Mitra, A.; Li, Y.-F.; Shimizu, T.; Schroeder, J.; Schlegel, J.; Morfill, G.; Stolz, W.; Zimmermann, J., Ex vivo human skin experiments for the evaluation of safety of new cold atmospheric plasma devices. *Clinical Plasma Medicine* **2013,** *1* (1), 36-44.

215.     Wu, A. S.; Kalghatgi, S.; Dobrynin, D.; Sensenig, R.; Cerchar, E.; Podolsky, E.; Dulaimi, E.; Paff, M.; Wasko, K.; Arjunan, K. P., Porcine intact and wounded skin responses to atmospheric nonthermal plasma. *Journal of Surgical Research* **2013,** *179* (1), e1-e12.

216.     Rutkowski, R.; Daeschlein, G.; von Woedtke, T.; Smeets, R.; Gosau, M.; Metelmann, H.-R., Long-term risk assessment for medical application of cold atmospheric pressure plasma. *Diagnostics* **2020,** *10* (4), 210.

217.     Vanbever, R.; Preat, V., In vivo efficacy and safety of skin electroporation. *Advanced drug delivery reviews* **1999,** *35* (1), 77-88.

218.     Singhal, M.; Lapteva, M.; Kalia, Y. N., Formulation challenges for 21st century topical and transdermal delivery systems. *Expert opinion on drug delivery* **2017,** *14* (6), 705-708.

219.     Prausnitz, M. R., A practical assessment of transdermal drug delivery by skin electroporation. *Advanced drug delivery reviews* **1999,** *35* (1), 61-76.

220.     Pathan, I. B.; Setty, C. M., Chemical penetration enhancers for transdermal drug delivery systems. *Tropical Journal of Pharmaceutical Research* **2009,** *8* (2).

221.     Peralta, M. F.; Guzmán, M. L.; Pérez, A.; Apezteguia, G. A.; Fórmica, M. L.; Romero, E. L.; Olivera, M. E.; Carrer, D. C., Liposomes can both enhance or reduce drugs penetration through the skin. *Scientific reports* **2018,** *8* (1), 1-11.

222.     Priya, B.; Rashmi, T.; Bozena, M., Transdermal iontophoresis. *Expert opinion on drug delivery* **2006,** *3* (1), 127-138.

223.     Sersa, G.; Miklavcic, D.; Cemazar, M.; Rudolf, Z.; Pucihar, G.; Snoj, M., Electrochemotherapy in treatment of tumours. *European Journal of Surgical Oncology (EJSO)* **2008,** *34* (2), 232-240.

224.     Somiari, S.; Glasspool-Malone, J.; Drabick, J. J.; Gilbert, R. A.; Heller, R.; Jaroszeski, M. J.; Malone, R. W., Theory and in vivo application of electroporative gene delivery. *Molecular Therapy* **2000,** *2* (3), 178-187.

225.     Van Meirvenne, S.; Straetman, L.; Heirman, C.; Dullaers, M.; De Greef, C.; Van Tendeloo, V.; Thielemans, K., Efficient genetic modification of murine dendritic cells by electroporation with mRNA. *Cancer gene therapy* **2002,** *9* (9), 787-797.

226.     Hsiao, C.-Y.; Yang, S.-C.; Alalaiwe, A.; Fang, J.-Y., Laser ablation and topical drug delivery: a review of recent advances. *Expert opinion on drug delivery* **2019,** *16* (9), 937-952.

227.     Park, D.; Park, H.; Seo, J.; Lee, S., Sonophoresis in transdermal drug deliverys. *Ultrasonics* **2014,** *54* (1), 56-65.

228.     Sakai, Y.; Khajoee, V.; Ogawa, Y.; Kusuhara, K.; Katayama, Y.; Hara, T., A novel transfection method for mammalian cells using gas plasma. *Journal of biotechnology* **2006,** *121* (3), 299-308.

229.     Ogawa, Y.; Morikawa, N.; Ohkubo-Suzuki, A.; Miyoshi, S.; Arakawa, H.; Kita, Y.; Nishimura, S., An epoch-making application of discharge plasma phenomenon to gene-transfer. *Biotechnology and bioengineering* **2005,** *92* (7), 865-870.

230.     Rybenkov, V. V.; Vologodskii, A. V.; Cozzarelli, N. R., The effect of ionic conditions on the conformations of supercoiled DNA. I. Sedimentation analysis. *Journal of molecular biology* **1997,** *267* (2), 299-311.

231.     Leduc, M.; Guay, D.; Leask, R.; Coulombe, S., Cell permeabilization using a non-thermal plasma. *New Journal of Physics* **2009,** *11* (11), 115021.

232.     Dhaneshwar, S.; Bhilare, N.; Roy, S., Dextran Pharmaceutical Applications. In *Polysaccharides of Microbial Origin: Biomedical Applications*, Springer: 2021; pp 1-28.

233.     Striesow, J.; Lackmann, J.-W.; Ni, Z.; Wenske, S.; Weltmann, K.-D.; Fedorova, M.; von Woedtke, T.; Wende, K., Oxidative modification of skin lipids by cold atmospheric plasma (CAP): A standardizable approach using RP-LC/MS2 and DI-ESI/MS2. *Chemistry and physics of lipids* **2020,** *226*, 104786.

234.     Pearson, J.; Cölfen, H., ICCD camera technology with constant illumination source and possibilities for application in multiwavelength analytical ultracentrifugation. *RSC advances* **2018,** *8* (71), 40655-40662.

235.     Bruggeman, P. J.; Sadeghi, N.; Schram, D. C.; Linss, V., Gas temperature determination from rotational lines in non-equilibrium plasmas: a review. *Plasma Sources Sci. Technol.* **2014,** *23* (2), 32.

236.     Lee, H.-C.; Chung, C.-W., Effect of electron energy distribution on the hysteresis of plasma discharge: Theory, experiment and modeling. *Scientific reports* **2015,** *5* (1), 1-9.

237.     Belmonte, T.; Noël, C.; Gries, T.; Martin, J.; Henrion, G., Theoretical background of optical emission spectroscopy for analysis of atmospheric pressure plasmas. *Plasma Sources Science and Technology* **2015,** *24* (6), 064003.

238.     Sneep, M.; Ubachs, W., Direct measurement of the Rayleigh scattering cross section in various gases. *J. Quant. Spectrosc. Radiat. Transf.* **2005,** *92* (3), 293-310.

239.     Engeln, R.; Klarenaar, B.; Guaitella, O., Foundations of optical diagnostics in low-temperature plasmas. *Plasma Sources Science and Technology* **2020,** *29* (6), 063001.

240.     Onyshchenko, I.; De Geyter, N.; Morent, R., Improvement of the plasma treatment effect on PET with a newly designed atmospheric pressure plasma jet. *Plasma Process. Polym.* **2017,** *14* (8), 1600200.

241.     Early, I., Column properties that make an impact on ion chromatography.

242.     Lahesmaa-Korpinen, A.-M., Computational approaches in high-throughput proteomics data analysis. **2012**.

243.     Drabik, A.; Bodzoń-Kułakowska, A.; Silberring, J., Gel electrophoresis. In *Proteomic profiling and analytical chemistry*, Elsevier: 2016; pp 115-143.

244.     Pachnerová Brabcová, K.; Sihver, L.; Ukraintsev, E.; Štěpán, V.; Davídková, M., How detection of plasmid DNA fragmentation affects radiation strand break yields. *Radiation protection dosimetry* **2019,** *183* (1-2), 89-92.

245.     Jethva, K. D.; Bhatt, D. R.; Zaveri, M. N., Antimycobacterial screening of selected medicinal plants against Mycobacterium tuberculosis H37Rv using agar dilution method and the microplate resazurin assay. *International Journal of Mycobacteriology* **2020,** *9* (2), 150.

246.     Britannica, CT. Information Architects of Encyclopaedia (2022, March 7). polymerase        chain        reaction.        Encyclopedia        Britannica. http's://www.britannica.com/facts/polymerase-chain-reaction.

247.     Penkov, O. V.; Khadem, M.; Lim, W. S.; Kim, D. E., A review of recent applications of atmospheric pressure plasma jets for materials processing. *J. Coat. Technol. Res.* **2015,** *12* (2), 225-235.

248.     Tendero, C.; Tixier, C.; Tristant, P.; Desmaison, J.; Leprince, P., Atmospheric pressure plasmas: A review. *Spectroc. Acta Pt. B-Atom. Spectr.* **2006,** *61* (1), 2-30.

249.     Weltmann, K. D.; von Woedtke, T., Plasma medicine-current state of research and medical application. *Plasma Phys. Control. Fusion* **2017,** *59* (1), 11.

250.     Weltmann, K. D.; Kindel, E.; von Woedtke, T.; Hahnel, M.; Stieber, M.; Brandenburg, R., Atmospheric-pressure plasma sources: Prospective tools for plasma medicine. *Pure Appl. Chem.* **2010,** *82* (6), 1223-1237.

251.     Isbary, G.; Zimmermann, J.; Shimizu, T.; Li, Y.-F.; Morfill, G.; Thomas, H.; Steffes, B.; Heinlin, J.; Karrer, S.; Stolz, W., Non-thermal plasma—More than five years of clinical experience. *Clinical Plasma Medicine* **2013,** *1* (1), 19-23.

252.     Von Woedtke, T.; Metelmann, H. R.; Weltmann, K. D., Clinical plasma medicine: state and perspectives of in vivo application of cold atmospheric plasma. *Contributions to Plasma Physics* **2014,** *54* (2), 104-117.

253.     Winter, J.; Brandenburg, R.; Weltmann, K. D., Atmospheric pressure plasma jets: an overview of devices and new directions. *Plasma Sources Sci. Technol.* **2015,** *24* (6), 19.

254.     Park, G. Y.; Park, S. J.; Choi, M. Y.; Koo, I. G.; Byun, J. H.; Hong, J. W.; Sim, J. Y.; Collins, G. J.; Lee, J. K., Atmospheric-pressure plasma sources for biomedical applications. *Plasma Sources Sci. Technol.* **2012,** *21* (4), 21.

255.     Selwyn, G.; Herrmann, H.; Park, J.; Henins, I., Materials Processing Using an Atmospheric Pressure, RF-Generated Plasma Source. *Contributions to Plasma Physics* **2001,** *41* (6), 610-619.

256.     Niemi, K.; Schulz-Von Der Gathen, V.; Döbele, H., Absolute atomic oxygen density measurements by two-photon absorption laser-induced fluorescence

spectroscopy in an RF-excited atmospheric pressure plasma jet. *Plasma Sources Science and Technology* **2005,** *14* (2), 375.

257.    Wang, S.; Schulz-Von der Gathen, V.; Döbele, H., Discharge comparison of nonequilibrium atmospheric pressure Ar/O 2 and He/O 2 plasma jets. *Applied physics letters* **2003,** *83* (16), 3272-3274.

258.    Laux, C. O.; Spence, T. G.; Kruger, C. H.; Zare, R. N., Optical diagnostics of atmospheric pressure air plasmas. *Plasma Sources Sci. Technol.* **2003,** *12* (2), 125-138.

259.    Sarani, A.; Nikiforov, A. Y.; Leys, C., Atmospheric pressure plasma jet in Ar and Ar/H2O mixtures: Optical emission spectroscopy and temperature measurements. *Phys. Plasmas* **2010,** *17* (6), 8.

260.    Murphy, A.; Farmer, A., Temperature measurement in thermal plasmas by Rayleigh scattering. *Journal of Physics D: Applied Physics* **1992,** *25* (4), 634.

261.    Van Gessel, A.; Carbone, E.; Bruggeman, P.; Van der Mullen, J., Laser scattering on an atmospheric pressure plasma jet: disentangling Rayleigh, Raman and Thomson scattering. *Plasma Sources Science and Technology* **2012,** *21* (1), 015003.

262.    Kuhn, M.; Kuhn-Kauffeldt, M.; Schein, J.; Belinger, A., Plasma actuators for active flow control based on a glow discharge. In *14th High-Tech Plasma Processes Conference*, Uhrlandt, D.; Teulet, P.; Schein, J., Eds. Iop Publishing Ltd: Bristol, 2017; Vol. 825.

263.    Neretti, G.; Ricchiuto, A. C.; Borghi, C. A., Measurement of the charge distribution deposited by an annular plasma synthetic jet actuator over a target surface. *J. Phys. D-Appl. Phys.* **2018,** *51* (32), 9.

264.    Klarenaar, B. L. M.; Grofulovic, M.; Morillo-Candas, A. S.; van den Bekerom, D. C. M.; Damen, M. A.; van de Sanden, M. C. M.; Guaitella, O.; Engeln, R., A rotational Raman study under non-thermal conditions in a pulsed CO2 glow discharge. *Plasma Sources Sci. Technol.* **2018,** *27* (4), 12.

265.    Miles, R. B.; Lempert, W. R.; Forkey, J. N., Laser Rayleigh scattering. *Meas. Sci. Technol.* **2001,** *12* (5), R33-R51.

266.    deRegt, J. M.; deGroote, F. P. J.; vanderMullen, J. A. M.; Schram, D. C., Air entrainment in an inductively coupled plasma measured by Raman and Rayleigh scattering. *Spectroc. Acta Pt. B-Atom. Spectr.* **1996,** *51* (12), 1527-1534.

267.    Brehmer, F.; Welzel, S.; Klarenaar, B. L. M.; van der Meiden, H. J.; van de Sanden, M. C. M.; Engeln, R., Gas temperature in transient CO2 plasma measured by Raman scattering. *J. Phys. D-Appl. Phys.* **2015,** *48* (15), 6.

268.    Jia, F. D.; Sumi, N.; Ishikawa, K.; Kano, H.; Inui, H.; Kularatne, J.; Takeda, K.; Kondo, H.; Sekine, M.; Kono, A.; Hori, M., Laser Scattering Diagnosis of a 60-Hz Non-Equilibrium Atmospheric Pressure Plasma Jet. *Appl. Phys. Express* **2011,** *4* (2), 3.

269.    Penney, C. M.; Stpeters, R. L.; Lapp, M., ABSOLUTE ROTATIONAL RAMAN CROSS-SECTIONS FOR N2, O2, AND CO2. *Journal of the Optical Society of America* **1974,** *64* (5), 712-716.

270.    Penney, C.; Peters, R. S.; Lapp, M., Absolute rotational Raman cross sections for N 2, O 2, and CO 2. *JOSA* **1974,** *64* (5), 712-716.

271.    Long, D. A.; Long, D., *Raman spectroscopy*. McGraw-Hill New York: 1977; Vol. 206.

272.    Hoskins, L. C., Pure rotational Raman spectroscopy of diatomic molecules. *Journal of Chemical Education* **1975,** *52* (9), 568.

273.    Sneep, M.; Ubachs, W., Direct measurement of the Rayleigh scattering cross section in various gases. *Journal of Quantitative Spectroscopy and Radiative Transfer* **2005,** *92* (3), 293-310.

274.    Eckbreth, A. C., *Laser diagnostics for combustion temperature and species*. CRC Press: 1996; Vol. 3.

275.    Klarenaar, B. L. M.; Brehmer, F.; Welzel, S.; van der Meiden, H. J.; van de Sanden, M. C. M.; Engeln, R., Note: Rotational Raman scattering on CO2 plasma using a volume Bragg grating as a notch filter. *Rev. Sci. Instrum.* **2015,** *86* (4), 3.

276.    Deng, X.; Nikiforov, A. Y.; Ionita, E.-R.; Dinescu, G.; Leys, C., Absolute and relative emission spectroscopy study of 3 cm wide planar radio frequency atmospheric pressure bio-plasma source. *Applied Physics Letters* **2015,** *107* (5), 053702.

277.    Winchester, M. R.; Payling, R., Radio-frequency glow discharge spectrometry: A critical review. *Spectroc. Acta Pt. B-Atom. Spectr.* **2004,** *59* (5), 607-666.

278.    Nilsson, J. W.; Riedel, S. A., *Introductory circuits for electrical and computer engineering*. Pearson Education: 2001.

279.    Yanguas-Gil, A.; Focke, K.; Benedikt, J.; Von Keudell, A., Optical and electrical characterization of an atmospheric pressure microplasma jet for Ar∕ CH 4 and Ar∕ C 2 H 2 mixtures. *J. Appl. Phys.* **2007,** *101* (10), 103307.

280.    Reuter, S., *Formation mechanisms of atomic oxygen in an atmospheric pressure plasma jet characterised by spectroscopic methods*. Cuvillier Verlag: 2008.

281.    Cullen, P. J.; Milosavljevic, V., Spectroscopic characterization of a radio-frequency argon plasma jet discharge in ambient air. *Prog. Theor. Exp. Phys.* **2015,** (6), 17.

282.    Kawamura, E.; Lieberman, M.; Lichtenberg, A.; Chabert, P.; Lazzaroni, C., Particle-in-cell and global simulations of α to γ transition in atmospheric pressure Penning-dominated capacitive discharges. *Plasma Sources Sci. Technol* **2014,** *23* (035014), 0963-0252.

283.    Mitchner, M.; Kruger, C., Partially Ionized Gasses. Wiley&Sons. *New York* **1973**.

284.    Ellis, H.; Pai, R.; McDaniel, E.; Mason, E.; Viehland, L., Transport properties of gaseous ions over a wide energy range. *Atomic Data and Nuclear Data Tables* **1976,** *17* (3), 177-210.

285.    Nikiforov, A. Y.; Ionita, E.-R.; Dinescu, G.; Leys, C., Characterization of a planar 8 mm atmospheric pressure wide radiofrequency plasma source by spectroscopy techniques. *Plasma Phys. Control. Fusion* **2015,** *58* (1), 014013.

286.    Winchester, M. R.; Payling, R., Radio-frequency glow discharge spectrometry:: A critical review. *Spectrochimica Acta Part B: Atomic Spectroscopy* **2004,** *59* (5), 607-666.

287.    Raizer, Y. P., Gas discharge physics. **1991**.

288.    Vorac, J., massiveOES. *Atlassian Inc.,[Online]. Available: [https://bitbucket](https://bitbucket). org/OES_muni/massiveoes.[Accessed 26 11 2018]*.

289.    Bruggeman, P.; Iza, F.; Guns, P.; Lauwers, D.; Kong, M. G.; Gonzalvo, Y. A.; Leys, C.; Schram, D. C., Electronic quenching of OH(A) by water in atmospheric pressure plasmas and its influence on the gas temperature determination by OH(A-X) emission. *Plasma Sources Sci. Technol.* **2010,** *19* (1), 7.

290.    Laroussi, M., Low temperature plasma-based sterilization: Overview and state-of-the-art. *Plasma Process. Polym.* **2005,** *2* (5), 391-400.

291.    Weltmann, K. D.; von Woedtke, T., Plasma medicine-current state of research and medical application. *Plasma Phys. Controlled Fusion* **2017,** *59* (1), 014031.

292.    Kong, M. G.; Kroesen, G.; Morfill, G.; Nosenko, T.; Shimizu, T.; van Dijk, J.; Zimmermann, J. L., Plasma medicine: an introductory review. *New Journal of Physics* **2009,** *11*, 35-.

293.    Fridman, A. A.; Lin, A.; Miller, V.; Bekeschus, S.; Wende, K.; Weltmann, K.-D., The Plasma Treatment Unit: An Attempt to Standardize Cold Plasma Treatment for Defined Biological Effects. *Plasma Medicine* **2018,** *8* (2), 195-201.

294.    Stratmann, B.; Costea, T. C.; Nolte, C.; Hiller, J.; Schmidt, J.; Reindel, J.; Masur, K.; Motz, W.; Timm, J.; Kerner, W.; Tschoepe, D., Effect of Cold Atmospheric Plasma Therapy vs Standard Therapy Placebo on Wound Healing in Patients With Diabetic Foot Ulcers: A Randomized Clinical Trial. *JAMA Netw Open* **2020,** *3* (7), e2010411.

295.    Shome, D.; von Woedtke, T.; Riedel, K.; Masur, K., The HIPPO Transducer YAP and Its Targets CTGF and Cyr61 Drive a Paracrine Signalling in Cold Atmospheric Plasma-Mediated Wound Healing. *Oxid. Med. Cell. Longev.* **2020,** *2020*, 4910280.

296.    Lin, A.; Gorbanev, Y.; Cos, P.; Smits, E.; Bogaerts, A., Plasma Elicits Immunogenic Death In Melanoma Cells. *Clin. Plas. Med.* **2018,** *9*.

297.    Bekeschus, S.; Moritz, J.; Helfrich, I.; Boeckmann, L.; Weltmann, K.-D.; Emmert, S.; Metelmann, H.-R.; Stoffels, I.; von Woedtke, T., Ex Vivo Exposure of Human Melanoma Tissue to Cold Physical Plasma Elicits Apoptosis and Modulates Inflammation. *Applied Sciences* **2020,** *10* (6), 1971.

298.    Schmidt, A.; von Woedtke, T.; Vollmar, B.; Hasse, S.; Bekeschus, S., Nrf2 signaling and inflammation are key events in physical plasma-spurred wound healing. *Theranostics* **2019,** *9* (4), 1066-1084.

299.    Privat-Maldonado, A.; Schmidt, A.; Lin, A.; Weltmann, K. D.; Wende, K.; Bogaerts, A.; Bekeschus, S., ROS from Physical Plasmas: Redox Chemistry for Biomedical Therapy. *Oxid Med Cell Longev* **2019,** *2019*, 9062098.

300.    Brandenburg, R., Dielectric barrier discharges: progress on plasma sources and on the understanding of regimes and single filaments. *Plasma Sources Sci. Technol.* **2017,** *26* (5), 053001.

301.    Sato, M.; Ohgiyama, T.; Clements, J. S., Formation of chemical species and their effects on microorganisms using a pulsed high-voltage discharge in water. *IEEE Transactions on Industry applications* **1996,** *32* (1), 106-112.

302.    Burlica, R.; Grim, R.; Shih, K. Y.; Balkwill, D.; Locke, B., Bacteria inactivation using low power pulsed gliding arc discharges with water spray. *Plasma Process. Polym.* **2010,** *7* (8), 640-649.

303.    Maguire, P.; Mahony, C.; Kelsey, C.; Bingham, A.; Montgomery, E.; Bennet, E.; Potts, H.; Rutherford, D.; McDowell, D.; Diver, D., Controlled microdroplet

transport in an atmospheric pressure microplasma. *Applied Physics Letters* **2015,** *106* (22), 224101.

304.     Oinuma, G.; Nayak, G.; Du, Y.; Bruggeman, P. J., Controlled plasma–droplet interactions: A quantitative study of OH transfer in plasma–liquid interaction. *Plasma Sources Science and Technology* **2020,** *29* (9), 095002.

305.     Sremački, I.; Jurov, A.; Modic, M.; Cvelbar, U.; Wang, L.; Leys, C.; Nikiforov, A. Y., On diagnostics of an annular shape RF plasma jet operating in Ar at atmospheric conditions. *Plasma Sources Science and Technology* **2020**.

306.     Sremački, I.; Wang, L.; Jurov, A.; Modic, M.; Cvelbar, U.; Leys, C.; Nikiforov, A. In *Radio-frequency plasma in combination with aerosol injection for biomedical applications*, 24th International Symposium on Plasma Chemistry, International Plasma Chemistry Society (IPCS): 2019.

307.     Hendawy, N.; McQuaid, H.; Mariotti, D.; Maguire, P., Continuous gas temperature measurement of cold plasma jets containing microdroplets, using a focussed spot IR sensor. *Plasma Sources Science and Technology* **2020,** *29* (8), 085010.

308.     von Woedtke, T.; Schmidt, A.; Bekeschus, S.; Wende, K.; Weltmann, K.-D., Plasma Medicine: A field of applied redox biology. *in vivo* **2019,** *33* (4), 1011-1026.

309.     Weidinger, A.; Kozlov, A. V., Biological activities of reactive oxygen and nitrogen species: oxidative stress versus signal transduction. *Biomolecules* **2015,** *5* (2), 472-484.

310.     Strollo, R.; Vinci, C.; Arshad, M. H.; Perrett, D.; Tiberti, C.; Chiarelli, F.; Napoli, N.; Pozzilli, P.; Nissim, A., Antibodies to post-translationally modified insulin in type 1 diabetes. *Diabetologia* **2015,** *58* (12), 2851-60.

311.     Bruno, G.; Heusler, T.; Lackmann, J.-W.; Von Woedtke, T.; Weltmann, K.-D.; Wende, K., Cold physical plasma-induced oxidation of cysteine yields reactive sulfur species (RSS). *Clinical Plasma Medicine* **2019,** *14*, 100083.

312.     Klinkhammer, C.; Verlackt, C.; Smilowicz, D.; Kogelheide, F.; Bogaerts, A.; Metzler-Nolte, N.; Stapelmann, K.; Havenith, M.; Lackmann, J. W., Elucidation of Plasma-induced Chemical Modifications on Glutathione and Glutathione Disulphide. *Sci Rep* **2017,** *7* (1), 13828.

313.     Takai, E.; Kitamura, T.; Kuwabara, J.; Ikawa, S.; Yoshizawa, S.; Shiraki, K.; Kawasaki, H.; Arakawa, R.; Kitano, K., Chemical modification of amino acids by atmospheric-pressure cold plasma in aqueous solution. *J. Phys. D-Appl. Phys.* **2014,** *47* (28), 285403.

314.     Lackmann, J. W.; Wende, K.; Verlackt, C.; Golda, J.; Volzke, J.; Kogelheide, F.; Held, J.; Bekeschus, S.; Bogaerts, A.; Schulz-von der Gathen, V.; Stapelmann, K., Chemical fingerprints of cold physical plasmas - an experimental and computational study using cysteine as tracer compound. *Sci Rep* **2018,** *8* (1), 7736.

315.     Go, Y. M.; Chandler, J. D.; Jones, D. P., The cysteine proteome. *Free Radic Biol Med* **2015,** *84*, 227-245.

316.     Tresp, H.; Hammer, M. U.; Winter, J.; Weltmann, K. D.; Reuter, S., Quantitative detection of plasma-generated radicals in liquids by electron paramagnetic resonance spectroscopy. *Journal of Physics D: Applied Physics* **2013,** *46* (43).

317.    Jablonowski, H.; Santos Sousa, J.; Weltmann, K. D.; Wende, K.; Reuter, S., Quantification of the ozone and singlet delta oxygen produced in gas and liquid phases by a non-thermal atmospheric plasma with relevance for medical treatment. *Sci Rep* **2018**, *8* (1), 12195.

318.    Jablonowski, H.; Schmidt-Bleker, A.; Weltmann, K. D.; von Woedtke, T.; Wende, K., Non-touching plasma-liquid interaction - where is aqueous nitric oxide generated? *Phys Chem Chem Phys* **2018**, *20* (39), 25387-25398.

319.    Verlackt, C. C. W.; Van Boxem, W.; Bogaerts, A., Transport and accumulation of plasma generated species in aqueous solution. *Phys Chem Chem Phys* **2018**, *20* (10), 6845-6859.

320.    Bruggeman, P.; Iza, F.; Lauwers, D.; Gonzalvo, Y. A., Mass spectrometry study of positive and negative ions in a capacitively coupled atmospheric pressure RF excited glow discharge in He–water mixtures. *Journal of Physics D: Applied Physics* **2009,** *43* (1), 012003.

321.    Rosen, G. M.; Tsai, P.; Weaver, J.; Porasuphatana, S.; Roman, L. J.; Starkov, A. A.; Fiskum, G.; Pou, S., The role of tetrahydrobiopterin in the regulation of neuronal nitric-oxide synthase-generated superoxide. *J Biol Chem* **2002,** *277* (43), 40275-80.

322.    Tong, H.; Arangio, A. M.; Lakey, P. S. J.; Berkemeier, T.; Liu, F.; Kampf, C. J.; Brune, W. H.; Pöschl, U.; Shiraiwa, M., Hydroxyl radicals from secondary organic aerosol decomposition in water. *Atmospheric Chemistry and Physics* **2016,** *16* (3), 1761-1771.

323.    Lisovskaya, A. G.; Edimecheva, I. P.; Shadyro, O. I., A Novel Pathway of Photoinduced Decomposition of Sphingolipids. *Photochemistry and Photobiology* **2012,** *88* (4), 899-903.

324.    Zvereva, G. N., Using vacuum ultraviolet radiation to obtain highly reactive radicals. *J Opt Technol+* **2012,** *79* (8), 477-483.

325.    Jablonowski, H.; Bussiahn, R.; Bundscherer, L.; Monden, A.; Hammer, M. U.; Masur, K.; Weltmann, K. D.; Reuter, S., Plasma Jet (V) UV-Radiation Impact on Biologically Relevant Liquids and Cell Suspension. *Bulletin of the American Physical Society* **2014,** *59*.

326.    Attri, P.; Kim, Y. H.; Park, D. H.; Park, J. H.; Hong, Y. J.; Uhm, H. S.; Kim, K. N.; Fridman, A.; Choi, E. H., Generation mechanism of hydroxyl radical species and its lifetime prediction during the plasma-initiated ultraviolet (UV) photolysis. *Sci Rep* **2015,** *5*, 9332.

327.    Hoigne, J.; Bader, H., Ozonation of Water - Kinetics of Oxidation of Ammonia by Ozone and Hydroxyl Radicals. *Environmental Science \& Technology* **1978,** *12 %6* (1), 79-84 %&.

328.    Hoigné, J., The Chemistry of Ozone in Water. **1988**, 121-141.

329.    Flyunt, R.; Leitzke, A.; Mark, G.; Mvula, E.; Reisz, E.; Schick, R.; von Sonntag, C., Determination of•OH, O2•-, and Hydroperoxide Yields in Ozone Reactions in Aqueous Solution†. *The Journal of Physical Chemistry B* **2003,** *107* (30), 7242-7253.

330.    Gorbanev, Y.; O'Connell, D.; Chechik, V., Non-Thermal Plasma in Contact with Water: The Origin of Species. *Chemistry* **2016,** *22* (10), 3496-3505.

331.    Winter, J.; Wende, K.; Masur, K.; Iseni, S.; Dunnbier, M.; Hammer, M. U.; Tresp, H.; Weltmann, K. D.; Reuter, S., Feed gas humidity: a vital parameter affecting

a cold atmospheric-pressure plasma jet and plasma-treated human skin cells. *J. Phys. D-Appl. Phys.* **2013,** *46* (29).

332.    Hideg, E.; Deak, Z.; Hakala-Yatkin, M.; Karonen, M.; Rutherford, A. W.; Tyystjarvi, E.; Vass, I.; Krieger-Liszkay, A., Pure forms of the singlet oxygen sensors TEMP and TEMPD do not inhibit Photosystem II. *Biochim Biophys Acta* **2011,** *1807* (12), 1658-61.

333.    Schmidt-Bleker, A.; Winter, J.; Bosel, A.; Reuter, S.; Weltmann, K. D., On the plasma chemistry of a cold atmospheric argon plasma jet with shielding gas device. *Plasma Sources Sci. Technol.* **2016,** *25* (1), 015005.

334.    Zhang, S. Q.; van Gaens, W.; van Gessel, B.; Hofmann, S.; van Veldhuizen, E.; Bogaerts, A.; Bruggeman, P., Spatially resolved ozone densities and gas temperatures in a time modulated RF driven atmospheric pressure plasma jet: an analysis of the production and destruction mechanisms. *J. Phys. D-Appl. Phys.* **2013,** *46* (20), 205202.

335.    Pekárek, S., Non-Thermal Plasma Ozone Generation. *Acta Polytechnica* **2003,** *43*, 5.

336.    Reuter, S.; von Woedtke, T.; Weltmann, K. D., The kINPen-a review on physics and chemistry of the atmospheric pressure plasma jet and its applications. *J. Phys. D-Appl. Phys.* **2018,** *51* (23).

337.    Quiller, R. G.; Baker, T. A.; Deng, X.; Colling, M. E.; Min, B. K.; Friend, C. M., Transient hydroxyl formation from water on oxygen-covered Au(111). *J Chem Phys* **2008,** *129* (6), 064702.

338.    Lifshitz, C., Reaction mechanism of mononegative atomic oxygen + water .fwdarw. hydroxide + hydroxyl at low incident ion energies. *The Journal of Physical Chemistry* **1982,** *86* (18), 3634-3637.

339.    Lackmann, J.-W.; Bruno, G.; Jablonowski, H.; Kogelheide, F.; Offerhaus, B.; Held, J.; Schulz-von der Gathen, V.; Stapelmann, K.; von Woedtke, T.; Wende, K., Nitrosylation vs. oxidation - How to modulate cold physical plasmas for biological applications. *PLoS One* **2019,** *14* (5), e0216606.

340.    Zoschke, K.; Bornick, H.; Worch, E., Vacuum-UV radiation at 185 nm in water treatment--a review. *Water Res* **2014,** *52*, 131-45.

341.    Goldstein, S.; Rabani, J., Mechanism of Nitrite Formation by Nitrate Photolysis in Aqueous Solutions: The Role of Peroxynitrite, Nitrogen Dioxide, and Hydroxyl Radical. *Journal of the American Chemical Society* **2007,** *129* (34), 10597-10601.

342.    Gölzenleuchter, H.; Gericke, K.-H.; Josef Comes, F.; Linde, P. F., Photodissociation of hydrogen peroxide at 157 nm: rotational distribution of nascent OH(2Σ+, υ', N'). *Chemical Physics* **1984,** *89* (1), 93-102.

343.    Nakamura, K.; Shirato, M.; Tenkumo, T.; Kanno, T.; Westerlund, A.; Ortengren, U.; Sasaki, K.; Niwano, Y., Hydroxyl radicals generated by hydrogen peroxide photolysis recondition biofilm-contaminated titanium surfaces for subsequent osteoblastic cell proliferation. *Sci Rep* **2019,** *9* (1), 4688.

344.    Ikai, H.; Nakamura, K.; Shirato, M.; Kanno, T.; Iwasawa, A.; Sasaki, K.; Niwano, Y.; Kohno, M., Photolysis of hydrogen peroxide, an effective disinfection system via hydroxyl radical formation. *Antimicrob Agents Chemother* **2010,** *54* (12), 5086-91.

345.     France, J. L.; King, M. D.; Lee-Taylor, J., Hydroxyl (OH) radical production rates in snowpacks from photolysis of hydrogen peroxide (H2O2) and nitrate (NO3−). *Atmospheric Environment* **2007,** *41* (26), 5502-5509.

346.     Wende, K.; Bruno, G.; Lalk, M.; Weltmann, K.-D.; von Woedtke, T.; Bekeschus, S.; Lackmann, J.-W., On a heavy path – determining cold plasma-derived short-lived species chemistry using isotopic labelling. *RSC Advances* **2020,** *10* (20), 11598-11607.

347.     Bailey, J. L.; Cole, R. D., Studies on the Reaction of Sulfite with Proteins. *Journal of Biological Chemistry* **1959,** *234* (7), 1733-1739.

348.     Gunnison, A. F.; Palmes, E. D., Species variability in plasma S-sulfonate levels during and following sulfite administration. *Chemico-Biological Interactions* **1978,** *21* (2-3), 315-329.

349.     Gunnison, A. F.; Benton, A. W., Sulfur dioxide: Sulfite. Interaction with mammalian serum and plasma. *Arch Environ Health* **1971,** *22* (3), 381-8.

350.     Darwent, B. d., *Bond dissociation energies in simple molecules*. U.S. National Bureau of Standards; for sale by the Supt. of Docs., U.S. Govt. Print. Off.: [Washington], 1970; p iv, 48 p.

351.     Mackle, H., The thermochemistry of sulphur-containing molecules and radicals—II. *Tetrahedron* **1963,** *19* (7), 1159-1170.

352.     Jablonowski, H.; Bussiahn, R.; Hammer, M. U.; Weltmann, K.-D.; von Woedtke, T.; Reuter, S., Impact of plasma jet vacuum ultraviolet radiation on reactive oxygen species generation in bio-relevant liquids. *Phys. Plasmas* **2015,** *22* (12), 122008.

353.     Kalyanaraman, B., Thiyl radicals in biological systems: significant or trivial? *Biochem Soc Symp* **1995,** *61*, 55-63.

354.     Sevilla, M. D.; Becker, D.; Yan, M., The formation and structure of the sulfoxyl radicals RSO(.), RSOO(.), RSO2(.), and RSO2OO(.) from the reaction of cysteine, glutathione and penicillamine thiyl radicals with molecular oxygen. *Int J Radiat Biol* **1990,** *57* (1), 65-81.

355.     Collet, G.; Robert, E.; Lenoir, A.; Vandamme, M.; Darny, T.; Dozias, S.; Kieda, C.; Pouvesle, J. M., Plasma jet-induced tissue oxygenation: potentialities for new therapeutic strategies. *Plasma Sources Science and Technology* **2014,** *23* (1), 012005.

356.     Schmidt, A.; Bekeschus, S.; Wende, K.; Vollmar, B.; von Woedtke, T., A cold plasma jet accelerates wound healing in a murine model of full-thickness skin wounds. *Experimental dermatology* **2017,** *26* (2), 156-162.

357.     Daeschlein, G.; Scholz, S.; Ahmed, R.; von Woedtke, T.; Haase, H.; Niggemeier, M.; Kindel, E.; Brandenburg, R.; Weltmann, K.-D.; Juenger, M., Skin decontamination by low-temperature atmospheric pressure plasma jet and dielectric barrier discharge plasma. *Journal of Hospital Infection* **2012,** *81* (3), 177-183.

358.     Daeschlein, G.; Napp, M.; Lutze, S.; Arnold, A.; von Podewils, S.; Guembel, D.; Jünger, M., Skin and wound decontamination of multidrug-resistant bacteria by cold atmospheric plasma coagulation. *JDDG: Journal der Deutschen Dermatologischen Gesellschaft* **2015,** *13* (2), 143-149.

359.     De Masi, G.; Gareri, C.; Cordaro, L.; Fassina, A.; Brun, P.; Zaniol, B.; Cavazzana, R.; Martines, E.; Zuin, M.; Marinaro, G., Plasma coagulation controller: a

low-power atmospheric plasma source for accelerated blood coagulation. *Plasma Medicine* **2018,** *8* (3).

360.    Fridman, G.; Peddinghaus, M.; Fridman, A.; Balasubramanian, M.; Gutsol, A.; Friedman, G. In *Use of non-thermal atmospheric pressure plasma discharge for coagulation and sterilization of surface wounds*, 32nd IEEE International Conference on Plasma Science, 2005; p 257.

361.    Hasse, S.; Duong Tran, T.; Hahn, O.; Kindler, S.; Metelmann, H. R.; von Woedtke, T.; Masur, K., Induction of proliferation of basal epidermal keratinocytes by cold atmospheric-pressure plasma. *Clinical and experimental dermatology* **2016,** *41* (2), 202-209.

362.    Park, J.; Lee, H.; Lee, H. J.; Kim, G. C.; Kim, S.-S.; Han, S.; Song, K., Non-thermal atmospheric pressure plasma is an excellent tool to activate proliferation in various mesoderm-derived human adult stem cells. *Free Radical Biology and Medicine* **2019,** *134*, 374-384.

363.    Khlyustova, A.; Labay, C.; Machala, Z.; Ginebra, M.-P.; Canal, C., Important parameters in plasma jets for the production of RONS in liquids for plasma medicine: A brief review. *Frontiers of Chemical Science and Engineering* **2019,** *13* (2), 238-252.

364.    Privat-Maldonado, A.; Gorbanev, Y.; O'Connell, D.; Vann, R.; Chechik, V.; Van der Woude, M., Nontarget biomolecules alter macromolecular changes induced by bactericidal low–temperature plasma. *IEEE transactions on radiation and plasma medical sciences* **2017,** *2* (2), 121-128.

365.    Kurita, H.; Haruta, N.; Uchihashi, Y.; Seto, T.; Takashima, K., Strand breaks and chemical modification of intracellular DNA induced by cold atmospheric pressure plasma irradiation. *PloS one* **2020,** *15* (5), e0232724.

366.    Reuter, S.; Tresp, H.; Wende, K.; Hammer, M. U.; Winter, J.; Masur, K.; Schmidt-Bleker, A.; Weltmann, K.-D., From RONS to ROS: tailoring plasma jet treatment of skin cells. *IEEE Trans. Plasma Sci.* **2012,** *40* (11), 2986-2993.

367.    Kim, S. J.; Chung, T., Cold atmospheric plasma jet-generated RONS and their selective effects on normal and carcinoma cells. *Scientific reports* **2016,** *6* (1), 1-14.

368.    Bauer, G.; Sersenová, D.; Graves, D. B.; Machala, Z., Cold atmospheric plasma and plasma-activated medium trigger RONS-based tumor cell apoptosis. *Scientific reports* **2019,** *9* (1), 1-28.

369.    Di Meo, S.; Reed, T. T.; Venditti, P.; Victor, V. M., Role of ROS and RNS sources in physiological and pathological conditions. *Oxidative medicine and cellular longevity* **2016,** *2016*.

370.    Xu, G. M.; Zhang, G. J.; Shi, X. M.; Ma, Y.; Wang, N.; Li, Y., Bacteria Inactivation Using DBD Plasma Jet in Atmospheric Pressure Argon. *Plasma Sci. Technol.* **2009,** *11* (1), 83-88.

371.    Brandenburg, R.; Lange, H.; von Woedtke, T.; Stieber, M.; Kindel, E.; Ehlbeck, J.; Weltmann, K.-D., Antimicrobial effects of UV and VUV radiation of nonthermal plasma jets. *IEEE Trans. Plasma Sci.* **2009,** *37* (6), 877-883.

372.    Pathak, M.; Krämer, D.; Güngerich, U., Formation of thymine dimers in mammalian skin by ultraviolet radiation in vivo. *Photochemistry and photobiology* **1972,** *15* (2), 177-185.

373.    Pfeifer, G. P.; Besaratinia, A., UV wavelength-dependent DNA damage and human non-melanoma and melanoma skin cancer. *Photochemical & photobiological sciences* **2012,** *11* (1), 90-97.

374.    Molho-Pessach, V.; Lotem, M., Ultraviolet radiation and cutaneous carcinogenesis. *Environmental Factors in Skin Diseases* **2007,** *35*, 14-27.

375.    Meinhardt, M.; Krebs, R.; Anders, A.; Heinrich, U.; Tronnier, H., Wavelength-dependent penetration depths of ultraviolet radiation in human skin. *Journal of biomedical optics* **2008,** *13* (4), 044030.

376.    Brozyna, A.; Zbytek, B.; Granese, J.; Carlson, J. A.; Ross, J.; Slominski, A., Mechanism of UV-related carcinogenesis and its contribution to nevi/melanoma. *Expert review of dermatology* **2007,** *2* (4), 451-469.

377.    Beani, J.-C., Ultraviolet A-induced DNA damage: role in skin cancer. *Bulletin de l'Academie nationale de medecine* **2014,** *198* (2), 273-295.

378.    Bahre, H.; Lange, H.; Schulz-von der Gathen, V.; Foest, R., Vacuum ultraviolet (VUV) emission of an atmospheric pressure plasma jet (μ-APPJ) operated in helium-oxygen mixtures in ambient air. *Acta Tech* **2011,** *56* (T199).

379.    Cámara-Torres, M.; Sinha, R.; Scopece, P.; Neubert, T.; Lachmann, K.; Patelli, A.; Mota, C.; Moroni, L., Tuning Cell Behavior on 3D Scaffolds Fabricated by Atmospheric Plasma-Assisted Additive Manufacturing. *ACS applied materials & interfaces* **2021,** *13* (3), 3631-3644.

380.    Alavi, S. K.; Lotz, O.; Akhavan, B.; Yeo, G.; Walia, R.; McKenzie, D. R.; Bilek, M. M., Atmospheric Pressure Plasma Jet Treatment of Polymers Enables Reagent-Free Covalent Attachment of Biomolecules for Bioprinting. *ACS Applied Materials & Interfaces* **2020,** *12* (34), 38730-38743.

381.    Nakajima, Y.; Mukai, K.; Rahayu, H. S. E.; Nur, M.; Ishijima, T.; Enomoto, H.; Uesugi, Y.; Sugama, J.; Nakatani, T., Cold plasma on full-thickness cutaneous wound accelerates healing through promoting inflammation, re-epithelialization and wound contraction. *Clinical Plasma Medicine* **2014,** *2* (1), 28-35.

382.    Xu, G. M.; Shi, X. M.; Cai, J. F.; Chen, S. L.; Li, P.; Yao, C. W.; Chang, Z. S.; Zhang, G. J., Dual effects of atmospheric pressure plasma jet on skin wound healing of mice. *Wound Repair and Regeneration* **2015,** *23* (6), 878-884.

383.    Sremački, I.; Bruno, G.; Jablonowski, H.; Leys, C.; Nikiforov, A. Y.; Wende, K., Influence of aerosol injection on the liquid chemistry induced by an RF argon plasma jet. *Plasma Sources Science and Technology* **2021**.

384.    McMahon, S. J.; Currell, F. J., A robust curve-fitting procedure for the analysis of plasmid DNA strand break data from gel electrophoresis. *Radiation Research* **2011,** *175* (6), 797-805.

385.    Sremački, I.; Jurov, A.; Modic, M.; Cvelbar, U.; Wang, L.; Leys, C.; Nikiforov, A., On diagnostics of annular-shape radio-frequency plasma jet operating in argon in atmospheric conditions. *Plasma Sources Science and Technology* **2020,** *29* (3), 035027.

386.    Eruslanov, E.; Kusmartsev, S., Identification of ROS using oxidized DCFDA and flow-cytometry. In *Advanced protocols in oxidative stress II*, Springer: 2010; pp 57-72.

387.    Chen, X.; Zhong, Z.; Xu, Z.; Chen, L.; Wang, Y., 2′, 7′-Dichlorodihydrofluorescein as a fluorescent probe for reactive oxygen species

measurement: forty years of application and controversy. *Free radical research* **2010,** *44* (6), 587-604.

388.     Reiniers, M. J.; van Golen, R. F.; Bonnet, S.; Broekgaarden, M.; van Gulik, T. M.; Egmond, M. R.; Heger, M., Preparation and practical applications of 2', 7'-dichlorodihydrofluorescein in redox assays. *Analytical chemistry* **2017,** *89* (7), 3853-3857.

389.     Moreau, E., Airflow control by non-thermal plasma actuators. *Journal of physics D: applied physics* **2007,** *40* (3), 605.

390.     Li, G.; Li, H.-P.; Wang, L.-Y.; Wang, S.; Zhao, H.-X.; Sun, W.-T.; Xing, X.-H.; Bao, C.-Y., Genetic effects of radio-frequency, atmospheric-pressure glow discharges with helium. *Applied physics letters* **2008,** *92* (22), 221504.

391.     Brabcová, K. P.; Jamborová, Z.; Michaelidesová, A.; Davídková, M.; Kodaira, S.; Šefl, M.; Štěpán, V., Radiation-induced plasmid DNA damage: effect of concentration and length. *Radiation protection dosimetry* **2019,** *186* (2-3), 168-171.

392.     Meyers, J. A.; Sanchez, D.; Elwell, L. P.; Falkow, S., Simple agarose gel electrophoretic method for the identification and characterization of plasmid deoxyribonucleic acid. *Journal of bacteriology* **1976,** *127* (3), 1529-1537.

393.     Dujardin, N.; Smissen, P. V. D.; Préat, V., Topical gene transfer into rat skin using electroporation. *Pharmaceutical research* **2001,** *18* (1), 61-66.

394.     Lademann, J. M.; Richter, H.; Alborova, A.; Humme, D.; Patzelt, A.; Kramer, A.; Weltmann, K.-D.; Hartmann, B.; Ottomann, C.; Fluhr, J. W., Risk assessment of the application of a plasma jet in dermatology. *Journal of biomedical optics* **2009,** *14* (5), 054025.

395.     Singer, A. J.; Clark, R. A., Cutaneous wound healing. *New England journal of medicine* **1999,** *341* (10), 738-746.

396.     Vaughan, M. B.; Howard, E. W.; Tomasek, J. J., Transforming growth factor-β1 promotes the morphological and functional differentiation of the myofibroblast. *Experimental cell research* **2000,** *257* (1), 180-189.

397.     Fridman, G.; Friedman, G.; Gutsol, A.; Shekhter, A. B.; Vasilets, V. N.; Fridman, A., Applied plasma medicine. *Plasma Process. Polym.* **2008,** *5* (6), 503-533.

398.     Privat-Maldonado, A.; Schmidt, A.; Lin, A.; Weltmann, K.-D.; Wende, K.; Bogaerts, A.; Bekeschus, S., ROS from physical plasmas: Redox chemistry for biomedical therapy. *Oxidative Medicine and Cellular Longevity* **2019,** *2019*.

399.     Sremački, I.; Kos, S. p.; Bošnjak, M. a.; Jurov, A.; Serša, G.; Modic, M.; Leys, C.; Cvelbar, U.; Nikiforov, A., Plasma Damage Control: From Biomolecules to Cells and Skin. *ACS Applied Materials & Interfaces* **2021,** *13* (39), 46303-46316.

400.     Park, J. H.; Kim, M.; Shiratani, M.; Cho, A. E.; Choi, E. H.; Attri, P., Variation in structure of proteins by adjusting reactive oxygen and nitrogen species generated from dielectric barrier discharge jet. *Scientific reports* **2016,** *6* (1), 1-14.

401.     Livak, K. J.; Schmittgen, T. D., Analysis of relative gene expression data using real-time quantitative PCR and the 2− ΔΔCT method. *methods* **2001,** *25* (4), 402-408.

402.     Smith, M.; Barbenel, J.; Courtney, J.; Grant, M., Novel quantitative methods for the determination of biomaterial cytotoxicity. SAGE Publications Sage UK: London, England: 1992.

403.    Yonson, S.; Coulombe, S.; Leveille, V.; Leask, R., Cell treatment and surface functionalization using a miniature atmospheric pressure glow discharge plasma torch. *Journal of Physics D: Applied Physics* **2006,** *39* (16), 3508.

404.    Afratis, N. A.; Nikitovic, D.; Multhaupt, H. A.; Theocharis, A. D.; Couchman, J. R.; Karamanos, N. K., Syndecans–key regulators of cell signaling and biological functions. *The FEBS journal* **2017,** *284* (1), 27-41.

405.    Lukes, P.; Dolezalova, E.; Sisrova, I.; Clupek, M., Aqueous-phase chemistry and bactericidal effects from an air discharge plasma in contact with water: evidence for the formation of peroxynitrite through a pseudo-second-order post-discharge reaction of H2O2 and HNO2. *Plasma Sources Science and Technology* **2014,** *23* (1), 015019.

406.    Bradu, C.; Kutasi, K.; Magureanu, M.; Puač, N.; Živković, S., Reactive nitrogen species in plasma-activated water: generation, chemistry and application in agriculture. *Journal of Physics D: Applied Physics* **2020,** *53* (22), 223001.

407.    Breen, C.; Pal, R.; Elsegood, M. R.; Teat, S. J.; Iza, F.; Wende, K.; Buckley, B. R.; Butler, S. J., Time-resolved luminescence detection of peroxynitrite using a reactivity-based lanthanide probe. *Chemical science* **2020,** *11* (12), 3164-3170.

408.    Jandy, M.; Noor, A.; Nelson, P.; Dennys, C. N.; Karabinas, I. M.; Pestoni, J. C.; Singh, G. D.; Duc, L.; Devyldere, R.; Perdomo, N., Peroxynitrate nitration of Tyr 56 in Hsp90 induces PC12 cell death through P2X7R-dependent PTEN activation. *Redox Biology* **2022**, 102247.

409.    Zielonka, J.; Sikora, A.; Joseph, J.; Kalyanaraman, B., Peroxynitrite Is the Major Species Formed from Different Flux Ratios of Co-generated Nitric Oxide and Superoxide: DIRECT REACTION WITH BORONATE-BASED FLUORESCENT PROBE*♦. *Journal of Biological Chemistry* **2010,** *285* (19), 14210-14216.

410.    Bauer, G., The synergistic effect between hydrogen peroxide and nitrite, two long-lived molecular species from cold atmospheric plasma, triggers tumor cells to induce their own cell death. *Redox biology* **2019,** *26*, 101291.

411.    Sardella, E.; Mola, M. G.; Gristina, R.; Piccione, M.; Veronico, V.; De Bellis, M.; Cibelli, A.; Buttiglione, M.; Armenise, V.; Favia, P., A synergistic effect of reactive oxygen and reactive nitrogen species in plasma activated liquid media triggers astrocyte wound healing. *International journal of molecular sciences* **2020,** *21* (9), 3343.

412.    Haertel, B.; Von Woedtke, T.; Weltmann, K.-D.; Lindequist, U., Non-thermal atmospheric-pressure plasma possible application in wound healing. *Biomolecules & therapeutics* **2014,** *22* (6), 477.

413.    Huang, S.; Huang, G., Preparation and drug delivery of dextran-drug complex. *Drug delivery* **2019,** *26* (1), 252-261.

414.    Ludtke, J. J.; Sebestyén, M. G.; Wolff, J. A., The effect of cell division on the cellular dynamics of microinjected DNA and dextran. *Molecular Therapy* **2002,** *5* (5), 579-588.

415.    Larina, I. V.; Evers, B. M.; Esenaliev, R. O., Optimal drug and gene delivery in cancer cells by ultrasound-induced cavitation. *Anticancer research* **2005,** *25* (1A), 149-156.

416.    Guignet, E. G.; Meyer, T., Suspended-drop electroporation for high-throughput delivery of biomolecules into cells. *Nature methods* **2008,** *5* (5), 393-395.

417.     Stoffels, E.; Sakiyama, Y.; Graves, D. B., Cold atmospheric plasma: charged species and their interactions with cells and tissues. *IEEE Trans. Plasma Sci.* **2008,** *36* (4), 1441-1457.

An annular-shaped plasma jet coupled with aerosol is a promising tool in new biomedical technologies.